UNIVERSITY OF CALIFORNIA SAN DIEGO
SAN DIEGO STATE UNIVERSITY

Dynamic Modeling of Pulse-like Earthquakes and Ground Motions

A dissertation submitted in partial satisfaction of the
requirements for the degree
Doctor of Philosophy

in

Geophysics

by

Yongfei Wang

Committee in charge:

University of California San Diego

Professor Peter Shearer, Co-Chair
Professor Yuri Fialko
Professor Jiun-Shyan Chen

San Diego State University

Professor Steven Day, Co-Chair
Professor Kim Olsen
Professor Samuel Shen

2019

The dissertation of Yongfei Wang is approved, and it is acceptable in quality and form for publication on microfilm and electronically:

_____

_____

_____

_____

_____
Co-Chair

_____
Co-Chair

University of California San Diego

San Diego State University

2019

DEDICATION

To my wife Shiying Nie

and my two little cuties Charlotte Emily and Vincent Steven Wang.

EPIGRAPH

Dubito, ergo sum, vel, quod idem est, cogito, ergo sum.
I doubt, therefore I am – or what is the same – I think, therefore I am.
— Rene Descartes

When nothing seems to help, I go and look at a stonecutter hammering away at his rock perhaps a hundred times without as much as a crack showing in it. Yet at the hundred and first blow it will split in two, and I know it was not that blow that did it – but all that had gone before.
— Jacob Riis

TABLE OF CONTENTS

LIST OF FIGURES

LIST OF TABLES

ACKNOWLEDGEMENTS

Time of being a student for almost two decades finally comes to an end. During the years I spent in San Diego, I received enormous help from many people here. My foremost gratitude goes to my advisor, Professor Steven Day. Since when I came here, his guidance through the scientific world has been invaluable. He literally shapes my thinking about earthquakes, seismic waves, computations and bearing a good person, with his depth and breadth of knowledge and professionalism. He introduced me to the world of numerical simulations of earthquake dynamics. I still remembered how struggling I was to figure out numerous equations, thousands lines of codes and spuriously striking results from erroneous model setups. His door is always open for all my these either silly or frustrating questions. Specially sincere gratitude also goes to his off-hand mentorship and a free land he created for me because he by all means technically and emotionally supports me to freely explore the questions interesting myself with any restrictions (e.g., fundings). What I learn from him is not only how to become an independent researcher, but also how to become a caring person. His whole life is what I persistently pursue in my rest of life and I sincerely hope my daughter named by Steve and my son named after Steve will follow Steve's example in their life and work. Professor Peter Shearer as my co-advisor guides me in understanding seismological data. I am always impressed by his intuitive judgements about some special phenomena in seismic waveforms, which all the time turn out correct, and his ability of using a very simple mathematical equation to capture the cores of problems, exactly as he does in his classic textbook: Introduction to Seismology. His pursuit of a robust seismological feature by stacking abundant observed recordings (e.g., seismic waves and spectra) either in studying the earth deep structure or earthquake source property, teaches me never to overinterpret.

I would like to thanks my dissertation committee members, Professor Kim Olsen, Professor Yuri Fialko, Professor Jiun-Shyan Chen and Professor Samuel Shen for their support and help on my PhD research. The committee's feedback and comments were very helpful in improving this dissertation.

During my graduate studies, I took many useful classes from excellent lecturers. I want to address my deep gratitudes to them: Dr. Duncan Agnew, Dr. Peter Shearer, Dr. Guy Masters, Dr. David Sandwell, Dr. Hubert Staudigel, Dr. Kevin Brown, Dr. John Orcutt, and Dr. Dave Stegman in Scripps Institution of Oceanography at UCSD, Dr. Steve Day, Dr. Shuo Ma, Dr. Kim Olsen in Department of geological sciences at SDSU.

I owe a great debt of gratitude to my outstanding fellows for their broad-spectrum supports. I am grateful to friends in talented geophysics cohort of which I was part of: Wei, Adrian, Dara, Jessie, John and Matt. I also appreciate the support and friendship from JDP fellows: Zheqiang, Evan, Kyle, Qian, Bill, Eric, Zhao, Yuxiang, Nan, Zhifeng and Teh-Yang. They makes our daily life enjoyable with shared new ideals about gourmet restaurants, hiking trips and alien adventure. I also would like to acknowledge my other geophysicist friends: Marine who impresses me with her ehnthusiastics in research, Shanna who is forever filled with all kinds of interesting ideas, Jiuxun who is another trying to connect rupture dynamics to observational seismology, Taka who supports my theory with his dataset and Xiaohua who introduces me some fundamental earthquake geodetic concepts.

Finally, my endless love goes to my family. To my wife, Shiying Nie, you make me realize a big valuable piece of whole my life, living a maybe simple but happy life, which was missed in my past years. To my daughter Charlotte and son Vincent, you are the source of my exhilaration about life and motive me towards eternal happiness. To my parents and my sister, you are always supportive whenever I need you from any respects.

Chapter 2, in full, is a reformatted version of the material as it appears in Journal of Geophysical Research-Solid Earth: Wang, Y. and Day, S. M., "Seismic Source Spectral Properties of Crack-like and Pulse-like Modes of Dynamic Rupture", *Journal of Geophysical Research-Solid Earth*, 122, 2017. I was the primary investigator and author of this paper.

Chapter 3, in full, is a reformatted version of the material as it appears in Journal of Geophysical Research-Solid Earth: Wang, Y., Day, S. M. and Denolle, M. A., "Geometric

Controls on Pulse-Like Rupture in a Dynamic Model of the 2015 Gorkha Earthquake", *Journal of Geophysical Research-Solid Earth*, 124, 2019. I was the primary investigator and author of this paper.

Chapter 4, in full, is a reformatted version of a paper currently being prepared for submission for publication Journal of Geophysical Research-Solid Earth: Wang, Y. and Day, S. M., "Effects of Off-fault Inelasticity on Near-fault Directivity Pulses ", *Journal of Geophysical Research-Solid Earth*, 2019. I was the primary investigator and author of this paper.

VITA

2013	B. S. in Geophysics (*Best thesis*), University of Science and Technology of China
2014-2018	Graduate Teaching/Research Assistant, San Diego State University
2016	Visiting Graduate Researcher, Harvard University
2019	Ph. D. in Geophysics, University of California San Diego and San Diego State University

PUBLICATIONS

Wang, Y. and Day, S. M., "Seismic Source Spectral Properties of Crack-like and Pulse-like Modes of Dynamic Rupture", *Journal of Geophysical Research-Solid Earth*, 122, 2017.

Nie, S., Wang, Y., Olsen, K. B. and Day, S. M., "Fourth-Order Staggered-Grid Finite-Difference Seismic Wavefield Estimation Using a Discontinuous Mesh Interface (WEDMI)", *Bulletin of the Seismological Society of America*, 107(5), 2017.

Wang, Y., Day, S. M. and Denolle, M. A., "Geometric Controls on Pulse-Like Rupture in a Dynamic Model of the 2015 Gorkha Earthquake", *Journal of Geophysical Research-Solid Earth*, 124, 2019.

Wang, Y. and Day, S. M., "Effects of Off-fault Inelasticity on Near-fault Directivity Pulses", *submitted to Journal of Geophysical Research-Solid Earth*, 2019.

ABSTRACT OF THE DISSERTATION

Dynamic Modeling of Pulse-like Earthquakes and Ground Motions

by

Yongfei Wang

Doctor of Philosophy in Geophysics

University of California San Diego, 2019
San Diego State University, 2019

Professor Steven Day, Co-Chair
Professor Peter Shearer, Co-Chair

Growth of major populated cities near active faults (e.g., Los Angeles and San Francisco in USA, Tokyo and Osaka in Japan) has significantly elevated the seismic hazards. Understanding complex paradigm of near-fault ground motions is crucial in order to mitigate seismic hazards. Since the 1994 Mw 6.7 Northridge earthquake, there has been much discussion about the adequacy of building code and a term of "pulse". The engineering effects of near-fault pulse-like ground motions were strikingly exhibited in the 1994 Northridge earthquake in which great seismic damage was attributed to the large impulsive ground shaking of this type. Such near-fault pulse-like ground motions with high intensity and damage potentials are hypothetically associated to

either pulse-like rupture on fault or the rupture directivity. These mechanisms will be introduced and studied.

In Chapter 2, we study far-field effects of a self-healing pulse-like rupture mode with dynamic weakening. Pulse-like rupture leads to development of a second corner frequency, and the intermediate spectral slope is approximately 2 in most cases. The focal-sphere-averaged lower P and S wave corner frequencies are systematically higher for pulse-like models than crack models of comparable rupture velocity. The slip-weighted stress drop $\Delta\sigma_E$ exceeds the moment-based stress drop $\Delta\sigma_M$ for pulse-like ruptures, with the ratio ranging from about 1.3 to 1.65, while they are equal for the crack-like case. The transition from arresting- to growing-pulse rupture is accompanied by a large (factor of $\sim$1.6) increase in the radiation ratio. Thus, variations in rupture mode may account for the portion of the scatter in observational spectral estimates of source parameters.

In Chapter 3, we confirm the pulse-like ground motion in the 2015 Nepal Gorkha earthquake is related with the causing fault geometry of the Main Himalayan Thrust (MHT). Our dynamic rupture simulations in an elastoplastic medium yield earthquake parameters comparable to those deduced from kinematic inversions, including seismic moment and rupture velocity. The simulations reproduce pulse-like behavior predicting pulse widths in agreement with those kinematic studies and supporting an interpretation in which the pulse-like time dependence of slip is principally controlled by rupture geometry and it is observationally supported by near-field high-rate GPS recording at station KKN4.

In Chapter 4, we discuss the directivity-induced pulse-like ground motions and assess the extent to which plastic yielding, which is absent in standard kinematic models, may systematically affect the amplitude, frequency content, and distance scaling of directivity pulse. We perform some simple 2D kinematic and 3D spontaneous dynamic ruptures with and without plastic yielding on flat and rough faults, and find that each of the four 3D models (flat and rough faults, with and without off-fault yielding), scaled to approximately magnitude 7, predicts a

fault-normal pulse with characteristic behavior of observed pulses. Plastic yielding systematically reduces pulse amplitude and increases its dominant period, relative to models that neglect off-fault yielding. Yielding saturates near-fault peak ground velocity (PGV) with greater stress drops, alternatively interpreting observed magnitude saturation of PGV near a magnitude of 7, and provides physics-based implications for period-dependent distance taper and along-strike saturation of directivity-induced amplification, weakening the wedge-shaped directivity zone.

Chapter 1

Introduction

1.1 Motivation

The Growth of major populated cities near active faults (e.g., Los Angeles and San Francisco in USA, Tokyo and Osaka in Japan) has significantly elevated the seismic hazards. Hall et al. [1995] claimed that "Occurrence of large earthquakes close to cities in California is inevitable", which is also true for some other cities all over the world, especially to some vulnerable to earthquake-induced secondary hazards. For example, the 2008 M 8 Wenchuan earthquake struck an area where residents were living near seismically active faults (e.g., Lomgmenshan fault generated by continental collision between Eurasian and Indo-Australian plates), the extensive and deep Chengdu Basin, and soft mountainous terrains, and directly caused more than 15,000 geohazards in the form of landslides, rockfalls, and debris flows which resulted in about 20,000 deaths. Along with the knowledge that near-fault ground motions impose larger demands on civil structures than far from the fault, understanding the complex nature of near-fault ground motions is crucial in order to mitigate seismic hazards.

While in the past decades, more and more near-fault ground motion data has been collected, a deeper and closer look at ground motions of a large earthquake magnitude range is always

hindered by the limited number of observations. At moment magnitudes larger than 6, there is a great shortage of observations close to the source (within 10 km), and potential gain from supplementing those observations with simulations. Computational success has been gained at low frequencies ($<$1 Hz or so) in simulating strong ground motions, along with investigating attributes of earthquake sources and underground structure. Recently, computational ability has advanced to facilitate 3D simulations of high-frequency earthquake ground motions at very remote stations from the source. This is important because a larger range of synthetic ground-motion frequency content (e.g., 0.1 $\sim$ 10 Hz) can resolve seismic hazards for buildings with varying heights: a rough approximation is 0.1 second period per story (e.g., 10 story building would have a roughly natural frequency near 1 Hz and higher than 1 Hz for any shorter building). Within this frequency band, there are numerous ground-motion characteristics and their causative mechanisms worthwhile to explore both for their inherent scientific interest and for their applications to earthquake seismology and engineering.

Since the 1994 Mw 6.7 Northridge earthquake, there has been much discussion about the adequacy of building codes and the term "pulse" has had a prominent place in discussions of hazardous ground motions [Hall et al. 1995]. The term "pulse" has been used with reference to a significant long-period content of ground motion. Distinct from the oscillatory long-period motions arising from soft-soil effects or basin response, the compact long-period motion in displacement or velocity is associated directly with the fault-rupture process and source-to-site geometry. These strong pulse-like near-fault ground motions are of great interest in earthquake seismology and engineering. The engineering effects of near-fault pulse-like ground motions were strikingly exhibited in the 1994 Northridge earthquake (Figure 1.1) in which great seismic damage was attributed to the large impulsive ground shaking [Strasser and Bommer 2009] of this type. Such near-fault pulse-like ground motions with high intensity and damage potential, also found for example in the 1979 Imperial Valley, the 1992 Landers, the 2015 Nepal Gorkha and the 2002 Denali earthquakes, are hypothetically associated to either pulse-like rupture on fault or the

rupture directivity. These mechanisms will be introduced and studied in detail below.

1.2 Pulse-like rupture

Heaton [1990] inferred from seismic finite-fault inversions that most earthquake ruptures propagate in a pulse-like mode. That study was followed by others, including the recent synthesis of Melgar and Hayes [2017] who examined a larger and newer dataset of over 150 finite-fault rupture models (Mw 7 to 9) and favored the preponderance of pulse-like signatures (slip rise times much shorter than the source duration) (Figure 1.2). This is in contrast to the crack-like mode of rupture, in which the slip continues to expand until the rupture reaches the outer arresting edges and the rise time is comparable to the overall event time. The pulse-like fault kinematics shown in such seismic inversions can be caused by multiple on-fault mechanisms: velocity-dependent friction, heterogeneity of fault strength/stress, and finite downdip rupture dimension [Beeler and Tullis 1996; Beroza and Mikumo 1996; Cochard and Madariaga 1996; Day 1982; Day et al. 1998; Gabriel et al. 2012; Johnson 1992; Noda et al. 2009; Oglesby and Day 2002; Zheng and Rice 1998]. However, it is difficult on the basis of kinematic analysis alone to distinguish these effects on any individual rupture.

Despite the fact that the causative effects are difficult to distinguish given the frequency band applied in inferring current finite-fault models, they can be categorized into two major groups. The first group, containing velocity-dependent friction and heterogeneity of fault strength/stress, involves control of slip rise times by localized processes independent of the whole fault dimension, so that slip lasts no longer than that caused by fault geometry. This is termed “self-healing” rupture pulse. Velocity-dependent friction (dynamic-weakening friction, e.g., flash heating and thermal pressurization). Figure 1.3) is an example of the self-healing group and has been proposed as a mechanism to sustain the well-known weak San Andreas Fault (Hickman and Zoback [2004] estimate that the ratio between shear and normal stress on the SAF is only 0.2 - 0.4). The other

group in which slip duration is controlled by the overall fault geometry is often found to be consistent with finite-fault inversion and dynamic models, because natural earthquakes commonly have one characteristic scale length dictated by fault properties (e.g., seismogenic depth). Here we designate this the "geometry-induced" rupture pulse. A simple approximation of the rise time is the length of the finite dimension divided by 2 times rupture velocity [Day 1982]. If the fault shape transitions from a rectangle with a big length-to-width ratio to a square or circle, the geometry-induced pulse-like rupture will turn into a crack-like rupture as the rise time becomes comparable to the rupture duration.

A pulse-like rupture mode produces distinct effects (relative to crack-like rupture). Wang and Day [2017] in Chapter 2 find that a secondary spectral corner of the far-field seismic spectrum is introduced by a pulse-like source and seismic radiation efficiency is increased owing to a larger dynamic stress drop relative to the static stress drop. Wang et al. [2019] in Chapter 3 confirm the rupture pulse in 2015 Nepal Gorkha earthquake is strongly associated with the geologically plausible fault geometry of MHT (Main Himalayan Thrust) by matching the near-field impulsive high-rate GPS recording (15 km above the fault) without applying any filter. Aagaard and Heaton [2008] showed that the mechanism of pulse-like rupture can affect near-field ground motions in that the self-healing rupture can potentially compact the fault-normal pulse in a near-fault range. In contrast, a geometry-induced rupture pulse has longer rise time, and generates a broader directivity pulse.

1.3 Directivity pulse

When a rupture is propagating towards a site, directivity effects can cause much of the seismic energy to arrive in one large pulse polarized predominantly normal to the fault [Somerville et al. 1997]. The large, fault-normal velocity pulses mentioned above are observed when forward directivity conditions have been met. These conditions are that the rupture front is propagating

towards a site on the surface, and the direction of slip on the fault is aligned toward the site. They are readily met during simple strike-slip faulting, and can be observed qualitatively at site A in the simple case of a moving point source in Figure 1.4. Somerville et al. [1997] describe the general effects of directivity: an increase in amplitude as measured by pseudospectral acceleration (SA), a decrease in duration, and variation in the ratio of fault-normal to fault-parallel motions. To the extent that far-field approximations apply, the seismic energy resulting from a propagating rupture will be frequency-shifted in a manner analogous to the Doppler shifted radiation from a moving point source [Douglas et al. 1988]

In Chapter 4, we will discuss the directivity-induced pulse-like ground motions and assess the extent to which plastic yielding, which is absent in standard kinematic models, may systematically affect the amplitude, frequency content, and distance scaling of directivity pulse. Off-fault inelastic deformation during earthquake rupture results in a redistribution of stresses that in turn affect the subsequent rupture history and associated ground motion. These effects have been modeled in the framework of continuum plasticity (e.g. Drucker-Prager, Mohr-Coulomb and End-cap type) in recent studies [Andrews 2005; Duan and Day 2008; Dunham et al. 2011a; Dunham et al. 2011b; Ma and Hirakawa 2013; Shi and Day 2013; Roten et al. 2014; Hirakawa and Ma 2016]. These models suggest that the inelastic deformation not only reduces long-period ground motions [Roten et al. 2014] (Figure 1.5), but also partially filters out high frequency seismic motions [Ma and Hirakawa 2013]. It is important to understand how directivity-enhanced velocity pulses behave very close to the rupture surface, where plastic yielding is likely to affect their amplitude and waveforms.

While studies of ground-motion pulses have focused principally on the fault-normal component, there are some events in which pulse-like fault-parallel ground motions were also clearly observed (e.g., the 2002 Denali, the 1999 Kocaeli (Izmit) and Duzce earthquakes) in the near-fault regime. Moreover, the pulse periods of fault-parallel and fault-normal components with similar arrival times are very similar (Table 2 and 3 in Akkar and Gulkan [2002]). For the

2002 Denali earthquake, Dunham and Archuleta [2004] demonstrated that the initial pulses on both the fault-normal and fault-parallel components are due to a supershear rupture. Supershear-induced Mach waves characterized by a pulse of large amplitude and short duration are also observed in both the 1999 Kocaeli and Duzce earthquakes [Bouchon et al. 2000; Bouchon et al. 2001]. At steady-state supershear speed, S waves radiate and their velocity waveform on both the fault-normal and fault-parallel components is identical to the slip-velocity history. In contrast, a subshear rupture velocity results in a distance-dependent attenuation factor in near-fault ground motions [Dunham and Archuleta 2005]. An example in which both pulse types occur is the Pump station 10 recording of the 2002 Denali earthquake. There, the later-arriving pulse (corresponding to the later subshear rupture) is only manifest in fault-normal component. In summary, the fault-parallel impulsive motions are sensitive to the relativeness of the rupture velocity to the shear wave speed.

References

Aagaard, B. T. and Heaton, T. H. (2008). "Constraining fault constitutive behavior with slip and stress heterogeneity". In: *Journal of Geophysical Research-Solid Earth* 113.B04301.

Akkar, S. and Gulkan, P. (2002). "A critical examination of near-field accelerograms from the sea of Marmara region earthquakes". In: *Bulletin of the Seismological Society of America* 92.1, pp. 428–447.

Andrews, D. J. (2005). "Rupture dynamics with energy loss outside the slip zone". In: *Journal of Geophysical Research-Solid Earth* 110.B1.

Beeler, N. M. and Tullis, T. E. (1996). "Self-healing slip pulses in dynamic rupture models due to velocity-dependent strength". In: *Bulletin of the Seismological Society of America* 86.4, pp. 1130–1148.

Beroza, G. C. and Mikumo, T. (1996). "Short slip duration in dynamic rupture in the presence of heterogeneous fault properties". In: *Journal of Geophysical Research-Solid Earth* 101.B10, pp. 22449–22460.

Bouchon, M., Toksoz, N., Karabulut, H., Bouin, M. P., Dietrich, M., Aktar, M., and Edie, M. (2000). "Seismic imaging of the 1999 Izmit (Turkey) rupture inferred from the near-fault recordings". In: *Geophysical Research Letters* 27.18, pp. 3013–3016.

Bouchon, M., Bouin, M. P., Karabulut, H., Toksoz, M. N., Dietrich, M., and Rosakis, A. J. (2001). "How fast is rupture during an earthquake? New insights from the 1999 Turkey earthquakes". In: *Geophysical Research Letters* 28.14, pp. 2723–2726.

Cochard, A. and Madariaga, R. (1996). "Complexity of seismicity due to highly rate-dependent friction". In: *Journal of Geophysical Research-Solid Earth* 101.B11, pp. 25321–25336.

Day, S. M. (1982). "Three-dimensional finite difference simulation of fault dynamics: rectangular faults with fixed rupture velocity". In: *Bulletin of the Seismological Society of America* 72.3, pp. 705–727.

Day, S. M., Yu, G., and Wald, D. J. (1998). "Dynamic stress changes during earthquake rupture". In: *Bulletin of the Seismological Society of America* 88.2, pp. 512–522.

Douglas, A., Hudson, J. A., and Pearce, R. G. (1988). "Directivity and the Doppler-Effect". In: *Bulletin of the Seismological Society of America* 78.3, pp. 1367–1372.

Duan, B. and Day, S. M. (2008). "Inelastic strain distribution and seismic radiation from rupture of a fault kink". In: *Journal of Geophysical Research-Solid Earth* 113.B12.

Dunham, E. M. and Archuleta, R. J. (2004). "Evidence for a supershear transient during the 2002 Denali fault earthquake". In: *Bulletin of the Seismological Society of America* 94.6, S256–S268.

Dunham, E. M. and Archuleta, R. J. (2005). "Near-source ground motion from steady state dynamic rupture pulses". In: *Geophysical Research Letters* 32.3.

Dunham, E. M., Belanger, D., Cong, L., and Kozdon, J. E. (2011a). "Earthquake ruptures with strongly rate-weakening friction and off-fault plasticity, part 1: Planar faults". In: *Bulletin of the Seismological Society of America* 101.5, pp. 2296–2307.

— (2011b). "Earthquake Ruptures with Strongly Rate-Weakening Friction and Off-Fault Plasticity, Part 2: Nonplanar Faults". In: *Bulletin of the Seismological Society of America* 101.5, pp. 2308–2322.

Gabriel, A. A., Ampuero, J. P., Dalguer, L. A., and Mai, P. M. (2012). "The transition of dynamic rupture styles in elastic media under velocity-weakening friction". In: *Journal of Geophysical Research-Solid Earth* 117.

Goldsby, D. L. and Tullis, T. E. (2011). "Flash Heating Leads to Low Frictional Strength of Crustal Rocks at Earthquake Slip Rates". In: *Science* 334.6053, pp. 216–218.

Hall, J. F., Heaton, T. H., Halling, M. W., and Wald, D. J. (1995). "Near-Source Ground Motion and its Effects on Flexible Buildings". In: *Earthquake Spectra* 11.4, pp. 569–605.

Heaton, T. H. (1990). "Evidence for and Implications of Self-Healing Pulses of Slip in Earthquake Rupture". In: *Physics of the Earth and Planetary Interiors* 64.1, pp. 1–20.

Hickman, S. and Zoback, M. (2004). "Stress orientations and magnitudes in the SAFOD pilot hole". In: *Geophysical Research Letters* 31.15.

Hirakawa, E. and Ma, S. (2016). "Dynamic fault weakening and strengthening by gouge compaction and dilatancy in a fluid-saturated fault zone". In: *Journal of Geophysical Research-Solid Earth* 121.8, pp. 5988–6008.

Johnson, E. (1992). "The Influence of the Lithospheric Thickness on Bilateral Slip". In: *Geophysical Journal International* 108.1, pp. 151–160.

Ma, S. and Hirakawa, E. T. (2013). "Dynamic wedge failure reveals anomalous energy radiation of shallow subduction earthquakes". In: *Earth and Planetary Science Letters* 375, pp. 113–122.

Melgar, D. and Hayes, G. P. (2017). "Systematic observations of the slip pulse properties of large earthquake ruptures". In: *Geophysical Research Letters* 44.19, pp. 9691–9698.

Noda, H., Dunham, E. M., and Rice, J. R. (2009). "Earthquake ruptures with thermal weakening and the operation of major faults at low overall stress levels". In: *Journal of Geophysical Research-Solid Earth* 114.

Oglesby, D. D. and Day, S. M. (2002). "Stochastic fault stress: Implications for fault dynamics and ground motion". In: *Bulletin of the Seismological Society of America* 92.8, pp. 3006–3021.

Roten, D., Olsen, K. B., Day, S. M., Cui, Y., and Fah, D. (2014). "Expected seismic shaking in Los Angeles reduced by San Andreas fault zone plasticity". In: *Geophysical Research Letters* 41.8, pp. 2769–2777.

Shi, Z. Q. and Day, S. M. (2013). "Rupture dynamics and ground motion from 3-D rough-fault simulations". In: *Journal of Geophysical Research-Solid Earth* 118.3, pp. 1122–1141.

Somerville, P. G., Smith, N. F., Graves, R. W., and Abrahamson, N. A. (1997). "Modification of Empirical Strong Ground Motion Attenuation Relations to Include the Amplitude and Duration Effects of Rupture Directivity". In: *Seismological Research Letters* 68.1, pp. 199–222.

Strasser, F. O. and Bommer, J. J. (2009). "Review: Strong Ground Motions-Have We Seen the Worst?" In: *Bulletin of the Seismological Society of America* 99.5, pp. 2613–2637.

Wang, G., Zhang, S., Wang, C., and Yu, M. (2014). "Seismic performance evaluation of dam-reservoir-foundation systems to near-fault ground motions". In: *Natural Hazards* 72.2, pp. 651–674.

Wang, Y. and Day, S. M. (2017). "Seismic source spectral properties of crack-like and pulse-like modes of dynamic rupture". In: *Journal of Geophysical Research-Solid Earth* 122.8, pp. 6657–6684.

Wang, Y., Day, S. M., and Denolle, M. A. (2019). "Geometric Controls on Pulse-Like Rupture in a Dynamic Model of the 2015 Gorkha Earthquake". In: *Journal of Geophysical Research: Solid Earth* 124.2, pp. 1544–1568.

Zheng, G. and Rice, J. R. (1998). "Conditions under which velocity-weakening friction allows a self-healing versus a cracklike mode of rupture". In: *Bulletin of the Seismological Society of America* 88.6, pp. 1466–1483.

Tables and Figures

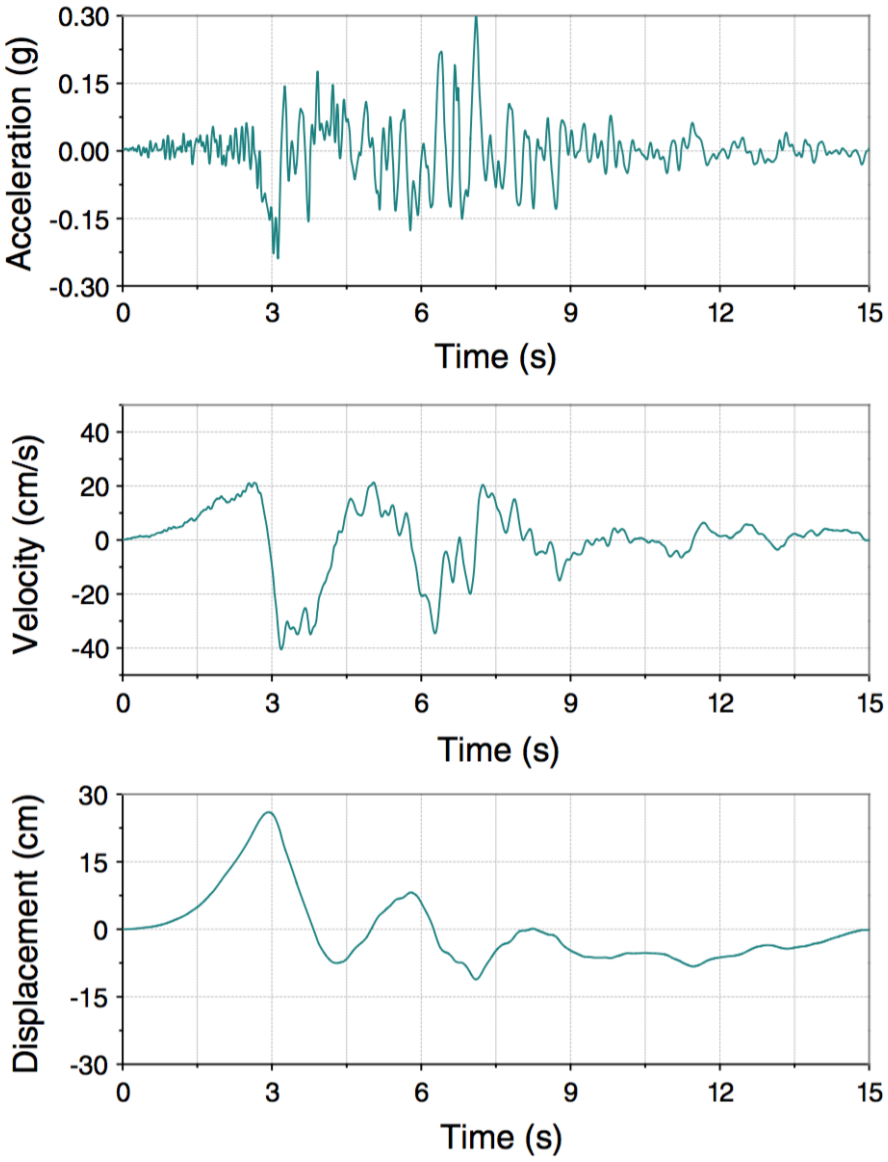

Figure 1.1: Sample of acceleration, velocity and displacement time histories for a near-fault ground motion recorded at Jensen Filtration Plant station in the 1994 Northridge earthquake. Source: Wang, G. et al. (2014). "Seismic performance evaluation of dam-reservoir-foundation systems to near-fault ground motions". In: *Natural Hazards* 72.2, pp. 651–674

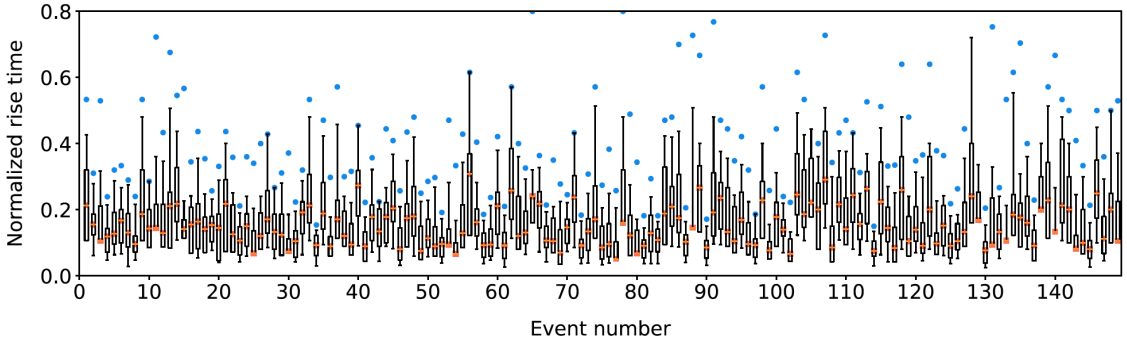

Figure 1.2: Summary statistics for the distribution of rise times for each inversion. The box indicates the 25th and 75th percentiles, and the red line is the median rise time. The whiskers are the 10th and 90th percentiles, and the blue dot is the maximum allowed rise time in each inversion. The rise times have been normalized by the total source duration such that a rise time value of 1.0 is equivalent to the entire source duration. Source: Melgar, D. and Hayes, G. P. (2017). "Systematic observations of the slip pulse properties of large earthquake ruptures". In: *Geophysical Research Letters* 44.19, pp. 9691–9698

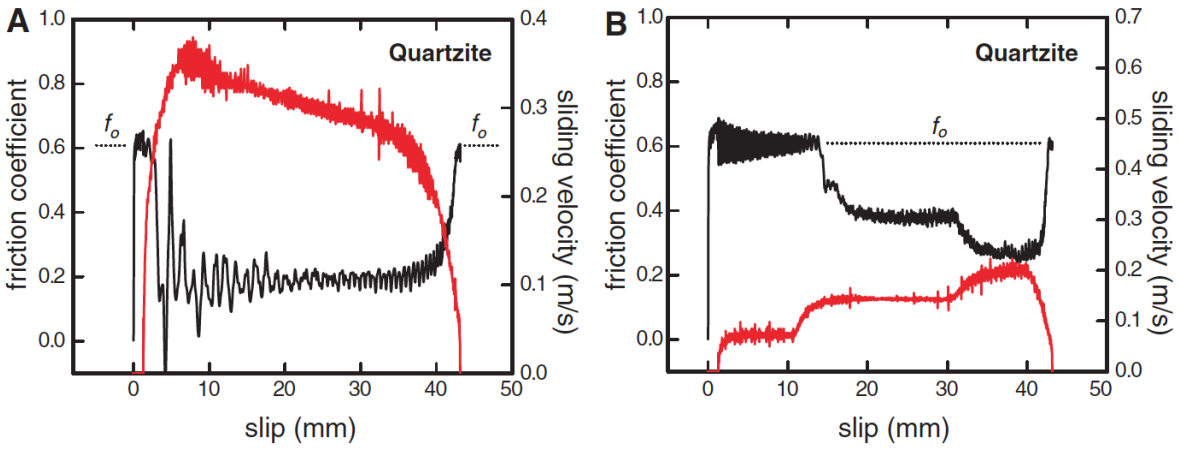

Figure 1.3: (A) Friction coefficient (black trace) and sliding velocity (red trace) plotted against sliding displacement, for a high-speed friction experiment on quartzite. The friction versus slip curve is essentially a mirror image (across a horizontal mirror plane) of the velocity versus slip curve above the weakening velocity V_w. The friction coefficient at low slip rates, f_o, obtains nearly identical values before and after sliding at rapid slip rates. (B) Friction coefficient (black trace) and sliding velocity (red trace) plotted against slip for a VS test on quartzite. As in (A), above a characteristic weakening velocity V_w, the friction curve is essentially a mirror image of the velocity curve. The friction coefficient at low slip rates, f_o, obtains nearly identical values before and after rapid slip. On acceleration from 0.06 to 0.13 m/s, weakening is not observed until a slip of 3 mm has accrued above $V = 0.10$m/s. Source: Goldsby, D. L. and Tullis, T. E. (2011). "Flash Heating Leads to Low Frictional Strength of Crustal Rocks at Earthquake Slip Rates". In: *Science* 334.6053, pp. 216–218

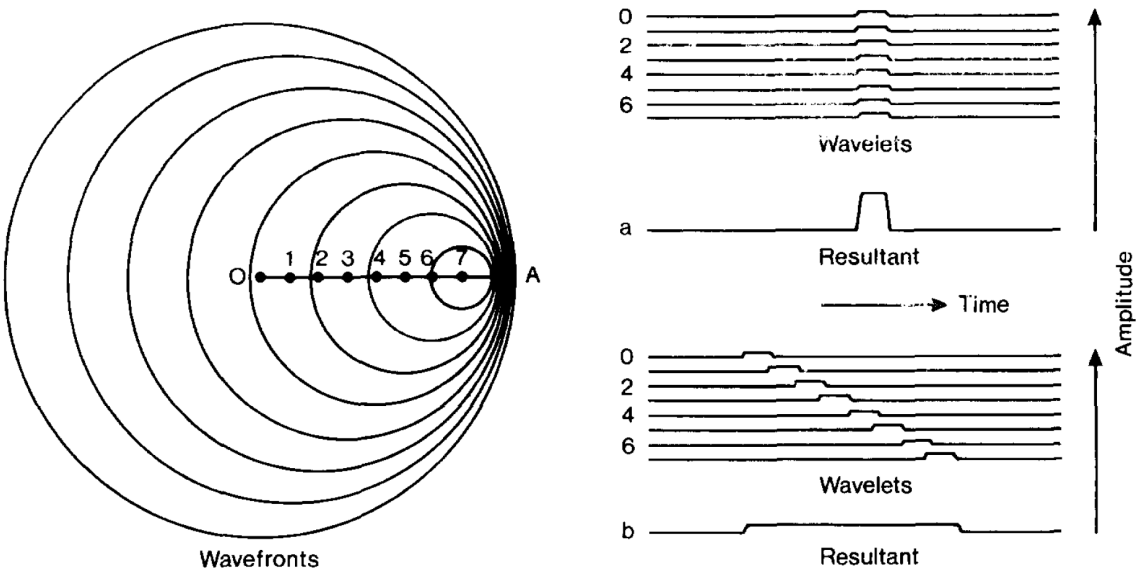

Figure 1.4: Rupture process approximated as a moving point source, and the resulting motion (modified after Douglas, A. et al. (1988). "Directivity and the Doppler-Effect". In: *Bulletin of the Seismological Society of America* 78.3, pp. 1367–1372). Absent radiation patterns, at sites in the forward and backward directions relative to rupture propagation, this shows qualitatively the forward (a) and backward (b) amplitude and duration variation due to directivity

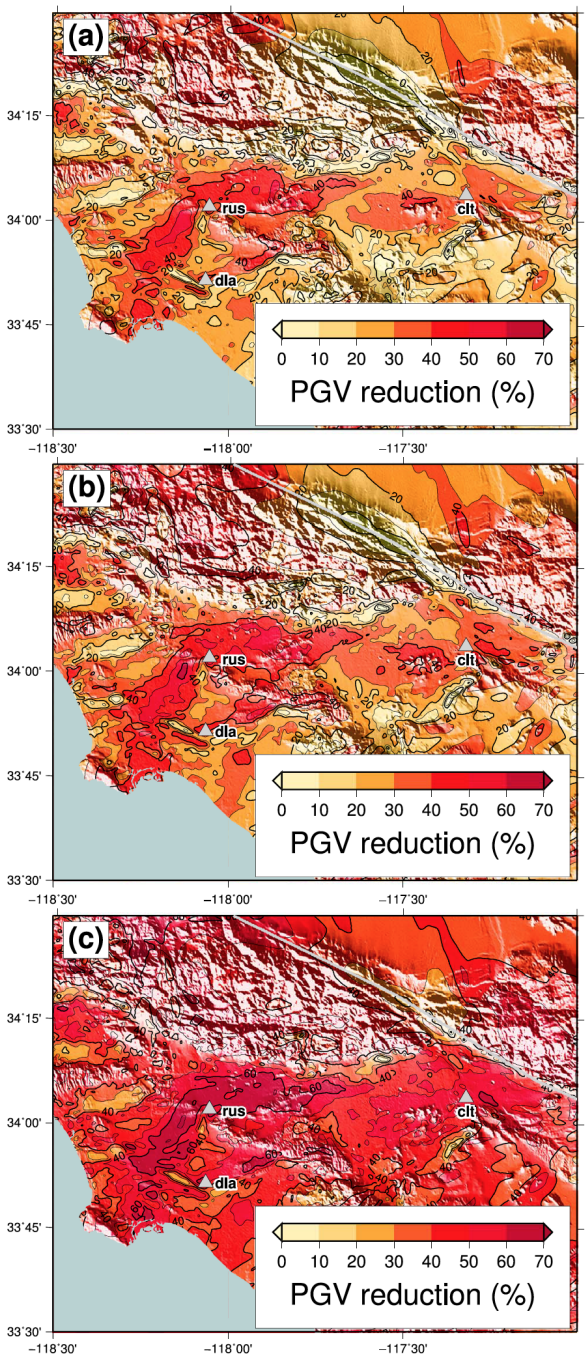

Figure 1.5: Reduction in horizontal peak ground velocities (%) obtained with varying cohesion models (a) 1, (b) 2, and (c) 3 (see Equations 3, 4 and 5 in Roten, D. et al. (2014). "Expected seismic shaking in Los Angeles reduced by San Andreas fault zone plasticity". In: *Geophysical Research Letters* 41.8, pp. 2769–2777) with respect to the viscoelastic solution.

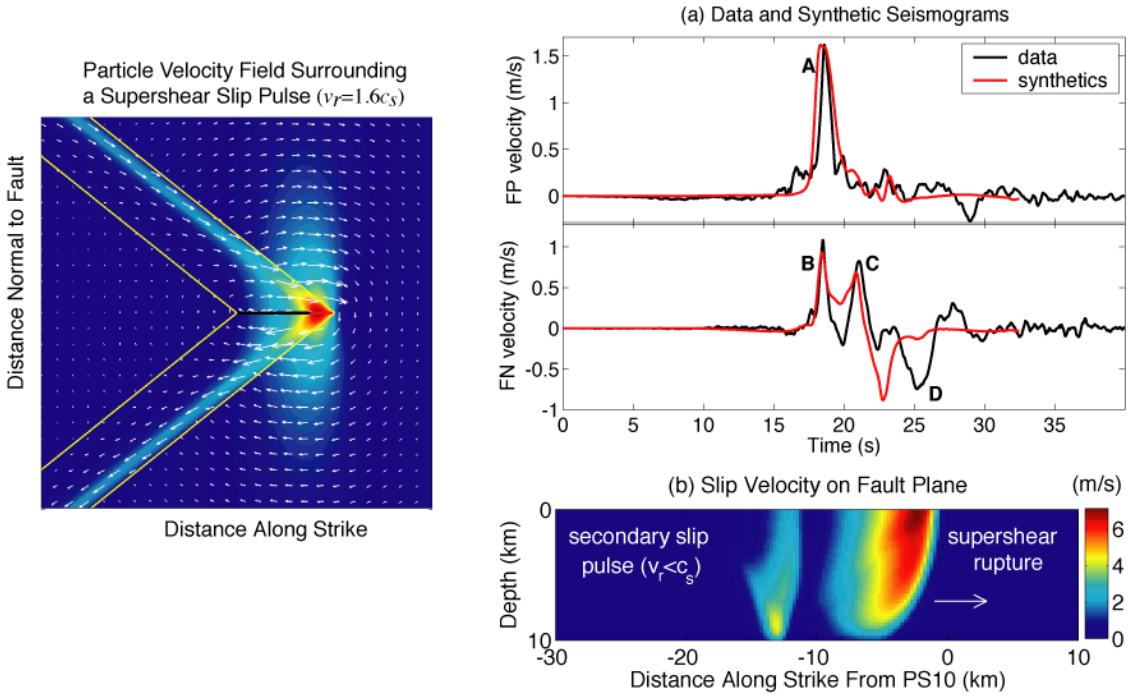

Figure 1.6: Both analytical and numerical solutions give insight into supershear rupture dynamics. The plot on the left shows the particle velocity field surrounding a slip pulse propagating at a supershear velocity. This was calculated using an analytical solution I derived for a two-dimensional mode II rupture. The shear Mach fronts are clearly visible and the sense of motion (transverse to the Mach front) within the Mach region is consistent with that of radiating shear waves radiating from the fault. Source: modified from Dunham, E. M. and Archuleta, R. J. (2005). "Near-source ground motion from steady state dynamic rupture pulses". In: *Geophysical Research Letters* 32.3

Chapter 2

Seismic source spectral properties of crack-like and pulse-like modes of dynamic rupture

Earthquake source properties such as seismic moment and stress drop are routinely estimated from far-field body-wave amplitude spectra. Some quantitative but model-dependent relations have been established between seismic spectra and source parameters. However, large variability is seen in the parameter estimates, and it is uncertain how the variability is partitioned among real variability in the source parameters, observational error and modeling error due to complexity of earthquake behaviors. Earthquake models with dynamic weakening have been found to exhibit two different modes of rupture: expanding crack and self-healing pulse modes. Four representative models are generated to model the transition from crack-like to pulse-like. Pulse-like rupture leads to development of a second corner frequency and the intermediate spectral slope is approximately 2 in most cases. The focal-sphere-averaged lower P and S wave corner frequencies are systematically higher for pulse-like models than crack models of comparable rupture velocity. The slip-weighted stress drop $\Delta\sigma_E$ exceeds the moment-based stress drop $\Delta\sigma_M$

for pulse-like ruptures, with the ratio ranging from about 1.3 to 1.65, while they are equal for the crack-like case. The variations in rupture mode introduce variability of the order of a factor of two in standard (i.e., crack-model based) spectral estimates of stress drop. The transition from arresting- to growing-pulse rupture is accompanied by a large (factor of $\sim$1.6) increase in the radiation ratio. Thus, variations in rupture mode may account for the portion of the scatter in observational spectral estimates of source parameters.

2.1 Introduction

Estimates of earthquake source parameters such as seismic moment and rupture area are important to our understanding the physics of source processes and provide important input for the quantification of seismic hazards. These parameters are routinely measured from far-field seismic spectra. Low-frequency spectral level, corner frequency and the high-frequency spectral decay slope are related to seismic moment, rupture area and high-frequency energy radiation, respectively. Static stress drop, the difference between the average shear stress on the rupture surface before and after faulting, provides insights into surrounding tectonic environments where earthquakes are generated [e.g., Kanamori and Anderson 1975; Allmann and Shearer 2007; Allmann and Shearer 2009]. Observational studies for worldwide Mb 5.5 earthquakes give stress drop estimates in the range of 0.3 to 50 MPa and, despite the large scatter, the mean value is at most weakly dependent on magnitude [Allmann and Shearer 2009]. In engineering applications, stress drop is recognized as an important parameter that scales high-frequency ground motion [e.g., Hanks and McGuire 1981; Boore 1983]. Moreover, the apparent magnitude independence of stress drops provides potential physical constraints on the magnitude dependence of empirically-based ground motion prediction equations (GMPEs) [Baltay and Hanks 2014].

Stress drop may be estimated from measurements of coseismic slip and rupture area [Eshelby 1957]. For earthquakes without extensive surface rupture, those quantities are not

accessible to direct measurement, and (apart from relatively large events with extensive geodetic observations) they must be inferred from the spectral content of far-field P and S waves. The seismic moment and source dimension, estimated from low-frequency limit and corner frequency f_c of seismic spectra, respectively, are then used to derive stress drop estimates. Variability in determinations of stress drop arises not only from uncertainties and biases in observational data selection and processing, but also from the source model assumptions used [e.g., Savage 1966; Brune 1970; Sato and Hirasawa 1973; Molnar et al. 1973; Dahlen 1974; Madariaga 1976; Kaneko and Shearer 2014; Kaneko and Shearer 2015] and the methodology used in fitting the spectra to the model spectral shape [Shearer et al. 2006]. Moreover, there is no agreement among investigators on which types of theoretical models should be used for estimating the source dimensions, and what degree of model simplification is appropriate [Kaneko and Shearer 2014].

The analytical solution for the elliptical uniform stress drop crack model in a homogeneous Poissonian medium with major and minor axes A and B [Eshelby 1957; Madariaga 1977b] gives a relationship between moment, area and stress drop,

$$\Delta\sigma = \frac{M_0}{c_1 SB}, \tag{2.1}$$

where M_0 is the seismic moment, S is the source area and c_1 is a geometric parameter. For slip along the major axis, c_1 is defined as:

$$c_1 = \frac{4}{3E(m) + [E(m) - \frac{B^2}{A^2}K(m)]/m^2}, \tag{2.2}$$

where $m = \sqrt{1 - B^2/A^2}$ and $K(m)$ and $E(m)$ are complete elliptical integrals of the first and second kinds, respectively [Eshelby 1957; Madariaga 1977b]. In the special case of a circular

source ($R = A = B$), the relationship (Equation 2.1) simplifies to

$$\Delta\sigma = \frac{7M_0}{16R^3}, \tag{2.3}$$

where R is the rupture radius. Given a theoretical model of the source parameterized by the single length scale R, the source radius can be inferred from the focal-sphere average of corner frequency $\overline{f_c}$ of the P or S wave through [Brune 1970; Madariaga 1976]

$$\overline{f_c} = k\frac{\beta}{R}, \tag{2.4}$$

where β is the shear wave speed and k is a constant that is model dependent. Hence, estimates of stress drop can be computed as combinations of the expressions above:

$$\Delta\sigma = \frac{7}{16}(\frac{\overline{f_c}}{k\beta})^3 M_0. \tag{2.5}$$

Among these variables involved in stress drop determination under the assumption of a circular crack, only the value of k depends on which theoretical relationship is used to associate corner frequency with source radius. Both f_c and k (but not their ratio) depend on wavetype, which we will indicate with superscripts. The model proposed by Brune [1970] presumes a simple circular fault and obtained $k^S = 0.37$, a value which is frequently used for inferring source dimension and stress drop [e.g., Hanks and Thatcher 1972; Archuleta et al. 1982; Baltay et al. 2011]. An alternative is the source model of Sato and Hirasawa [1973], which includes nucleation, constant-velocity spreading and instantaneous stopping of circular rupture. This model is established by presuming the Eshelby [1957] static solution; given rupture velocity $V_r = 0.9\beta$, the model gives $k^P = 0.42$ and $k^S = 0.29$. Although this model is consistent with a known static solution [Eshelby 1957] and explicitly incorporates propagation and stopping of the

rupture front followed by slip cessation, and is favored by many investigators [e.g., Prejean and Ellsworth 2001; Stork and Ito 2004; Imanishi and Ellsworth 2006], a defect is that slip ceases at the same instant everywhere over the fault plane. Accordingly, some refinements have been proposed; for example, Molnar et al. [1973] make modifications such that slip at a point starts with the arrival of the rupture front and continues until information from the edges of the fault is radiated back to the point. Dahlen [1974] extended the analysis of rupture kinematics to an elliptical crack that keeps on growing with the same shape.

The model of Madariaga [1976] has been widely accepted and used [e.g., Abercrombie 1995; Prieto et al. 2004; Shearer et al. 2006; Allmann and Shearer 2007; Allmann and Shearer 2009; Denolle et al. 2015]. Madariaga [1976] simulated a dynamic singular crack model with constant rupture velocity using a staggered-grid finite-difference method and found that $k^P = 0.32$ for P wave and $k^S = 0.21$ for S wave for $V_r = 0.9\beta$. Kaneko and Shearer [2014] constructed a dynamic model of expanding rupture on a circular fault with cohesive zone that prevents a stress singularity at the rupture front. Their solutions (obtained with a spectral element method) give $k^P = 0.38$ and $k^S = 0.26$ for the same rupture speed. Moreover, Kaneko and Shearer [2015] extended their analysis to symmetric and asymmetric circular and elliptical models with subshear and supershear ruptures.

Previous studies using dynamic theoretical source models [e.g., Madariaga 1976; Kaneko and Shearer 2014; Kaneko and Shearer 2015] for quantifying relationship between seismic spectra and stress drop are all based on so-called crack-like rupture models, i.e., those in which the duration of slip at a point on the fault is comparable to the overall duration of rupture. They have also been limited to source models with constant rupture velocity and prescribed rupture termination edges. An alternative rupture mode, the so-called pulse-like rupture, has not been considered in the development of dynamic model-based spectral theories (though the purely kinematic model of Haskell [1964] is pulse-like). Pulse-like rupture, in which slip duration at a representative point (i.e., slip risetime) is short relative to the rupture duration, may

occur when dynamic weakening occurs during the most rapid sliding phase and is followed by restrengthening. Pulse-like rupture can also result from the presence of secondary length scales (e.g., in the fault geometry, frictional parameter distribution, or stress field) shorter than the overall rupture dimension. Short slip risetimes inferred from kinematic source inversions were first interpreted as evidence of a local healing mechanism by Heaton [1990]. This mechanism has also been introduced to explain the complexity of seismicity patterns [Cochard and Madariaga 1996] and the lack of heat flow anomaly on the San Andreas Fault [Noda et al. 2009]. Theoretical self-similar solution for pulse-like rupture has been derived by [Nielsen and Madariaga 2003]. Both crack- and pulse-like modes have been observed in laboratory experiments and numerical simulations [e.g., Lu et al. 2010; Zheng and Rice 1998]. The mechanisms behind the pulse-like rupture modes that have been proposed include: the velocity dependent friction [Heaton 1990; Beeler and Tullis 1996; Zheng and Rice 1998; Gabriel et al. 2012], coupling between slip and dynamic normal stress changes along bimaterial faults [Andrews and Ben-Zion 1997; Ampuero and Ben-Zion 2008; Dalguer and Day 2009], the spatial heterogeneity of fault strength and initial shear stress [Beroza and Mikumo 1996; Day et al. 1998; Oglesby and Day 2002], the finite downdip width of the seismogenic zone [Day 1982; Johnson 1992] or the reflected waves within the fault zone [Huang and Ampuero 2011].

Here we simulate 4 simplified models of rupture propagating and (in one case) stopping spontaneously in expanding crack and self-healing pulse-like modes. The spontaneous rupture model, described in Section 3.1, incorporates strong velocity weakening in a regularized rate- and state-dependent friction framework [Noda et al. 2009; Rojas et al. 2009]. Section 2.3 gives a qualitative description of the simulation results. Computation of far-field radiated spectra is described in Section 2.4, and spectral parameters are discussed in Sections 2.4,2.5 and 2.7 discusses retrieval of energy and stress drop estimates.

2.2 Crack-like and pulse-like modes generation with forced or spontaneous termination

Among multiple mechanisms already mentioned for the generation of self-healing rupture, here we focus on velocity dependent friction. The rate and state framework on which we base the friction law we use in this paper has its basis in laboratory experiments [e.g., Dieterich 1979; Ruina 1983; Marone 1998]. We use the regularized formulation of the friction coefficient f as proposed by Lapusta et al. [2000] (see also Shi and Day [2013], Appendix B),

$$f(V,\psi) = a\sinh^{-1}[\frac{V}{2V_0}\exp(\frac{\psi}{a})], \tag{2.6}$$

where the state variable ψ evolves according to a slip law

$$\dot{\psi} = -\frac{V}{L}[\psi - \psi_{ss}(V)], \tag{2.7}$$

$$\psi_{ss}(V) = a\ln\{\frac{2V_0}{V}\sinh[\frac{f_{ss}(V)}{a}]\}, \tag{2.8}$$

where V is slip velocity and $f_{ss}(V)$ is the steady-state friction coefficient at slip velocity V. In this study, the steady-state friction coefficient takes the form (following Dunham et al. [2011] and Shi and Day [2013], which is a smoothed version of the form used by Noda et al. [2009] and Rojas et al. [2009])

$$f_{ss}(V) = f_w + \frac{f_{lv} - f_w}{[1+(V/V_w)^8]^{1/8}}, \tag{2.9}$$

which has a strongly velocity-weakening feature such that when $V \gg V_w$, f_{ss} approaches a fully weakened friction coefficient f_w. V_w is called weakening slip velocity. When $V << V_w$, f_{ss}

approaches a low-velocity steady-state friction coefficient f_{lv}, i.e.,

$$f_{lv}(V) = f_0 - (b-a)\ln(V/V_0). \tag{2.10}$$

In the foregoing equations, the constants a and b are the direct-effect and state-evolution parameters, respectively, and f_0 and V_0 are the reference values for the friction coefficient and slip rate, respectively.

One commonly-applied way to generate a transition from crack-like to pulse-like rupture mode is to alter the background shear stress level [e.g., Cochard and Madariaga 1996; Perrin et al. 1995; Beeler and Tullis 1996; Zheng and Rice 1998; Noda et al. 2009; Dunham et al. 2011; Gabriel et al. 2012]. Figure 2.1, based on the analysis of Zheng and Rice [1998] shows this schematically. The transition from pulse-like to crack-like rupture mode is controlled by the relative values of the initial shear stress τ^b and a critical stress value τ_{pulse}, where the latter, as defined by Zheng and Rice [1998], is equal to the zero-velocity intercept of the radiation damping line (blue dashed line) tangent to the steady-state weakening curve (red solid curve). The rupture mode can be changed from pulse-like to crack-like by varying the initial shear stress from below to above a fixed τ_{pulse}. For convenience in comparing stress drop, we apply here an alternative scheme that maintains initial stress state and instead varies the weakening slip rate V_w. As Figure 2.1 shows, this variation can also generate a transition between crack-like and pulse-like modes as it shifts the steady-state velocity-weakening curve towards the right, thus shifting τ_{pulse} from below to above a fixed initial shear stress.

We examine rupture of a planar surface embedded in an infinite homogeneous Poissonian medium (Figure 2), with velocity weakening friction (i.e., $a < b$) operating on the interior of a circle of radius R, with velocity strengthening ($b < a$) on the exterior (as a device to limit the rupture extent, with the ratio of $(b-a)/a$ exceeding 10, an essentially unbreakable barrier). The material properties and initial stress state are given in Table 2.1. For convenience of comparison

among multiple simulation scenarios, the initial stress state is held fixed, as are the frictional parameters, apart from the weakening slip velocity V_w. Variations of the latter parameter are used to generate the transition from crack-like to pulse-like rupture. Rupture is initiated by imposing a shear stress perturbation $\Delta\tau^0(x_1,x_2)$ at the center of prescribed circular region (yellow circle in Figure 2), which elevates the initial shear stress to $\tau^b(x_1,x_2)+\Delta\tau^0(x_1,x_2)$. $\Delta\tau^0(x_1,x_2)$ has the following expression:

$$\Delta\tau^0(x_1,x_2) = c\exp(\frac{l^2}{l^2-R_n^2})H(R_n-l)\tau^b(x_1,x_2), \tag{2.11}$$

where c is coefficient representing over-stress amplitude, l is the distance between fault point (x_1,x_2) and hypocenter (x_1^h,x_2^h), $l=\sqrt{(x_1-x_1^h)^2+(x_2-x_2^h)^2}$, R_n is the nucleation region radius, H is the Heaviside step function and $\tau^b(x_1,x_2)$ is the uniform equilibrium initial shear stress on the fault. The chosen shape function in Equation 2.11 is smooth (infinitely differentiable and of compact support) in order to prevent singular behavior at the edge of the nucleation zone. The amplitude of the shear stress perturbation and the size of nucleation may affect the rupture mode, and we have chosen values that, in combination with the chosen range of frictional parameters and background shear stress, permit rupture in either crack-like or pulse-like mode. We examine the slip rate and stress evolution along two perpendicular profiles through the hypocenter, an inplane profile (aligned with the initial shear stress) and an antiplane profile (perpendicular to initial shear stress). In addition to admitting pulse-like ruptures, the study further differs from related numerical studies of seismic spectra [Madariaga 1976; Kaneko and Shearer 2014; Kaneko and Shearer 2015], in that it is based on a spontaneous rupture model rather than a fixed rupture-velocity model. Rupture velocity is determined as part of the problem solution, and may fluctuate in response to, e.g., local background stress state, fault geometry and frictional conditions.

Accurate numerical results require adequate resolution of the cohesive zone, i.e., the portion of the fault surface (at a given instant of time) which is slipping at an appreciable rate but

has not yet fully weakened. Based upon rough estimates [e.g., Shi and Day 2013; Dunham et al. 2011] and detailed measurements [e.g., Rojas et al. 2009] of the size of cohesive zone, we expect a cohesive zone dimension averaging 500 m or so, and we formulate the numerical simulations to ensure at least 20 nodes within the cohesive zone. Based on this level of resolution, the benchmark solutions in simulations done using slip weakening and rate- and state-based friction laws investigated by Day et al. [2005] and Rojas et al. [2009], respectively, all indicated relative rms errors for peak slip rate are much below 10 percent, with one to two orders of magnitude smaller error for their other metrics (e.g., mean static slip and rupture velocity).

We solve 3-D problem of rupture in a viscoelastic medium using SORD (Support Operator Rupture Dynamics) [Ely et al. 2008; Ely et al. 2009]. This code uses a generalized finite difference method with spatial and temporal second-order accuracy. The frictional equations 2.6 through 2.10 are solved using the staggered velocity-state method of Rojas et al. [2009]. The full methodology has been verified in tens of benchmark scenarios developed by the Southern California Earthquake Center [Harris et al. 2009] and this code has been used in numerous studies of spontaneous dynamic rupture simulation and strong ground motion [e.g., Ely et al. 2010; Ben-Zion et al. 2012; Shi and Day 2013; Song et al. 2013; Baumann and Dalguer 2014; Song 2015; Vyas et al. 2016].

2.3 Numerical simulation results

In this section, we present simulation results representing a range of rupture modes from crack-like to pulse-like, as obtained by adjusting the weakening slip velocity V_w (letting it range from 0.05 m/s to 0.1 m/s). We examine four examples, including an expanding crack case and three pulse-like cases. The latter are denoted growing, steady-state, and arresting pulse models, following commonly-used terminology, [e.g., Noda et al. 2009; Gabriel et al. 2012]. These names reflect the spatial pattern of slip, as seen in Figure 2.3, which shows some details of the

slip distributions for these cases. Figures 2.3a and 3b show the slip distribution at equal time intervals (1s), for profiles on the inplane (Mode II) and antiplane (Mode III) axes, respectively. For the expanding crack case, slip amplitude is strongly dependent on the distance to hypocenter, whereas all three pulse-like ruptures show more nearly uniform slip distributions. The mechanism for generating pulse-like rupture is that hypothesized by Heaton [1990], and can be seen from the shear stress spatial and temporal evolution near the crack tip in Figure 2.3c and 2.3d. In the expanding crack example, shear stress remains almost constant following full weakening, whereas, in pulse-like ruptures, the shear stress increases in response to slip-rate reduction behind the rupture front, eventually healing the rupture and creating a pulse-like slip rate function.

Further details of the crack-like rupture example are shown are Figure 2.4. The characteristic decrease of slip amplitude from the center toward the unbreakable barrier is evident in Figure 2.4a. This shape is, however, not identical with the standard elliptical slip distribution (as a function of radial distance) for a purely static crack, because there is some degree of variability of the static stress change (Figure 2.4b) with slightly larger static stress drop along the anti-plane direction and at the edges, due to the barrier as well as the directional dependence of rupture velocity that is shown in Figure 2.4c. The slip rate function, shown in Figure 2.4d and 2.4e, has the familiar long-tailed shape, terminated by stopping phases from the rupture edge, and shows the characteristic increase in peak slip rate with the distance away from the hypocenter.

Details of the growing pulse example are shown in Figure 2.5. Due to the self-healing behavior, the slip distribution in this case (Figure 2.5a, with corresponding stress changes in Figure 2.5b) is more uniform than in the expanding crack model, but there are high-slip lobes along anti-plane direction, near the rupture edge. These two high slip lobes are the result of the differing rupture velocities along the two axes indicated in Figure 2.5c. Also seen in Figures 2.5a is a large slip patch associated with the artificial nucleation at the center of the fault. The principal difference relative to the expanding-crack model is in the shape of the slip rate function, shown in Figures 2.5d and 2.5e. The slip rate takes the form of a pulse with nearly constant rise time

(weakly dependent upon distance). Stopping phases are no longer evident at the stations close to boundary. However, the slip rate function in this case still retains the feature of the expanding crack model that peak slip rate increases from center to edge. This feature has a significant effect (to be discussed later) on far-field wave shapes for the growing pulse case.

Most features of the steady-state pulse model are similar to those of the growing pulse, but slip is more uniformly distributed and smaller on average, while mean stress drop and rupture velocity are both decreased (Figure 2.6a, 2.6b and 2.6c). The slip rate function is again pulse shaped, but with reduced rise time compared with the growing-pulse case, and now the peak slip rate is almost invariant with the distance to edges (Figure 2.6d and 2.6e). The duration of the slip rate function is also almost invariant with distance, as in the growing pulse model. That is, the rupture front velocity is close to the healing front velocity (outside the nucleation zone), and this is consistent with simulated results of Gabriel et al. [2012].

The arresting pulse case (Figure 2.7) corresponds to a weakening slip velocity that is close to the maximum value that permits a rupture to escape the nucleation area, and results in a rupture model that stops spontaneously, i.e., before reaching the imposed velocity-strengthening barrier. In Figure 2.7d and 2.7e, peak slip rate decays to zero as hypocentral distance increases. This feature of spontaneous arrest distinguishes this case from the other three models. It is also a departure from previous rupture models used in the study of the far-field spectrum, all of which involve arrest by edge barriers, with the result that the high-frequency spectral character in those previous models is dominated by stopping phases.

2.4 Detailed analysis of properties of far-field displacements and spectra

In this section, we present for each source model, the far-field displacements, the corresponding spectra, and the consequent spherical distribution of the corner frequencies and fall-off rates obtained from the spectral fitting. We begin by summarizing the variation of the spectral corner frequency and fall-off rate over the focal sphere, interpreting them in terms of the rupture characteristics identified in Section 2.2. For that purpose, we select 8 receivers with different take-off angle (defined as the angle between the vector normal to the fault and the vector pointing to the receiver from the source), and fixed azimuthal angle (22.5 degrees to the x axis). Their displacements and spectra, with stars representing computed corner frequencies, are plotted in Figure 2.8. The models representing the four different rupture modes can be distinguished by the four colors (and this color convention for the four rupture modes is followed throughout the paper).

In discussing the far-field displacements, it is common to refer to their time-domain form as "displacement pulses." These radiated pulses are not to be confused with the pulses of fault-surface slip velocity that characterizes the pulse-like rupture models. Similarly, we follow convention and use "rise time" in this section to refer to the time between the onset and peak of the far-field displacement, which is not to be confused with our (also conventional) use of the same term to refer to the duration of the slip pulses in the pulse-like rupture models.

Several factors affecting the far-field displacement pulses and corresponding spectral shapes in Figure 2.8 should be noted. In these multilateral ruptures, the pulse rise times (duration between onset and peak value of displacement pulse) are shorter in directions at low angle to the fault plane (high take-off angle) than they are in directions nearly normal to the fault. The rise time is controlled by both the focusing due to directivity and increasing peak slip rate in the direction of rupture propagation [Brune et al. 1979]. The overall pulse width is longer at high take-off

angle, which is a (well-known) rupture directivity effect. The pulse width is heavily influenced by stopping phases generated from the edges [Madariaga 1976]. In the case where rupture velocity is constant and stopping occurs on a circular boundary, delay times of the stopping phases from the nearest and farthest points on the edge of the fault would be

$$t = R(\frac{1}{V_R} \mp \frac{\sin\theta}{c}), \tag{2.12}$$

where R means fault size, V_R is rupture velocity, c is wave speed, θ is take-off angle, minus sign denotes the nearest, and positive sign denotes the farthest, stopping phases. In Figure 2.8, the peak value of displacement is usually controlled by the nearest stopping phase and the approximate pulse width is controlled by the farthest stopping phase, but the pattern is complicated by rupture velocity changes and variations in the rupture mode and slip-velocity distribution. Nucleation phases are common to all models (i.e., the four curves overlap during first few tenths of a unit of dimensionless time), since they result from a common rupture-initiation procedure.

As the take-off angle is increased, the rise time is shortened while the overall duration is lengthened, as suggested by Equation 2.14. These two factors have opposing influences on high- to low-frequency spectral ratios, with the result that the trend of corner frequency with takeoff angle is non-monotonic, especially for the crack-like model, consistent with the studies of Madariaga [1976] and Kaneko and Shearer [2014]. Compared with the crack-like rupture mode, the pulse-like ruptures have P and S waveforms with sharper peaks, in the case of growing and steady-state pulse models, and smoother shapes, in the arresting pulse case (due to disappearance of the stopping phase). These effects generate more complex behavior of the seismic spectra, reflected in the variations in spherically-average values of corner frequency and fall-off rate among 4 models shown in Table 2.2. The rupture velocities given in Table 2.2, V_r^2 and V_r^3, are along the X (inplane motion) and Y (antiplane motion) coordinate axes, respectively. Each is computed by a linear integral $\int V_r dl/L$ along the ruptured portion of the coordinate axis, excluding the

nucleation zone. In this equation, V_r is the local rupture velocity, l is the distance variable, and L is the rupture length excluding the nucleation zone.

In the remainder of this section, we elaborate on the features of far-field displacement pulses, their corresponding spectral amplitudes, and the spatial distributions (on the focal sphere) of the spectral parameters, for the four representative rupture models described in Section 2.3, illustrated in Figures 2.9- 2.12.

Figure 2.9 shows results for the expanding crack model. Figures 2.9a and 2.9b show the spherical distributions (calculated at 5 degree intervals) of normalized corner frequency (corner frequency divided by the ratio of source radius to S velocity) and spectral fall-off rate, while 2.9c shows the far-field body wave displacement pulses and 9d shows their spectra. We use the same notation as Madariaga [1976], Kaneko and Shearer [2014] and Kaneko and Shearer [2015]. Near the fault surface (equator or low latitudes in Figure 2.9), the resultant corner frequencies are generally smaller than average, as a result of the wider displacement pulse width, as indicated in Figure 2.9c. The variation of pulse width is due to source directivity and duration, which reflects the differential traveling time between the near and far side of fault termination signals (Equation 2.15). In addition, spectral fall-off rates are generally larger at higher latitudes stations. There are, in addition, some complexities in the corner-frequency and fall-off rate distributions that arise from dynamic effects not present in previous, fixed rupture velocity models. For example, four lobes of high fall-off rate at high latitude (i.e., at take-off angle near fault normal), result from the dissimilar rupture behaviors along the in-plane and anti-plane directions typical in spontaneous rupture models (though corner frequencies do not show a corresponding strong azimuthal dependence). We obtain the following spherically averaged corner frequencies and fall-off rates for P and S waves,

$$\begin{aligned} \overline{f_c^P} &= k^P \frac{\beta}{R} = 0.35 \frac{\beta}{R} \\ \overline{f_c^S} &= k^S \frac{\beta}{R} = 0.27 \frac{\beta}{R}. \end{aligned} \tag{2.13}$$

The k values are sometimes called normalized corner frequency and for the convenience of comparing results with previous studies and other scenarios here, we use normalized corner frequency, instead of original corner frequency. Rupture velocities average 0.88β along inplane and 0.84β along antiplane direction, respectively. Spherically averaged spectral fall-off rates for P and S waves, termed as n^P and n^S, are 2.2 and 1.9, respectively. The values of k^P and k^S found here are very close to results of symmetrical circular rupture with fixed rupture speed of 0.8β in Kaneko and Shearer [2014]. This is because for our spontaneously propagating expanding crack model, the far-field pulse width is mainly dominated by anti-plane rupture, which has the lower rupture velocity. Slight differences with Kaneko and Shearer [2014] in the distributions of corner frequencies and spectral fall-off rates is attributable to spontaneity of ruptures, effects of the rupture-initiation method and frequency band used in spectral fitting.

Figure 2.10 shows the results for the growing pulse model. The variation of waveform pulse width with take-off angle seen in the expanding crack model is still apparent, while the azimuthal dependency is slightly reduced. Relative to the expanding crack case, the growing-pulse corner frequencies are higher and spectral decaying slopes are steeper (Figure 2.10a and 2.10b), as can be inferred from the narrower far-field displacement pulse width (Figure 2.10c). The estimated rupture velocities of 0.85β along inplane and 0.81β along antiplane direction are not appreciably (less than 4%) different from the expanding crack case. The spherically averaged corner frequencies for the growing pulse case are

$$\begin{aligned} \overline{f_c^P} &= k^P \frac{\beta}{R} = 0.40\frac{\beta}{R} \\ \overline{f_c^S} &= k^S \frac{\beta}{R} = 0.36\frac{\beta}{R}, \end{aligned} \tag{2.14}$$

and spherically averaged n^P and n^S are 2.0 and 1.9, respectively. The normalized P and S corner frequencies are increased by about 14% and 33%, respectively, relative to the expanding crack. This corner frequency shift and the reduced spectral fall-off rates result from the shorter slip

duration in the growing pulse model. The P to S corner frequency ratio ($\sim$1.1) is lower for the growing pulse rupture than for crack-like models ($\sim$1.3 in our spontaneous crack model and $\sim$1.35 in the crack model of Kaneko and Shearer [2014] with similar rupture velocity).

Figure 2.11 shows results for the steady-state pulse model. In this case, in addition to the effect of take-off angle, there are also slight azimuthal variations (Figure 2.11a). Nucleation phases (sharp onset of wave pulses) are larger relative to the overall pulse amplitude than in the crack and growing-pulse models. Spectral decay slopes are lower compared with the growing crack and growing pulse models, and there is an accompanying downward shift in corner frequency. Somewhat smaller rupture velocities (0.78β along inplane and 0.74β along antiplane) also contribute to the reduction of corner frequencies. The spherically averaged corner frequencies for the steady-state pulse case are

$$\begin{aligned} \overline{f_c^P} &= k^P \frac{\beta}{R} = 0.31 \frac{\beta}{R} \\ \overline{f_c^S} &= k^S \frac{\beta}{R} = 0.31 \frac{\beta}{R}, \end{aligned} \tag{2.15}$$

and spherically averaged fall-off rates for P and S waves are 1.8 and 1.8, respectively. The ratio between P and S wave corner frequencies is $\sim$1.0, a reduction relative to the previously discussed cases, consistent with previous studies showing near-equality of P and S corner frequencies for complex sources (e.g., the asymmetrical circular model of Kaneko and Shearer [2015]).

Figure 2.12 shows results for the arresting pulse model. This is the only case in which rupture growth stops spontaneously, without encountering the circular barrier. The absence of distinct stopping phases introduces some significant differences compared with the previous models. The most prominent difference is the smoothing of the peak of the radiated waveforms (Figure 2.12c), which were sharply cusped in the other models. In addition, for the arresting-pulse case the initiation phase is relatively large compared to the overall amplitude of the radiated waveform. The normalized corner frequency for P waves (Figure 2.12a) has a pattern similar

to that of the other cases, with somewhat lower values for receivers at focal-sphere equatorial receivers (at high angle to the fault normal) relative to near-polar receivers (low angle to the fault normal). But for S waves, that pattern is reversed, with corner frequencies lower near the fault normal. Moreover, the fall-off rates of S waves near the focal equator are much larger than those at other locations. Average rupture velocities for the arresting-pulse rupture (0.72β along inplane and 0.66β along antiplane) are somewhat lower than for the previous cases. The spherically averaged corner frequencies for the arresting pulse model are

$$\overline{f_c^P} = k^P \frac{\beta}{\sqrt{AB}} = 0.28 \frac{\beta}{\sqrt{AB}}$$
$$\overline{f_c^S} = k^S \frac{\beta}{\sqrt{AB}} = 0.34 \frac{\beta}{\sqrt{AB}}, \tag{2.16}$$

where A and B are major and minor axes of elliptical slip distribution in Figure 7a. The spherically averaged n^P and n^S are 1.7 and 1.9, respectively. The high-frequency asymptotic slope reflects the lowest-order singularity present in a waveform, so it might seem paradoxical that the n values (especially n^P) are reduced in this case, given that the waveform cusps have been smoothed. The reason is that we (deliberately) calculate n values using a frequency band appropriate to observational studies (as explained in Section 2.4). In the presence of the complexities introduced by pulse-like rupture, the resulting n values actually characterize an intermediate spectral slope, not the ultimate high-frequency asymptote. This issue is discussed in detail in the next section. The P corner frequency is slightly ($\sim$10%) larger than for the corresponding fixed rupture-velocity crack-model estimate [Kaneko and Shearer 2014], while the S corner frequency is $\sim$30% larger. In fact, the arresting-pulse model has a P to S corner frequency ratio of $\sim$0.82, the only one of our cases in which the ratio is less than one. This apparently anomalous behavior is partly a consequence of the high spectral fall-off rate for S at low latitudes of the focal sphere. The higher spectral slope at the low latitudes has the effect of shifting the corner frequency to higher frequencies, even though the high-frequency spectral energy is actually diminished in the arresting-

pulse model relative to the other models. The P wave corner frequency, in contrast, decreases relative to the steady-pulse model, roughly by the amount expected due to the decreased rupture velocity (following Kaneko and Shearer [2014]).

These results are compared with those of previous studies [Brune 1970; Sato and Hirasawa 1973; Madariaga 1976; Kaneko and Shearer 2014], all of which were limited to crack-like modes with fixed rupture velocity. As shown in Table 2.3, the spherical average corner frequencies of pulse-like modes shows dependency on rupture velocity, which is also observed in previous models [Sato and Hirasawa 1973; Kaneko and Shearer 2014], though rupture velocity has less impact on the S corner frequency than on the P corner. Both P and S wave corner frequencies are affected by rupture mode transition from crack-like to pulse-like. Results in Table 2.2 also indicate that rupture mode only minimally affects the spectral fall-off rate estimates; apart from the arresting pulse case, these slope estimates are near 2, consistent with other studies [Brune 1970; Madariaga 1976; Kaneko and Shearer 2014]. The P wave spectral slope estimate for the arresting pulse case is lower, around 1.7. We emphasize that all spectral slope estimates were made using the procedure and bandwidth described in Section 2.4, which is intended to be consistent with observational practice. As shown in the next section, the estimates for the pulse-like models actually represent intermediate spectral trends, not asymptotic slopes.

2.5 Properties of stacked spectra

In the previous section, the average corner frequency estimate $\overline{f_c}$ is an average of corner frequency of each spectrum weighted by spherical subarea (following the methodology of Madariaga [1976], Kaneko and Shearer [2014] and Kaneko and Shearer [2015]). On the other hand, observational studies [e.g., Prieto et al. 2004; Shearer et al. 2006] frequently use an alternative corner frequency estimate, $\overline{f_c}$, derived directly from spectral stacks. That approach may provide a more robust estimation, since it reduces effects of spectral distortion due to source and

propagation complexities. To investigate the effects of our rupture models on source parameter estimates, we recalculate the average corner frequencies of P and S waves by stacking the logarithms of all individual spectra of each wave type, evenly sampling the focal sphere. In Table 2.2, the values of k^P_{stack}, k^S_{stack}, n^P_{stack} and n^S_{stack} derived from stacked spectra are compared with those estimated by averaging individual spectral parameters in the previous section. The mean differences between the two averages (considering all four rupture models together) are 4%, 8%, 1% and 3% for k^P, k^S, n^P and n^S, respectively, confirming that observational estimates of source parameters are only minimally affected by performing the parameter estimation on the spectral stack.

Stacked spectra for the four models are shown in Figure 2.13, along with Brune spectra fit to them by the method described in Section 2.4. The spectra in Figure 2.13 are only shown for frequencies well below the high-frequency resolution limit of the numerical simulations. In the expanding crack model, the Brune spectral function represents the stacked spectra of P and S waves with negligible misfit (Figures 2.13b and 2.13c, respectively). This is also consistent with previous studies [Madariaga 1976; Kaneko and Shearer 2014; Kaneko and Shearer 2015]. The three pulse-like models, however, have systematic misfits at high frequency. The mismatch takes the form of a secondary corner frequency that becomes progressively better developed as the rupture mode progresses from growing to arresting pulse behavior.

Double corner frequency spectra are common in both theoretical and empirical seismic studies. Kinematically, the lower and higher corner frequencies typically correspond to rupture duration (controlled by fault dimension) and slip rise time (duration of the slip-velocity pulse), respectively [e.g., Ben-Menahem 1962; Haskell 1964]. Physically, the explanation of the secondary corner in our pulse-like models is similar in spirit to the partial stress-drop model suggested by Brune [1970]. In Brune's partial-stress-drop model (in contrast to the conventional Brune model), slip is hypothesized to be arrested early, such that static stress drop is less than dynamic stress drop, which is what occurs in our pulse-like spontaneous rupture models (and similar behavior

is implicit in some barrier and asperity models [e.g., Boatwright 1988; Uchide and Imanishi 2016]). The development of slip pulses was previously related to the occurrence of a secondary spectral corner in the numerical modeling of Shaw [2003]. Numerous observational studies have proposed double corner frequency spectral models [e.g., Atkinson and Silva 1997], and the issue deserves renewed attention in light of observational results such as those of Denolle and Shearer [2016] documenting a systematic emergence of a secondary spectral corner for the largest events in the global dataset and Archuleta and Ji [2016] documenting a break in scaling of LogPGA and LogPGV versus moment magnitude **M** around $\mathbf{M} \sim 5.3$.

Anticipating that the second corner frequency can be related to slip rise time (by analogy with the Haskell fault model), we investigate the distributions (histograms) of slip duration for each model (Figure 2.13a). In Figure 2.13a, the ordinate gives the percentage of the total rupture area having slip-rate duration within the 0.5 second wide bin centered at the abscissa value. The expanding crack model has a very broad distribution of slip duration over the interval from 0.5s to 10s (the curve of the expanding crack is scaled by a factor of 3 to highlight this feature in Figure 2.13a), but all of the pulse-like ruptures have relatively narrow distributions of slip duration. This can be partially understood as a result of a diminished influence of the overall rupture geometry for pulse-like ruptures compared with crack-like modes; both total slip and slip velocity of these pulse-like ruptures are controlled principally by local shear stress and frictional properties rather than by global rupture features such as rupture edge diffractions. We assume that the second corner frequency scales inversely with the mean slip duration time:

$$f_c^{2nd} = \frac{K}{\overline{T}}, \tag{2.17}$$

where $\overline{T}$ is mean slip velocity duration and K is a constant to be determined. In Figure 2.13b and 2.13c, solid and dashed lines are spectral stacks computed from the simulations and Brune's model spectra, respectively. The presence of a second corner frequency shows up as a clear

departure from the constant spectral slope of the Brune model. The dotted lines in Figures 2.13b and 2.13c are curves of K/T distribution derived from Figure 2.13a, for a fixed value of K for each wave type (around 1.8 and 1.5 for P and S wave respectively) that was determined, by trial and error adjustment, such that the distribution peak (from the dashed curves) coincides with the lowest frequency where the spectral stack departs visibly from the best fit Brune model. The proportionality between this frequency and $\overline{T}$ confirms, unsurprisingly, that, if a secondary corner frequency is interpreted in terms of pulse-like rupture, its value provides an estimate of mean slip duration. The upper spectral asymptote is not well determined in the simulations, however, so this estimate of K provides only a lower bound on the value of the second corner frequency (where the latter is defined as the frequency of intersection of the intermediate and upper spectral asymptotes), and thus may not be directly comparable with other K estimates (for example, a similar parameter in Savage [1972] equals 1 and in Denolle and Shearer [2016] equals $1/\pi$).

As the rupture model evolves from a growing- to an arresting-pulse mode, the spectral decay above the second corner becomes steeper, as seen in Figures 2.13b and 2.13c. This transition reflects the relative suppression of stopping phases, especially in the decaying pulse model, consistent with the expected dominance of stopping phases in the high-frequency limit [Madariaga 1976; Madariaga 1977a]. In the presence of the second corner and increased rate of high-frequency decay, fitting over a broad frequency band to the conventional, single corner frequency Brune spectral function can bias the estimate of the first corner frequency, leading to uncertainties and bias in the stress drop estimate. For example, for shallow thrust earthquakes, Denolle and Shearer [2016] find that the conventional Brune model with a single-corner frequency is unable to fit spectra for high-magnitude events, and a double-corner frequency model improves the fitting and gives more consistent estimates of the first corner frequency in the sense that the subsequent stress drop estimates are roughly invariant with seismic moment (given additional scaling assumptions, i.e., the length to width scaling of Leonard [2010]).

2.6 Energy partitioning and stress drop

The partitioning of radiated energy between P and S waves is rupture-model dependent, and we use our four source models to show the effect of rupture mode on the P/S energy ratio. Radiated energy can be calculated from each simulation using fault-plane stresses and velocities via [Rudnicki and Freund 1981]

$$E_r = \iint \frac{\tau_0 + \tau_f}{2} \Delta u dS - \int_0^\infty \iint \tau(t) \Delta \dot{u}(t) dS dt, \tag{2.18}$$

where $\Delta \dot{u}$ is the slip velocity, τ_0 and τ_f are initial and final shear stress and $\tau(t)$ is the shear stress as a function of time. The corresponding estimate of radiated energy from far-field body-wave displacements is

$$E_r' = \rho \int_0^\infty \int_0^\infty [\alpha (V^P)^2 + \beta (V^S)^2] d\Sigma dt, \tag{2.19}$$

where V^P and V^S are far-field velocities of P and S waves, the integration is over a sphere surrounding the fault and the prime symbol here denotes the parameter derived from far-field observations instead of from the fault surface. Before considering the P and S contributions separately, we first verify the internal consistency of our calculations by comparing estimates (20) and (21) for the total energy. These two energy estimates, for each source model, are listed in Table 2.4, and show differences of the order of 1 or 2% (which we attribute to errors from focal-sphere sampling, together with effects of the small artificial viscosity used in the simulations and neglected in the energy balance calculations) verifying the self-consistency of the far-field and on-fault estimates.

The computed P and S radiated energies for the crack-like and pulse-like rupture models are shown in Table 2.4. The P/S ratio for the crack-like rupture mode, 20, is similar to values of 24.4 for the analytical model of Sato and Hirasawa [1973] and 21.8 for the numerical model of Kaneko and Shearer [2014]. The S/P energy ratio is larger for pulse-like ruptures than for the

crack-like case, and larger for growing and steady-state pulses than for the arresting pulse rupture mode. This pattern mirrors the behavior of the radiation ratio η_R [Noda et al. 2013], also shown in Table 2.4, and examined further in the Discussion section. We also note that our radiated energy ratios differ markedly from what would be predicted if the rms P- and S-wave spectral shapes were scaled (both amplitude and frequency axes) versions of each other (something also noted by Kaneko and Shearer [2014]). As shown by Boatwright and Fletcher [1984], the latter estimate is

$$\frac{E_r^S}{E_r^P} = 1.5(\frac{\alpha}{\beta})^5(\frac{f_c^S}{f_c^P})^3. \tag{2.20}$$

As Table 2.4 shows, this estimate under-predicts the energy ratio of the crack-like model by about a factor of two and over-predicts that of the arresting pulse model by a similar factor.

Fault slip and stresses from the simulations provide two complementary measures of average stress drop, denoted $\Delta\sigma_E$ and $\Delta\sigma_M$ by Noda et al. [2013]. The former is the average static stress drop weighted by the final slip,

$$\Delta\sigma_E = \frac{\iint \Delta\sigma \Delta u dS}{\iint \Delta u dS}, \tag{2.21}$$

where $\Delta\sigma$ is the static stress drop as a function of position on the fault surface. As Shao et al. [2012] point out, $\Delta\sigma_E$ is just twice the ratio of so-called "available elastic energy" [Kanamori and Rivera 2006] to the seismic potency. Values obtained directly from Equation 2.23 are listed in Table-4. An alternative measure, called moment-based stress drop [Noda et al. 2013] is stress drop weighted by the slip distribution E due to a (hypothetical) uniform stress drop on the same fault surface,

$$\Delta\sigma_M = \frac{\iint \Delta\sigma E dS}{\iint E dS}. \tag{2.22}$$

For the circular rupture, Equation 2.24 gives the standard formula Equation 2.3, with the left-hand

side interpreted now as $\Delta\sigma_M$ (and a similar expression can be derived for an elliptical rupture). The corresponding values of $\Delta\sigma_M$ for the simulations are listed in Table-4 for comparison with $\Delta\sigma_E$ values. If Equation 2.3 is applied, with rupture radius R estimated from corner frequency (Equation 2.4) using a crack-like model for k, those radius estimates will be biased for the pulse-like models by the ratio of the crack- to pulse-like k values in Table 2.3 (i.e., factors of 0.87, 1.13, and 1.25 for P waves, and 0.75, 0.87, and 0.8 for S waves, for growing, steady-state, and arresting pulse, respectively). Subsequently using Equation 2.3 to estimate stress drop from radius would lead to stress drop biased by the cube of those factors (Equation 2.5), if the relationship between mean slip (or moment) and stress drop followed the crack-like model like Equation 2.1 or 2.3. However, actual biases in the stress drop estimates are generally more complex than that, because the relationship between mean slip and stress drop also becomes modified for pulse-like ruptures.

We can examine the variability in spectral estimates of stress drop resulting from presumably unknown variations in rupture mode. Using values of k^P and k^S from each of four crack-like models (1. Madariaga [1976], 2. Kaneko and Shearer [2014], 3. Brune [1970], and the expanding crack model of the current study), we make "blind" stress drop ($\Delta\sigma_M$) estimates from spectral parameters M_0 and f_c obtained from the growing, steady-state, and arresting pulse models, respectively. These estimates are denoted $\Delta\sigma_{Ma}$, $\Delta\sigma_{KS}$, $\Delta\sigma_B$, and $\Delta\sigma_{crack}$, respectively. Results for the four stress drop estimates, normalized by each of the actual stress drops $\Delta\sigma_M$ of the pulse-like ruptures (from Table 2.4) are shown in Figure 2.14. For P-wave estimates, the rupture mode introduces over- and under-estimates ranging over roughly a factor of two either way. The S-wave estimates have a somewhat larger range, due to a substantial overestimate of $\Delta\sigma_M$ by the Madariaga [1976] model.

The S wave estimates based on Kaneko and Shearer [2014] and the crack-like model of the current study are very similar, each biased high by about a factor of two for the pulse-like ruptures, and each showing about a factor of two variability about that factor. The upward bias is what would be expected as a consequence of the S-wave rupture radius underestimates noted

above. That upward bias is sharply reduced, however, when we compare with $\Delta\sigma_E$ (open squares in Figure 2.14) instead of $\Delta\sigma_M$, since both spectral estimates $\Delta\sigma_{KS}$ ([Kaneko and Shearer 2014]) and $\Delta\sigma_{crack}$ (current study) represent quite accurate $\Delta\sigma_E$ values for the steady-state and arresting pulse ruptures. The Brune estimate is low for the crack-like rupture model, but within plus/minus 40% for the pulse-like ruptures.

This reduction of bias when bias is taken relative to $\Delta\sigma_E$ is a result of the differences in spatial distribution of slip of the pulse- versus crack-like models. For the pulse-like models, $\Delta\sigma_E$ exceeds $\Delta\sigma_M$, with the excess being related to the level of heterogeneity of stress drop [Noda et al. 2013]. As indicated in Table 2.4 and Figure 2.14, $\Delta\sigma_E$ and $\Delta\sigma_M$ for the expanding crack are nearly identical as expected. However, in pulse-like ruptures, $\Delta\sigma_M$ is 24%, 28% and 40% smaller than $\Delta\sigma_E$ in growing, steady-state and arresting pulse, respectively. Such a phenomenon is similarly observed in [Noda et al. 2013]. The reason is that the healing of the pulse-like rupture freezes in the static slip before it reaches the elliptic shape of the circular static crack, which has the form [Eshelby 1957]:

$$\Delta u(l) = I\sqrt{R^2 - l^2}[1 - H(l - R)], \tag{2.23}$$

where I is a constant proportional to the stress drop, R is the rupture radius, l is the distance to hypocenter and H is a Heaviside function. In Figure 2.15, the dashed and solid lines denote the best fit solutions of the form of Equation 2.23 and the simulated models (shown along the inplane direction), respectively. As expected, the crack-like rupture model closely follows the Eshelby solution, consistent with the close agreement we found between $\Delta\sigma_M$ and $\Delta\sigma_E$. The pulse-like model deviates much more from the Elshelby solution, with the main difference being weaker dependency of slip on hypocentral distance (apart from the region right around the nucleation patch). The resulting contrast in spatial patterns of slip between crack- and pulse-like rupture elevates $\Delta\sigma_E$ relative to $\Delta\sigma_M$ in the pulse-like case.

2.7 Discussion

The slip-pulse durations in our models are mostly in the range of 1-2 seconds (Figure 13a). This range is also representative of slip-pulse durations inferred in observational studies, at least for shallow crustal earthquakes [e.g., Heaton 1990; Somerville et al. 1999]. The source dimension of our simulations is such that the secondary corner introduced by the occurrence of these pulse-like ruptures only affects the spectral shape at frequencies exceeding the lower corner frequency by at least a factor of 20. The spectral fitting procedure used here (motivated by standard observational practice) appears to provide reliable estimates of the lower corner frequency and the intermediate spectral slope in this case, since the frequency band used in fitting, $0.05f_c < f < 20f_c$, is entirely below the higher corner frequency. As indicated in Figure 2.16, further narrowing the frequency band to $0.05f_c < f < 10f_c$, as in Kaneko and Shearer [2014; 2015] only slightly alters the spectral fit, (and only at low take-off angles). The use of the narrower band suppresses some of the azimuthal variation in the corner-frequency distribution (e.g., near the z axis in Figure 11a), but has little effect on the averaged values, which are summarized in Table 2.5. Compared with the results from the narrower band, k and n estimates from the broader band differ by a maximum of around 10% and 12% respectively (comparing Tables 2 and 5). When we increase the upper frequency limit to $30f_c$ (very near to the second corner frequency), there is no significant change in the estimates of k and n. In summary, the results are fairly insensitive to our choice the spectral range, although this conclusion depends upon the fact that the rupture dimension in the models was large enough to provide good separation between the corner frequencies.

In observational studies, there exists great variability in estimates of earthquake parameters derived from seismic spectra, such as stress drop and radiated energy. Simulations, for which the earthquake parameters are precisely known (from near-field calculations) are a valuable aid in the interpretation of spectra in terms of earthquake parameters and can provide useful insight into the

origin of the variability of spectrally-derived estimates. Our analysis of the spectral consequences of the rupture type transition from classic crack-like to pulse-like mode may have application in the estimation of earthquake parameters for particular earthquakes. For example, we may be able to sharpen some parameter estimates in cases where we have independent evidence of rupture mode, e.g., from finite-fault inversion. In such cases, our results for empirical parameters k^P and k^S (Section 2.6) and for the effect of pulse-like rupture on stress drop estimation (Section 2.7) may be used to refine spectral estimates of source parameters. Likewise, the spectral fall-off rates (n^P and n^S) could help refine frequency-domain radiated energy estimates (obtained by the application of Parseval's theorem to Equation 2.21), which are highly dependent on presumed spectral shapes [e.g., Hirano and Yagi 2017]. In other cases, absent detailed kinematic inversion results (especially for small to intermediate earthquakes), rupture types are usually unknown to us. In those cases, the results (Section 2.5) showing double corner frequency spectral shapes of pulse-like models may provide interpretive guidance. For example, Denolle and Shearer [2016] find a double corner frequency model fits their analysis of large, shallow thrust earthquakes, and since the upper corner appears to be too high in frequency to be related to a fault dimension, a possible interpretation would relate the upper corner to slip pulse duration (and Denolle and Shearer [2016] discuss other interpretations). Future work resolving higher frequency spectral properties, may provide more quantitative constraints on the association of pulse width with the second corner frequency, the extent to which pulse width may scale with other parameters (e.g., moment), and the asymptotic decay slope for pulse-like ruptures.

As noted earlier, the simulations provide precise values of radiated energy, seismic moment and static stress drop for all the rupture models, and this enables us to consider the implications of rupture mode for other quantities derived from these source parameters. The radiation ratio (we follow the terminology of Noda et al. [2013] for what is sometimes called the radiation efficiency,

though its value can exceed 1), defined as

$$\eta_R = \frac{2\mu E_R}{M_0 \Delta\sigma_E}, \tag{2.24}$$

is an interesting example, and values are compiled in Table 2.4 and shown in Figure 2.17a (red triangles). It is required to clarify that the static stress drop here denotes $\Delta\sigma_E$ because in considering energy partitioning, we need energy-based stress drop estimates instead of moment-based estimates ($\Delta\sigma_M$) although they are not easy to seismologically distinguish them. The blue star symbol denotes the average amplitude of the final slip spatial gradient, which can serve as a good indicator of rupture type (the small value of slip gradient implies flat slip distribution, as in the more pulse-like ruptures, and the large value denotes crack-like mode. Its mathematical expression is $\int_L |\frac{d\Delta u(x)}{dx}| dl/L$ in which L is rupture length along the inplane direction (X), l is the distance variable and Δu is the slip function). When the rupture type transits from pulse-like to crack-like (from left to right in Fig 17a), the radiation ratio initially increases, has a maximum for the growing pulse case, and then falls for the crack-like case. This behavior is probably a consequence of the undershoot of the static stress drop, relative to the maximum dynamic stress drop, in pulse-like models, as seen in Figure 2.3b. To verify that this dependence of radiation ratio on rupture mode is not specific to our method of inducing the rupture mode transition (via scaling of V_w), we do a similar set of simulations, but inducing the transition from pulse-like to crack-like modes by raising initial shear stress (with V_w fixed). We also add more simulations (a total of 22) to refine the resolution of the rupture-mode transition. The results, shown in Figure 2.17b, confirm that the transition of rupture from decaying to growing pulse-like behavior is associated with a large (up to factor of 1.6), systematic increase in radiation ratio, and that the transition to crack-like rupture corresponds to an equally large drop in radiation ratio (the small increases in efficiency for the highest initial-stress case is associated with a supershear rupture transition).

2.8 Conclusions

Spontaneous rupture simulations with rate and state friction and dynamic weakening show a rupture mode transition from crack- to pulse-like under adjustment of the critical weakening velocity V_w. Four representative models provide a basis for examining the effect of rupture mode on source parameter estimates: an expanding crack, a growing pulse (increasing peak slip velocity with rupture radius), a steady-state pulse (nearly constant peak slip velocity), and an arresting pulse (with spontaneous rupture termination). Relative to a crack-like rupture with similar geometry, a pulse-like rupture leads to additional complexity in the far-field displacement spectra, including a double corner-frequency structure, with the higher corner frequency inversely proportional to pulse duration. The focal-sphere-averaged lower P and S wave corner frequencies (normalized to source dimension) are systematically higher for pulse-like models than for crack models of comparable rupture velocity (Table 2.3), while the lower P-wave corner is less sensitive to rupture mode. The P/S corner frequency ratio also varies systematically with rupture mode, from $\sim$1.3 for the crack model to $\sim$0.9 for the arresting pulse (Table 2.2). The spectral slope (above the lower corner) in most cases is only slightly affected by rupture mode; in nearly all cases, this slope is in the range -2 ± 0.2, with the P spectral slope more sensitive to rupture mode than the S slope (Table 2.2).

The slip-weighted stress drop $\Delta\sigma_E$ exceeds the moment-based stress drop $\Delta\sigma_M$ for pulse-like ruptures, with the ratio ranging from about 1.3 to 1.65, while they are equal for the crack-like case. The variations in rupture mode modeled in this study introduce variability of the order of a factor of two in standard (i.e., crack-model based) spectral estimates of stress drop, accompanied by some systematic bias. The S-wave spectral estimates for the pulse-like ruptures are biased high by about a factor of two when stress drop is interpreted as $\Delta\sigma_M$, but show little bias when stress drop is interpreted as $\Delta\sigma_E$ (and P-wave estimates show less systematic bias). The transition from arresting- to growing-pulse rupture is accompanied by a large (factor of $\sim$1.6) increase in the

radiation ratio (”radiation efficiency”), with a comparable drop in that ratio at the transition from growing-pulse to crack-like rupture. Thus, variations in rupture mode may account for portion of the scatter in observational spectral estimates of source parameters, and, in instances in which independent constraints on rupture mode are available, the results derived here (in particular, values for rupture style-dependent normalized corner frequencies k^P and k^S and spectral slopes n^P and n^S) may help sharpen those estimates.

Acknowledgements

The authors thank Peter Shearer, Marine Denolle, and Yoshihiro Kaneko for the helpful discussions and suggestions. We also thank Editor Yehuda Ben-Zion, the Associate Editor, Ralph Archuleta, and an anonymous reviewer for their constructive comments that improved this manuscript. The simulations were performed on Blue Waters at the National Center for Supercomputing Applications (NCSA). This work was supported by NSF award EAR-1135455. The rupture dynamics code used in this paper is cited in the reference list, and the data generating figures and tables in this paper are available by contacting the corresponding author at yow004@ucsd.edu.

Chapter 2, in full, is a reprint of the material as it appears in Journal of Geophysical Research-Solid Earth: Wang, Y. and Day, S. M., “Seismic Source Spectral Properties of Crack-like and Pulse-like Modes of Dynamic Rupture”, *Journal of Geophysical Research-Solid Earth*, 122, 2017. I was the primary investigator and author of this paper.

References

Abercrombie, R. E. (1995). "Earthquake source scaling relationships from -1 to 5 ML using seismograms recorded at 2.5-km depth". In: *Journal of Geophysical Research-Solid Earth* 100.B12, pp. 24015–24036.

Allmann, B. P. and Shearer, P. M. (2007). "Spatial and temporal stress drop variations in small earthquakes near Parkfield, California". In: *Journal of Geophysical Research-Solid Earth* 112.

— (2009). "Global variations of stress drop for moderate to large earthquakes". In: *J. Geophys. Res.* 114.

Ampuero, J. P. and Ben-Zion, Y. (2008). "Cracks, pulses and macroscopic asymmetry of dynamic rupture on a bimaterial interface with velocity-weakening friction". In: *Geophysical Journal International* 173.2, pp. 674–692.

Andrews, D. J. and Ben-Zion, Y. (1997). "Wrinkle-like slip pulse on a fault between different materials". In: *Journal of Geophysical Research-Solid Earth* 102.B1, pp. 553–571.

Archuleta, R. J., Cranswick, E., Mueller, C., and Spudich, P. (1982). "Source parameters of the 1980 mammoth lakes, california, earthquake sequence". In: *Journal of Geophysical Research* 87.B6, pp. 4595–4607.

Archuleta, R. J. and Ji, C. (2016). "Moment rate scaling for earthquakes 3.3---M ---5.3 with implications for stress drop". In: *Geophysical Research Letters* 43.23, pp. 12,004–12,011.

Atkinson, G. M. and Silva, W. (1997). "An empirical study of earthquake source spectra for California earthquakes". In: *Bulletin of the Seismological Society of America* 87.1, pp. 97–113.

Baltay, A. and Hanks, T. (2014). "Understanding the magnitude dependence of PGA and PGV in NGA-West 2 data". In: *Bulletin of the Seismological Society of America* 104.6, pp. 2851–2865.

Baltay, A., Ide, S., Prieto, G., and Beroza, G. (2011). "Variability in earthquake stress drop and apparent stress". In: *Geophysical Research Letters* 38.

Baumann, C. and Dalguer, L. A. (2014). "Evaluating the compatibility of dynamic rupture-based synthetic ground motion with empirical ground-motion prediction equation". In: *Bulletin of the Seismological Society of America* 104.2, pp. 634–652.

Beeler, N. M. and Tullis, T. E. (1996). "Self-healing slip pulses in dynamic rupture models due to velocity-dependent strength". In: *Bulletin of the Seismological Society of America* 86.4, pp. 1130–1148.

Ben-Menahem, A. (1962). “Radiation of seismic body waves from a finite moving source in the Earth”. In: *Journal of Geophysical Research* 67.1, pp. 345–350.

Ben-Zion, Y., Rockwell, T. K., Shi, Z. Q., and Xu, S. Q. (2012). “Reversed-polarity secondary deformation structures near fault stepovers”. In: *Journal of Applied Mechanics* 79.3, p. 031025.

Beroza, G. C. and Mikumo, T. (1996). “Short slip duration in dynamic rupture in the presence of heterogeneous fault properties”. In: *Journal of Geophysical Research-Solid Earth* 101.B10, pp. 22449–22460.

Boatwright, J. (1988). “The Seismic Radiation from Composite Models of Faulting”. In: *Bulletin of the Seismological Society of America* 78.2, pp. 489–508.

Boatwright, J. and Fletcher, J. B. (1984). “The partition of radiated energy between P-wave and S-wave”. In: *Bulletin of the Seismological Society of America* 74.2, pp. 361–376.

Boore, D. M. (1983). “Stochastic simulation of high-frequency ground motions based on seismological models of the radiated spectra”. In: *Bulletin of the Seismological Society of America* 73.6, pp. 1865–1894.

Brune, J. N. (1970). “Tectonic stress and spectra of seismic shear waves from earthquakes”. In: *Journal of Geophysical Research* 75.26, pp. 4997–5009.

Brune, J. N., Archuleta, R. J., and Hartzell, S. (1979). “Far-field S-wave spectra, corner frequencies, and pulse shapes”. In: *Journal of Geophysical Research* 84.B5, pp. 2262–2272.

Cochard, A. and Madariaga, R. (1996). “Complexity of seismicity due to highly rate-dependent friction”. In: *Journal of Geophysical Research-Solid Earth* 101.B11, pp. 25321–25336.

Dahlen, F. A. (1974). “On the ratio of P-wave to S-wave corner frequencies for shallow earthquake sources”. In: *Bulletin of the Seismological Society of America* 64.4, pp. 1159–1180.

Dalguer, L. A. and Day, S. M. (2009). “Asymmetric rupture of large aspect-ratio faults at bimaterial interface in 3D”. In: *Geophysical Research Letters* 36.

Day, S. M. (1982). “Three-dimensional finite difference simulation of fault dynamics: rectangular faults with fixed rupture velocity”. In: *Bulletin of the Seismological Society of America* 72.3, pp. 705–727.

Day, S. M., Yu, G., and Wald, D. J. (1998). “Dynamic stress changes during earthquake rupture”. In: *Bulletin of the Seismological Society of America* 88.2, pp. 512–522.

Day, S. M., Dalguer, L. A., Lapusta, N., and Liu, Y. (2005). “Comparison of finite difference and boundary integral solutions to three-dimensional spontaneous rupture”. In: *Journal of Geophysical Research-Solid Earth* 110.

Denolle, M. A. and Shearer, P. M. (2016). “New perspectives on self-similarity for shallow thrust earthquakes”. In: *Journal of Geophysical Research-Solid Earth* 121.9, pp. 6533–6565.

Denolle, M. A., Fan, W. Y., and Shearer, P. M. (2015). “Dynamics of the 2015 M7.8 Nepal earthquake”. In: *Geophysical Research Letters* 42.18, pp. 7467–7475.

Dieterich, J. H. (1979). “Modeling of rock friction: 1. Experimental results and constitutive equations”. In: *Journal of Geophysical Research* 84.B5, pp. 2161–2168.

Dunham, E. M., Belanger, D., Cong, L., and Kozdon, J. E. (2011). “Earthquake ruptures with strongly rate-weakening friction and off-fault plasticity, part 1: Planar faults”. In: *Bulletin of the Seismological Society of America* 101.5, pp. 2296–2307.

Ely, G. P., Day, S. M., and Minster, J.-B. (2008). “A support-operator method for viscoelastic wave modelling in 3-D heterogeneous media”. In: *Geophysical Journal International* 172.1, pp. 331–344.

— (2009). “A support-operator method for 3-D rupture dynamics”. In: *Geophysical Journal International* 177.3, pp. 1140–1150.

— (2010). “Dynamic Rupture Models for the Southern San Andreas Fault”. In: *Bulletin of the Seismological Society of America* 100.1, pp. 131–150.

Eshelby, J. D. (1957). “The determination of the elastic field of an ellipsoidal inclusion, and related problems”. In: *Proceedings of the Royal Society of London Series a-Mathematical and Physical Sciences* 241.1226, pp. 376–396.

Gabriel, A. A., Ampuero, J. P., Dalguer, L. A., and Mai, P. M. (2012). “The transition of dynamic rupture styles in elastic media under velocity-weakening friction”. In: *Journal of Geophysical Research-Solid Earth* 117.

Hanks, T. C. and McGuire, R. K. (1981). “The character of high-frequency strong ground motion”. In: *Bulletin of the Seismological Society of America* 71.6, pp. 2071–2095.

Hanks, T. C. and Thatcher, W. (1972). “Graphical representation of seismic source parameters”. In: *Journal of Geophysical Research* 77.23, pp. 4393–4405.

Harris, R. A., Barall, M., Archuleta, R., Dunham, E., Aagaard, B., Ampuero, J. P., Bhat, H., Cruz-Atienza, V., Dalguer, L., Dawson, P., Day, S., Duan, B., Ely, G., Kaneko, Y., Kase, Y., Lapusta, N., Liu, Y., Ma, S., Oglesby, D., Olsen, K., Pitarka, A., Song, S., and Templeton, E. (2009). “The SCEC/USGS dynamic earthquake rupture code verification exercise”. In: *Seismological Research Letters* 80.1, pp. 119–126.

Haskell, N. A. (1964). “Total energy and energy spectral density of elastic wave radiation from propagating faults”. In: *Bulletin of the Seismological Society of America* 54.6A, pp. 1811–1841.

Heaton, T. H. (1990). "Evidence for and Implications of Self-Healing Pulses of Slip in Earthquake Rupture". In: *Physics of the Earth and Planetary Interiors* 64.1, pp. 1–20.

Hirano, S. and Yagi, Y. (2017). "Dependence of seismic and radiated energy on shorter wavelength components". In: *Geophysical Journal International* 209.3, pp. 1585–1592.

Huang, Y. H. and Ampuero, J. P. (2011). "Pulse-like ruptures induced by low-velocity fault zones". In: *Journal of Geophysical Research-Solid Earth* 116.

Imanishi, K. and Ellsworth, W. L. (2006). "Source scaling relationships of microearthquakes at Parkfield, CA, determined using the SAFOD Pilot Hole Seismic Array". In: *Earthquakes: Radiated Energy and the Physics of Faulting*. Geophysical Monograph Series. American Geophysical Union, pp. 81–90. ISBN: 978-0-87590-435-1.

Johnson, E. (1992). "The Influence of the Lithospheric Thickness on Bilateral Slip". In: *Geophysical Journal International* 108.1, pp. 151–160.

Kanamori, H. and Anderson, D. L. (1975). "Theoretical Basis of Some Empirical Relations in Seismology". In: *Bulletin of the Seismological Society of America* 65.5, pp. 1073–1095.

Kanamori, H. and Rivera, L. (2006). "Energy Partitioning During an Earthquake". In: *Earthquakes: Radiated Energy and the Physics of Faulting*. American Geophysical Union, pp. 3–13. ISBN: 9781118666272.

Kaneko, Y. and Shearer, P. M. (2014). "Seismic source spectra and estimated stress drop derived from cohesive-zone models of circular subshear rupture". In: *Geophysical Journal International* 197.2, pp. 1002–1015.

— (2015). "Variability of seismic source spectra, estimated stress drop, and radiated energy, derived fromcohesive-zonemodels of symmetrical and asymmetrical circular and elliptical ruptures". In: *Journal of Geophysical Research-Solid Earth* 120.2, pp. 1053–1079.

Lapusta, N., Rice, J. R., Ben-Zion, Y., and Zheng, G. T. (2000). "Elastodynamic analysis for slow tectonic loading with spontaneous rupture episodes on faults with rate- and state-dependent friction". In: *Journal of Geophysical Research-Solid Earth* 105.B10, pp. 23765–23789.

Leonard, M. (2010). "Earthquake Fault Scaling: Self-Consistent Relating of Rupture Length, Width, Average Displacement, and Moment Release". In: *Bulletin of the Seismological Society of America* 100.5a, pp. 1971–1988.

Lu, X., Lapusta, N., and Rosakis, A. J. (2010). "Pulse-like and crack-like dynamic shear ruptures on frictional interfaces: experimental evidence, numerical modeling, and implications". In: *International Journal of Fracture* 163.1-2, pp. 27–39.

Madariaga, R. (1976). “Dynamics of an expanding circular fault”. In: *Bulletin of the Seismological Society of America* 66.3, pp. 639–666.

— (1977a). “High-frequency radiation from crack (stress drop) models of earthquake faulting”. In: *Geophysical Journal of the Royal Astronomical Society* 51.3, pp. 625–651.

Madariaga, R. (1977b). “Implications of stress-drop models of earthquakes for the inversion of stress drop from seismic observations”. In: *Pure and Applied Geophysics PAGEOPH* 115.1-2, pp. 301–316.

Marone, C. (1998). “Laboratory-derived friction laws and their application to seismic faulting”. In: *Annual Review of Earth and Planetary Sciences* 26, pp. 643–696.

Molnar, P., Tucker, B. E., and Brune, J. N. (1973). “Corner frequencies of P and S waves and models of earthquake sources”. In: *Bulletin of the Seismological Society of America* 63.6, pp. 2091–2104.

Nielsen, S. and Madariaga, R. (2003). “On the self-healing fracture mode”. In: *Bulletin of the Seismological Society of America* 93.6, pp. 2375–2388.

Noda, H., Dunham, E. M., and Rice, J. R. (2009). “Earthquake ruptures with thermal weakening and the operation of major faults at low overall stress levels”. In: *Journal of Geophysical Research-Solid Earth* 114.

Noda, H., Lapusta, N., and Kanamori, H. (2013). “Comparison of average stress drop measures for ruptures with heterogeneous stress change and implications for earthquake physics”. In: *Geophysical Journal International* 193.3, pp. 1691–1712.

Oglesby, D. D. and Day, S. M. (2002). “Stochastic fault stress: Implications for fault dynamics and ground motion”. In: *Bulletin of the Seismological Society of America* 92.8, pp. 3006–3021.

Perrin, G., Rice, J. R., and Zheng, G. (1995). “Self-healing slip pulse on a frictional surface”. In: *Journal of the Mechanics and Physics of Solids* 43.9, pp. 1461–1495.

Prejean, S. G. and Ellsworth, W. L. (2001). “Observations of earthquake source parameters at 2 km depth in the Long Valley Caldera, eastern California”. In: *Bulletin of the Seismological Society of America* 91.2, pp. 165–177.

Prieto, G. A., Shearer, P. M., Vernon, F. L., and Kilb, D. (2004). “Earthquake source scaling and self-similarity estimation from stacking P and S spectra”. In: *Journal of Geophysical Research-Solid Earth* 109.

Rojas, O., Dunham, E. M., Day, S. M., Dalguer, L. A., and Castillo, J. E. (2009). “Finite difference modelling of rupture propagation with strong velocity-weakening friction”. In: *Geophysical Journal International* 179.3, pp. 1831–1858.

Rudnicki, J. W. and Freund, L. B. (1981). “On energy radiation from seismic sources”. In: *Bulletin of the Seismological Society of America* 71.3, pp. 583–595.

Ruina, A. (1983). “Slip instability and state variable friction laws”. In: *Journal of Geophysical Research* 88.B12, pp. 359–370.

Sato, T. and Hirasawa, T. (1973). “Body wave spectra from propagating shear cracks”. In: *Journal of Physics of the Earth* 21.4, pp. 415–431.

Savage, J. C. (1966). “Radiation from a realistic model of faulting”. In: *Bulletin of the Seismological Society of America* 56.2, pp. 577–592.

— (1972). “Relation of Corner Frequency to Fault Dimensions”. In: *Journal of Geophysical Research* 77.20, pp. 3788–+.

Shao, G., Ji, C., and Hauksson, E. (2012). “Rupture process and energy budget of the 29 July 2008Mw5.4 Chino Hills, California, earthquake”. In: *Journal of Geophysical Research: Solid Earth* 117.B7.

Shaw, B. E. (2003). “Magnitude dependence of radiated energy spectra: Far-field expressions of slip pulses in earthquake models”. In: *Journal of Geophysical Research-Solid Earth* 108.B2.

Shearer, P. M., Prieto, G. A., and Hauksson, E. (2006). “Comprehensive analysis of earthquake source spectra in southern California”. In: *Journal of Geophysical Research-Solid Earth* 111.

Shi, Z. Q. and Day, S. M. (2013). “Rupture dynamics and ground motion from 3-D rough-fault simulations”. In: *Journal of Geophysical Research-Solid Earth* 118.3, pp. 1122–1141.

Somerville, P., Irikura, K., Graves, R., Sawada, S., Wald, D., Abrahamson, N., Iwasaki, Y., Kagawa, T., Smith, N., and Kowada, A. (1999). “Characterizing crustal earthquake slip models for the prediction of strong ground motion”. In: *Seismological Research Letters* 70.1, pp. 59–80.

Song, S. G. (2015). “The effect of fracture energy on earthquake source correlation statistics”. In: *Bulletin of the Seismological Society of America* 105.2a, pp. 1042–1048.

Song, S. G., Dalguer, L. A., and Mai, P. M. (2013). “Pseudo-dynamic source modelling with 1-point and 2-point statistics of earthquake source parameters”. In: *Geophysical Journal International* 196.3, pp. 1770–1786.

Stork, A. L. and Ito, H. (2004). “Source parameter scaling for small earthquakes observed at the western Nagano 800-m-deep borehole, central Japan”. In: *Bulletin of the Seismological Society of America* 94.5, pp. 1781–1794.

Uchide, T. and Imanishi, K. (2016). “Small Earthquakes Deviate from the Omega-Square Model as Revealed by Multiple Spectral Ratio Analysis”. In: *Bulletin of the Seismological Society of America* 106.3, pp. 1357–1363.

Vyas, J. C., Mai, P. M., and Galis, M. (2016). “Distance and azimuthal dependence of ground-motion variability for unilateral strike-slip ruptures”. In: *Bulletin of the Seismological Society of America* 106.4, pp. 1584–1599.

Zheng, G. and Rice, J. R. (1998). “Conditions under which velocity-weakening friction allows a self-healing versus a cracklike mode of rupture”. In: *Bulletin of the Seismological Society of America* 88.6, pp. 1466–1483.

Tables and Figures

Table 2.1: Models Parameter Values

Parameter	Symbol	Value
	Bulk Properties	
Compressive wave speed	V_P	6000 m/s
Density	ρ	2670 kg/m^3
Poisson's ratio	ν	0.25
	Frictional Parameters	
Direct effect parameter	a	0.01
Evolution effect parameter	b	0.014
Reference slip velocity	V_0	1 μm/s
Steady-state friction coefficient at V_0	f_0	0.7
State-evolution distance	L	0.4 m
Weakening slip velocity	V_w	variable
Fully weakened friction coefficient	f_w	0.2
	Initial Conditions	
Normal stress on fault	σ^0	120 MPa
Background shear stress	τ^b	38 MPa
Initial slip velocity	V_{ini}	2×10^{-9}m/s
Prescribed rupture radius	R	18 km
	Nucleation Parameters	
Nucleation radius	R_n	3000 m
Overstress	$\Delta\tau^0$	$1 \times \tau^b$

Table 2.2: Spectral parameters of P and S waves among 4 models [a]

	Expanding crack	Growing pulse	Steady-state pulse	Arresting pulse
V_r^2	0.88β	0.85β	0.78β	0.72β
V_r^3	0.84β	0.81β	0.74β	0.66β
k^P	0.35	0.40	0.31	0.28
k^S	0.27	0.36	0.31	0.34
$\frac{k^P}{k^S}$	1.3	1.1	1.0	0.8
n^P	2.2	2.0	1.8	1.7
n^S	1.9	1.9	1.8	1.9
k^P_{stack}	0.38	0.43	0.31	0.28
k^S_{stack}	0.30	0.39	0.31	0.31
$\frac{k^P_{stack}}{k^S_{stack}}$	1.3	1.1	1.0	0.9
n^P_{stack}	2.2	2.0	1.8	1.8
n^S_{stack}	2.0	1.8	1.8	1.9

[a] V_r^2 and V_r^3 denote rupture velocity along inplane and antiplane direction. k^P and k^S are normalized corner frequencies, $f_c\beta/R$, for the P and S wave, respectively. n^P and n^S are (absolute values of) the spectral slopes for the P and S wave, respectively. Unsubscripted quantities are obtained by averaging separate spectral estimates obtained from each receiver direction. Subscript "stack" indicates that the quantity is an estimate obtained from an amplitude spectrum ("stack") formed by averaging the individual amplitude spectra from all receiver directions.

Table 2.3: Spectral parameters compared with previous studies.[a]

Model name	V_r^2/β	V_r^3/β	k^P	k^S	k_{KS}^P	k_{KS}^S	k_{Ma}^P	k_{Ma}^S	k_{SH}^P	k_{SH}^S	k_B^S
Brune's model	Infinite	Infinite									0.37
$KS-Ma-SH$ models	0.9	0.9			0.38	0.26	0.32	0.21	0.42	0.29	
$\star$ **Expanding crack**	0.88	0.84	0.35	0.27							
$\star$ **Growing pulse**	0.85	0.81	0.40	0.36							
$KS-SH$ models	0.8	0.8			0.35	0.26			0.39	0.28	
$\star$ **Steady-state pulse**	0.78	0.74	0.31	0.31							
$KS-SH$ models	0.7	0.7			0.32	0.26			0.36	0.27	
$\star$ **Arresting pulse**	0.72	0.66	0.28	0.34							
$KS-SH$ models	0.6	0.6			0.30	0.25			0.34	0.27	

[a] *KS*: [Kaneko and Shearer 2014], *Ma*: [Madariaga 1976], *SH*: [Sato and Hirasawa 1973] and *B*: [Brune 1970]. The models labeled with stars are from the current study (their fonts are bold), and k^P and k^S are the parameters derived for those models.

Table 2.4: Comparison energy partitioning and static stress drop among 4 models.

	Expanding crack	Growing pulse	Steady-state pulse	Arresting pulse
Radiated Energy				
$\underline{E_r}(10^{15}\text{J})$	21.01	9.29	2.92	1.14
$\overline{E_r'}(10^{15}\text{J})$	20.89	9.17	2.88	1.12
Ratio between E_r^S and E_r^P				
$\underline{E_r^S/E_r^P}$	20	29	27	24
$\overline{E_r^S/E_r^P}$*	11	18	23	46
Static stress drop				
$\underline{\Delta\sigma_E}$(MPa)	15.69	9.37	6.41	5.53
$\underline{\Delta\sigma_M}$(MPa)	15.66	7.13	4.61	3.36
Radiation ratio				
$\underline{\eta_R}$	0.40	0.65	0.46	0.41

All parameters underlined are computed directly from fault-plane stresses and slip from the numerical simulations. Parameters labeled with $'$ are derived from far-field displacements or spectra calculated from the simulations. The energy ratio labeled with * represents results from Equation 2.22 [Boatwright and Fletcher 1984].

Table 2.5: Spectral parameters of P and S waves for the 4 models obtained, using modified frequency band $0.05f_c < f < 10f_c$

	Expanding crack	Growing pulse	Steady-state pulse	Arresting pulse
V_r^2	0.88β	0.85β	0.78β	0.72β
V_r^3	0.84β	0.81β	0.74β	0.66β
k^P	0.38	0.40	0.32	0.30
k^S	0.29	0.35	0.32	0.34
$\frac{k^P}{k^S}$	1.3	1.1	1.0	0.9
n^P	2.3	2.0	1.9	1.9
n^S	2.0	1.7	1.8	1.9
k^P_{stack}	0.40	0.43	0.34	0.30
k^S_{stack}	0.31	0.38	0.32	0.32
$\frac{k^P_{stack}}{k^S_{stack}}$	1.3	1.1	1.1	1.0
n^P_{stack}	2.3	2.0	1.9	1.9
n^S_{stack}	2.0	1.8	1.8	1.9

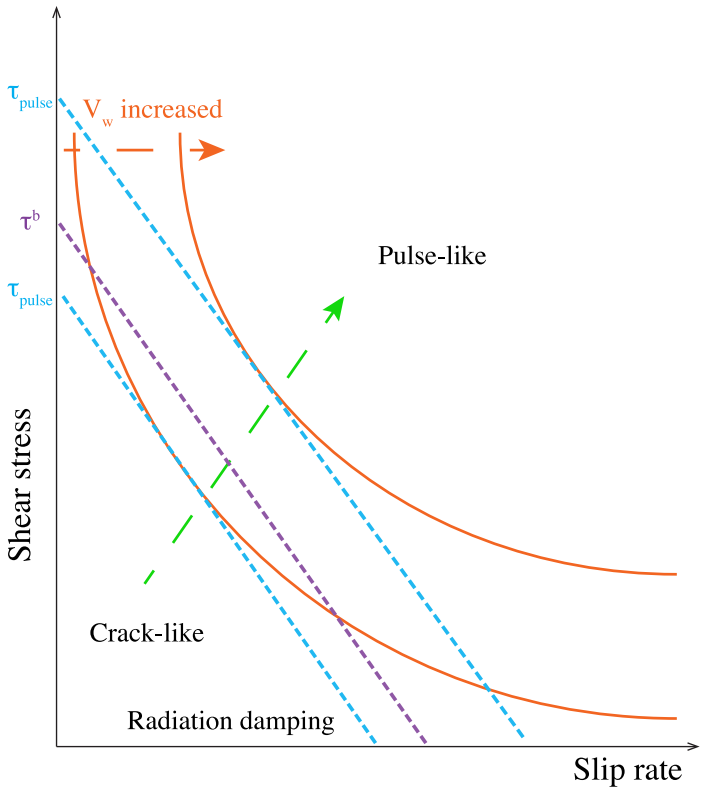

Figure 2.1: Schematic illustration indicating how the weakening slip rate V_w generates the rupture mode transition between crack-like and pulse-like. The red solid lines denote steady-state shear stress dependent on slip rate. Blue and purple dashed lines are radiation damping lines corresponding to different V_w values. For the small value of V_w, the corresponding critical τ_{pulse} is below initial background shear stress and a crack-like rupture mode is obtained. With V_w increased such that τ_{pulse} is elevated above the initial shear stress, based on the analysis in Zheng and Rice [1998], the rupture mode becomes pulse-like.

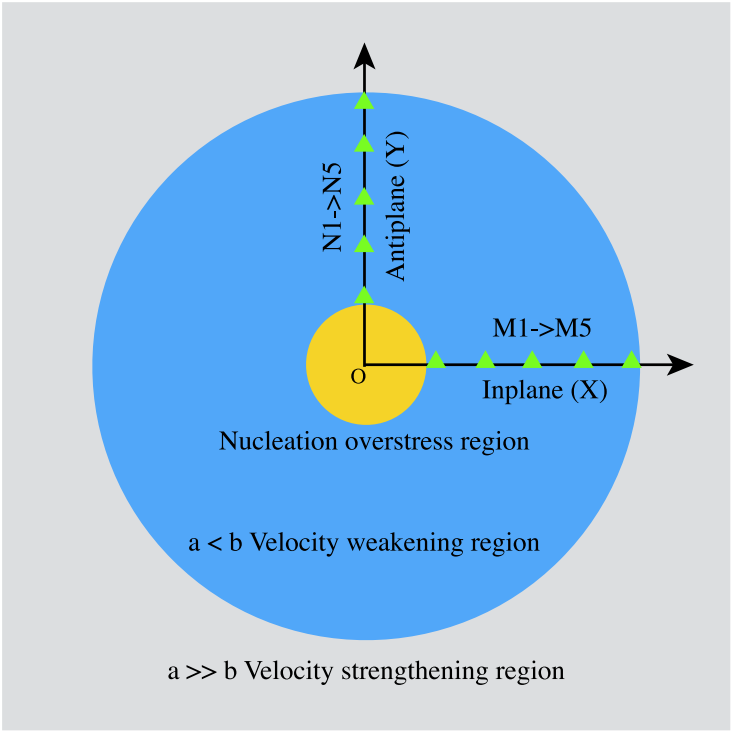

Figure 2.2: Circular fault model for generating the transition between crack-like and pulse-like ruptures. The yellow circle in the center is the nucleation area with overstress. The blue circular patch is velocity weakening region where $a < b$ and rupture is allowable. Outer grey region requires $a >> b$, velocity strengthening, to arrest rupture. X and Y axis correspond to inplane and antiplane direction along which the green triangular symbols are receivers used to record slip rate function in Figure 2.3- 2.7.

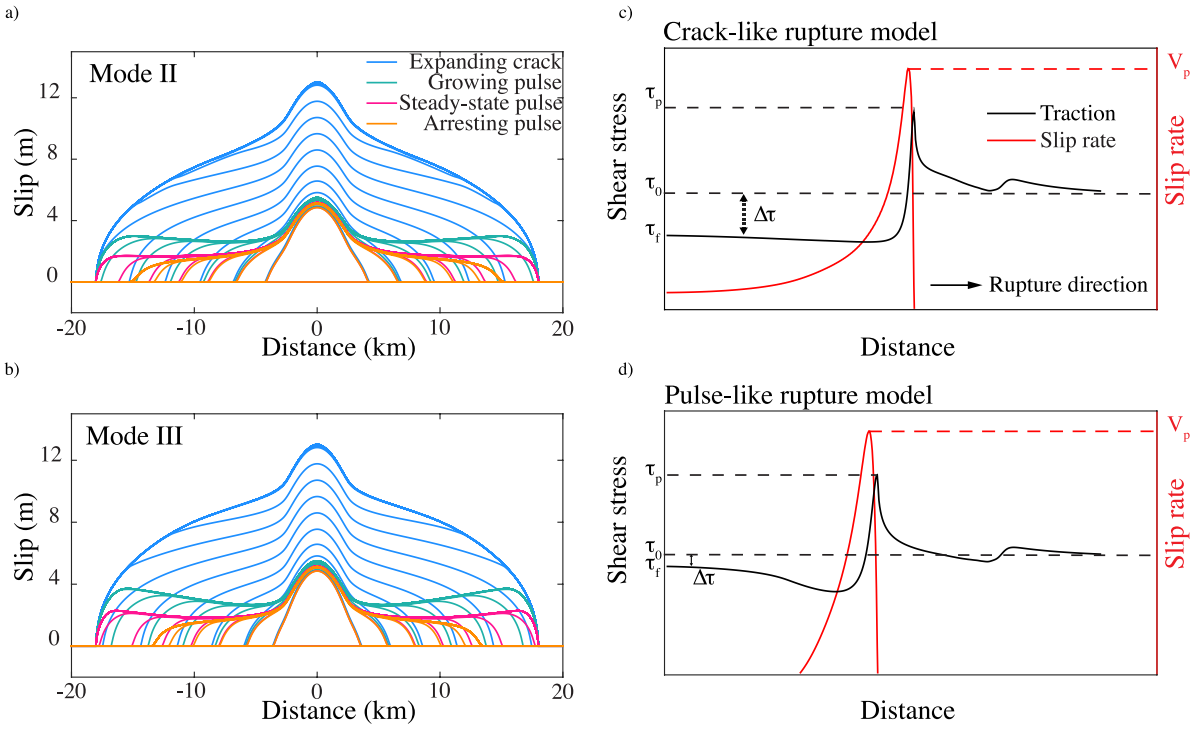

Figure 2.3: Numerical simulation results of 4 rupture models: expanding crack (blue), growing pulse (green), steady-state pulse (pink) and arresting pulse (orange). (a) and (b) show time dependent slip (1s interval) along inplane and antiplane direction, and the characteristic slip profiles of the respective rupture modes are observed. The dependence of slip on the distance from the hypocenter is minimal in pulse-like mode, but (apart from the nucleation zone) has the expected elliptical shape in the crack-like case. (c) and (d) show shear stress (black line) and slip rate (red line) for crack-like and pulse-like ruptures. In the pulse-like mode (d), shear stress has a re-strengthening phase that heals the rupture and reduces the slip duration, in contrast to the flat residual shear stress and longer slip duration in the crack-like rupture (c).

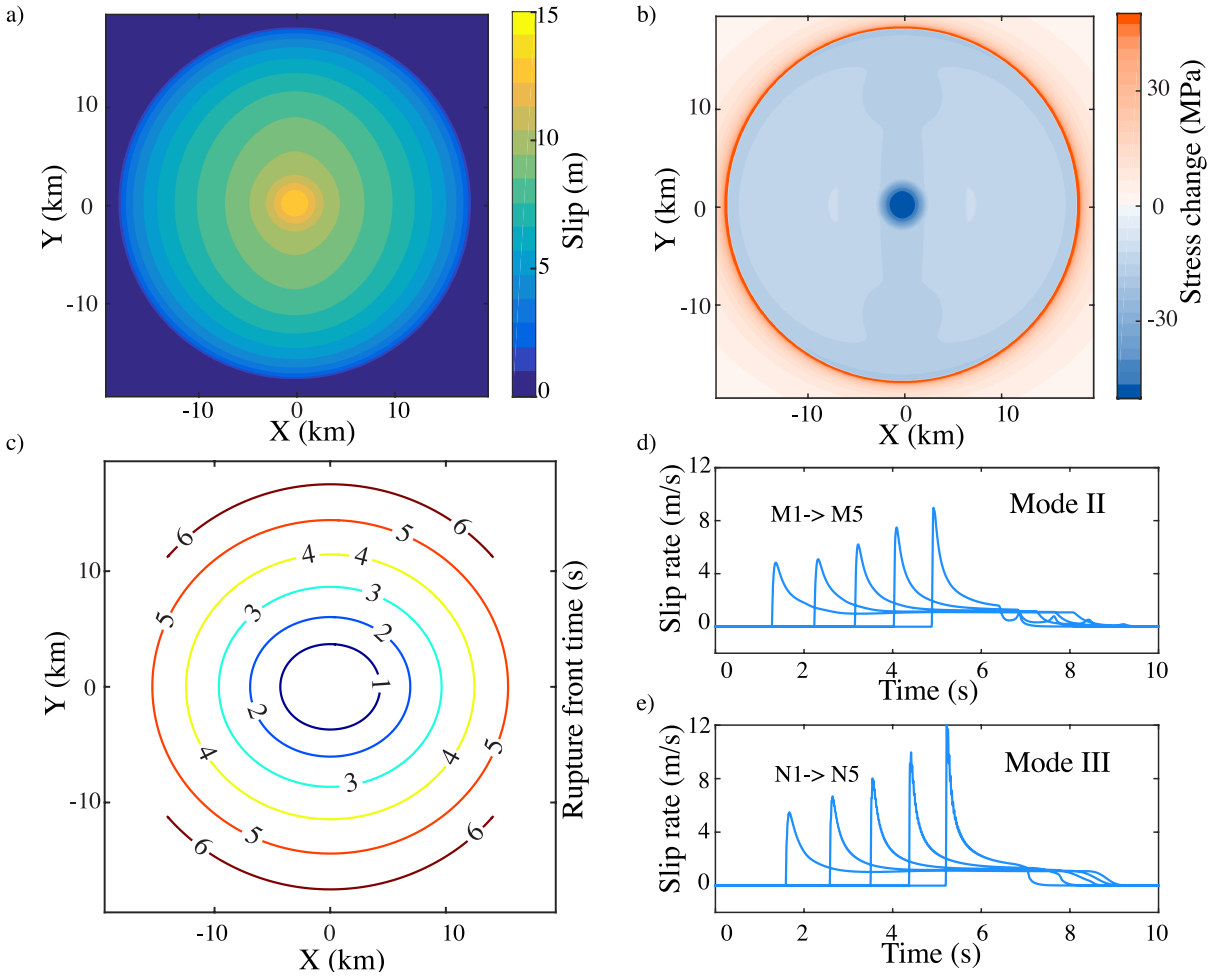

Figure 2.4: Details of expanding crack, showing slip (a), static stress change (blue region means stress drop) (b), rupture front time (c) and slip rate functions (d) and (e).

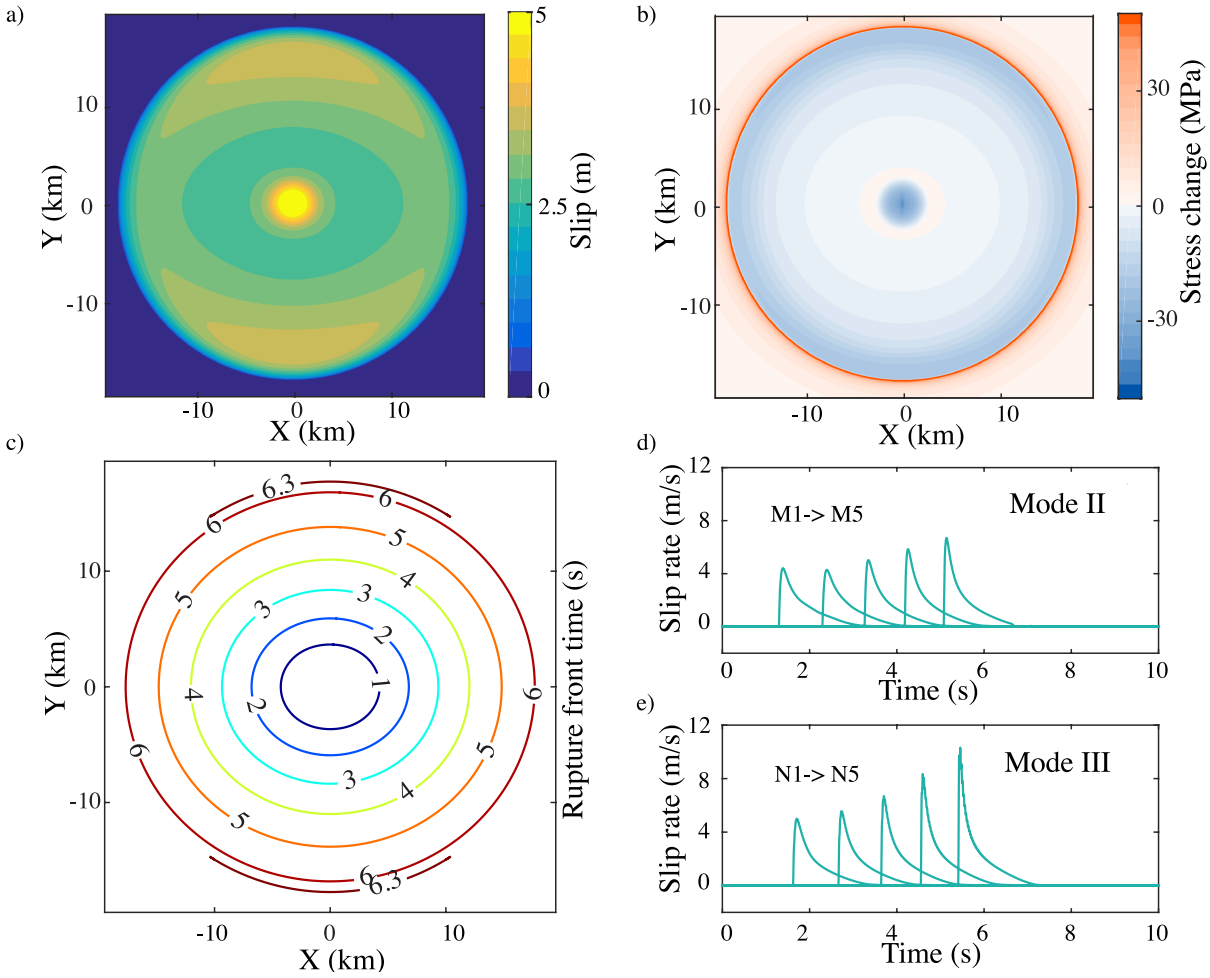

Figure 2.5: Details of growing pulse, showing slip (a), static stress change (b), rupture front time (c) and slip rate functions (d) and (e).

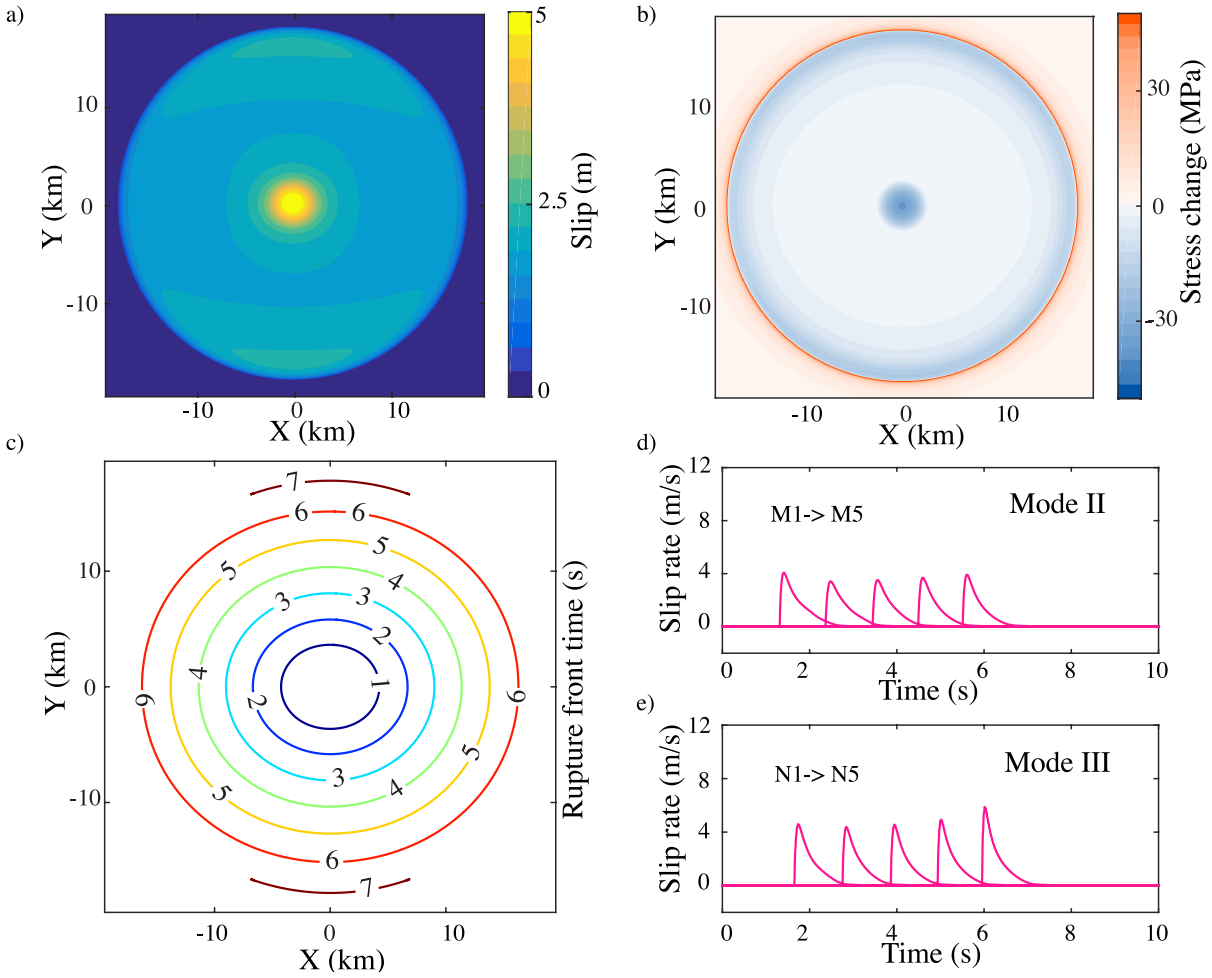

Figure 2.6: Details of steady-state pulse, slip (a), static stress change (b), rupture front time (c) and slip rate functions (d) and (e).

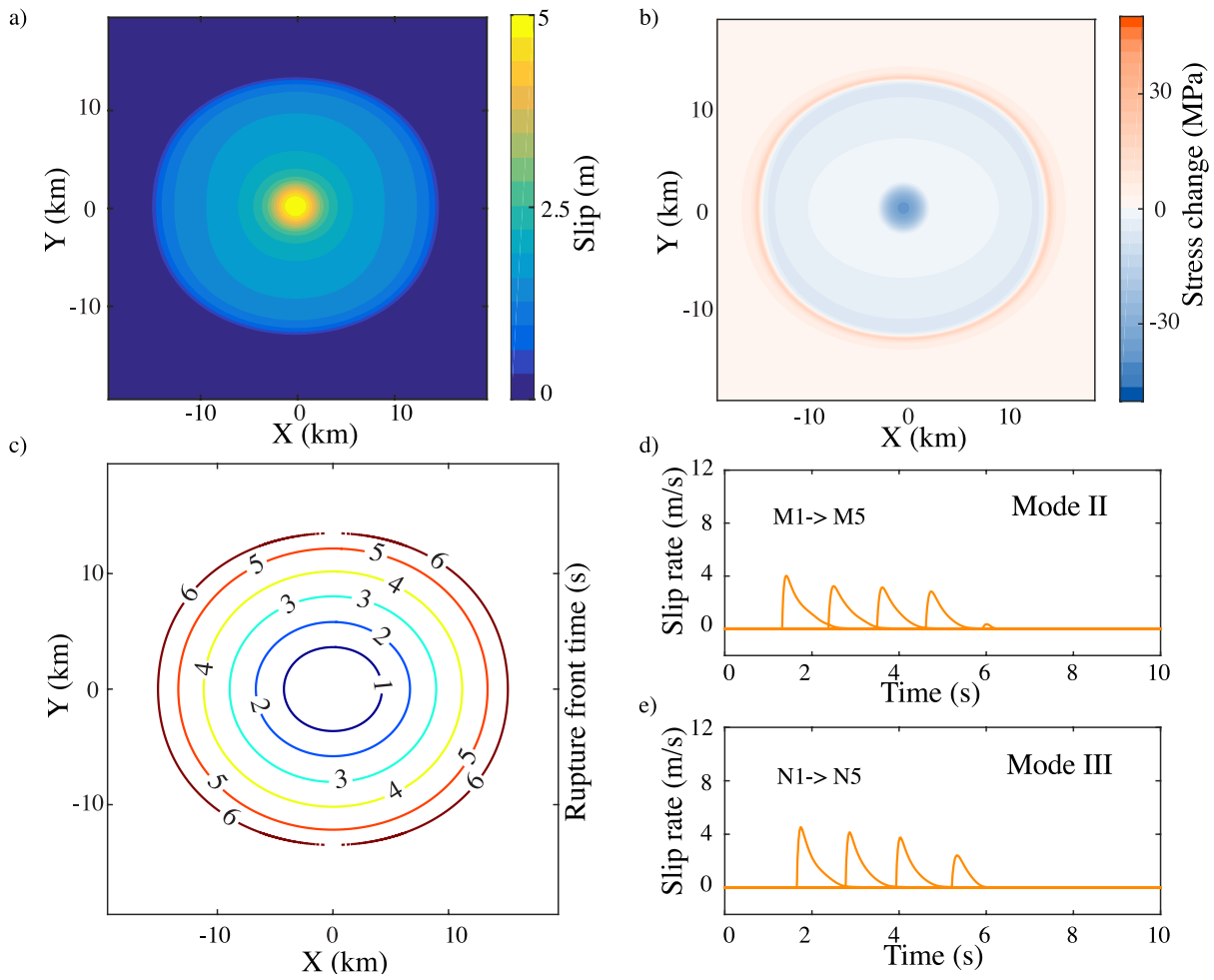

Figure 2.7: Details of arresting pulse, showing slip (a), static stress change (b), rupture front time (c) and slip rate functions (d) and (e).

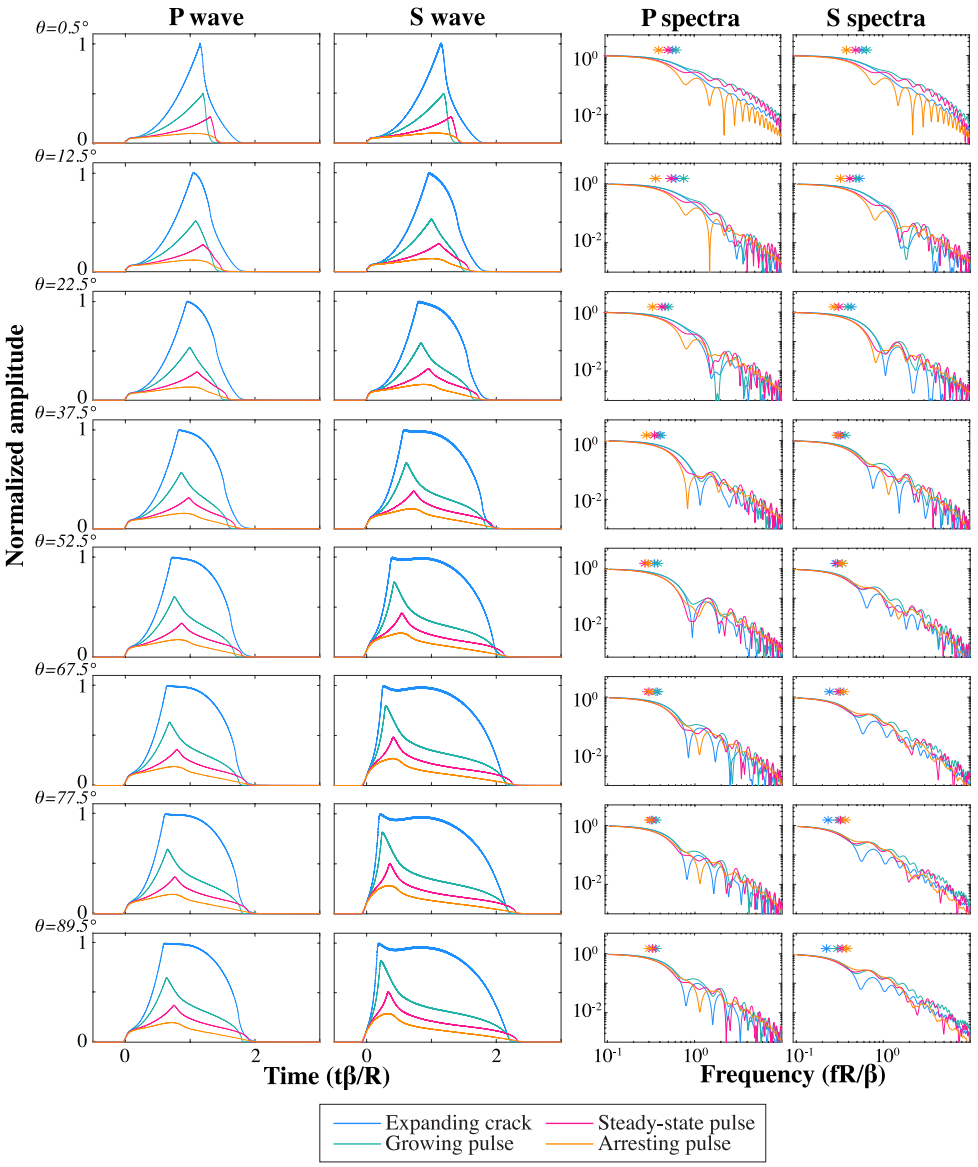

Figure 2.8: The radiated P and S displacement and spectra at 8 take-off angles from 4 dynamic rupture models (denoted by 4 colors). Best fit corner frequency f_c of each spectrum is indicated by a star.

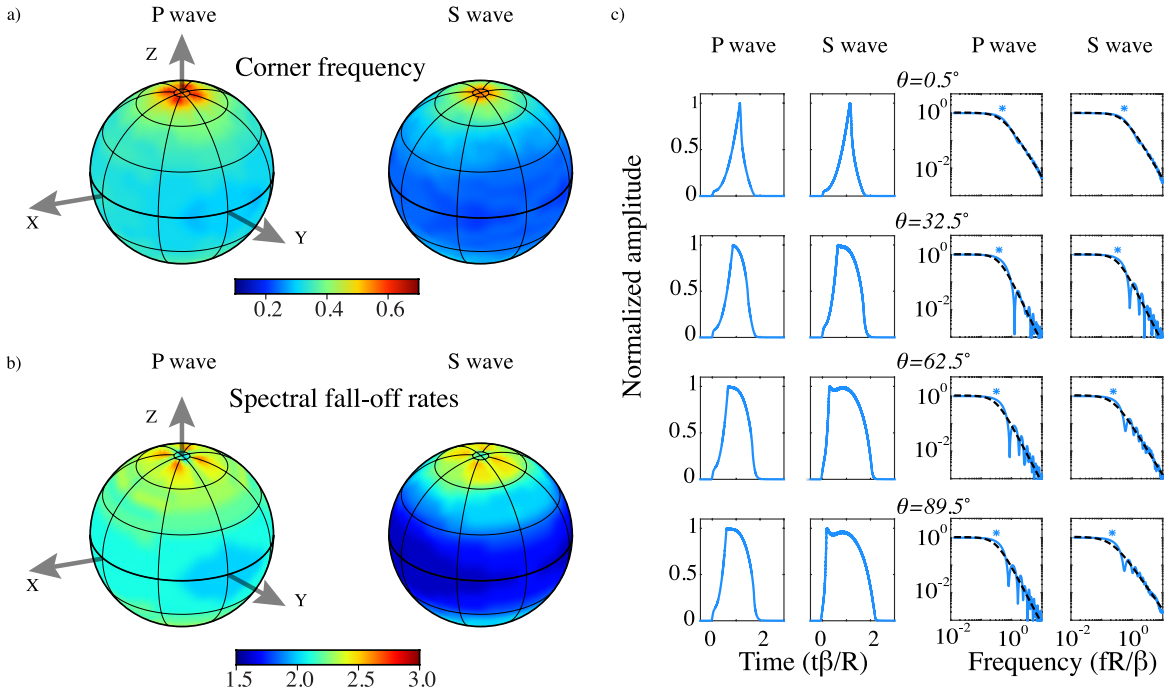

Figure 2.9: Far-field displacements, spectra, normalized corner frequencies ($f_c R/\beta$) and fall-off rates for expanding crack model. (a) Distributions of P and S spectral corner frequencies ($f_c R/\beta$) over the focal sphere. X and Y axes are identical with those in Figures 4-7. (b) Distributions of P and S spectral fall-off rate over the focal sphere. (c) 4 sampled displacements and spectra of P and S waves. Black dashed lines are best fit Brune model and star symbol denotes best fit corner frequency.

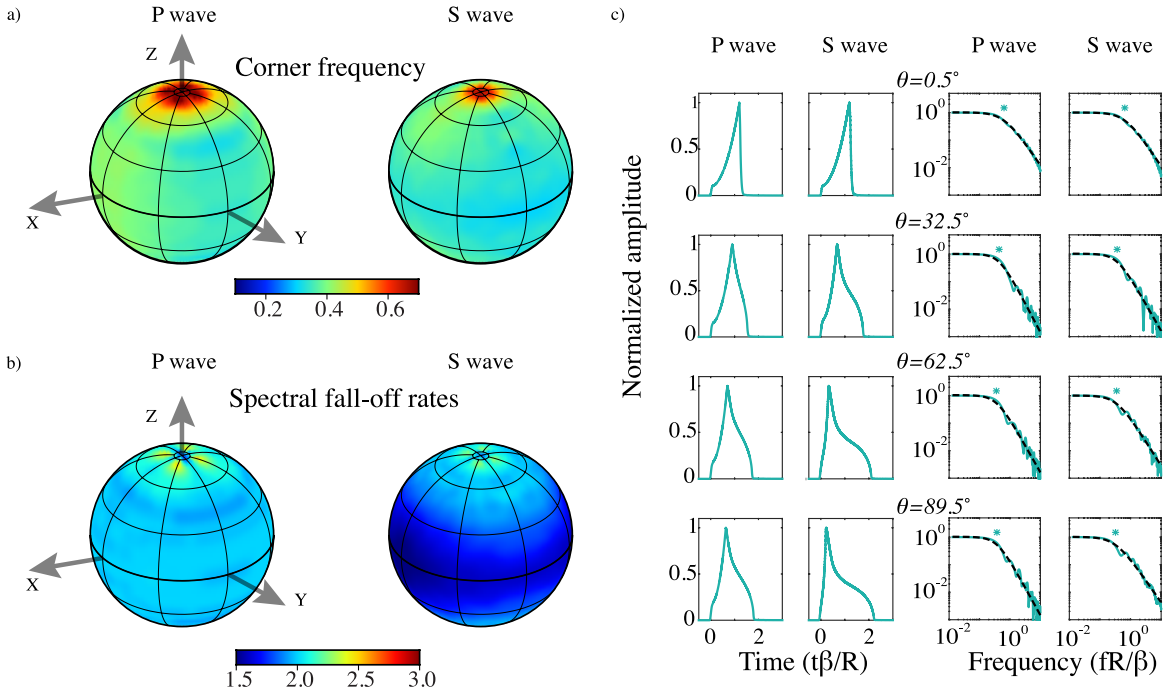

Figure 2.10: Far-field displacements, spectra, normalized corner frequencies and fall-off rates for growing pulse model. (a) Distributions of P and S spectral corner frequencies over the focal sphere. (b) Distributions of P and S spectral fall-off rate over the focal sphere. (c) 4 sampled displacements and spectra of P and S waves. Black dashed lines are best fit Brune model and star symbol denotes best fit corner frequency.

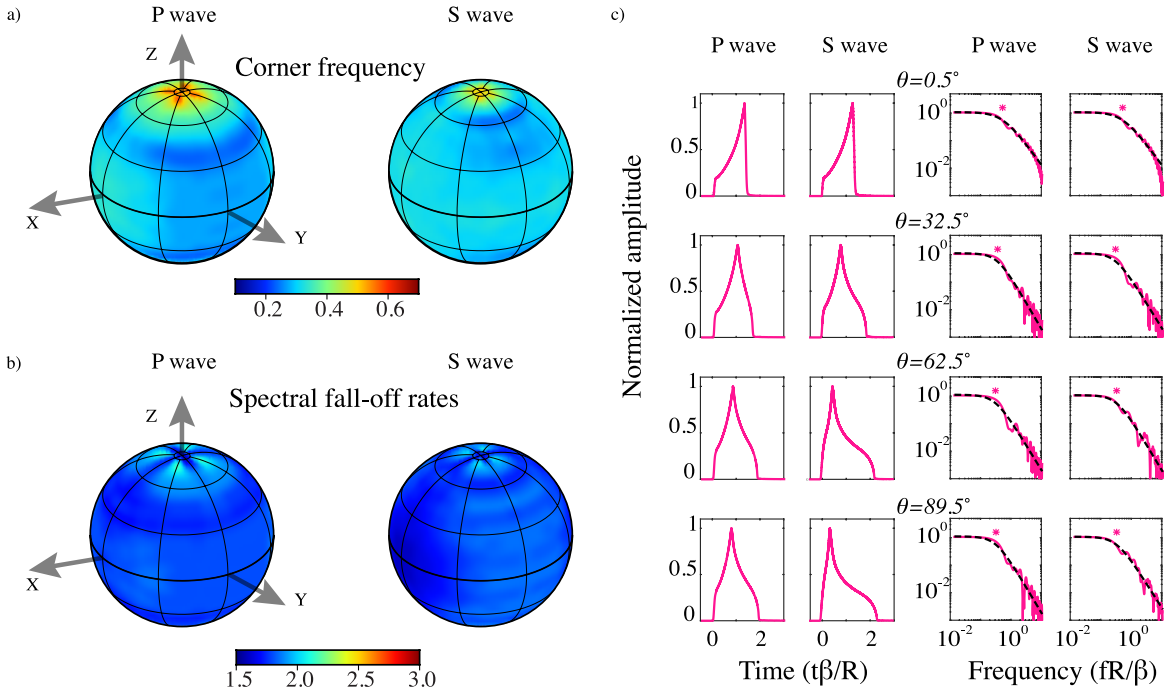

Figure 2.11: Far-field displacements, spectra, normalized corner frequencies and fall-off rates for steady-state pulse model. (a) Distributions of P and S spectral corner frequencies over the focal sphere. (b) Distributions of P and S spectral fall-off rate over the focal sphere. (c) 4 sampled displacements and spectra of P and S waves. Black dashed lines are best fit Brune model and star symbol denotes best fit corner frequency.

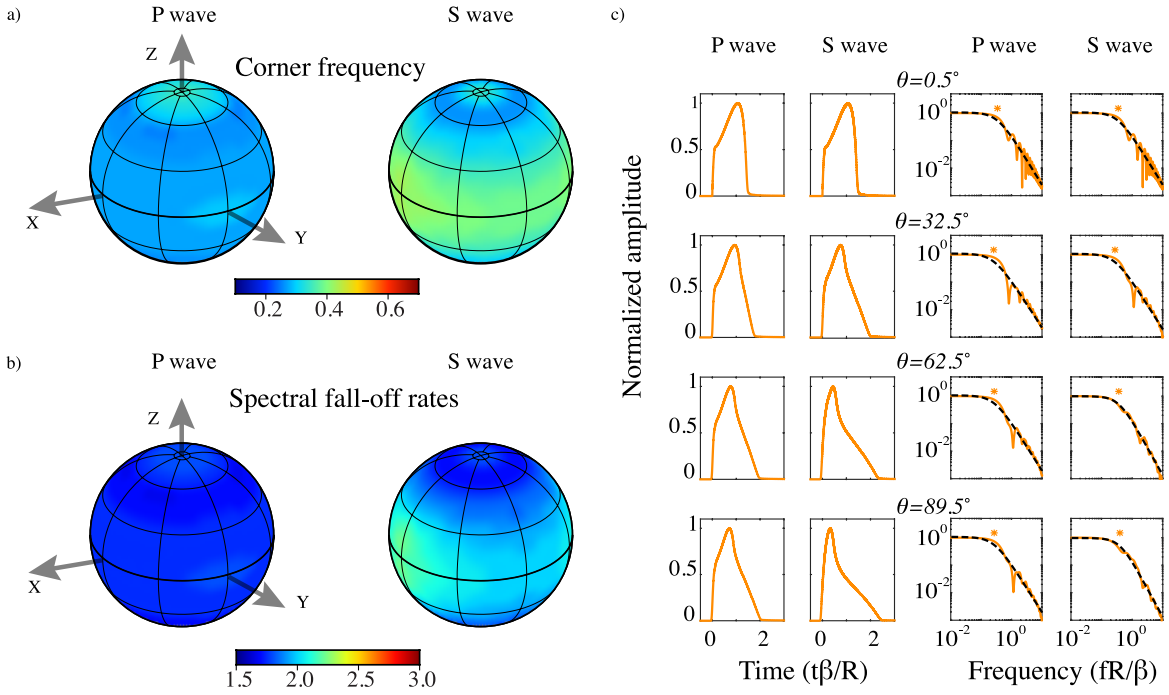

Figure 2.12: Far-field displacements, spectra, normalized corner frequencies and fall-off rates for arresting pulse model. (a) Distributions of P and S spectral corner frequencies over the focal sphere. (b) Distributions of P and S spectral fall-off rate over the focal sphere. (c) 4 sampled displacements and spectra of P and S waves. Black dashed lines are best fit Brune model and star symbol denotes best fit corner frequency.

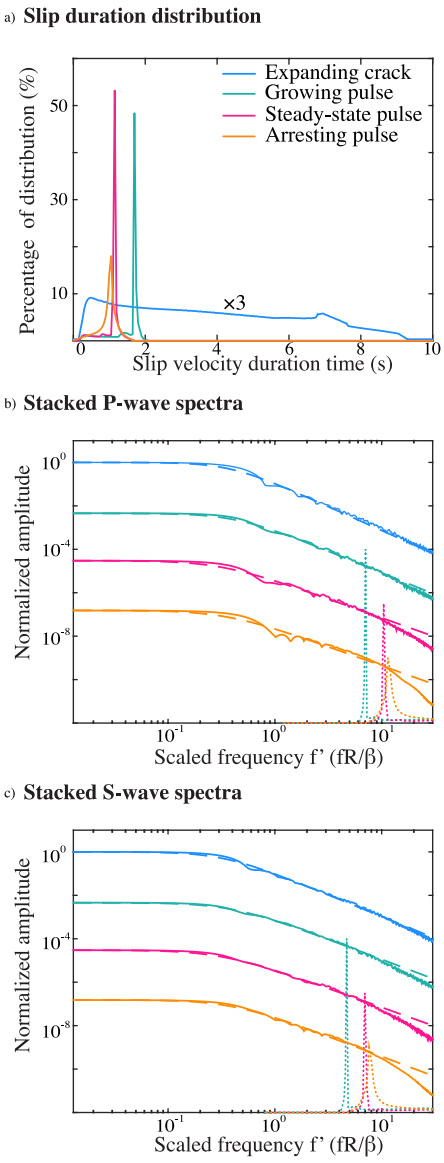

Figure 2.13: Slip rate duration distribution and stacked spectra of P and S waves for each model. (a) The distributions of slip rate durations for each model (we scale the curve of expanding crack with a factor of 3 to highlight the linearly decreasing distribution of slip duration). (b) Stacked P wave spectra (solid lines) and best fitted Brune model (dashed lines). Dotted curves are frequency distribution of K/T, with K scaled such that K/T is a rough indicator of the second corner frequency. (c) Stacked S wave spectra and best fit Brune model.

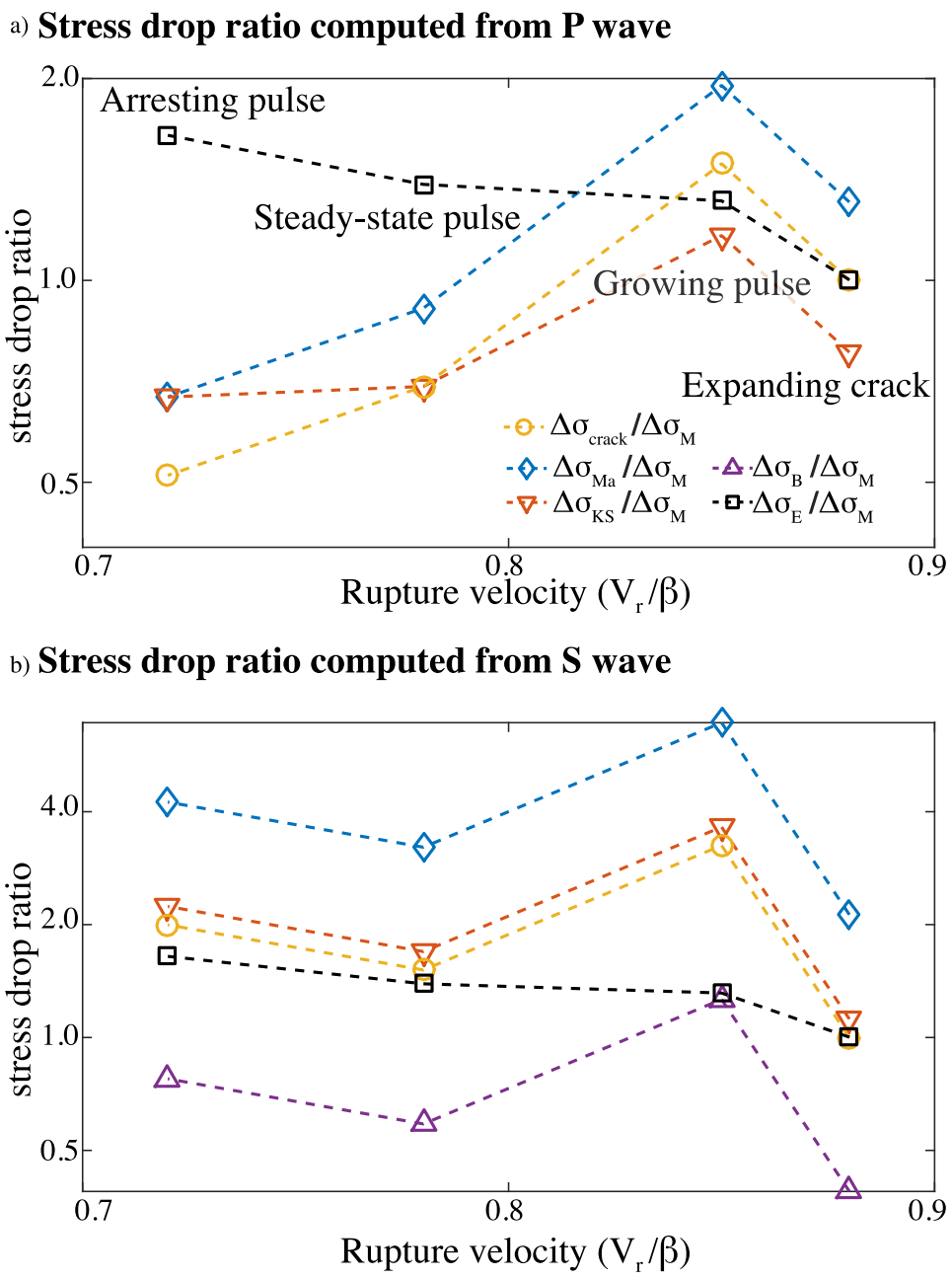

Figure 2.14: The ratio between spectrally estimated stress drop and actual moment-based stress drop for the 4 simulated rupture models. Four sets of parameters, k^P and k^S are used to investigate how large the variabilities of estimations can be. The vertical axis is logarithmic. Also shown is the ratio between $\Delta\sigma_E$ and $\Delta\sigma_M$ for each simulation, denoted by black squares, demonstrating the divergence of these two averages as rupture mode changes from crack-like to pulse-like.

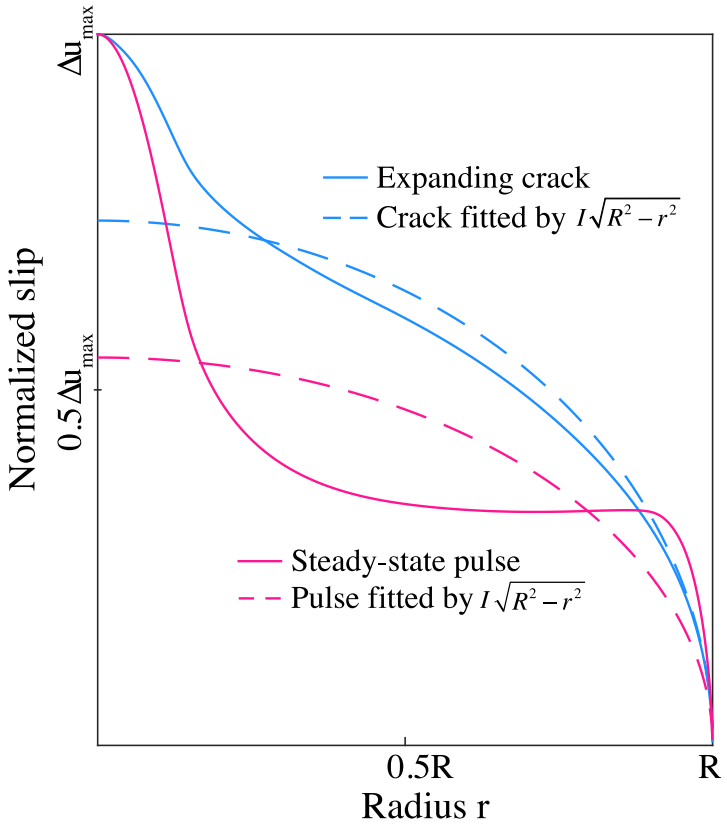

Figure 2.15: Slip distribution, comparing crack-like and pulse-like models. The blue solid and dashed lines are the final slip distribution from expanding crack model and best fitted Eshelby's solution. The pink solid and dashed lines are the final slip distribution from expanding crack model and best fit Eshelby solution. In both sets of lines, the degree of discrepancy between obtained models and the theoretical static solution determines the appropriateness of conventional Equation 2.1 or Equation 2.3 for computing static stress drop. The misfit at small radius is due to the nucleation effect (different stress drop in the nucleation zone).

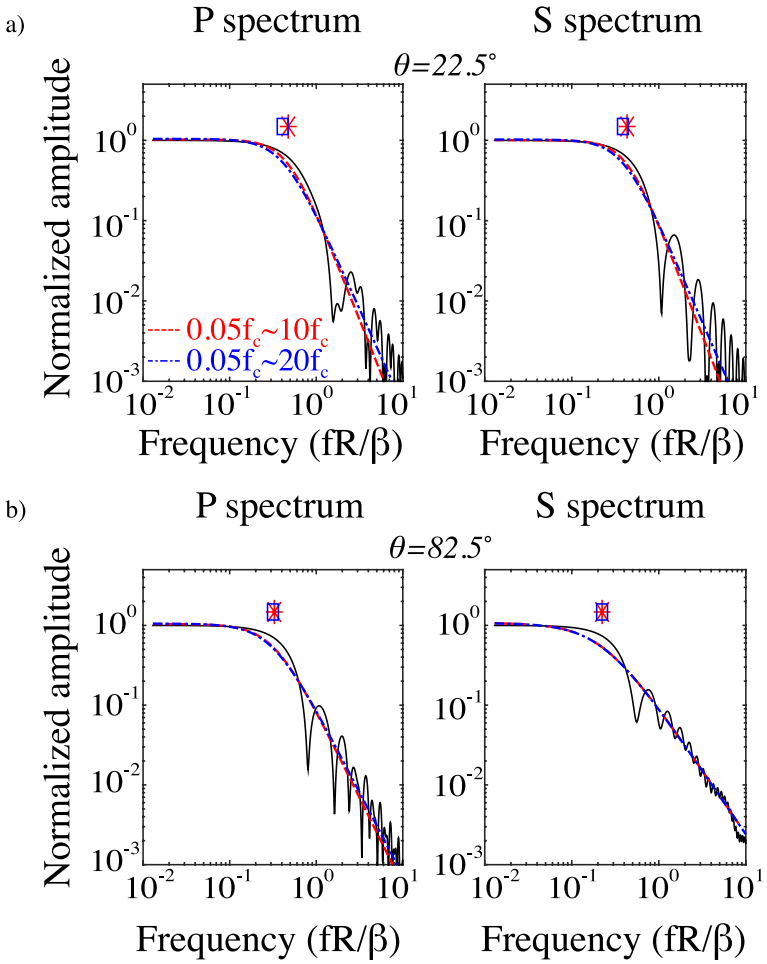

Figure 2.16: Effect of frequency band on spectral fitting. (a) Black solid lines are P and S spectrum at 22.5° take-off angle. The red and blue dashed lines are best fit Brune model using $0.05f_c \sim 10f_c$ and $0.05f_c \sim 20f_c$, respectively. At low take-off angle, slight difference of fitting occurs at high frequency. (b) Black solid lines are P and S spectrum at 82.5°. The red and blue dashed lines are best fit Brune model using $0.05f_c \sim 10f_c$ and $0.05f_c \sim 20f_c$, respectively. At high take-off angle, both bands result in identical fitting.

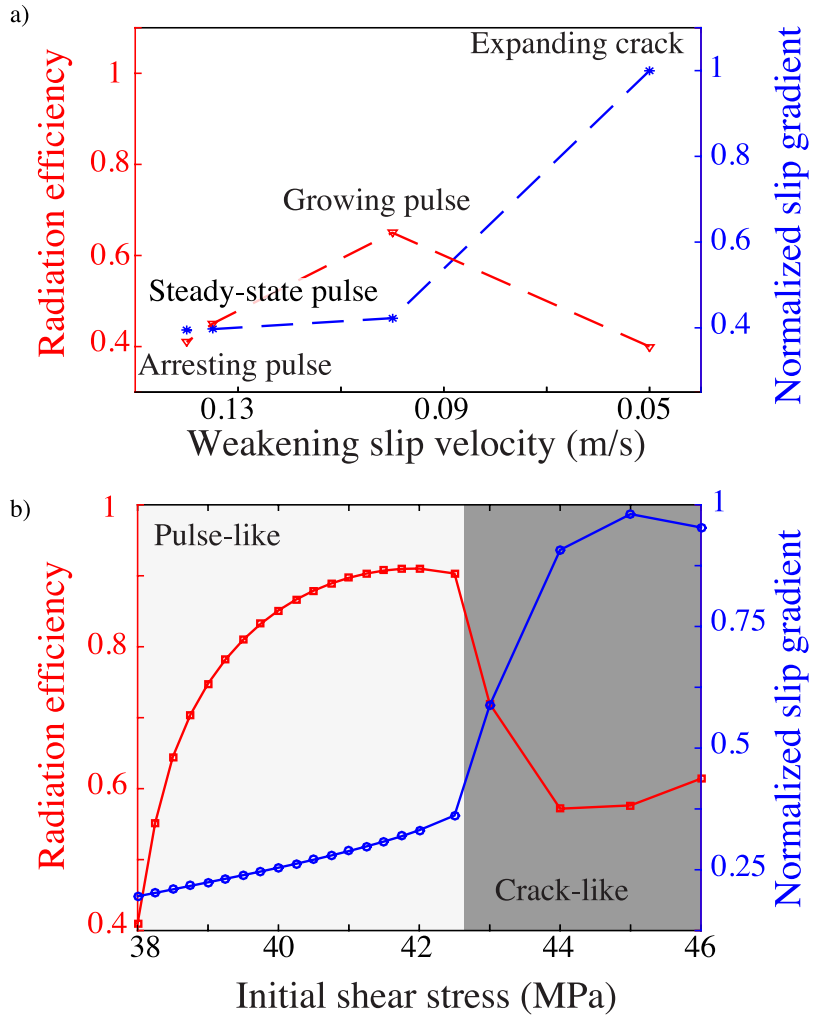

Figure 2.17: Radiation ratio variation with rupture mode transition. (a) radiation ratio (red dashed line) and slip gradient (rupture type indicator, blue dashed line) of 4 models show with rupture mode is changed to crack-like, radiation ratio has an apparent reduction. (b) Similar pattern can be observed when we switch to adjust initial shear stress to regenerate a rupture mode transition.

Chapter 3

Geometric controls on pulse-Like rupture in a dynamic model of the 2015 Gorkha Earthquake

The 15 April 2015 M_w 7.8 Nepal Gorkha earthquake occurred on a shallowly dipping portion of the Main Himalayan Thrust (MHT). Notable features of the event include (1) the dominance of a slip pulse of about 6-s duration that unlocked the lower edge of the MHT and (2) the near-horizontal fault geometry, which, combined with proximity of the free surface, allows surface-reflected phases to break the across-fault symmetries of the seismic wavefield. Our dynamic rupture simulations in an elastoplastic medium yield earthquake parameters comparable to those deduced from kinematic inversions, including seismic moment and rupture velocity. The simulations reproduce pulse-like behavior predicting pulse widths in agreement with those kinematic studies and supporting an interpretation in which the pulse-like time dependence of slip is principally controlled by rupture geometry. This inference is strongly supported by comparison of synthetic ground velocity with the near-field high-rate GPS recording at station KKN4, which shows close agreement in pulse width, amplitude, and pulse shape. That comparison also

constrains the updip extent of rupture and disfavors significant coseismic slip on the shallow ramp segment. Over most of the rupture length, the simulated rupture propagates at a near-constant maximum velocity ($\sim$ 90% of the S wave speed) that is controlled by the antiplane geometry and off-fault plastic yielding. Simulations also reveal the role of reflected seismic waves from the free surface, which may have contributed $\sim$ 30% elongation of the slip pulse, and show the potential for significant free-surface interaction effects in shallow events of similar geometry.

3.1 Introduction

On 25 April 2015, a devastating earthquake occurred along the convergent boundary between Eurasian and Indo-Australian plates. Its epicenter is about 77 km northwest of Kathmandu, the capital, and most populous city, of Nepal. The active thrust system in this region, which includes the Main Frontal Thrust along the southern edge of the Sub-Himalayan foothills and the Main Himalayan Thrust (hereafter MHT) dipping gently to the north, has hosted several large, damaging earthquakes, for example, earthquakes in 1505 and 1934 with magnitudes greater than 8. This 2015 earthquake was the largest decollement event in the past 80 years. Its hypocentral depth of 15 km and the absence of observed surface rupture, as well as results from inversions of seismic and geodetic data, all indicate that this event ruptured a portion of the MHT, whose dip angle can then be inferred from the low-angle thrust focal mechanism of the event. A number of essential features of this earthquake have been revealed by multiple types of observations. This M_w 7.8 earthquake, with a peak slip of 5-8 m, ruptured $\sim$140 km along the strike direction and $\sim$60 km along the dip direction and propagated unilaterally southeastward at a velocity of $\sim$3.0 km/s. These first-order results have been derived from finite-fault inversions [Avouac et al. 2015; Galetzka et al. 2015; Grandin et al. 2015; Qiu et al. 2016; Wang and Fialko 2015; Yue et al. 2017] and P-wave teleseismic back-projections [Avouac et al. 2015; Fan and Shearer 2015; Grandin et al. 2015; Meng et al. 2016; Yagi and Okuwaki 2015]. The event had a pulse-like rupture mode

[Galetzka et al. 2015; Yue et al. 2017] with a slip pulse of $\sim$ 20 km in spatial width and $\sim$6 s in temporal duration [Galetzka et al. 2015]. Moreover, depth- and frequency-varying rupture properties [Denolle et al. 2015; Yin et al. 2017; Yue et al. 2017] have been observed, with patterns broadly resembling those seen on subduction megathrusts [Yao et al. 2013].

Fault morphology plays an important role in earthquake rupture–from initiation, to evolution, to eventual termination–by modifying localized stress conditions and thereby impacting rupture extent, near-field ground motion, and aftershock triggering [Andrews 1994; King et al. 1994; Oglesby and Mai 2012]. There have been extensive studies of the MHT fault geometry, upon which the most destructive earthquakes in the region have occurred. Multiple techniques have been used to explore its geometry in central Nepal, for example, receiver functions [Duputel et al. 2016; Nabelek et al. 2009; Schulte-Pelkum et al. 2005], structural geology [Avouac 2007; Hubbard et al. 2016; Pearson and DeCelles 2005], electromagnetic investigations [Lemonnier et al. 1999], microseismicity and focal mechanism studies [Pandey et al. 1995; Wang et al. 2017], geodetic inversion [Elliott et al. 2016], geodynamical modeling [Cattin and Avouac 2000; Chamlagain and Hayashi 2007; Robinson 2008]. Among the shared inferences from these studies are that the MHT serves as a decollement, with a very low dip angle underneath the Lesser Himalaya, steepening along a ramp down to the north beneath the Higher Himalaya and ramping up to the south to merge with the shallower Main Frontal Thrust. While there is broad agreement on the overall geometry, there remains substantial uncertainty in the dip angles and the dimensions of MHT segments. Recently, Hubbard et al. [2016] have incorporated geophysical and geological results (e.g., surface geology, topography, and seismicity) to formulate a detailed fault morphological model. The model contains two ramps truncating the edge of the nearly flat decollement segment along the dip direction and two pinch points confining the dimension of this shallow-dip segment along the strike direction (Figure 3.1). In this study, we adopt this fault representation of the MHT because this fault geometry is suggested by previous studies to be particularly related to the Gorkha earthquake. For instance, (1) the pattern of coseismic

slip for the Gorkha event [Avouac et al. 2015] is in good agreement with expectations from the Hubbard et al. [2016] model, (2) the refined relocations and focal mechanisms determined for 16 aftershocks ([Wang et al. 2017], especially their Figure 3.8), shown in Figure 3.1, also suggest a double-ramp geometry of the MHT in the region of the mainshock in the form of a concentration of hypocenters delineating a slope change at the northern edge of the main area of coseismic slip, and (3) earthquake cycle modeling based on this fault geometry [Qiu et al. 2016] suggests that the 2015 Gorkha rupture area was limited by fault geometrical features. In the current paper, our aim is to apply dynamic rupture modeling, in conjunction with seismic and geodetic constraints, to examine the physical relationship between the time-dependent aspects of the earthquake (e.g., rupture propagation, slip-rate function, and near-fault ground motion) and the rupture geometry. The geometrical bounds on rupture in our models were inspired by the underlying model of fault geometry, but the rupture bounds are enforced by imposing fault strength variations that are not explicitly geometrical in origin.

In addition to the fault morphology, the free surface can play a role in the dynamics of rupture. Surface reflected waves not only interfere with the direct seismic waves from the rupture surface but may also have an effect on the rupture evolution itself [Denolle et al. 2015; Oglesby et al. 1998; Rudnicki and Wu 1995]. It is reasonable to expect this effect to become more prominent in a shallow-thrust scenario such as the Gorkha earthquake. On a shallowly dipping fault, free-surface reflections break the symmetry that pertains for an isolated fault or for a near-surface vertical fault and thereby induce normal stress fluctuations, correspondingly altering fault strength. These fluctuations, and accompanying fluctuations in shear stress, have the potential to interact with rupture processes. Some theoretical studies [e.g., Smith et al. 2005] have found little or no effect on teleseismic peak-to-peak amplitudes from wave-slip interaction associated with surface reflected phases, but this result may be quite model dependent, and, in any case, it does not imply that near-fault seismic observables are unaffected by those interactions. Additional fault properties such as the presence of a bimaterial interface could further complicate

this interaction and lead to enhanced hanging/foot wall effects [Ma and Beroza 2008]. In the case of a normal fault, theory indicates that the free surface can even trigger a shallow nucleation ahead of the main rupture, which could explain the level of high-frequency radiation originating at shallow depth from some normal-faulting events [Nielsen 1998]. In contrast to the models in the foregoing studies, the Gorkha earthquake was an essentially antiplane (Mode III) rupture event on a shallow, and very shallowly dipping, fault surface, a geometry for which free-surface interactions have not been previously modeled (free-surface interactions in 2-D models of the Tohoku earthquake, (e.g., Kozdon and Dunham [2013] and Huang et al. [2014], are for purely Mode II rupture). Therefore, we include in our modeling an exploration of the interaction between free-surface-reflected waves and the rupture process in this event and characterize the extent to which that interaction may affect the character and duration of coseismic slip.

As demonstrated by finite-fault inversions [Galetzka et al. 2015; Yue et al. 2017], the Gorkha rupture propagated unilaterally eastward in a pulse-like slip mode. Pulse-like rupture is one of the two principal endmember models for the space-time dependence of coseismic slip (in contrast to "crack-like") and has been recognized in many seismological, analytical, computational, and experimental studies [Beeler and Tullis 1996; Day 1982; Day et al. 1998; Gabriel et al. 2012; Haskell 1964; Heaton 1990; Huang and Ampuero 2011; Lu et al. 2010; Nielsen and Madariaga 2003; Noda et al. 2009; Oglesby and Day 2002; Wang and Day 2017; Zheng and Rice 1998]. Melgar and Hayes [2017] examined a database of over 150 finite-fault rupture models (M_w 7 to 9) and inferred a pulse-like signature (slip rise times much shorter than the source duration) for the preponderance of them.

A pulse-like rupture mode produces distinct effects (relative to crack-like rupture) on both far-field seismic observations (e.g., a secondary spectral corner, as in Wang and Day, 2017) and near-field ground motions (e.g., compact directivity phases in the fault-normal ground velocity as in Aagaard and Heaton [2008]. Numerous mechanisms have been hypothesized to contribute to pulse-like rupture, including velocity dependent friction, heterogeneity of fault strength and initial

shear stress, and finite downdip rupture dimension. [Beeler and Tullis 1996; Beroza and Mikumo 1996; Cochard and Madariaga 1996; Day 1982; Day et al. 1998; Gabriel et al. 2012; Johnson 1992; Noda et al. 2009; Oglesby and Day 2002; Zheng and Rice 1998]. However, it is difficult on the basis of kinematic analysis alone to distinguish these effects on any individual rupture. One complicating factor is uncertainty in the retrieval of the slip-pulse shape, due to factors such as a prior selection of a functional form to represent the source time function, the choice of a singlewindow or multiwindow inversion method, and ambiguity in defining the end time of the pulse. Some efforts have been made to improve inversions for slip pulses by using insights from dynamic models. Tinti et al. [2005] propose a new source-time function called regularized Yoffe function that is inspired by a self-similar pulse-like solution [Nielsen and Madariaga 2003] and approximates some generic characteristics of slip calculated in dynamic models of rupture propagation. Apart from these essentially observational limitations, however, kinematic analysis does not address the fundamental uncertainty about how the various hypothesized factors, taken individually, affect pulse shape and duration and, moreover, how those factors may interact.

In this paper, we investigate factors controlling the slip pulse of the 2015 Gorkha earthquake by forward dynamic modeling. We specify a priori the fault geometry and the large-scale stress and frictional preconditions and enforce observational constraints on total seismic moment. The model prediction for rupture velocity compares favorably with observational estimates (as inferred from backprojection studies), and the near-source velocity waveform compares favorably with a very near source high-rate GPS recording that appears to be relatively free of path effects. The results support an interpretation in which slip-pulse duration is principally controlled by the along-dip extent of the rupture. The Gorkha rupture probably interacted with free-surface reflections, which may have added $\sim$30% to the average slip-pulse width. The simulations also support the interpretation that the Gorkha event ruptured, over much of its length, at velocities near the terminal velocity for an antiplane rupture subject to finite yield strength.

3.2 Problem Formulation and Model Setup

We first describe the geographical area for modeling the 2015 Gorkha earthquake and the discretization of the MHT fault surface and surrounding volume. Then we describe our models for the bulk material properties, the hypothesized initial stress state, and constitutive properties on the fault. Finally, we outline the numerical method and computational platform employed.

3.2.1 Computational Domain and Discretization

The model area of interest is enclosed by an orange box in Figure 3.2a. The dimensions along the x axis (horizontally directed from the southeast to the northwest), y axis (horizontally directed from the southwest to northeast), and z axis (vertically directed downward from the Earth surface) are 200 km, 80 km, and 60 km, respectively. Inside this box, the fault geometry of the MHT is taken from Hubbard et al. [2016]. Multiple alternative fault models have been proposed for the source region of the 2015 Gorkha earthquake. [e.g., Avouac 2007; Duputel et al. 2016; Elliott et al. 2016; Lemonnier et al. 1999; Nabelek et al. 2009; Schulte-Pelkum et al. 2005].

From among these, we adopted the fault geometry of Hubbard et al. [2016] (hereafter referred to simply as the Hubbard model) because of its close relationship with the coseismic slip of the 2015 Gorkha event. The Hubbard model, while based on structural data that are independent of kinematic inversions of the Gorkha earthquake, has a geometry that is consistent with the spatial limits of coseismic rupture. In the Hubbard model there are two ramps along the dip direction, and we will refer to the upper (southern) one as the updip ramp and the lower (northern) one as the downdip ramp. These are separated by an intervening decollement (which we will also refer to as the flat segment) that is terminated along strike, both to the east and to the west, by "pinch points" where the upper and lower ramps merge to yield a single ramp (Figure 3.1 and 3.2). A decollement of this form, terminated at narrow junctions, correlates well with the coseismic patch in the Gorkha event. Consequently, the Hubbard model geometry is

an appropriate starting point for models of rupture dynamics. The dynamic models can, in turn, help assess the extent to which that geometry controls the time-dependent rupture behavior. We interpolated the triangularized fault surface representation of the Hubbard model (GOCAD data format) onto the structured hexahedral grid employed in our dynamic rupture simulation method. In that grid, the x and y axes are equally and orthogonally gridded (100-m intervals), and z intervals are variable, as required to ensure that both the fault surface and the free surface conform to grid coordinate surfaces. To enhance numerical accuracy in computation of fault-surface tractions, the elements adjacent to the fault on either side have identical shapes and sizes. All remaining z intervals in the structured, hexahedrally gridded volume are linearly interpolated between the fault and, respectively, the free surface and bottom perfectly matched layer zone (illustrated in Figure 3.2b). In total, our final mesh is composed of $\sim$960 million hexahedral elements with variable element sizes and shapes.

3.2.2 Bulk Material, Initial Stress State and Fault Constitutive Law

We assume a homogeneous, elastoplastic bulk material in this region. This simplification is appropriate to our objective of investigating the relationship between the complex fault geometry and the dynamics of the rupture. The rupture extent will be constrained by comparing the predicted and observed ground velocity pulse at the KKN4 high-rate GPS station, which, by virtue of its siting on rock directly above the rupture surface of this event, is relatively insensitive to path effects. We assign the elastic properties (given in Table 3.1) based upon their values at the hypocentral depth, as given by the 1-D model of Avouac et al. [2015]. We represent departures from linearly elastic behavior through the Drucker-Prager elastoplastic model [Drucker and Prager 1952], which has been widely used in geomechanics to model pressure-dependent inelastic yielding. It has been long recognized that, if modeled by linear elasticity, the high stresses at the rupture front are likely to exceed the rock strength [Andrews 1976], and dynamic effects of

near-fault plasticity have been the subject of several recent studies [Andrews 2005; Duan and Day 2008; Dunham et al. 2011; Gabriel et al. 2013; Ma and Andrews 2010; Roten et al. 2014; Roten et al. 2017; Shi and Day 2013]. The introduction of plasticity into dynamic models of the Gorkha earthquake reduces the unphysically high shear stresses, and the accompanying high peak slip rates, that develop near the rupture front in purely elastodynamic models. Furthermore, the reduction of the maximum slip rate increases the length of the frictional cohesive zone, which in turn serves to control the contraction of the cohesive zone associated with rupture acceleration toward terminal velocity [Day et al. 2005]. Therefore, because numerical solution accuracy requires that the computational grid resolve the minimum cohesive zone [Andrews 1976; Day et al. 2005], plastic yielding has the ancillary effect in this case (though not in general) of improving numerical accuracy. The Drucker-Prager model formulation is given in Appendix A, and parameter values used in the simulations are listed in Table 3.1. The initial stress state is subject to large uncertainties. Even with many simplifying assumptions, geodynamic simulations of frictional sliding on the MHT in Nepal predict complex compressive and tensional stress fields around the fault plane [Chamlagain and Hayashi 2007], with details sensitive to the details of the fault system geometry. To isolate the first-order dynamic effects associated with the assumed fault geometry (Hubbard model), we simplify the stress state by employing a homogeneous initial stress tensor. This choice neglects, in particular, any increase in effective normal stress with depth. However, in that respect the model is consistent with the suggestion by [Rice 1992] that below some depth, the pore pressure follows the lithostatic gradient instead of the hydrostatic trend (and the coseismic patch of the Gorkha event is everywhere below 8 km in depth). The initial stress tensor σ^0 is given by

$$\sigma^0 = \begin{bmatrix} \sigma_{xx} & 0 & 0 \\ 0 & \sigma_{yy} & \sigma_{yz} \\ 0 & \sigma_{yz} & \sigma_{zz} \end{bmatrix} \tag{3.1}$$

where the stress components are listed in Table 3.1 (the coordinate system is that of Figure 3.2). In designing this initial stress tensor, we attempt, in the interest of simplicity, to introduce the minimal set of nonzero stress components required to approximate a local stress field consistent with the faulting style and the very low dip angle of the decollement segment. Here, three nonzero normal components of the stress tensor (σ_{xx}, σ_{yy} and σ_{zz}) are first assigned (see Table 3.1). σ_{zz} is initially set as the effective normal stress of the overburden at a reference depth (initially taken as 8 km, but permitted to vary when we scale to seismic moment, as noted below), assuming hydrostatic pore pressure down to this depth. σ_{yy} is set to $2\sigma_{zz}$ to mimic a thrust faulting environment (as suggested in Chamlagain and Hayashi [2007], and σ_{xx} is set to the mean of σ_{yy} and σ_{zz}. Then, we require the ratio between the shear and the normal stress projected onto the fault to approach prior estimates of the apparent frictional properties compatible with the interseismic and long-term deformation. Cattin and Avouac [2000] simulated the long-term and interseismic deformation and infer a low apparent friction coefficient, less than $\sim$0.3, on the decollement segment, which allows thrusting on the MHT with negligible internal deformation of the hanging wall, with a larger value (up to 0.6) on the downdip ramp. Based on those inferences, we rotate the principal stress axes in the y-z plane by introducing another nonzero stress component σ_{yz}, in order to approximate a shear-tonormal stress ratio of 0.2-0.3 on the decollement segment and $\sim$0.4 on the ramps (these values are stated as approximations because the fault-segment surfaces are not planar, so the resolved stresses have some variation). The higher shear stress on the ramps, relative to the decollement segment, is also seen in earthquake cycle modeling [Michel et al. 2017] that did not impose fault topography but constrained the frictional transitions (velocity strengthening and weakening) based on interseismic observations. The foregoing considerations only fix the ratios of the four independent stress components in equation 3.1. We then scale these ratios by a constant that is determined by trial and error, such that the seismic moment of the simulation falls within the range of published observational estimates. The resultant shear and normal stresses are illustrated in Figures 3.3a and 3.3b.

We introduce an artificial initiation zone on the downdip ramp, near the western pinch point, to initiate the Gorkha earthquake simulation. We move the U.S. Geological Survey hypocenter (within its uncertainty bounds) closer to the western pinch point, because that adjustment reduces the level and spatial extent of the stress perturbation required to initiate a sustained rupture in our model (this is only a computational device to which we attribute no physical significance). Rupture is initiated on the ramp by imposing a Gaussian-shaped shear overstress within a 7,500-m radius of the hypocenter (the red circular overstress patch in Figure 3.3a), with peak amplitude 1.5 times the local initial shear stress τ^b (details can be found in Equation 11 in Wang and Day, 2017). The overstress in initiation zone results in a maximum ratio of shear to normal stress of 0.6.

The fault friction law is one of rate-dependent dynamic weakening, within a rate and state framework, that has its basis in laboratory experiments [e.g., Dieterich 1979; Marone 1998; Ruina 1983]. Here we use the regularized formulation of the friction coefficient proposed by Lapusta et al. [2000], and the steady state friction coefficient is formulated following Dunham et al. [2011], Shi and Day [2013], and Wang and Day [2017]. Details of the formulation are given by Equations 6 to 10 in Wang and Day [2017], and the numerical treatment is outlined in Rojas et al. [2009]. The evolution-effect parameter b, the reference slip rate V_0, and the weakening slip rate V_w are constant over the fault (see Table 3.1).

The other frictional parameters are variable and distributed as shown in Figures 3.3c-3.3f. We introduce a velocity-weakening portion of the plate interface consisting of the decollement segment, a narrow strip along the top of the downdip ramp down to 14.5-km depth, and a more extensive part of the downdip ramp corresponding to an asperity that appears in many source imaging studies [Avouac et al. 2015; Grandin et al. 2015; Hayes et al. 2015; McNamara et al. 2017; Qiu et al. 2016; Wei et al. 2018; Yue et al. 2017]. Apart from that asperity, the lower velocity-weakening boundary follows the 14.5-km depth contour (the white contour band in Figure 3.3c) and does not coincide exactly with the kink joining the decollement and downdip

ramp (dashed red curve in each of Figures 3.3c-3.3f). It instead extends a short distance onto the down-dip ramp, and the extra velocity-weakening area near the initiation zone simplifies the nucleation of a sustained rupture (which we just ascribe to the artificiality of our model of event initiation). The velocity-weakening area has direct-effect parameter a = 0.01 (b - a = 0.004), statevariable evolution distance L = 0.1 m, and fully velocity-weakened friction coefficient f_w= 0.2 (except on the narrow strip on the downdip ramp, where f_w is assigned a transitional value of 0.3). The remainder of the downdip ramp, as well as the entire updip ramp, are velocity strengthening, with a = 0.05, L = 0.8 m, and f_w= 0.6 (there is also a very narrow transitional strip between these velocity-strengthening and velocity-weakening regions in which the frictional parameters are smoothly interpolated).

We set the low-velocity friction coefficient f_0 to mirror the pattern of apparent frictional properties proposed by Cattin and Avouac [2000], that is, 0.3 on the decollement and 0.6 on the ramps, except that we reduce it to 0.5 on the asperity portion of the downdip ramp in order to facilitate rupture on that patch. The velocity weakening value of L is essentially determined by numerical requirements, in that it is near the minimum value that provides a well-regularized numerical solution, while its high value in the velocity-strengthening zone helps minimize rupture penetration beyond the velocity-weakening region. The value of f_w is not well constrained, and we chose a value that gives fairly strong dynamic weakening behavior (dynamic friction substantially below final static shear stress), that value trades off against the initial static stress, so the trial-and-error adjustment of the initial stress level (to conform to observational estimates of seismic moment) mentioned earlier is also affected by the choice of f_w.

The shallow velocity-strengthening zone (i.e., on the updip ramp) in our model serves as a barrier to rupture on the coseismic timescale ($\sim$60 s). The actual geophysical mechanism restricting the upward extent of rupture is not known and may instead be related to insufficient stress accumulation on a fully coupled shallow region [Gualandi et al. 2017; Michel et al. 2017; Stevens and Avouac 2015; Wang and Fialko 2018]. Our simulated ruptures are not affected by the

choice of confinement mechanism (e.g., velocity strengthening versus low stress accumulation).

We solve the 3-D problem of spontaneous rupture propagation within the elastoplastic medium using the Support Operator Rupture Dynamics [Ely et al. 2008; Ely et al. 2009; Shi and Day 2013]. This code implements a generalized finite-difference method that accommodates nonplanar surfaces and nonplanar fault ruptures in a hexahedral mesh. The full methodology has been verified in tens of test problems developed for the Southern California Earthquake Center/U.S. Geological Survey dynamic earthquake rupture code validation exercise [Harris et al. 2009]. This application requires $\sim$960 million elements to model the 2015 Gorkha (Nepal) earthquake during a 60-s period, each simulation consuming $\sim$1.3 hr using 16,384 processors on Mira at the Argonne Leadership Computing Facility (Argonne National Laboratory).

3.3 Numerical Simulation Results and Analysis

3.3.1 Simulated Rupture Propagation and Earthquake Parameters

The simulated dynamic rupture produces, overall, a relatively simple pattern of unilateral eastward rupture but with some complexities related to the fault morphology (Figure 3.4). The rupture shows a pattern of multiple phases, somewhat similar to that noted in Fan and Shearer [2015]. The rupture is first initiated on the downdip ramp close to the western pinch point (Figure 3.4a). Subsequently, the rupture climbs updip from the ramp onto the decollement segment and is shaped by the pinch-point feature in the west (Figure 3.4b). This can be associated with Stage 1 in Fan and Shearer [2015]. Rupture then evolves into a unilaterally propagating, nearly steady state slip pulse on the decollement segment (Figure 3.4c). This behavior is common to observation- and simulation-based studies of this event [Galetzka et al. 2015; Michel et al. 2017; Wei et al. 2018; Yue et al. 2017]. This phase of rupture corresponds to Stage 2 in Fan and Shearer [2015]. The slip-pulse width is roughly 20 km (an estimate of a slip rise time is based upon

a threshold slip-rate value for starting and ending of the rupture pulse of 0.1 m/s, alternative estimates are discussed in Text S1), which agrees with the estimate in Galetzka et al. [2015]. In dynamic models, slip-pulse width can be affected by multiple factors, including prestress level and dynamic weakening rate [Zheng and Rice 1998], asperity dimensions [Day et al. 1998], fault-zone low-velocity channels [Huang and Ampuero 2011], and rupture-surface roughness [Shi and Day 2013]. However, in relatively simple cases, pulse width has a direct relationship to fault width [Day 1982], so the consistency between observationally inferred and simulated pulse width during rupture of the updip decollement appears to lend support to the view that the rupture is largely confined to that segment. We explore this further in a later section.

The downdip asperity plays a marked role in the next stage of the simulated rupture. As seen in Figures 3.4d and 3.4e, the rupture bifurcates, with the major rupture continuing to the southeast and a second branch propagating northeast into the large downdip asperity, with a linear rupture front and shortened pulse width. This phase of the rupture simulation resembles Stage 3 of Fan and Shearer [2015] in location and rupture direction, and the short rise times on the downdip asperity may be related to the depth-dependent radiation inferred by Yue et al. [2017], who find relatively strong high-frequency radiation originating on the downdip asperity. The two branches of rupture are terminated at the eastern pinch point and the northeastern point in the downdip asperity, respectively (Figure 3.4f). In summary, the simulated dynamics are closely related to the fault geometry and the influence of geometry on fault-resolved shear and normal stress fields, with the shallower ($\sim$10-km depth) and deeper ($\sim$14-km depth) kinks controlling the rupture pulse width and the two pinch points defining the along-strike extent.

Next, we examine the final static values of coseismic slip and the corresponding changes in shear and normal stress. Recall that the simulation inputs were calibrated to agree with independent seismic moment estimates. The simulation moment is $6.4 \times 10^{20} N \cdot m$ (corresponding to M_w7.8), compared with an observational range of roughly 6-9$\times 10^{20} N \cdot m$ (M_w7.8-7.9) for the Gorkha earthquake [Avouac et al. 2015; He et al. 2015; Yue et al. 2017].

The coseismic slip in the simulation (Figure 3.5a) is composed of two slip patches: a major slip on the decollement and a somewhat smaller slip on the asperity on the downdip ramp. The peak slip of 8 m is located on the decollement segment, to the south of the asperity. This peak slip is slightly larger than most observationally inferred peak coseismic slips [5-7m Avouac et al. 2015; Galetzka et al. 2015; Grandin et al. 2015; Hayes et al. 2015; Lay et al. 2017; Wang and Fialko 2015; Wei et al. 2018; Yagi and Okuwaki 2015; Yue et al. 2017], because our velocity-weakening zone (motivated by the assumed shape and spatial extent of the decollement segment) restricted the rupture area in the simulation, requiring higher slip to conform with seismic moment estimates. This difference may also arise in part from smoothing in the finite-fault inversion. Notably, one slip inversion model that uses a similar fault geometry finds a value of peak slip very close to ours [Qiu et al. 2016]. The location of peak slip is along the northern edge of the decollement segment, just south of the downdip asperity (Figure 3.5a), which is also very similar to the location of the highest slip in the inversion of Qiu et al. [2016]. In the simulation, localization of peak slip in that area may be explained by the broadened fault width caused by the concurrent slip on the downdip asperity.

Figures 3.5b and 3.5c show the static shear and normal stress changes for the simulated event. In Figure 3.5b, the pattern of the shear stress change in areas where it is negative (areas of stress drop) is similar to that of the static slip. The region of stress drop is encompassed by positive shear stress change at its margins, where slip is abruptly suppressed by the transition from velocity weakening to velocity strengthening. The normal stress change in Figure 3.5c shows some complexities caused by the 3-D fault geometry. The dynamic slip occurring on the kink at the lower edge of the decollement, at $\sim$14-km depth, compresses the fault just below the kink and decompresses the fault above it, with corresponding changes in normal stress [Kase and Day 2006]. This effect is largest along the northeastern edge of the main rupture, where slip is largest (darker blue strip along the northeastern edge). Note also that the aftershocks (denoted by gray circles in Figure 3.5) have an apparent association with the rupture edge and the fault kink,

where large shear and normal stress are predicted by the simulation. Das and Henry [2003] note that aftershock clusters are found preferentially at the edges of unbroken barriers and in regions of high spatial gradient of slip. Thus, the aftershock locations are consistent with the decollement bounds used in the simulation. In our simulation, the average stress drop is $\sim$8 MPa. Due to the simplicity of our model (e.g., we ignore subsurface sediments, and the geometrical model we adopt places rather strict limits on the potential rupture area), this value may be best viewed as a rough upper bound on the average coseismic stress drop.

Finally, we show the rupture velocity for the simulation in Figure 3.5d. The spontaneity of rupture results in accelerated rupture, beginning at about 0.7 of the S wave speed as rupture breaks out of the initiation zone and then accelerating to a limiting velocity of about 0.9 of the S wave speed (i.e., about 3.1 km/s). The latter is maintained over most of the rupture extent. The saturation of rupture velocity just below the S speed can be understood from the fact that the Gorkha event approximates antiplane (Mode III) rupture over most of its length. As is well known, an antiplane rupture has a terminal velocity equal to the S wave speed in the elastodynamic case [Andrews 1976; Kostrov 1966]. Our terminal velocity of $\sim$0.9 of the S wave speed is somewhat lower than that, because of the plastic yielding at the rupture front. We confirmed this interpretation by also simulating rupture with the plastic yielding suppressed [Andrews 2005; Duan and Day 2008; Gabriel et al. 2013], in which case we find a terminal rupture velocity of 98% of the S wave speed, in close agreement with the elastodynamic theory. The simulation terminal velocity of 3.1 km/s is close to the center of the $\sim$2.8- to 3.3-km/s rupture velocity range inferred by backprojection analysis for the Gorkha earthquake [Avouac et al. 2015; Fan and Shearer 2015; Lay et al. 2017; Meng et al. 2016; Yagi and Okuwaki 2015], and the average rupture velocity in the simulation, approximately 2.9 km/s, is also well within that range. The rupture velocity is a quite robust prediction of the simulations, once both geometric bounds of the rupture and an initial stress level consistent with the seismic moment are imposed. It should be sensitive to energy dissipation in friction and plastic work near the rupture front (as

confirmed by the contrast between elastodynamic and elastoplastic simulations just alluded to), so the agreement with observational estimates provides some degree of validation of our models for those processes.

3.3.2 The Effect of Free Surface on the Dynamic Rupture

In addition to fault nonplanarity, the asymmetry imposed on a nonvertically dipping fault by the presence of the (near-horizontal) free surface can also modify shear and normal stresses, through free-surface-reflected waves [Brune et al. 1993; Oglesby et al. 1998; Oglesby et al. 2000]. Depending upon their strength and timing, these reflections may interact with and modify the rupture. Because the Gorkha earthquake is a large thrust event that is shallow relative to its spatial extent, simulations of the event provide an opportunity to assess the relative importance of such free-surface interactions.

We design a modified simulation that shares all model inputs except that the free surface has been replaced by a perfectly matched layer zone to mimic a whole-space model. In order to compare the rupture evolution for the two cases, we extract slip-rate time histories on an along-strike profile of the fault surface, as indicated in Figure 3.6a. In that figure, blue triangles denote the surface projections of two points, A and B, that will be used to illustrate the interactions of reflected seismic waves with the rupture. Figure 3.6b is a time-distance plot comparing slip rates for the Gorkha and modified models, any differences being attributable to rupture interactions with free-surface reflections in the Gorkha model. This time-distance plot shows similar pulselike rupture in both cases, but several distinctions are evident. First, some bifurcations of the slip-rate function, highlighted by gray dashed lines, appear in the unmodified Gorkha model (i.e., with free surface).

These bifurcations have the appearance of minor ruptures pursuing the main rupture front with higher speed and finally merging with it. But these bifurcations are absent in the model

without a free surface, and we can therefore interpret these features as minor ruptures reactivated by reflected seismic waves from the free surface. This interpretation in terms of free-surface reflections is reinforced by the simulation snapshots in Figure S3.1, where it is clear that the secondary reactivations coincide spatially and temporally with the reflected wave front seen on the cross section of that figure. Second, the model with a free surface has an identifiably longer pulse width. These differences are evident at check points A and B. At check point A (Figure 3.6c), which is the closer of the two to the hypocenter, the main discrepancy in slip-rate function is that in the half-space model, after the main rupture, a minor subsequent rupture is nucleated. That secondary slip has an amplitude of 0.5 m/s and coincides in time with a sharp reduction of normal stress (blue dashed line). The slip-rate difference is larger at point B (Figure 3.6d). There, the shape of the slip-rate function for the half-space model deviates markedly from the classic self-similar solution [Kostrov 1964], whereas the whole-space model resembles the self-similar pulse for several seconds (until it is terminated by effects of rupture finiteness). The slip pulse has been broadened by 1 s or more (depending upon the definition of pulse width that is employed, as discussed in Text S1), and reduction of normal stress is up to 4 MPa. In this geometry, the reflected S waves from free surface have particle motion that is vertically upward and horizontally southward at the advancing rupture front (i.e., the free-surface reflection approximately preserves the polarity of the S wave). Consequently, the returning S waves reduce the normal stress on the fault, lowering frictional resistance, reactivating minor rupture, and increasing slip duration.

To further quantify the effect of the free surface, we calculate the slip rise time (we use "slip rise time" and "pulse duration" interchangeably throughout the fault. These statistics can shed light on the extent to which free-surface effects similar to those predicted by the simulation might be seismologically resolvable. We retain the definition of rise time used in section 3.3.1 (and Figure 3.4), namely, the period between starting and ending threshold slip-rate values of 0.1 m/s. Figure 3.7 shows rise time spatial distribution across the fault in the Gorkha (half space) and modified (whole space) simulations (Figures 3.7a and 3.7b) and a comparison of their

histograms (Figure 3.7c). In each simulation, as seen in Figures 3.7a and 3.7b, the patterns for the decollement and downdip asperity segments are distinct from each other (as already noted in the discussion of Figure 3.4). There are also clear distinctions between the two models. First, as previously shown in Figure 3.6, rise time on the decollement segment for the half-space model is generally greater than for the whole space. Second, in the whole-space model (Figure 3.7b), a SE-NW trending pattern of high rise time (south of the downdip asperity) is present, but there is no corresponding coherent feature in the half-space model. The pattern is attributable to the increased fault width on the decollement segment and the corresponding delay of healing. In the half-space model, the rise time is partially controlled by the passage of reflected seismic waves and is less sensitive to healing phases from the rupture edges. The rise time on the downdip asperity remains nearly identical for the two models (Figures 3.7a and 3.7b), indicating that the downdip portion of the rupture is insensitivity to the free-surface effects. This insensitivity corresponds with the dependence upon dip angle of the normal-stress perturbation from reflected S waves, and, for the dip-angle range in the Hubbard model, the perturbation is stronger for the near-horizontal portion of the fault surface than for the higher-dip portions (e.g., Figure 3.2 in Oglesby et al. [1998] and Oglesby et al. [2000]). This contrast is evident in Figure 3.7c, where the two peaks (in each model) coincide, respectively, with concentrations of rise time on the decollement and downdip asperity segments. As noted, the rise time on the downdip asperity is only weakly affected by free-surface interaction, while the decollement part shows an average difference of roughly 2 s in rise time. This difference compares with the overall average rise time of approximately 6 s, which is in accord with the observational estimate of Galetzka et al. [2015]. A difference of this magnitude may be seismically resolvable, even though it might be difficult or impossible to unambiguously separate a free-surface interaction effect of this level from the many other factors potentially affecting rise time. On the other hand, for an otherwise similar event rupturing to shallower depths, we would expect the freesurface effect on rise time to be even greater, and it could become an essential component in interpreting the rupture kinematics.

3.3.3 The Comparison Between Simulated Near-Field Ground Motions and GPS Signals

Numerous kinematic studies have inferred a pulse-like rupture for the Gorkha earthquake [e.g., Galetzka et al. 2015; Yue et al. 2017], as also shown in the Gorkha dynamic rupture model. The kinematically inverted source models [e.g., Galetzka et al. 2015; Wei et al. 2018; Yue et al. 2017] vary somewhat in their estimates of the slip-pulse duration but typically give estimates near 6 s, close to the slip-weighted simulation mean (Figure 3.7). In simple dynamic models where neither heterogeneities (in, e.g., stress state and near-fault rock stiffness) nor dynamic weakening effects strongly affect rupture duration, pulse duration is controlled principally by the ratio of fault width to rupture velocity, as suggested by dimensional arguments and confirmed by numerical simulations [Day 1982]. If that is a reasonable first approximation for the Gorkha event (as it appears to be for our simulation), then the agreement between simulated and observationally inferred pulse duration may be further evidence supporting the spatial bounds on rupture that we have assumed (and which were, in turn, suggested by the underlying model for fault geometry that we adopted). We further explore that idea in this section by examining the sensitivity of the dynamic source model to downdip and updip geometrical bounds on the rupture. All other model inputs are kept identical to those of our preferred Gorkha model, so that other potential effects on pulse duration, such as the free-surface effects discussed above, are unchanged. Rupture velocity is a simulation result, not an input, but we note that it is not significantly affected by these geometric variations, remaining near the center of the 2.8- to 3.3-km/s range inferred by backprojection analysis for the Gorkha earthquake [Avouac et al. 2015; Fan and Shearer 2015; Lay et al. 2017; Meng et al. 2016; Yagi and Okuwaki 2015].

The 2015 Gorkha earthquake rupture surface on the MHT lies directly beneath a network of high-samplerate (5 Hz) continuous GPS (cGPS) stations. The pulse-like characteristics of fault slip are reflected in pulse-like ground motion recordings on this close-in network. A distinctly

pulse-like motion was recorded right above the rupture at the two cGPS stations, KKN4 and NAST, as well as on an accelerometer at site KATNP [Galetzka et al. 2015], and it is especially clear on the vertical components. The observed ground motion pulse at these stations is closely related to the slip-rate pulses, so these recordings provide constraints on the rupture model. Of these, stations NAST and KATNP are affected by strong oscillations centered at about 3- to 4-s periods and lasting for $\sim$20 s [Galetzka et al. 2015], due to the response of the subsurface sediment within the Kathmandu basin. As our focus is on the inference of source effects, we focus our analysis on the KKN4 station, which is on bedrock and is relatively free of such structure-related oscillations. By comparing the synthetic ground motion at station KKN4 with the observed GPS time history, we assess the factors controlling the simulated slip pulse and obtain some constraints on the geometry of rupture.

Once the initial stress state and frictional parameter values are fixed, the principal remaining factor affecting the simulation results is the location of the frictional transitions (velocity weakening to velocity strengthening) limiting the spatial extent of rupture. We examine the sensitivity of the simulated KKN4 ground motion to rupture geometry by adjusting the updip and downdip limits of the rupture surface (but without altering the geometry of the downdip asperity on the eastern part of the rupture surface). We consider a series of five cases. Case 1 is the preferred Gorkha dynamic rupture model that we have already described, in which we place the upper limit of velocity weakening at the lower edge of the updip ramp (i.e., it precludes rupture on the updip ramp), at a depth of 10.7 km, and the lower limit at 14.5 km. Case 2 is a modification that raises the upper limit of velocity weakening to 9-km depth, permitting a portion of the updip ramp to rupture. Cases 3 and 4 place the upper velocity-weakening limit at 8 and 7 km, respectively. Case 5 places the upper velocity-weakening limit at 10.7 km as in Case 1 but extends the lower limit down to 20 km, permitting rupture on an extended portion of the downdip ramp. These model variants are indicated in Figure 3.8a, where the blue segment indicates the extent of the velocity-weakening zone and the red segment shows the velocity-strengthening

zone.

Figure 3.8b is a free-surface snapshot illustrating the wing-like shape of the synthetic ground motion pulse (vertical component) that sweeps across the KKN4 station. The KKN4 GPS vertical-component time series (unfiltered) is shown by the gray curve in Figure 3.8c, along with the corresponding synthetic ground motions for the five cases. More detail about the synthetics can be found in Figure S3.2. The latter figure also shows that the vertical component has the highest sensitivity to the rupture extent, and we use that component as our primary indicator of model fitness. Our optimal dynamic rupture model, Case 1 (solid dotted curve), shows a very close agreement in shape and amplitude with the recorded KKN4 time series. In Cases 2 through 4 (dashed lines), a very distinct second peak has developed that is absent in the recorded data. This bifurcation of the pulse appears to be related to rupture stepping onto the updip ramp, with the change of dip angle between the flat decollement and shallow ramp complicating the radiation pattern in a manner inconsistent with the recorded waveform. The degradation of the waveform fit for Cases 2-4 suggests that little or no coseismic slip occurred on a shallow ramp during the Gorkha event. Adjustments to the lower rupture limit, in comparison, have a more minor effect on pulse shape but make the ground motion pulse wider than the recorded pulse (due to the extended fault width). In summary, the synthetic from our preferred model (Case 1) agrees closely in amplitude, duration, and shape with the recorded pulse (a good agreement in the frequency domain between the observed and synthetic ground velocity is also obtained below the maximum acceptable high-frequency limit beyond which the preevent noise level exceeds observed spectrum containing the velocity pulse; Figure S3.2), the comparisons favor our original choice of downdip rupture limit, and they strongly disfavor models with significant coseismic rupture of an updip ramp. These constraints on rupture extent, combined with aforementioned constraints from matching seismic moment (further supported by the resultant agreement with rupture velocity estimates), leave a very limited range to vary the average stress drop, which is $\sim$ 8 MPa in our preferred model.

3.4 Discussion

3.4.1 Rupture Extent on the Fault Surface

As shown in section 3.3.3, the shape and amplitude of the KKN4 time series favor a rupture that is limited in extent to the flat decollement and a portion of the deeper ramp (i.e., limited to the depth range 10.7 to 14.5 km). The synthetic second peak developed in Cases 2 through 4 strongly disfavors coseismic rupture on the shallower (i.e., southwestern) ramp, at least in the area to the west of the KKN4 station. That inference is further supported by the fact that sources of high-frequency seismic radiation have been imaged in the area near the lower kink but not near the upper kink where the shallow ramp and the flat decollement intersect [e.g Avouac et al. 2015; Yin et al. 2017]. KKN4 was the only bedrock-based recording sufficiently free of path and site effects for our purposes, and its recorded ground velocity pulse mainly reflects the rupture occurring below and to the west of KKN4. For that reason, there is more uncertainty in the updip rupture extent southeastern of KKN4, where we cannot rule out some rupture of the shallower ramp. Given a sufficiently realistic seismic velocity profile (e.g., for the Kathmandu basin), more near-field recordings (such as KATNP strong ground motion station) and SNDL (high-rate GPS station) might be exploited to infer the rupture extent in more detail. Such an effort might also shed some light on the origin of the longperiod secondary pulse in the KKN4 recording that immediately follows the main pulse and is unexplained in our model.

Compared with the fairly sharp results for the updip limit, the down-dip limit of rupture is rather weakly constrained by matching the KKN4 pulse width, but we can provide a rough estimate of sensitivity. As shown in Figure 3.8c (Case 5), moving the deeper limit from 14.5- to 20-km depth modifies KKN4 pulse width by about 2 s, corresponding (assuming a roughly linear relationship) to about 2.8-km variation in inferred depth extent per 1-s variation in pulse width. The preferred model (Case 1) fits the observed time series within a few tenths of a second, and rejection of models that predict pulse widths that differ from the preferred case by more than, say,

0.5 s would permit the downdip rupture extent to vary from the preferred model by at most 1.4 km in depth, or 3.2 km along dip. Of course, this estimate only considers one source of uncertainty, so it is no more than a lower bound on that uncertainty.

These findings suggest that the extent of the Gorkha earthquake rupture was limited by the geometry of the MHT fault surface, although that geometrical effect in our model was realized indirectly, by adopting a frictional parameterization compatible with fault topography. The along-dip and along-strike extents of the simulated rupture, and its oval-shaped coseismic slip distribution, in addition to being consistent with most published source models [e.g., Avouac et al. 2015; Galetzka et al. 2015; Wei et al. 2018], also closely correlate with the model of a flat decollement bounded by two ramps along the dip and two pinch points along the strike. The result is that only a small portion of the MHT ruptured during this event, unlike the nearby, devastating 1934 Mw 8.4 Nepal-Hihar earthquake that occurred nearby to the east and that ruptured all the way up to the ground surface. Although the updip limit of the Gorkha event coincides with transition from the decollement to upper ramp in the Hubbard model, the actual mechanism stopping the upward progress of the rupture across this transition is not known. A better understanding would improve our assessment of future seismic hazards from the shallow part of the fault. The partial rupture could result from the structural control of the fault geometry, statically (by modifying initial resolved stresses, as assumed in our model setup) and dynamically (by affecting the localized stresses associated with a kink in the rupture path, as occurs at the lower kink; Kase and Day [2006]. In addition, rupture barrier could arise from spatial variations of frictional or stress properties. The hypothesis that rupture was confined due to a frictional transition from velocity weakening to velocity strengthening at the upper edge of rupture does not appear to be supported by postseismic observations [Gualandi et al. 2017; Wang and Fialko 2018]. As an alternative, Michel et al. [2017] propose that ruptures tend to stay confined within a high-prestress zone near the transition from velocity strengthening to velocity weakening at the lower edge of the locked area, generating pulse-like ruptures that propagate along strike. The implications for

future earthquakes and ground motion require exploration through rupture simulations informed by a better understanding of the fault segmentation and mechanics, geological structure, seismic velocity structure, seismicity, and long-term crustal deformation.

3.4.2 Sensitivity of Ground Motion to Slip-Rate Function

Our preferred Gorkha earthquake simulation reproduces the observed near-field ground velocity pulse (at a site where path effects can be neglected) in both amplitude and shape, without any assumptions about the nature of the fault slip. We now consider the significance of that quantitative agreement by examining the sensitivity of the ground motion to the earthquake slip function.

Analytical formulations of a kinematic source typically consider slip onset time (i.e., rupture velocity, taking into account its spatial variations) and three important parameters of the slip-rate function: peak time (the time between onset and peak of the slip rate, which may in turn be dynamically related to a critical slip distance associated with loss of cohesion), rise time (synonymous with pulse duration, the time between onset and arrest of the slip rate, which may be dynamically related to rupture velocity and rupture extent), and total slip (or time integral of the slip-rate function, which may be related to stress drop and whose spatial integral is proportional to seismic moment). Our strategy here is to (1) extract these parameters (rupture velocity and the three slip-rate parameters) from our dynamic simulation, (2) construct a range of standard kinematic sources that preserve these parameters (which we will call "equivalent kinematic sources"), and then (3) examine the extent to which the equivalent kinematic sources produce ground motion distinguishable from that of the dynamic model (we illustrate this procedure in Figure S3.6). The representative kinematic sources employed here are those developed in [e.g., Graves and Pitarka 2004; Liu and Archuleta 2004; Tinti et al. 2005; Liu et al. 2006; Dreger et al. 2007]. In those sources, we fix onset time, peak time, rise time, and total slip to the

values extracted from our dynamic simulation, and we follow the authors' recommendations for other parameters derived from those four, (e.g., for the Liu and Archuleta [2004] source, the p controlling asymmetry in the slip-rate function is p = 5Tp/Tr as suggested in Crempien and Archuleta [2015], where Tp and Tr are the peak and rise time, respectively). For the analysis, we used the slip rate at a fault point near the center of the rupture area (directly below the point halfway between sites A and B in Figure 3.6a), which is a good representative of the slip over much of the rupture surface (see, e.g., Figure 3.6b). The slip-rate functions for the equivalent kinematic sources are displayed in Figure 3.9, where they are compared with the representative dynamic slip-rate function. As seen in Figure 3.9a2, the equivalent kinematic slip-rate functions differ in their time-domain shapes and in their spectra, especially at high frequency. Comparing Figures 3.9a1 and 3.9a2, it is evident that the equivalent kinematic sources differ from the dynamic simulation at high frequency, despite having the same peak time, rise time, and total slip. This result contrasts with that shown in Figures 3.9b1- 3.9b3, where we plot the corresponding synthetic ground velocities at KKN4 along with the recorded motion (both synthetic and recorded motion are presented without filtering) in the time and frequency domain. The equivalent kinematic sources reproduce the recorded motion about as well as does our original dynamic source (once the latter has been used to establish the rupture velocity and slip-rate parameters).

Moreover, we still obtain good agreement even if we relax the constraint that peak time agrees with the dynamic source, and instead apply the prior, empirically defined ratios of peak time over rise time that are recommended by Liu et al. [2006] and Graves and Pitarka [2004] for their respective kinematic sources, for example, 0.13 for Liu et al. [2006] and 0.2 for Graves and Pitarka [2004]. In that test, shown in Figure 3.9a3, we only require the rupture velocity, rise time, and total slip to agree with our dynamic model. The essential point is that the very sharp onsets of the slip-rate functions (as well as the spurious high-frequency oscillations of the dynamically simulated slip rate) are all filtered out by propagation to the KKN4 site, an effect also pointed out

by Wei et al. [2018]. The result is that, as shown in the last row in Figure 3.9, at this distance ($\sim$15 km), the near-field ground velocity pulse exhibits very weak sensitivity to high-frequency variations of sources, provided we keep the rupture velocity, rise time, and total slip fixed. Of course, in the dynamic Gorkha simulation, these are not free parameters but are all coupled and controlled by the dynamics of the rupture and the initial geometrical constraints.

The fact that ground motion in the near field of a steadily propagating, subshear rupture is a low-passfiltered image of the slip rate is well known and just reflects the fact that only evanescent waves are excited in that limit. This issue is discussed in detail by Dunham and Archuleta [2005], who also contrast this behavior with the supershear case, and they anticipate precisely the result we noted above ("the slip velocity function will have little effect on the ground motion, so long as the final slip and rise time are preserved"). In their notation, the attenuation factor for wavelength λ, at distance y, is $e^{-2\pi\alpha y/\lambda}$, where $\alpha = \sqrt{1-V^2/c_s^2}$ (V is the rupture pulse speed and c_s is S wave speed). For 15-km distance (approximately the Gorkha rupture depth), and our inferred rupture velocity of $\sim 0.9c_s$, wavelengths of the slip function shorter than about 10 km will be attenuated by a factor of at least e^{-4} (roughly a factor of 50). Therefore, estimates of rupture parameters such as the critical weakening slip D_c that require resolution of slip-rate features at a smaller spatial scale than that (e.g., the $\sim$5-m D_c estimate of Galetzka et al., 2015) are likely to represent, at best, only very weak upper bounds. To illustrate this limitation in the case of D_c, for example, we note that its estimation relies upon resolution of wavelengths comparable to the dimension Λ of the cohesive zone at the rupture front, which, for Mode III rupture, is of order $\alpha\mu D_c/\tau$, where μ is the shear modulus and τ the stress change across the cohesive zone (see, e.g., Equation 30a of Day et al. [2005]). We can insert a reasonable minimum wavelength requirement of $\sim 2\Lambda$ into the foregoing distance-attenuation factor, obtaining $e^{-\pi\tau y/(\mu D_c)}$, and make the rough approximations $\mu/\tau \approx 4\times 10^3$ and y = 15 km (approximate nearest distance at which the Gorkha event is recorded). If we assume that resolution is lost when distance attenuation is a factor of $\approx$10, then the minimum resolved D_c is $-\pi\tau y/\mu ln(0.1) = 5.1m$, and a lower D_c would be

undetectable at this station.

3.4.3 Terminal Rupture Velocity in Elastoplastic Antiplane Rupture

In our simulation, rupture velocity accelerates to 0.9 of the S wave speed and then maintains approximately that speed over most of the rupture length. This terminal rupture velocity is lower than the terminal rupture velocity (equal to the S wave speed) that would be approached asymptotically by an elastodynamic antiplane (Mode III) rupture. Moreover, when we suppress plastic yielding in the model, we recover the asymptotic Mode III result to high precision (terminal velocity $\sim$0.98 of S wave speed). Thus, we can unambiguously attribute the simulated rupture velocity to the additional rupture-front dissipation (over and above the modeled frictional losses) supplied by off-fault plastic yielding. Our rupture velocity is an independent (in the sense that it is a modeling result, not an input) and quite robust prediction of the simulations once we impose both the geometric bounds and prestress consistent with the seismic moment and include plastic yielding in the model. The simulated rupture velocity is also consistent with observational estimates (section 3.3.1) and contributes to a good agreement between the recorded and synthetic ground velocity pulses at KKN4 (section 3.3.3). The robustness of the simulation prediction for rupture velocity, its sensitivity to off-fault inelastic dissipation, and its apparent agreement with multiple observational inferences appear to support the validity of including a model that permits off-fault dissipation in our dynamic rupture simulation.

The physical rationale for modeling off-fault material as an elastoplastic solid is to accommodate concentrated strain at the rupture front that otherwise would imply very high stresses exceeding rock strength [Andrews 1976]. The consequent energy loss off the fault is known to modify the cohesive zone size and rupture velocity [Andrews 2005]. Figure 3.10 shows the time- and space-dependent nature of these effects in our Gorkha event simulation. As seen in Figure 3.10a, at an early phase (2 s) in the northwest (labeled as a), the difference in shear

stress and slip rate between elastic and elastoplastic simulations is negligible, indicating that stresses have remained below the yield surface. But at the later phase (25 s, Figure 3.10b) in the southeast (labeled as b), an appreciable difference is seen. The plastic-case rupture front has been left behind by the elastic-case rupture front, and the plastic-case peak slip rate is capped at about 15 m/s, while the elastic-case slip rate has reached 30 m/s. The rupture velocity for the plastic case has saturated to 90% of the S wave speed (near the center of the range of observational estimates), while that for the elastic case is still accelerating and subsequently saturate at 98% of S wave speed (above the range of observational estimates). Figure 3.10c shows the accumulated plastic strain magnitude (defined in Appendix A) in the upper material block adjacent to the fault, along with the slip contours for comparison. The plastic deformation generally increases with hypocentral distance, so that it is concentrated in the eastern patch (left side in Figure 3.10c) where the major slip and downdip asperity are located. This pattern correlates with the region where most aftershocks are clustered, including the biggest aftershock (M_w7.3), east of the Gorkha rupture (Figure 3.1). A possible interpretation of this association is that the inelastic deformation predicted by the simulation is realized as a distribution of near-fault microfractures that promote macroscopic aftershocks.

3.4.4 Free Surface Effects on Rupture Dynamics

We believe that section 3.3.2 makes a credible, though speculative, case that there was interaction between the free-surface reflections and the rupture dynamics in the Gorkha earthquake, and we suggest that such interactions would potentially be very significant in a future, shallower event. In the Gorkha simulation, free-surface interaction, on average, extends the slip duration (rise time) by 30% or more, acting preferentially on the low dip-angle segment. In the supplement (Figure S3.3), we also show that this conclusion is not sensitive to the precise way in which duration is defined. This interaction effect may increase in importance with increased ratio of

the spatial slip-pulse width to the rupture depth, because increase of that ratio enables waves from the rupture front to return to the fault surface, as free-surface reflections, before passage of the healing front. Additional analysis can be found in the supporting information [Guatteri et al. 2004; Tinti et al. 2005]. Text S1 confirms that the free-surface effect on slip-pulse duration is insensitive to the way we define that duration.

3.5 Conclusions

The Gorkha earthquake was dominated by a slip pulse that ruptured the lower edge of the MHT as it propagated along strike from the northwest to the southeast. Dynamic rupture modeling in an elastoplastic medium clarifies the principal physical factors controlling this slip pulse. The preferred model gives earthquake parameters consistent with published observational estimates (seismic moment $6.4\times10^{20} N\cdot m$, maximum slip $\sim$8 m, average stress drop $\sim$8 MPa, rupture velocity $\sim$3.1 km/s, average slip-pulse width $\sim$6 s). The agreement for slip-pulse width supports an interpretation that the pulse duration is principally controlled by the narrow dimension of the oval-shaped rupture, and the bounds of that rupture surface appear to reflect geometric features of the underlying fault model that we adopted. An important role for fault geometry is further suggested by comparison of the synthetic near-source velocity waveform with a high-rate GPS recording, which strongly disfavors the extension of significant rupture onto the shallow ramp portion of the model and instead favors confinement of rupture to the flat decollement and a limited, uppermost portion of the deeper ramp, plus a more extended asperity on the northeast portion of that ramp. After its initiation, the rupture front accelerates rapidly to a steady state velocity that is $\sim 90\%$ of the S wave speed, which we interpret as the maximum Mode III rupture velocity consistent with the plastic yielding model (because, when plastic yielding is suppressed in the model, the rupture velocity instead approaches within 2% the theoretical maximum for elastodynamic Mode III rupture). In the dynamic simulation, reflected seismic waves from the

free surface generate time-dependent normal stress perturbations, prolonging the slip pulse by $\sim 30\%$ (compared with whole-space comparison tests), raising the possibility of potentially significant free surface effects on both rupture propagation and slip in shallow events of similar geometry.

3.6 Appendix A: Formulations of Drucker-Prager Yield Criterion and Inelastic Deformation

The Drucker-Prager plasticity model [Drucker and Prager 1952] has been widely applied in geomechanics to incorporate inelastic yielding of materials such as rocks and concretes. The Drucker-Prager yield criterion is a smooth approximation to the Mohr-Coulomb yield criterion. The Drucker-Prager yield criterion employed in this study is given by

$$\bar{\tau} \leq \tau^y, \tag{3.2}$$

$$\bar{\tau} = \sqrt{\frac{1}{2} S_{ij} S_{ij}}, \tag{3.3}$$

$$\tau^y = -\frac{1}{3}\sigma_{kk} sin\phi + c\cos\phi, \tag{3.4}$$

where S_{ij} is the deviatoric stress component $S_{ij} = \sigma_{ij} - \frac{1}{3}\sigma_{kk}\delta_{ij}$, c is the cohesion, and ϕ is the internal friction angle, which together define the yield surface. Elastically calculated increments of S_{ij} are adjusted at each time step, in equal proportions, as required to bring stress back to the yield surface. During this process, there is no volumetric plastic strain. A measure of

accumulated plastic deformation, termed the plastic strain magnitude, is defined as

$$\eta = \int \frac{2}{3} d\varepsilon_{ij}^{P} d\varepsilon_{ij}^{P}, \tag{3.5}$$

$$d\varepsilon_{ij}^{P} = \frac{ds_{ij}}{2\mu} \tag{3.6}$$

where $d\varepsilon_{ij}^{P}$ is the plastic strain increment in each time step, related by (1.6) to the deviatoric stress adjustment ds_{ij}

Acknowledge

The authors thank Shengji Wei, Shuo Ma, Jean-Philippe Avouac, Jiuxun Yin, and Shiying Nie for their helpful discussions and suggestions. Thoughtful reviews from the Editor, Yehuda Ben-Zion, the Associated Editor, Sylvain Michel, and an anonymous reviewer led to significant improvements in the manuscript. This work was supported partially by The Paul G. Silver Young Scholar Research Enhancement Award at IGPP/UCSD and by NSF award EAR-1135455. The work was also supported by an award of computer time provided by the Innovative and Novel Computational Impact on Theory and Experiment (INCITE) program, through projects GMSeismicSim and SeismicHazard of the Southern California Earthquake Center. This research used resources of the Argonne Leadership Computing Facility, which is a DOE Office of Science User Facility supported under Contract DE-AC02-06CH11357. The postprocessed high-rate GPS records were provided by Shengji Wei. The raw data are available from the UNAVCO website. Most of the data processing and figure generation was carried out using Python, and some map figures were made using GMT (the Generic Mapping Tools, http://gmt.soest. hawaii.edu/home). The rupture dynamics code used in this paper is cited in the reference list, and the data for generating figures and tables in this paper are available by contacting the corresponding author at

yow004@ucsd.edu.

Chapter 3, in full, is a reprint of the material as it appears in Journal of Geophysical Research-Solid Earth: Wang, Y., Day, S. M. and Denolle, M. A., "Geometric Controls on Pulse-Like Rupture in a Dynamic Model of the 2015 Gorkha Earthquake", *Journal of Geophysical Research-Solid Earth*, 124, 2019. I was the primary investigator and author of this paper.

References

Aagaard, B. T. and Heaton, T. H. (2008). "Constraining fault constitutive behavior with slip and stress heterogeneity". In: *Journal of Geophysical Research-Solid Earth* 113.B04301.

Andrews, D. J. (1976). "Rupture propagation with finite stress in antiplane strain". In: *Journal of Geophysical Research* 81.20, pp. 3575–3582.

— (1994). "Fault geometry and earthquake mechanics". In: *Annals of Geophysics* 37.6, pp. 1341–1348.

— (2005). "Rupture dynamics with energy loss outside the slip zone". In: *Journal of Geophysical Research-Solid Earth* 110.B1.

Avouac, J. P. (2007). "Dynamic processes in extensional and compressional settings - Mountain building: From earthquakes to geological deformation". In: *Treatise on Geophysics*. Amsterdam: Elsevier, pp. 377–439. ISBN: 9780444527486.

Avouac, J. P., Meng, L. S., Wei, S. J., Wang, T., and Ampuero, J. P. (2015). "Lower edge of locked Main Himalayan Thrust unzipped by the 2015 Gorkha earthquake". In: *Nature Geoscience* 8.9, pp. 708–711.

Beeler, N. M. and Tullis, T. E. (1996). "Self-healing slip pulses in dynamic rupture models due to velocity-dependent strength". In: *Bulletin of the Seismological Society of America* 86.4, pp. 1130–1148.

Beroza, G. C. and Mikumo, T. (1996). "Short slip duration in dynamic rupture in the presence of heterogeneous fault properties". In: *Journal of Geophysical Research-Solid Earth* 101.B10, pp. 22449–22460.

Brune, J. N., Brown, S., and Johnson, P. A. (1993). "Rupture mechanism and interface separation in foam rubber models of earthquakes - a possible solution to the heat-flow paradox and the paradox of large overthrusts". In: *Tectonophysics* 218.1-3, pp. 59–67.

Cattin, R. and Avouac, J. P. (2000). "Modeling mountain building and the seismic cycle in the Himalaya of Nepal". In: *Journal of Geophysical Research-Solid Earth* 105.B6, pp. 13389–13407.

Chamlagain, D. and Hayashi, D. (2007). "Neotectonic fault analysis by 2D finite element modeling for studying the Himalayan fold-and-thrust belt in Nepal". In: *Journal of Asian Earth Sciences* 29.2-3, pp. 473–489.

Cochard, A. and Madariaga, R. (1996). "Complexity of seismicity due to highly rate-dependent friction". In: *Journal of Geophysical Research-Solid Earth* 101.B11, pp. 25321–25336.

Crempien, J. G. F. and Archuleta, R. J. (2015). “UCSB method for simulation of broadband ground motion from kinematic earthquake sources”. In: *Seismological Research Letters* 86.1, pp. 61–67.

Das, S. and Henry, C. (2003). “Spatial relation between main earthquake slip and its aftershock distribution”. In: *Reviews of Geophysics* 41.3.

Day, S. M. (1982). “Three-dimensional finite difference simulation of fault dynamics: rectangular faults with fixed rupture velocity”. In: *Bulletin of the Seismological Society of America* 72.3, pp. 705–727.

Day, S. M., Yu, G., and Wald, D. J. (1998). “Dynamic stress changes during earthquake rupture”. In: *Bulletin of the Seismological Society of America* 88.2, pp. 512–522.

Day, S. M., Dalguer, L. A., Lapusta, N., and Liu, Y. (2005). “Comparison of finite difference and boundary integral solutions to three-dimensional spontaneous rupture”. In: *Journal of Geophysical Research-Solid Earth* 110.

Denolle, M. A., Fan, W. Y., and Shearer, P. M. (2015). “Dynamics of the 2015 M7.8 Nepal earthquake”. In: *Geophysical Research Letters* 42.18, pp. 7467–7475.

Dieterich, J. H. (1979). “Modeling of rock friction: 1. Experimental results and constitutive equations”. In: *Journal of Geophysical Research* 84.B5, pp. 2161–2168.

Dreger, D., Tinti, E., and Cirella, A. (2007). *Slip velocity parameterization for broadband ground motion simulation*. Conference Paper.

Drucker, D. C. and Prager, W. (1952). “Soil mechanics and plastic analysis or limit design”. In: *Quarterly of Applied Mathematics* 10.2, pp. 157–165.

Duan, B. and Day, S. M. (2008). “Inelastic strain distribution and seismic radiation from rupture of a fault kink”. In: *Journal of Geophysical Research-Solid Earth* 113.B12.

Dunham, E. M. and Archuleta, R. J. (2005). “Near-source ground motion from steady state dynamic rupture pulses”. In: *Geophysical Research Letters* 32.3.

Dunham, E. M., Belanger, D., Cong, L., and Kozdon, J. E. (2011). “Earthquake ruptures with strongly rate-weakening friction and off-fault plasticity, part 1: Planar faults”. In: *Bulletin of the Seismological Society of America* 101.5, pp. 2296–2307.

Duputel, Z., Vergne, J., Rivera, L., Wittlinger, G., Farra, V., and Hetenyi, G. (2016). “The 2015 Gorkha earthquake: A large event illuminating the Main Himalayan Thrust fault”. In: *Geophysical Research Letters* 43.6, pp. 2517–2525.

Elliott, J.., Jolivet, R., Gonzlez, P. J., Avouac, J. P., Hollingsworth, J., Searle, M. P., and Stevens, V.. (2016). “Himalayan megathrust geometry and relation to topography revealed by the Gorkha earthquake”. In: *Nature Geoscience* 9.2, pp. 174–180.

Ely, G. P., Day, S. M., and Minster, J.-B. (2008). “A support-operator method for viscoelastic wave modelling in 3-D heterogeneous media”. In: *Geophysical Journal International* 172.1, pp. 331–344.

— (2009). “A support-operator method for 3-D rupture dynamics”. In: *Geophysical Journal International* 177.3, pp. 1140–1150.

Fan, W. Y. and Shearer, P. M. (2015). “Detailed rupture imaging of the 25 April 2015 Nepal earthquake using teleseismic P waves”. In: *Geophysical Research Letters* 42.14, pp. 5744–5752.

Gabriel, A. A., Ampuero, J. P., Dalguer, L. A., and Mai, P. M. (2012). “The transition of dynamic rupture styles in elastic media under velocity-weakening friction”. In: *Journal of Geophysical Research-Solid Earth* 117.

— (2013). “Source properties of dynamic rupture pulses with off-fault plasticity”. In: *Journal of Geophysical Research-Solid Earth* 118.8, pp. 4117–4126.

Galetzka, J., Melgar, D., Genrich, J. F., Geng, J., Owen, S., Lindsey, E. O., Xu, X., Bock, Y., Avouac, J. P., Adhikari, L. B., Upreti, B. N., Pratt-Sitaula, B., Bhattarai, T. N., Sitaula, B. P., Moore, A., Hudnut, K. W., Szeliga, W., Normandeau, J., Fend, M., Flouzat, M., Bollinger, L., Shrestha, P., Koirala, B., Gautam, U., Bhatterai, M., Gupta, R., Kandel, T., Timsina, C., Sapkota, S. N., Rajaure, S., and Maharjan, N. (2015). “Slip pulse and resonance of the Kathmandu basin during the 2015 Gorkha earthquake, Nepal”. In: *Science* 349.6252, pp. 1091–1095.

Grandin, R., Valle, M., Satriano, C., Lacassin, R., Klinger, Y., Simoes, M., and Bollinger, L. (2015). “Rupture process of the Mw=-7.9 2015 Gorkha earthquake (Nepal): Insights into Himalayan megathrust segmentation”. In: *Geophysical Research Letters* 42.20, pp. 8373–8382.

Graves, R. and Pitarka, A. (2004). *Broadband time history simulation using a hybrid approach*. Conference Paper.

Gualandi, A., Avouac, J.-P., Galetzka, J., Genrich, J. F., Blewitt, G., Adhikari, L. B., Koirala, B. P., Gupta, R., Upreti, B. N., Pratt-Sitaula, B., and Liu-Zeng, J. (2017). “Pre- and post-seismic deformation related to the 2015, Mw7.8 Gorkha earthquake, Nepal”. In: *Tectonophysics* 714, pp. 90–106.

Guatteri, M., Mai, P. M., and Beroza, G. C. (2004). “A pseudo-dynamic approximation to dynamic rupture models for strong ground motion prediction”. In: *Bulletin of the Seismological Society of America* 94.6, pp. 2051–2063.

Harris, R. A., Barall, M., Archuleta, R., Dunham, E., Aagaard, B., Ampuero, J. P., Bhat, H., Cruz-Atienza, V., Dalguer, L., Dawson, P., Day, S., Duan, B., Ely, G., Kaneko, Y., Kase, Y., Lapusta, N., Liu, Y., Ma, S., Oglesby, D., Olsen, K., Pitarka, A., Song, S., and Templeton,

E. (2009). “The SCEC/USGS dynamic earthquake rupture code verification exercise”. In: *Seismological Research Letters* 80.1, pp. 119–126.

Haskell, N. A. (1964). “Total energy and energy spectral density of elastic wave radiation from propagating faults”. In: *Bulletin of the Seismological Society of America* 54.6A, pp. 1811–1841.

Hayes, G. P., Briggs, R. W., Barnhart, W. D., Yeck, W. L., McNamara, D. E., Wald, D. J., Nealy, J. L., Benz, H. M., Gold, R. D., Jaiswal, K. S., Marano, K., Earle, P. S., Hearne, M. G., Smoczyk, G. M., Wald, L. A., and Samsonov, S. V. (2015). “Rapid characterization of the 2015 Mw 7.8 Gorkha, Nepal, earthquake sequence and its seismotectonic context”. In: *Seismological Research Letters* 86.6, pp. 1557–1567.

He, X. H., Ni, S., Ye, L. L., Lay, T., Liu, Q. X., and Koper, K. D. (2015). “Rapid seismological quantification of source parameters of the 25 april 2015 Nepal earthquake”. In: *Seismological Research Letters* 86.6, pp. 1568–1577.

Heaton, T. H. (1990). “Evidence for and Implications of Self-Healing Pulses of Slip in Earthquake Rupture”. In: *Physics of the Earth and Planetary Interiors* 64.1, pp. 1–20.

Huang, Y. H. and Ampuero, J. P. (2011). “Pulse-like ruptures induced by low-velocity fault zones”. In: *Journal of Geophysical Research-Solid Earth* 116.

Huang, Y. H., Ampuero, J. P., and Kanamori, H. (2014). “Slip-Weakening Models of the 2011 Tohoku-Oki Earthquake and Constraints on Stress Drop and Fracture Energy”. In: *Pure and Applied Geophysics* 171.10, pp. 2555–2568.

Hubbard, J., Almeida, R., Foster, A., Sapkota, S. N., Brgi, P., and Tapponnier, P. (2016). “Structural segmentation controlled the 2015 Mw7.8 Gorkha earthquake rupture in Nepal”. In: *Geology* 44.8, pp. 639–642.

Johnson, E. (1992). “The Influence of the Lithospheric Thickness on Bilateral Slip”. In: *Geophysical Journal International* 108.1, pp. 151–160.

Kase, Y. and Day, S. M. (2006). “Spontaneous rupture processes on a bending fault”. In: *Geophysical Research Letters* 33.10.

King, G. C. P., Stein, R. S., and Lin, J. (1994). “Static stress changes and the triggering of earthquakes”. In: *Bulletin of the Seismological Society of America* 84.3, pp. 935–953.

Kostrov, B. V. (1964). “Selfsimilar problems of propagation of shear cracks”. In: *Journal of Applied Mathematics and Mechanics* 28.5, pp. 1077–1087.

— (1966). “Unsteady propagation of longitudinal shear cracks”. In: *Journal of Applied Mathematics and Mechanics* 30.6, pp. 1241–1248.

Kozdon, J. E. and Dunham, E. M. (2013). "Rupture to the Trench: Dynamic Rupture Simulations of the 11 March 2011 Tohoku Earthquake". In: *Bulletin of the Seismological Society of America* 103.2b, pp. 1275–1289.

Lapusta, N., Rice, J. R., Ben-Zion, Y., and Zheng, G. T. (2000). "Elastodynamic analysis for slow tectonic loading with spontaneous rupture episodes on faults with rate- and state-dependent friction". In: *Journal of Geophysical Research-Solid Earth* 105.B10, pp. 23765–23789.

Lay, T., Ye, L., Koper, K. D., and Kanamori, H. (2017). "Assessment of teleseismically-determined source parameters for the April 25, 2015 M W 7.9 Gorkha, Nepal earthquake and the May 12, 2015 M W 7.2 aftershock". In: *Tectonophysics* 714-715, pp. 4–20.

Lemonnier, C., Marquis, G., Perrier, F., Avouac, J. P., Chitrakar, G., Kafle, B., Sapkota, S., Gautam, U., Tiwari, D., and Bano, M. (1999). "Electrical structure of the Himalaya of Central Nepal: high conductivity around the mid-crustal ramp along the MHT". In: *Geophysical Research Letters* 26.21, pp. 3261–3264.

Liu, P. C. and Archuleta, R. J. (2004). "A new nonlinear finite fault inversion with three-dimensional Green's functions: Application to the 1989 Loma Prieta, California, earthquake". In: *Journal of Geophysical Research-Solid Earth* 109.B2.

Liu, P. C., Archuleta, R. J., and Hartzell, S. H. (2006). "Prediction of broadband ground-motion time histories: Hybrid low/high-frequency method with correlated random source parameters". In: *Bulletin of the Seismological Society of America* 96.6, pp. 2118–2130.

Lu, X., Lapusta, N., and Rosakis, A. J. (2010). "Pulse-like and crack-like dynamic shear ruptures on frictional interfaces: experimental evidence, numerical modeling, and implications". In: *International Journal of Fracture* 163.1-2, pp. 27–39.

Ma, S. and Beroza, G. C. (2008). "Rupture dynamics on a bimaterial interface for dipping faults". In: *Bulletin of the Seismological Society of America* 98.4, pp. 1642–1658.

Ma, S. and Andrews, D. J. (2010). "Inelastic off-fault response and three-dimensional dynamics of earthquake rupture on a strike-slip fault". In: *Journal of Geophysical Research-Solid Earth* 115.

Marone, C. (1998). "Laboratory-derived friction laws and their application to seismic faulting". In: *Annual Review of Earth and Planetary Sciences* 26, pp. 643–696.

McNamara, D. E., Yeck, W. L., Barnhart, W. D., Schulte-Pelkum, V., Bergman, E., Adhikari, L. B., Dixit, A., Hough, S. E., Benz, H. M., and Earle, P. S. (2017). "Source modeling of the 2015 Mw 7.8 Nepal (Gorkha) earthquake sequence: Implications for geodynamics and earthquake hazards". In: *Tectonophysics* 714, pp. 21–30.

Melgar, D. and Hayes, G. P. (2017). "Systematic observations of the slip pulse properties of large earthquake ruptures". In: *Geophysical Research Letters* 44.19, pp. 9691–9698.

Meng, L. S., Zhang, A. L., and Yagi, Y. J. (2016). "Improving back projection imaging with a novel physics-based aftershock calibration approach: A case study of the 2015 Gorkha earthquake". In: *Geophysical Research Letters* 43.2, pp. 628–636.

Michel, S, Avouac, J., Lapusta, N, and Jiang, J. (2017). "Pulse-like partial ruptures and high-frequency radiation at creeping-locked transition during megathrust earthquakes". In: *Geophysical Research Letters* 44.16, pp. 8345–8351.

Nabelek, J., Hetenyi, G., Vergne, J., Sapkota, S., Kafle, B., Jiang, M., Su, H. P., Chen, J., Huang, B. S., and Hi, C. T. (2009). "Underplating in the Himalaya-Tibet Collision Zone Revealed by the Hi-CLIMB Experiment". In: *Science* 325.5946, pp. 1371–1374.

Nielsen, S. and Madariaga, R. (2003). "On the self-healing fracture mode". In: *Bulletin of the Seismological Society of America* 93.6, pp. 2375–2388.

Nielsen, S. B. (1998). "Free surface effects on the propagation of dynamic rupture". In: *Geophysical Research Letters* 25.1, pp. 125–128.

Noda, H., Dunham, E. M., and Rice, J. R. (2009). "Earthquake ruptures with thermal weakening and the operation of major faults at low overall stress levels". In: *Journal of Geophysical Research-Solid Earth* 114.

Oglesby, D. D. and Day, S. M. (2002). "Stochastic fault stress: Implications for fault dynamics and ground motion". In: *Bulletin of the Seismological Society of America* 92.8, pp. 3006–3021.

Oglesby, D. D. and Mai, P. M. (2012). "Fault geometry, rupture dynamics and ground motion from potential earthquakes on the North Anatolian Fault under the Sea of Marmara". In: *Geophysical Journal International* 188.3, pp. 1071–1087.

Oglesby, D. D., Archuleta, R. J., and Nielsen, S. B. (1998). "Earthquakes on dipping faults: the effects of broken symmetry". In: *Science* 280.5366, pp. 1055–9.

Oglesby, D. D., Archuleta, R. J., and Nielsen, S. B. (2000). "The three-dimensional dynamics of dipping faults". In: *Bulletin of the Seismological Society of America* 90.3, pp. 616–628.

Pandey, M. R., Tandukar, R. P., Avouac, J. P., Lave, J., and Massot, J. P. (1995). "Interseismic strain accumulation on the himalayan crustal ramp (Nepal)". In: *Geophysical Research Letters* 22.7, pp. 751–754.

Pearson, O. N. and DeCelles, P. G. (2005). "Structural geology and regional tectonic significance of the Ramgarh thrust, Himalayan fold-thrust belt of Nepal". In: *Tectonics* 24.4.

Qiu, Q., Hill, E. M., Barbot, S., Hubbard, J., Feng, W. P., Lindsey, E. O., Feng, L. J., Dai, K. R., Samsonov, S. V., and Tapponnier, P. (2016). "The mechanism of partial rupture of a locked megathrust: The role of fault morphology". In: *Geology* 44.10, pp. 875–878.

Rice, J. R. (1992). "Fault stress states, pore pressure distributions, and the weakness of the san andreas fault". In: *Fault Mechanics and Transport Properties of Rocks - A Festschrift in Honor of W. F. Brace*. Ed. by B. Evans and T.-f. Wong. Vol. 51. International Geophysics. San Diego: Academic Press, pp. 475–503. ISBN: 9780122437809.

Robinson, D. M. (2008). "Forward modeling the kinematic sequence of the central Himalayan thrust belt, western Nepal". In: *Geosphere* 4.5, pp. 785–801.

Rojas, O., Dunham, E. M., Day, S. M., Dalguer, L. A., and Castillo, J. E. (2009). "Finite difference modelling of rupture propagation with strong velocity-weakening friction". In: *Geophysical Journal International* 179.3, pp. 1831–1858.

Roten, D., Olsen, K. B., Day, S. M., Cui, Y., and Fah, D. (2014). "Expected seismic shaking in Los Angeles reduced by San Andreas fault zone plasticity". In: *Geophysical Research Letters* 41.8, pp. 2769–2777.

Roten, D., Olsen, K. B., and Day, S. M. (2017). "Off-fault deformations and shallow slip deficit from dynamic rupture simulations with fault zone plasticity". In: *Geophysical Research Letters* 44.15, pp. 7733–7742.

Rudnicki, J. W. and Wu, M. (1995). "Mechanics of dip-slip faulting in an elastic half-space". In: *Journal of Geophysical Research-Solid Earth* 100.B11, pp. 22173–22186.

Ruina, A. (1983). "Slip instability and state variable friction laws". In: *Journal of Geophysical Research* 88.B12, pp. 359–370.

Schulte-Pelkum, V., Monsalve, G., Sheehan, A., Pandey, M. R., Sapkota, S., Bilham, R., and Wu, F. (2005). "Imaging the Indian subcontinent beneath the Himalaya". In: *Nature* 435.7046, pp. 1222–1225.

Shi, Z. Q. and Day, S. M. (2013). "Rupture dynamics and ground motion from 3-D rough-fault simulations". In: *Journal of Geophysical Research-Solid Earth* 118.3, pp. 1122–1141.

Smith, D. E., Aagaard, B. T., and Heaton, T. H. (2005). "Teleseismic body waves from dynamically rupturing shallow thrust faults: Are they opaque for surface-reflected phases?" In: *Bulletin of the Seismological Society of America* 95.3, pp. 800–817.

Stevens, V. L. and Avouac, J. P. (2015). "Interseismic coupling on the main Himalayan thrust". In: *Geophysical Research Letters* 42.14, pp. 5828–5837.

Tinti, E., Fukuyama, E., Piatanesi, A., and Cocco, M. (2005). "A kinematic source-time function compatible with earthquake dynamics". In: *Bulletin of the Seismological Society of America* 95.4, pp. 1211–1223.

Wang, K. and Fialko, Y. (2015). "Slip model of the 2015 Mw 7.8 Gorkha (Nepal) earthquake from inversions of ALOS-2 and GPS data". In: *Geophysical Research Letters* 42.18, pp. 7452–7458.

— (2018). "Observations and modeling of coseismic and postseismic deformation due to the 2015 Mw 7.8 Gorkha (Nepal) earthquake". In: *Journal of Geophysical Research: Solid Earth* 123.1, pp. 761–779.

Wang, X., Wei, S. J., and Wu, W. B. (2017). "Double-ramp on the Main Himalayan Thrust revealed by broadband waveform modeling of the 2015 Gorkha earthquake sequence". In: *Earth and Planetary Science Letters* 473, pp. 83–93.

Wang, Y. and Day, S. M. (2017). "Seismic source spectral properties of crack-like and pulse-like modes of dynamic rupture". In: *Journal of Geophysical Research-Solid Earth* 122.8, pp. 6657–6684.

Wei, S. J., Chen, M., Wang, X., Graves, R., Lindsey, E., Wang, T., Karakas, C., and Helmberger, D. (2018). "The 2015 Gorkha (Nepal) earthquake sequence: I. Source modeling and deterministic 3D ground shaking". In: *Tectonophysics* 722.Supplement C, pp. 447–461.

Yagi, Y. and Okuwaki, R. (2015). "Integrated seismic source model of the 2015 Gorkha, Nepal, earthquake". In: *Geophysical Research Letters* 42.15, pp. 6229–6235.

Yao, H. J., Shearer, P. M., and Gerstoft, P. (2013). "Compressive sensing of frequency-dependent seismic radiation from subduction zone megathrust ruptures". In: *Proceedings of the National Academy of Sciences of the United States of America* 110.12, pp. 4512–4517.

Yin, J. X., Yao, H. J., Yang, H. F., Liu, J., Qin, W. Z., and Zhang, H. J. (2017). "Frequency-dependent rupture process, stress change, and seismogenic mechanism of the 25 April 2015 Nepal Gorkha M-w 7.8 earthquake". In: *Science China-Earth Sciences* 60.4, pp. 796–808.

Yue, H., Simons, M., Duputel, Z., Jiang, J., Fielding, E., Liang, C., Owen, S., Moore, A., Riel, B., Ampuero, J. P., and Samsonov, S. V. (2017). "Depth varying rupture properties during the 2015 Mw 7.8 Gorkha (Nepal) earthquake". In: *Tectonophysics* 714-715, pp. 44–54.

Zheng, G. and Rice, J. R. (1998). "Conditions under which velocity-weakening friction allows a self-healing versus a cracklike mode of rupture". In: *Bulletin of the Seismological Society of America* 88.6, pp. 1466–1483.

Tables and Figures

Table 3.1: Models Parameter Values

Parameter	Symbol	Value
Bulk Properties		
P wave speed	α	5,850 m/s
S wave speed	β	3,400 m/s
Density	ρ	2,640 kg/m^3
Cohesion	C	5 MPa
Internal friction coefficient	tan(ϕ)	0.5
Initial stress state		
Initial stress tensor components	σ_{xx}	-142.5 MPa
	σ_{yy}	-190.0 MPa
	σ_{zz}	-95.0 MPa
	σ_{yz}	19.0 MPa
Initial shear stress	τ^b	Variable
Initial normal stress	τ^n	Variable
Frictional properties		
Direct-effect parameter	a	Variable
Evolution-effect parameter	b	0.014
Reference slip rate	V_0	1μ m/s
Steady state coefficient at slip rate V_0	f_0	Variable
Evolution distance of state variable	L	Variable
Weakening slip rate	V_w	0.1 m/s
Fully weakened friction coefficient	f_w	Variable
Initial fault slip rate	V^{ini}	$6 \times 10^{-10} m/s$
Nucleation parameters		
Nucleation radius	R	7,500 m
Overstress	$\Delta\tau^b$	$0.5 \times \tau^b$

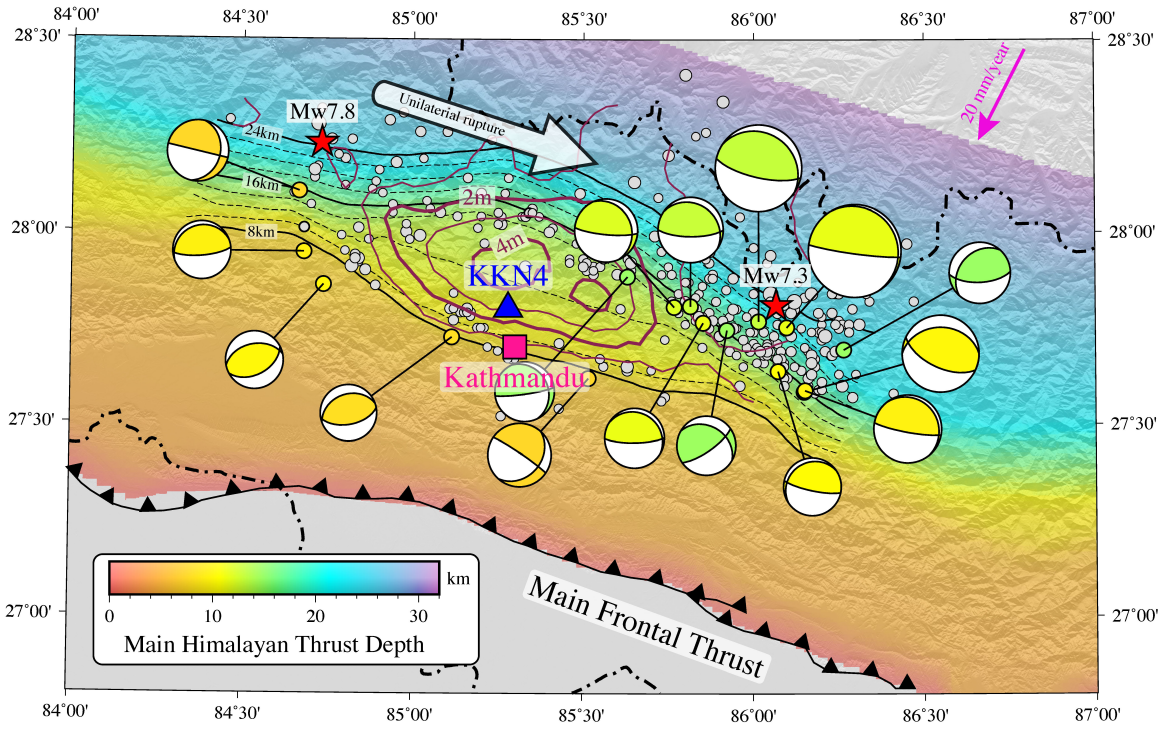

Figure 3.1: Map of the 2015 Gorkha earthquake source region. The fault geometry of the Main Himalayan Thrust (MHT; Hubbard et al., 2016) is illustrated. Wang et al. [2017] indicated that the focal mechanism and locations of relocated large aftershocks (the focal mechanisms are colored by the focal depths) delineate a double-ramp fault geometry that agrees with that in Hubbard et al. (2016; this is indicated by the correlation of the colors between 3-D locations of aftershocks and the Hubbard fault geometry). Black thin solid and dashed lines show the depth contours of adopted MHT geometry. Gray dots denote the location of aftershocks over magnitude 4 within the first 2 months (from the National Seismological Center, Kathmandu, Nepal). The dark red contour lines indicate the coseismic slip profile [Avouac et al. 2015] whose shape is in agreement with the confining edges of this MHT model. The blue triangle and the pink square symbols are the highrate GPS receiver KKN4 and the capital city Kathmandu, respectively.

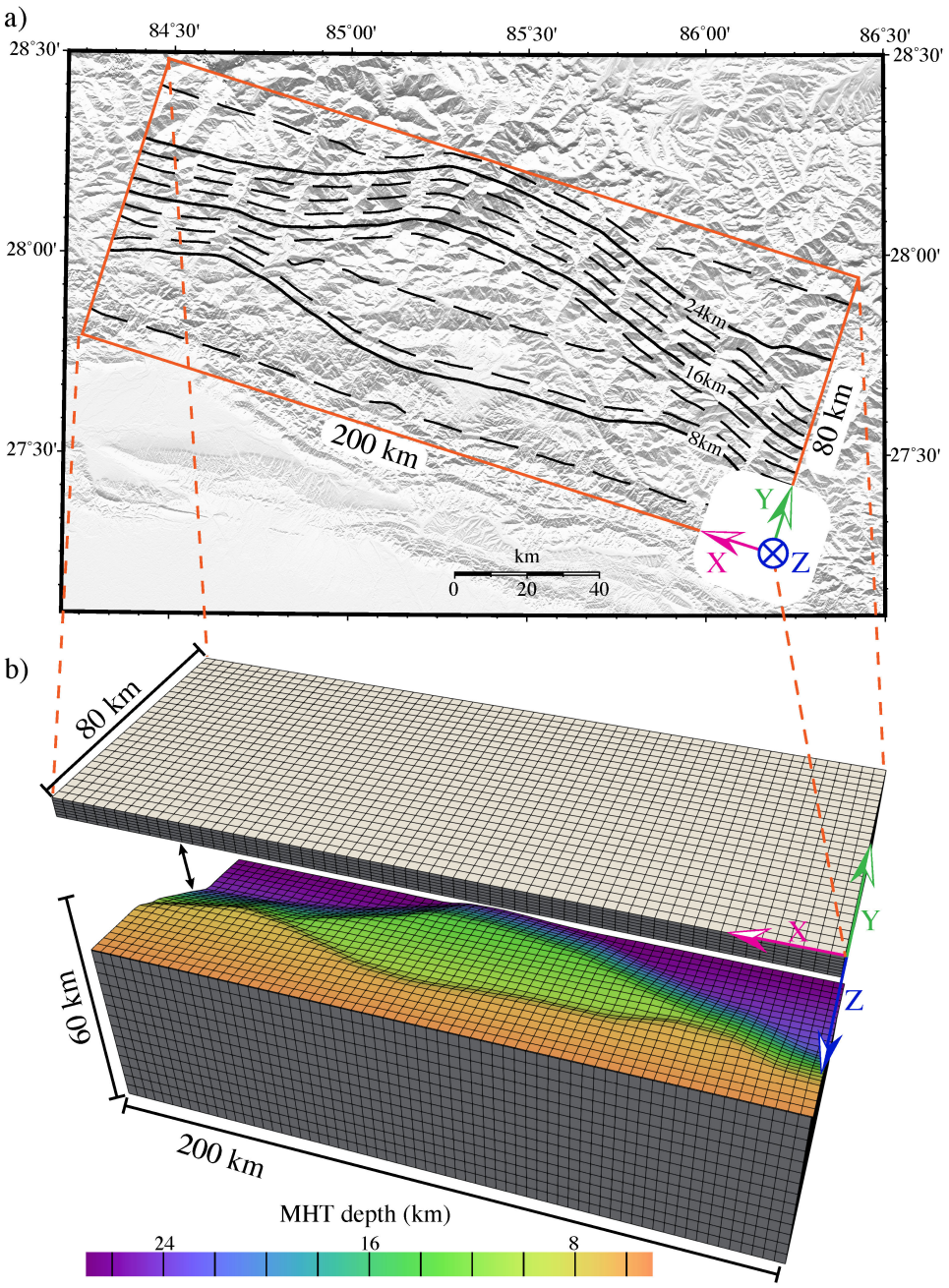

Figure 3.2: Computational domain and geographic map (200 km × 80 km × 60 km), showing schematically the discretization of this area by an irregular structural hexahedral mesh. The coordinate axes are indicated, with the origin in the southeast. (a) The contour lines show the geometry of the Main Himalayan Thrust (MHT) as given by the Hubbard model. (b) Schematic of the 3-D structured hexahedral mesh is shown, with a cutaway of the fault surface. This schematic mesh is downsampled for illustration purposes.

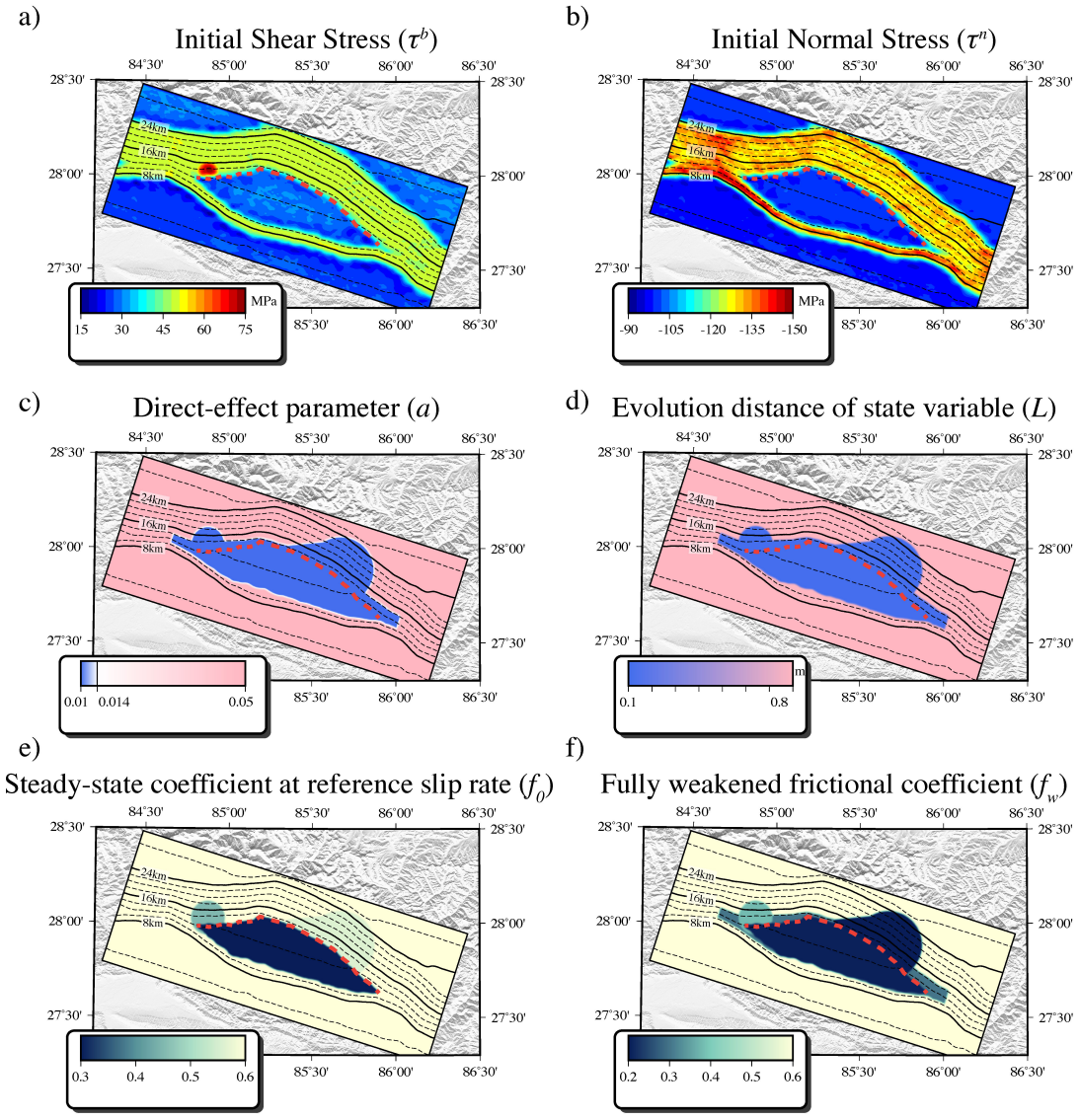

Figure 3.3: Model setup of the projected initial shear and normal stress on fault and four of the frictional parameters (the remaining frictional parameters are constant over the entire fault and are listed in Table 1). The nucleation zone and a lower ramp asperity each show up as intrusive bulges into the lower ramp. The red dashed line shows the lower kink line of the flat decollement. The very narrow white contour band along the downdip edge of the decollement in (c) results from the rapid transition from velocity weakening to velocity strengthening that we have assumed to occur over the depth range between the edge of the decollement and the 14.5-km depth contour.

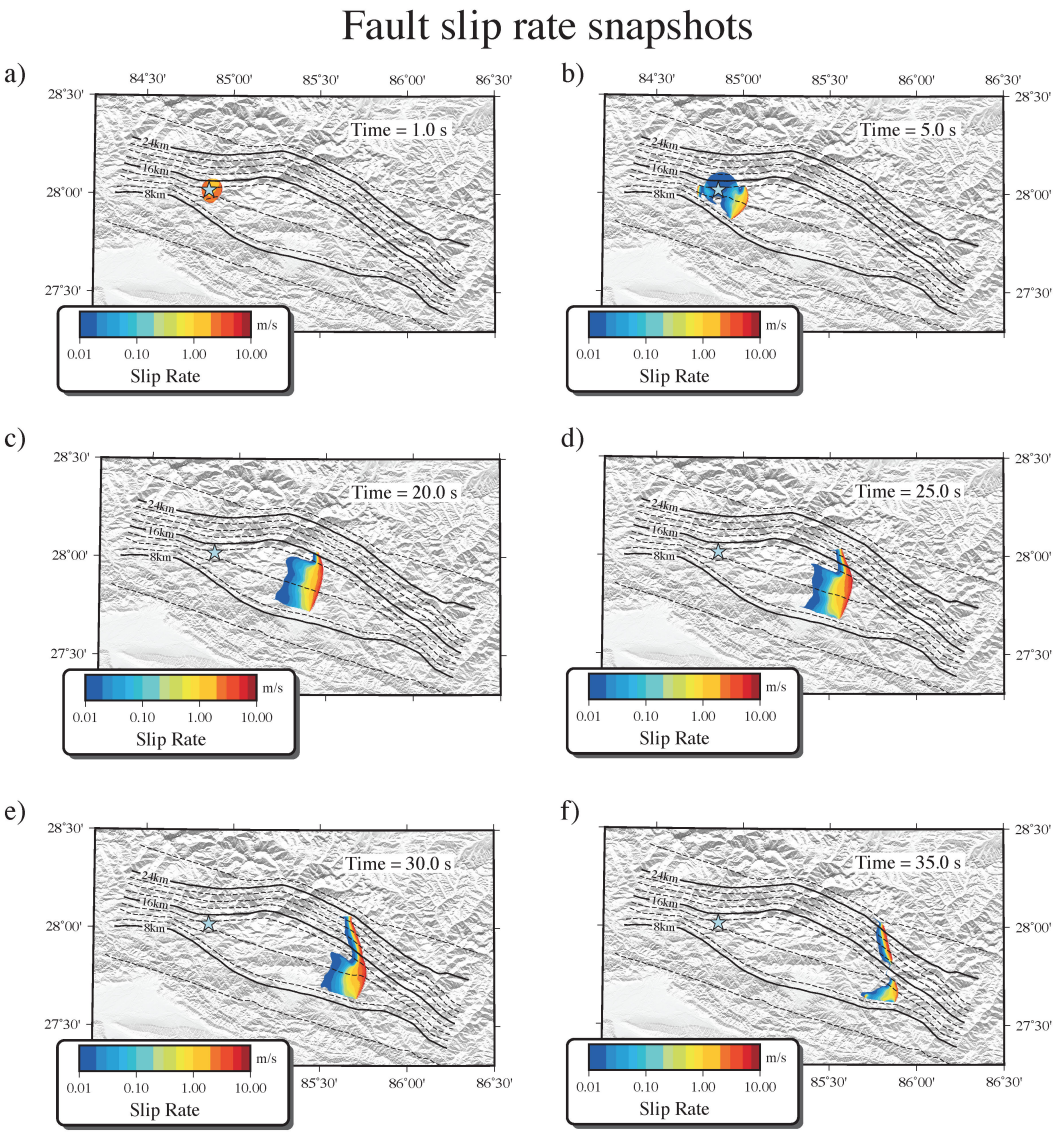

Figure 3.4: Snapshots of the simulated dynamic rupture model of the 2015 Gorkha earthquake at (a) 1, (b) 5, (c) 20, (d) 25, (e) 30, and (f) 35 s. They illustrate the multiple phases of the rupture propagation: the initiation on the lower ramp, the eastward unilateral rupture on the flat segment, the bifurcation of the rupture, and the termination. The light blue star denotes the hypocentral location.

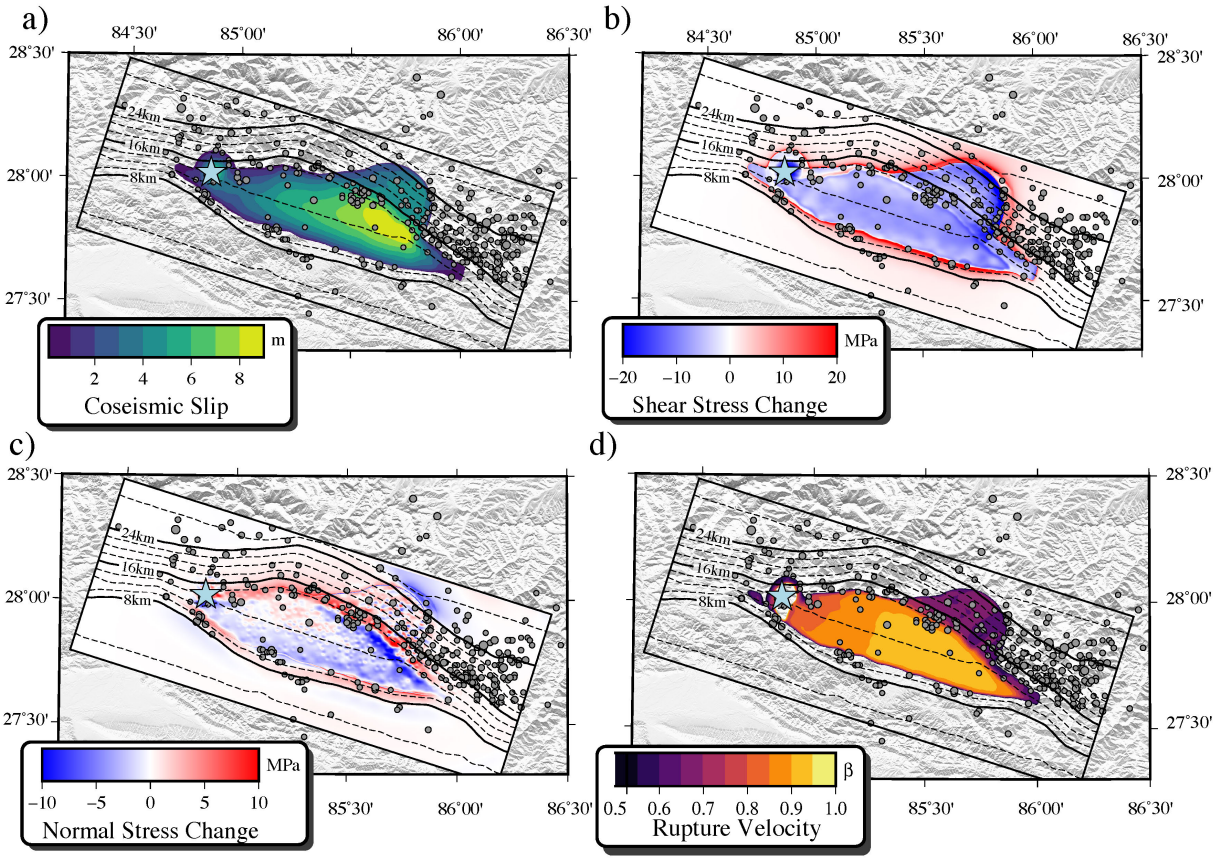

Figure 3.5: Earthquake parameters of simulated dynamic rupture model of the 2015 Gorkha earthquake: (a) coseismic slip, (b) shear stress change, (c) normal stress change, and (d) rupture velocity. Black solid lines enclose the simulated area, and gray dots depict the locations of aftershocks within 4 months of the mainshock. The light blue star denotes the hypocentral location.

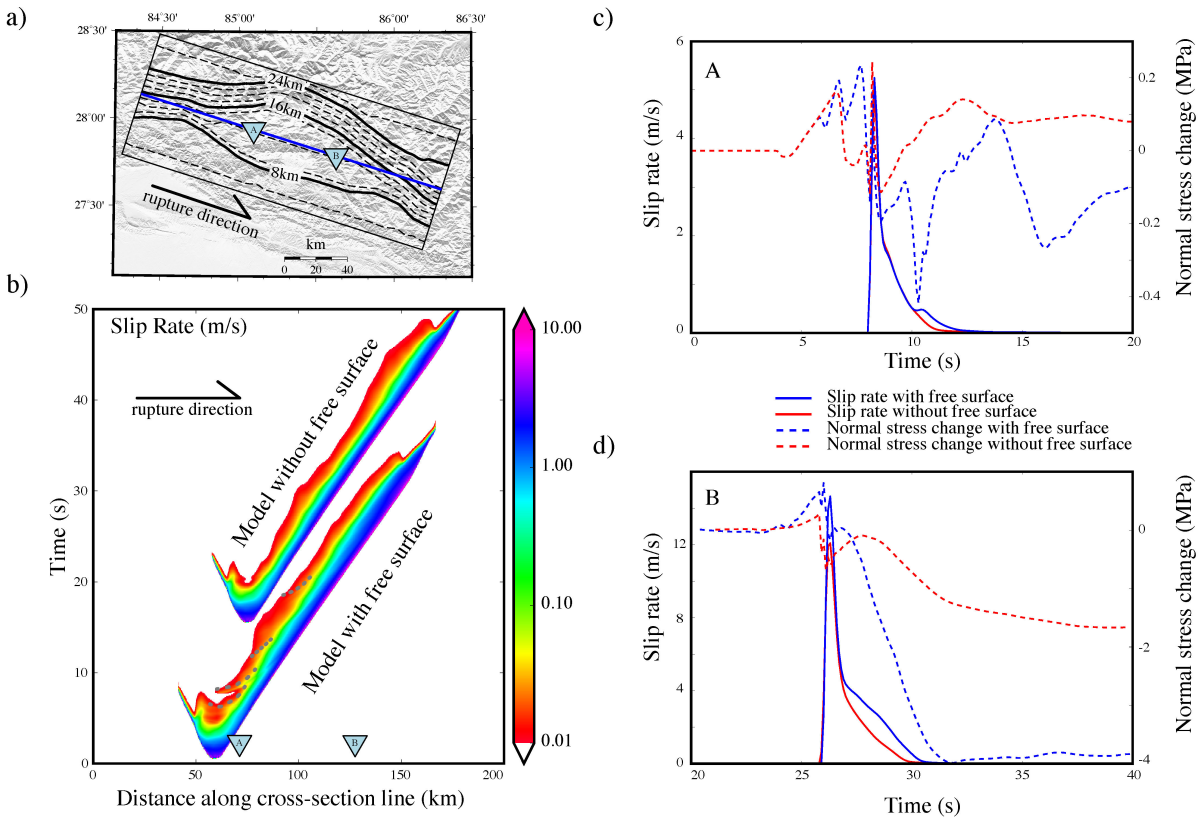

Figure 3.6: Effects of free surface on the rupture evolution. (a) Dark blue straight line shows where the slip-rate and stress histories are extracted. Two sample points on this line, A and B, will highlight the interactions between reflected seismic waves and rupture evolution. (b) The comparison between the model with and without free surface is shown in time-distance plots of the slip rate. The horizontal axis corresponds to the blue cross section from the northwest to the southeast in Figure 6a. (c) The comparison of slip-rate and normal stress histories for models with and without free surface, at point A (closer to the hypocenter). (d) The comparison of slip-rate and normal stress histories for models with and without free surface, at B point (further from the hypocenter).

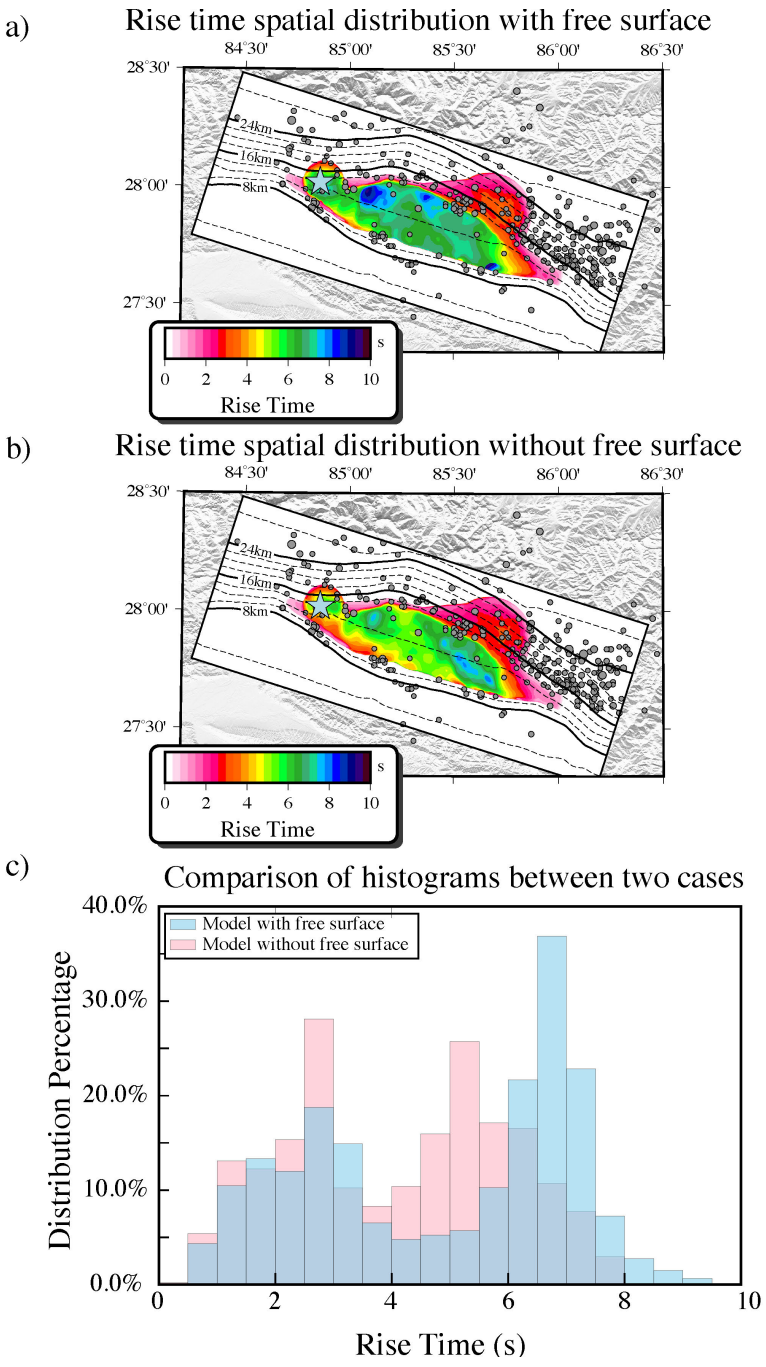

Figure 3.7: Rise time distributions on Main Himalayan Thrust rupture surface and a statistical comparison. (a) Rise time distribution of the half-space model. (b) Rise time distribution of the whole-space model. (c) Rise time histogram for each of the models.

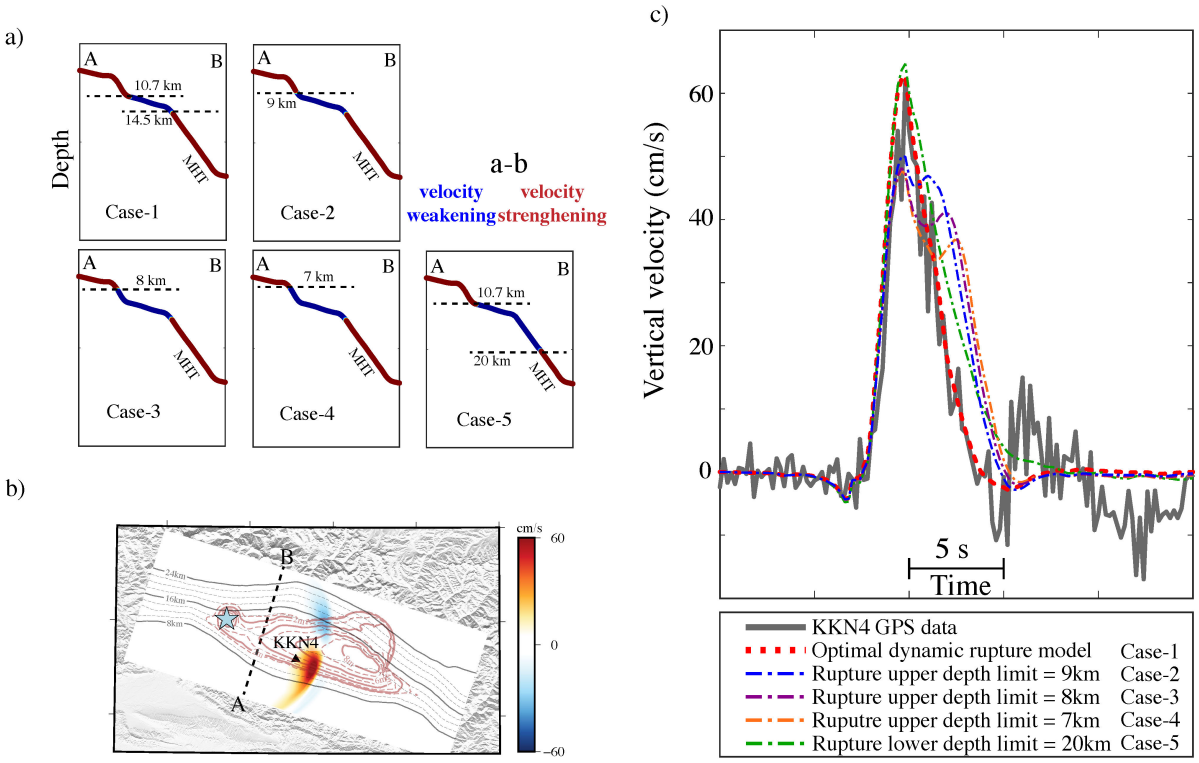

Figure 3.8: (a) The downdip rupture extent (blue and red segments are velocity weakening and strengthening, respectively) along a vertical (cross-section A-B shown in frame (b)) for each of the five simulations used to examine sensitivity to rupture geometry. Case 1 is our optimal model with the upper (10.7 km deep) and lower (14.5 km deep) rupture limits on the middle flat stage. Cases 2-4 are modifications of Case 1 in which the upper limit is raised to 9, 8, and 7 km in depth, respectively. Case 5 is a modification of Case 1 in which the lower limit is moved downward to 20 km. (b) A snapshot of the vertical ground motion at 20 s, along with a dashed line indicating the location of cross-section A-B. The light blue star and black triangle are the locations of the hypocenter and the GPS station (KKN4), respectively. The contours of the depth of the MHT and simulated coseismic slip are plotted by black and brown lines. (c) The simulated (red dotted line is the optimal dynamic rupture model; the blue, purple, orange, and green dashed lines are from other four alternative models) and recorded (gray solid line) vertical ground velocity at the site of KKN4.

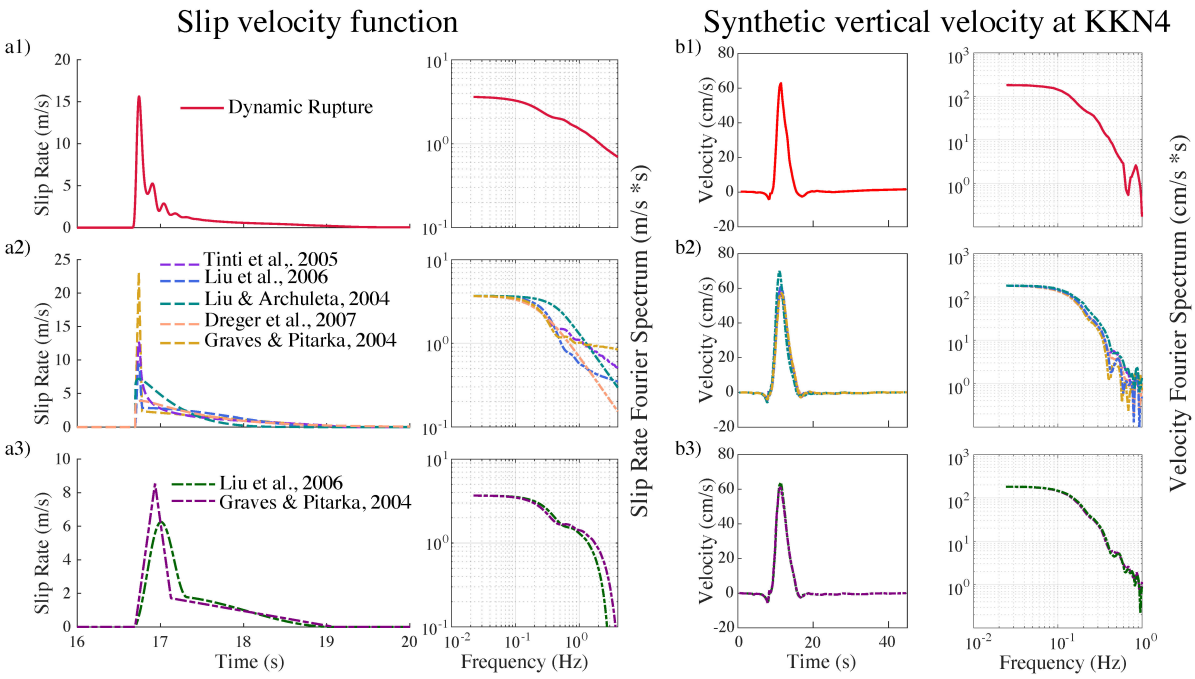

Figure 3.9: (left) Dynamic and equivalent kinematic slip rates, with (right) observed and synthetic vertical ground velocity at KKN4. The dynamic slip rate is from our preferred Gorkha simulation, on the fault surface directly below the point centered between sites A and B in Figure 6a. Equivalent kinematic slip rate is defined in section 4.2. (a1) The slip rate and Fourier amplitude spectrum of the dynamic model. (b1) The synthetic vertical ground velocity for dynamic model, compared with KKN4 record, with the corresponding spectra. (a2) The slip velocities and spectra of equivalent kinematic models (with rise-time, peak-time, and total-slip constraints). (b2) The synthetic vertical ground velocities at KKN4 from the equivalent kinematic models (with rise-time, peak-time, and total-slip constraints). (a3) The slip velocities and spectra of equivalent kinematic models (with rise-time and total-slip constraints only). (b3) The synthetic vertical ground velocities at KKN4 from equivalent kinematic models (rise-time and total-slip constraints only).

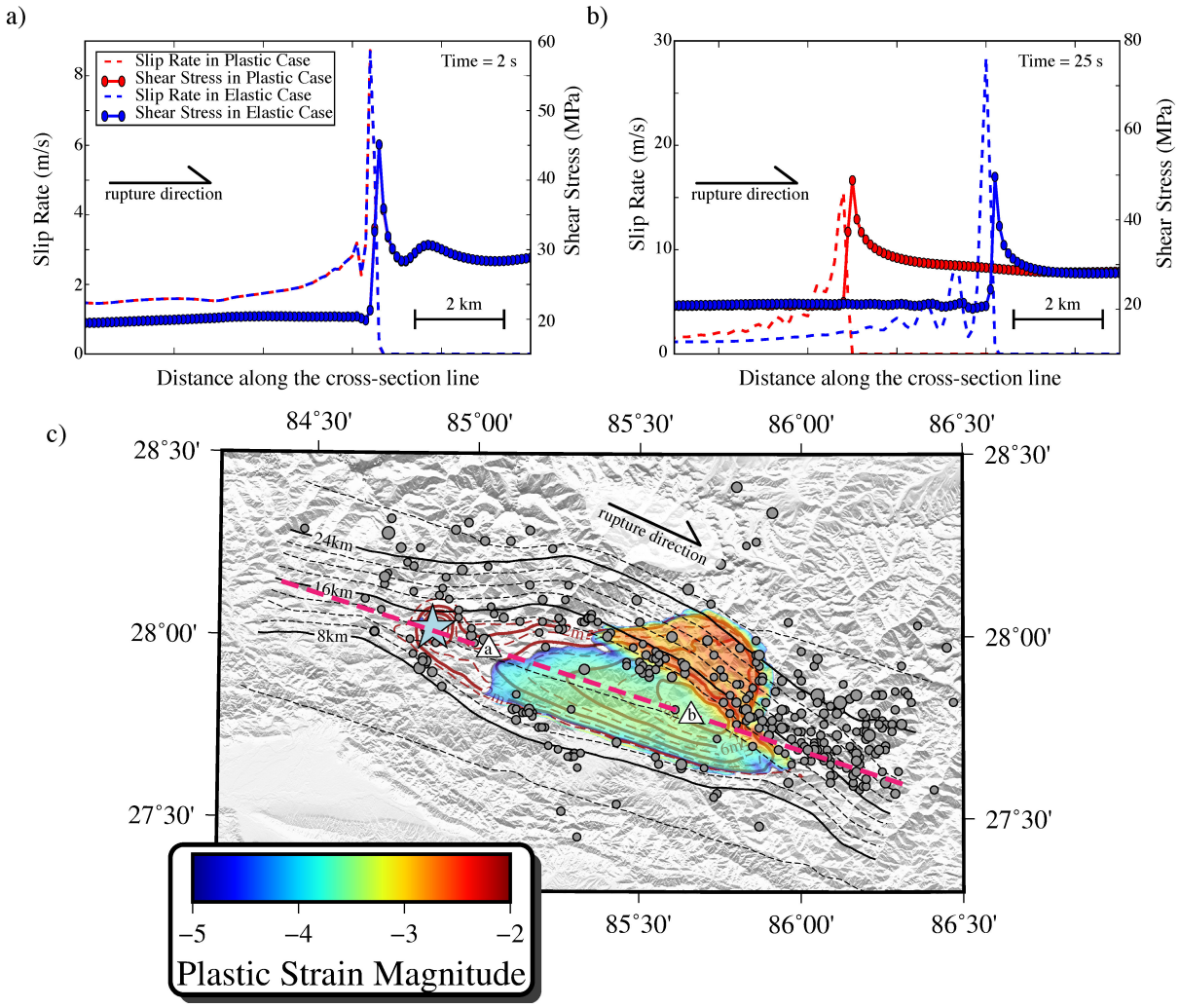

Figure 3.10: Effects of plasticity on the dynamic rupture model. (a) Snapshot, at 2 s, of the slip rate (dashed lines) and shear stress (solid lines with circles) at a local segment (labeled as a) of the cross section (pink dashed line from the northwest to the southeast in Figure 10c), for elastic (blue) and elastoplastic (red) cases. (b) Snapshot of slip rate and shear stress at 25 s at a local segment labeled as b. (c) The plastic strain magnitude (defined in Appendix A) above the MHT fault surface and synthetic coseismic slip on the Main Himalayan Thrust. Two triangles, labeled a and b, indicate the locations of stresses and slip rates plotted in Figures 10a and 10b.

Supplementary Material

3.6.1 Text S3.1

We investigate the robustness of the free surface effects illustrated in Section 3.2 by assessing their dependency on how slip rise time is defined. That sensitivity is related to the shape of slip-rate function. For example, the truncated Kostrov slip-rate function, with a sharp onset and arrest, is less sensitive to the rise time definition than is the Yoffe function, with its very smooth arrest. Our simulated dynamic slip-rate function shape is similar to the Yoffe function, and thus rise-time estimates for it are fairly sensitive to the rise-time definition. Denoting as Method 1 the 0.1 m/s threshold definition used in the main text, we test two other definitions of the rise time. Method 2 defines the rise time as the period when the time-dependent slip is in a range between 5% and 95% of the total slip (similar to Guatteri et al. [2004]). Method 3 defines rise time as the duration given by the best-fitting regularized Yoffe function [Tinti et al. 2005] constrained to match both the peak time (the time between onset and peak of slip rate) and final slip of our simulated model.The normalized slip rate for a representative point on the fault for the Gorkha simulation (with free surface) is shown in Figure S3.4a, and the corresponding slip-rate function in Figure S3.4b. As shown in the figures, the range of rise time estimates based on the three methods is a little more than 1 s. For the simulation with the free surface removed (Figures 3.3c and 3.3d), the range is roughly half that. But, regardless of rise-time definition, the effect of the free surface is, systematically, to increase the rise-time estimate. This systematic effect is more evident in Figure S5. Combined with Figure S3.7, S3.5 shows that the spatial pattern of rise time variations is similar for all three rise-time definitions, and that the corresponding rise-time histograms are affected by free-surface interactions in a similar manner. Those interactions prolong the rise times associated with slip on the decollement (i.e., the right-side peak in each histogram, which is also associated with the bulk of the slip) by $\sim$1sec. The slip-weighted average rise-time shift is $\sim$2 s. In summary, the rise-time definition has a significant effect of the numerical estimate, but little

effect on the estimate of pulse elongation due to free-surface interactions.

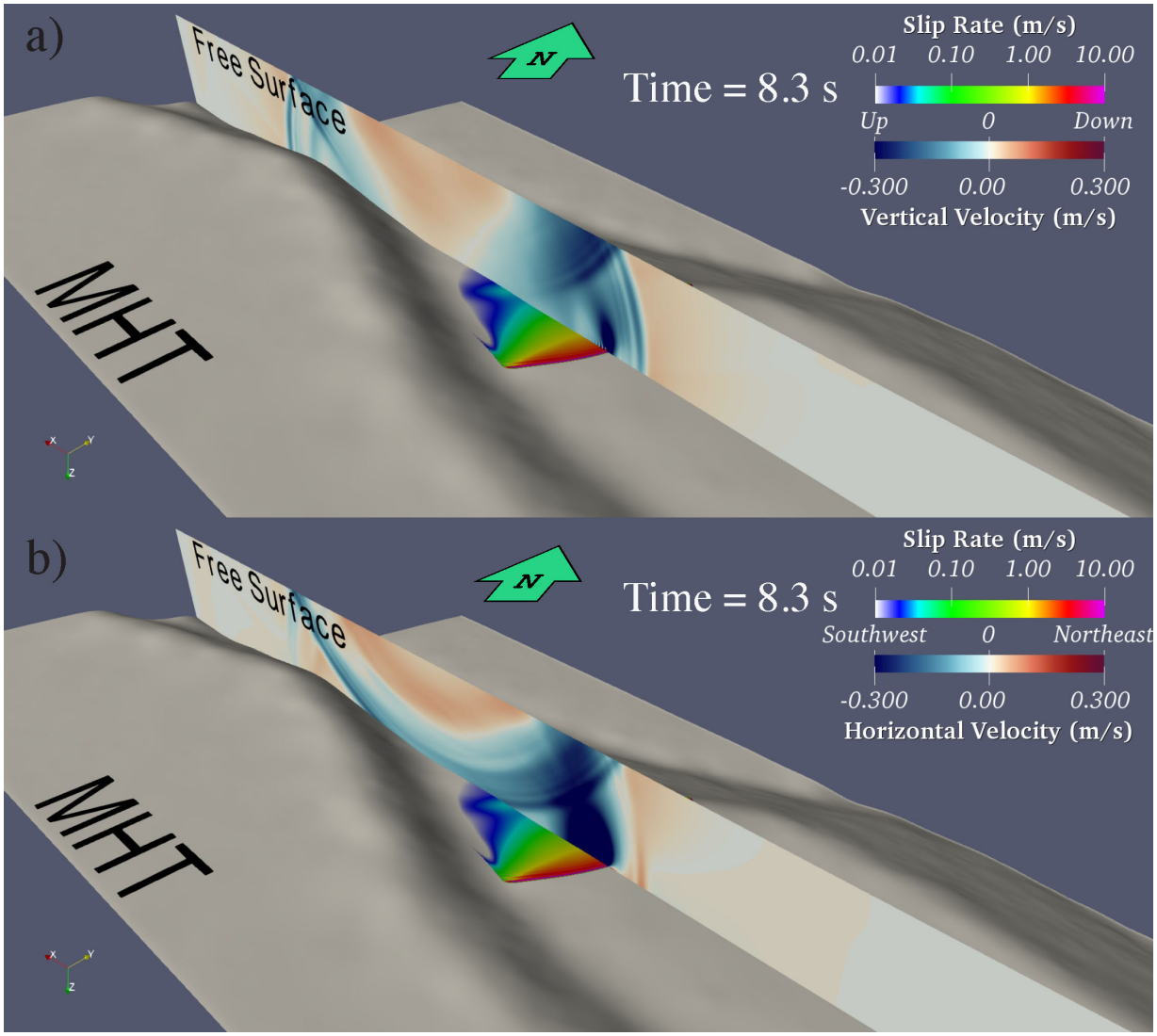

Figure S3.1: Snapshot showing the simulated slip rate on the MHT fault and seismic wavefields on the vertical cross-section from the free surface down to the fault. a) and b) show the horizontal component along dip (in the Y, i.e., southwest-northeast direction) and the vertical component of synthetic wavefields, respectively.

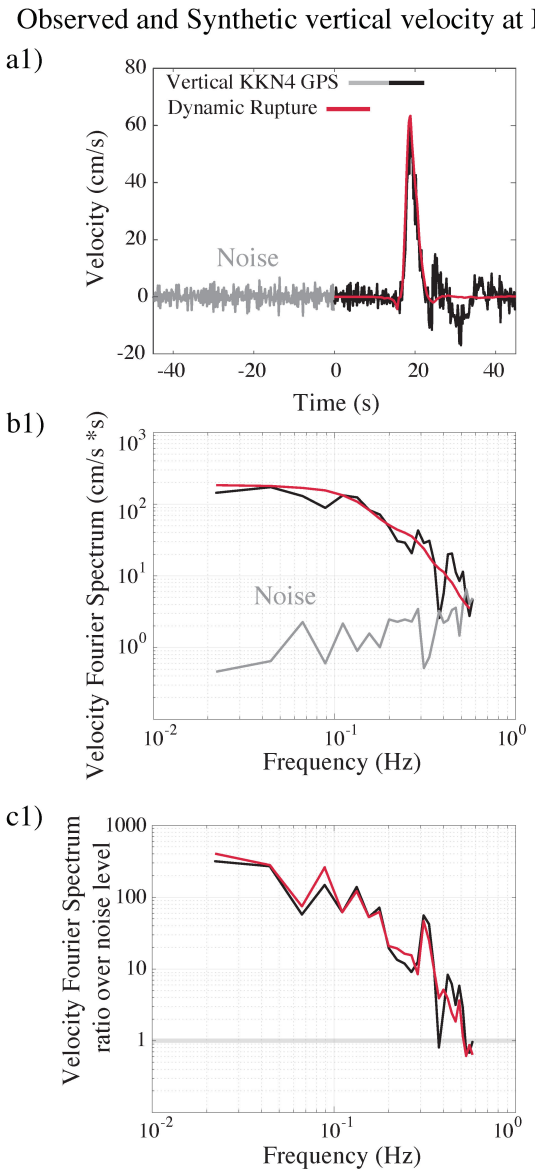

Figure S3.2: Synthetic seismic waveforms at the KKN4 site and snapshots corresponding to four scenarios in which only upper limit of rupture extent is varied. The four rows, from (a) to (d), show Cases 1 to 4, with the upper limit moved progressively upward. For each case, the three columns show, respectively, a schematic map of rupture extent, the 3 components of synthetic GPS time histories (with each corresponding KKN4 recording, in gray, for comparison) and a snapshot of the simulated seismic wavefield at the ground surface, at t = 20 s. The contours of the depth of MHT and simulated coseismic slip are plotted by black and brown lines.

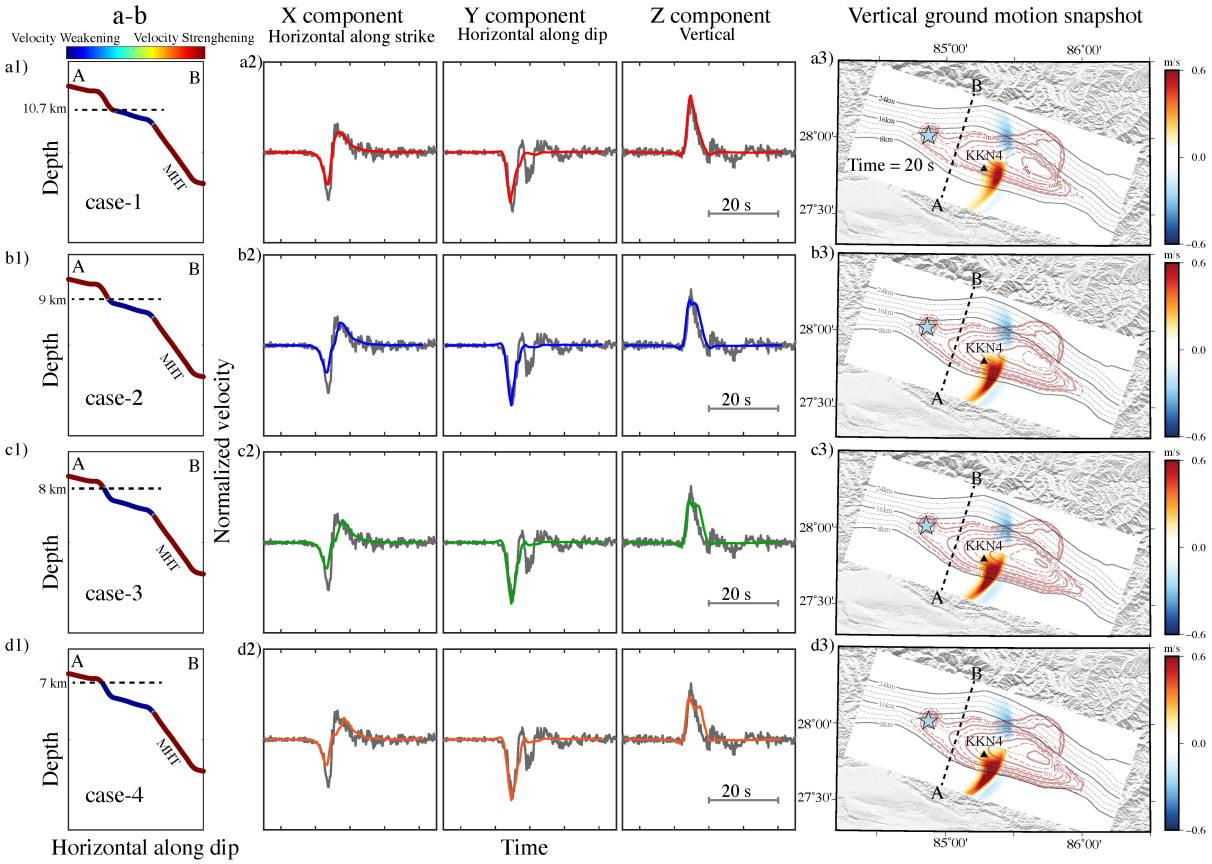

Figure S3.3: Observed and synthetic vertical ground velocity at KKN4 in time and frequency domain. a1) pre-event noise (gray line), recorded ground velocity (black line) and synthetic ground velocity (red line) of identical durations (45 s). b1) Fourier spectra of the noise, observed and synthetic ground velocity. c1) The spectral ratio of the observed and synthetic ground velocity over the noise level. The convergence of observed ground velocity pulse and pre-event noise indicates that the maximum acceptable high-frequency limit is about 0.5 Hz.

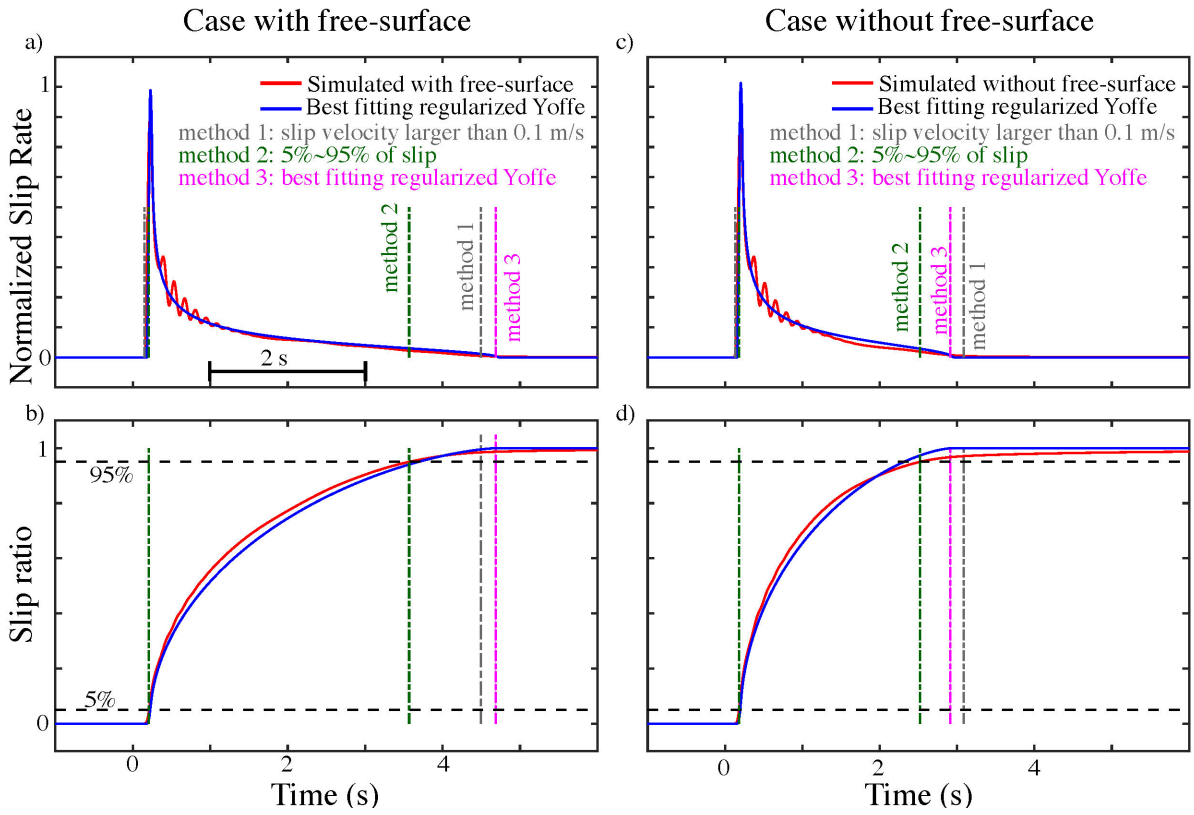

Figure S3.4: Different methods defining the slip rise time are applied to reevaluate the rise time across the fault. Representative slip rate (a and c) and slip (b and d) time histories (each normalized to unit maximum value) are sampled at the same site on the fault. In (a) and (b), the time histories are from the preferred Gorkha simulation, while in (c) and (d) results are for the test simulation without a free surface (discussed in Section 3.2). Red solid lines are from the simulations and blue solid lines are the best-fitting regularized Yoffe function [Tinti et al. 2005]. The different dashed lines pick the onset and finish time points based on various methods

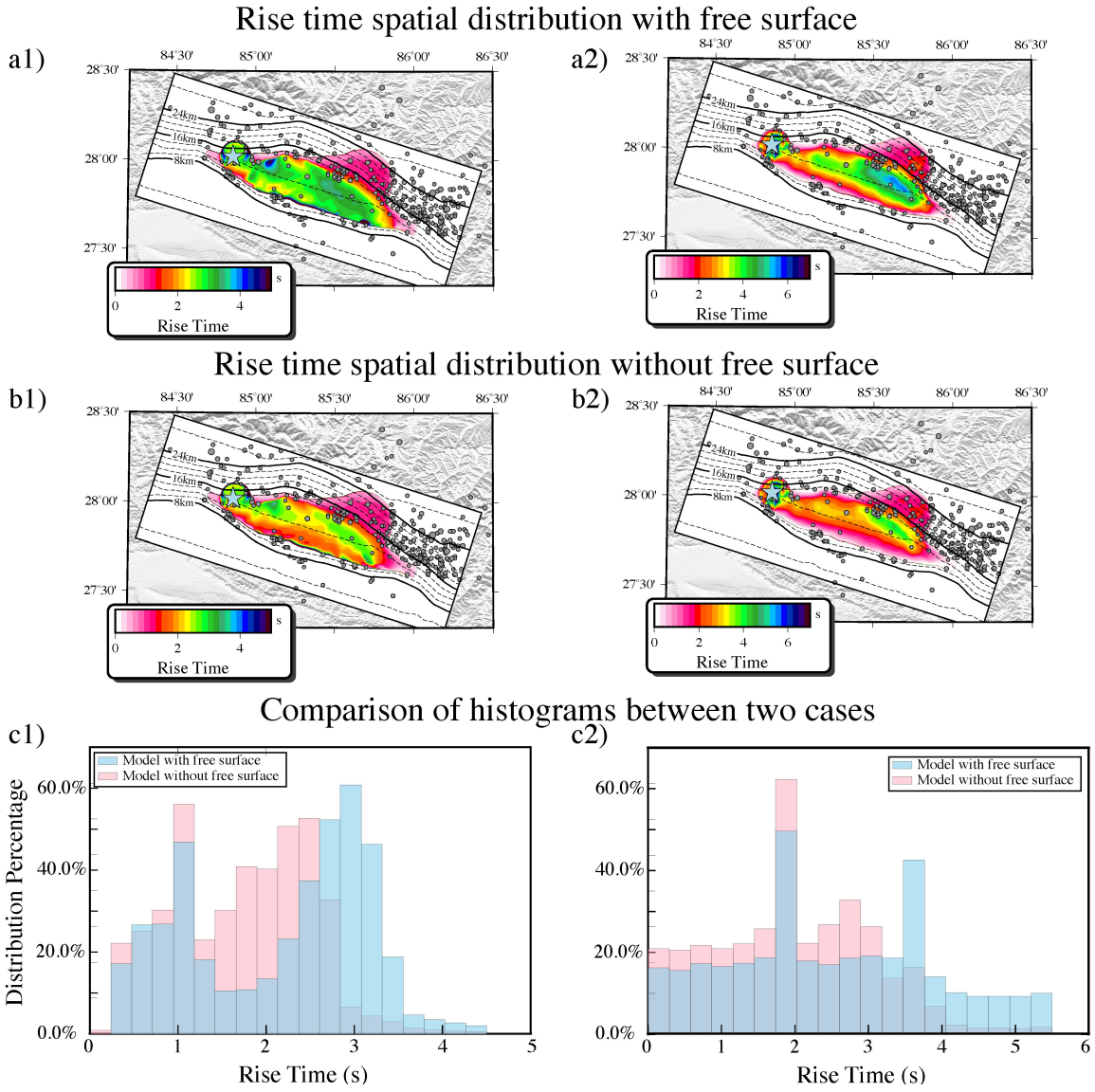

Figure S3.5: Slip rise time distributions from the simulations with and without a free surface, based on Methods 2 and 3 (for comparison with Method 1, shown in Figure 7). Method 2 defines the rise time as the period when the slip is between 5% and 95% of its final value (similar to Guatteri et al. [2004]). (a1) and (b1) show the Method 2 results, with and without a free surface, respectively, and (c1) show the corresponding histograms. Method 3 defines rise time as the duration given by the best-fitting regularized Yoffe function [Tinti et al. 2005] constrained to match both the peak time (the time between onset and peak of slip rate) and final slip of our simulated model.. (a2), (b2) and (c2), show the Method 3 results in the same format used for Method 2.

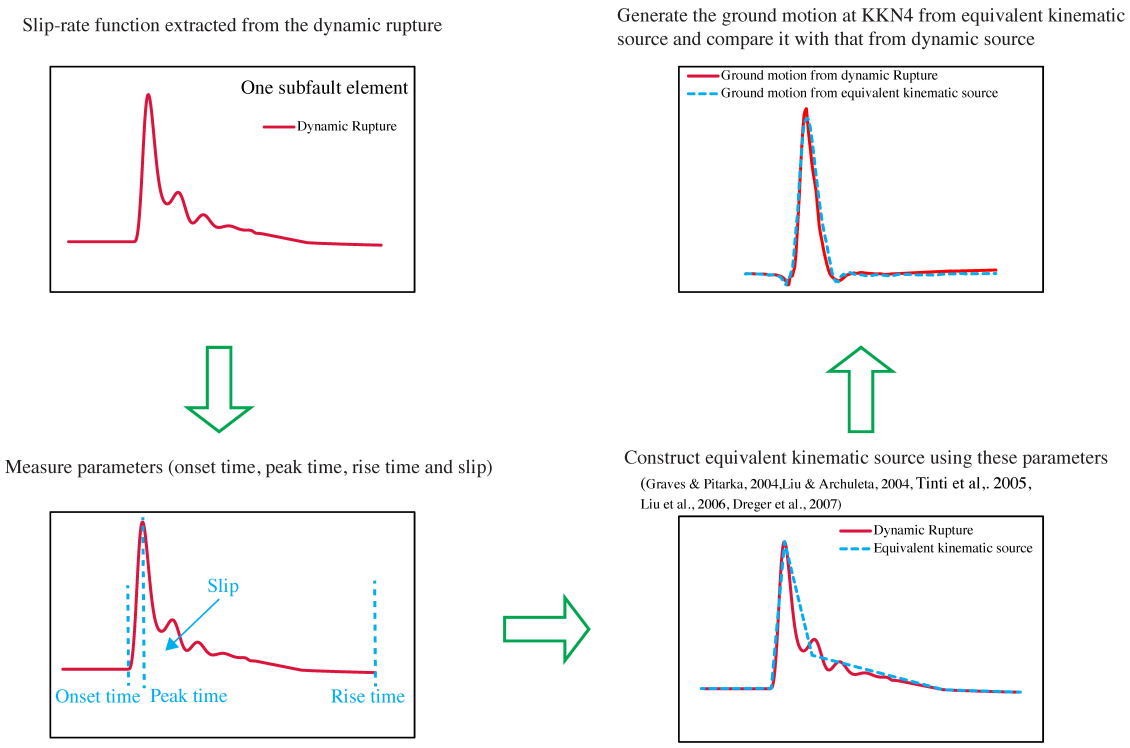

Figure S3.6: A chart of work flow to show how we compare ground motions from the dynamic source and equivalent kinematic sources. Once we obtain the slip-rate functions of our optimal dynamic rupture, we (1) extract these parameters (rupture velocity and the three slip-rate parameters) from our dynamic simulation, (2) construct a range of standard kinematic sources (equivalent kinematic source) that preserve these parameters, and then (3) examine the extent to which the equivalent kinematic sources produce ground motion distinguishable from that of the dynamic model.

Chapter 4

Effects of off-fault inelasticity on near-fault directivity pulses

Near-fault motion is often dominated by long-period, pulse-like particle velocities with fault-normal polarization that, when enhanced by directivity, may strongly excite mid- to high-rise structures. We assess the extent to which plastic yielding may affect amplitude, frequency content, and distance scaling of directivity pulses at points very close to the rupture surface. Dynamic simulations of strike-slip ruptures in 3D reveal significant plasticity effects, and these persist when geometrical fault roughness (with consequent increase in rupture complexity and incoherence) is added to the model. With and without off-fault yielding, these models (scaled to approximately magnitude 7) predict fault-normal pulse behavior similar to that of observed pulses (periods in the range 2-5 second, amplitudes increasing with distance in the forward-directivity direction but approaching a limiting amplitude), but yielding systematically reduces pulse amplitude and increases the dominant period. Yielding causes near-fault ($<\sim$ 2 km) peak ground velocity (PGV) to saturate with respect to increases in both stress drop and epicentral distance, i.e., PGV becomes insensitive to increases in either parameter when that parameter exceeds a threshold (but with the thresholds and the affected distance range dependent on the cohesive strength), and at small

rupture distance, yielding may contribute significantly to the observed magnitude saturation of PGV. The results support the following elements for functional forms in empirical pulse models: (i) a fault-normal distance saturation factor, (ii) a period-dependent and along-strike distance-dependent factor representing directivity, and (iii) an along-strike saturation factor to truncate growth of the directivity factor. In addition to the foregoing effects on long-period fault-normal pulses, the model with off-fault plasticity is very efficient in suppressing the high-frequency fault-parallel acceleration pulses that otherwise develop when local supershear rupture transients occur. The latter result may explain, at least in part, the absence (to date) of an observable Mach wave signature from supershear rupture.

4.1 Introduction

Near-fault ground motions featuring strong pulse-like velocities are of great interest in earthquake seismology and engineering. Pronounced low-frequency, pulse-like fault-normal (FN) ground motions have been widely recorded for earthquakes in strike- (e.g., the 1966 Parkfield, the 1971 San Fernando, the 1992 Landers and the 1994 Northridge earthquakes) and dip-slip (e.g., the 1999 Chi-Chi, the 2009 L'Aquila and the 2016 Meinong earthquakes) fault systems. The engineering effects of near-fault pulse-like ground motions were strikingly exhibited during the 1994 Northridge earthquake in which great structural damage was attributed to large, impulsive ground shaking [Strasser and Bommer 2009] of this type. Such pulse-like ground motions can have high elastic spectral acceleration, imposing a higher demand on building structures than non-pulse-like motions [Hall et al. 1995]. The ground motion models used to perform probabilistic seismic hazard analysis (PSHA) and inform building codes, if they do not fully consider this near-source effect, may underestimate potential seismic hazards.

The high intensity and damage potential of near-fault pulse-like ground motions is a result of the proximity to the fault and directivity effects [Hall et al. 1995; Somerville et al. 1997;

Makris and Black 2004; Mavroeidis et al. 2004; Day et al. 2008, e.g.,], and, as a consequence, they are frequently referred to as directivity pulses. In this context, directivity (or, more precisely, forward directivity) refers to the amplification of ground motion at sites whose direction from the hypocenter is aligned with (i.e., forms a small angle with) the rupture propagation direction. In this paper, we concentrate on near-fault directivity, namely the directivity effects occurring within a horizontal distance of the rupture surface that is less than, roughly, the seismogenic depth ($\sim$20 km). Forward rupture directivity effects occur when 1) the rupture front propagates towards the site, and 2) the direction of slip on the fault is consistent with the site direction [Somerville et al. 1997]. These two conditions are readily met for the fault-normal ground motion component in strike-slip faulting (Figure 4.1, based on Figures 2 and 3 of Somerville, et al. 1997). As depicted in Figure 4.1, radiation patterns of SV and SH waves imply that the dominant motion near the fault will be the fault-normal direction as a result of cumulative SH waves ahead of the propagating rupture. On the other hand, even when those conditions are met for a particular earthquake, the characteristic forward directivity effects are not always observed (e.g., the 2014 South Napa, California earthquake that is a unilateral rupture with a weak directivity effect) probably owing to three-dimensional heterogeneities and incoherent rupture fronts [Gritz 2009; Gallovic 2016]. Note also that, if far-field conditions were pertinent, the predominant frequency of directivity-enhanced seismic energy would be shifted in a manner analogous to the Doppler effect [Douglas et al. 1988], whereas in the near-fault region, especially adjacent to the rupture surface, that simple picture is overwritten by near-field and source-finiteness effects. The result is that so-called directivity pulses are predominantly a low-frequency ($<$ 1 Hz) phenomenon.

There has been substantial effort over the last couple of decades to develop adjustments to empirical ground-motion models (GMMs, also known as ground motion prediction equations (GMPEs)) to capture near-fault directivity effects. Adjustment approaches have been based on fitting empirical ground motion data to simple functional forms [e.g., Somerville et al. 1997] and/or theoretical models (e.g., isochrones theory, [Bernard and Madariaga 1984] that account for

the radiation pattern and general behaviors expected for near-fault seismic waves [e.g., Spudich and Chiou 2008]. These directivity adjustments mostly vary with the azimuthal angle and distance of an observing site to the fault, typically predicting amplifications distributed as a wedge centered along the fault trace, as illustrated in Figure 4.1. Typically, the functional forms in these models include tapers that reduce the predicted directivity effect at smaller magnitude ($M < 6.5$) and larger distance to the fault ($>$30 km), and sometimes assume that the directivity effect is saturated (i.e., ceases to increase) for rupture distances (along-strike) exceeding some threshold [Somerville et al. 1997; Abrahamson 2000; Bozorgnia and Campbell 2004; Donahue et al. 2019]. In this paper, we do not focus on gross azimuthal dependence (forward- and backward-directivity), but instead we concentrate on characterizing pulse-like ground motion within the near-fault forward-directivity zone, within a few km of the rupture surface, using the expressions "directivity pulse" and "near-fault pulse" synonymously. We use numerical simulations to investigate potential variabilities of forward directivity (e.g., spatial taper and saturation) with distance to epicenter (recalling that we restrict consideration to rupture-adjacent sites, so this is essentially the same as rupture distance toward the site), predominant period and source complexity. The results shed some light on physical mechanisms limiting pulse growth, and may prove useful in adjusting functional forms for the representation of pulse-like near-fault effects in empirical models.

Because of the nonlinearity of structural response to high-amplitude ground pulses, reliable analysis of the performance of a target structure requires characteristic constraints on the pulse waveform, particularly estimates of its amplitude and duration [Hall et al. 1995]. The peak ground velocity (sometimes exceeding 1m/s) and dominant period of the pulse are important features of high relevance to ground motion models and building design codes. A typical range of pulse duration in a magnitude range of M_w 5$\sim$8 is 1$\sim$10 s [Baker 2007; Shahi and Baker 2014; Fayjaloun et al. 2017] and expected value of this duration is also magnitude-dependent [Somerville 2003; Baker 2007; Shahi and Baker 2014].

Primary factors affecting the amplitude and shape of the pulse-like ground motions are,

as stated in Scala et al. [2018], the rupture velocity, hypocentral depth and the station location relativity to the fault (if in a framework of dipping fault, whether the station is on the hanging wall or on the footwall is also relevant–but our focus will be on vertical strike-slip faults). If the rupture velocity exceeds the shear wave speed (a supershear rupture), the near-fault ground motion changes character. In that case, the low-frequency fault-normal pulse commonly seen in subshear ruptures is substantially reduced, and the fault-parallel component becomes dominant [e.g., Aagaard and Heaton 2004; Dunham and Bhat 2008; Bizzarri et al. 2010]. Thus, the observation of a dominant fault-normal directivity pulse usually implies a rupture velocity below the local shear wave speed. Waveform modeling indicates that pulse duration is influenced by the average slip rise time [Fayjaloun et al. 2017; Scala et al. 2018]. Small-scale heterogeneity of coseismic frictional stress affects the amplitude and frequency dependence of pulse-like ground motions by weakening the coherence of the rupture front [e.g., Gritz 2009; Gallovic 2016]. Moreover, surface ruptures differ from buried ruptures in their excitation of pulse-like ground motions. For example, Somerville [2003] proposes that, while in both cases fault-normal pulses are recognizable, surface-rupturing earthquakes systematically generate weaker near-fault ground motion in a period range of around 0.3-3 sec than buried earthquakes. In addition, material heterogeneity tends to reduce the pulse period [Withers et al. 2018a], and the presence of a low-rigidity shallow layer can change the rupture front shape and thereby affect pulse shapes [Kaneko and Lapusta 2010].

Off-fault inelasticity (usually in the form of an elastoplastic model) has received considerable attention in model-based studies of rupture. Plastic yielding during rupture redistributes stresses near the rupture front, in turn affecting the subsequent rupture history and associated ground motion. These effects have been modeled in the framework of continuum plasticity (e.g., 3D Drucker-Prager, 2D Mohr-Coulomb, End-cap and Masing type) in recent studies [Andrews 2005; Duan and Day 2008; Dunham et al. 2011a; Shi and Day 2013; Roten et al. 2014; Hirakawa and Ma 2016; Roten et al. 2017b; Wang et al. 2019; Wollherr et al. 2018; Wollherr et al. 2019;

Esmaeilzadeh et al. 2019]. These models suggest that inelastic deformation can not only reduce peak ground motions [Dunham et al. 2011a; Roten et al. 2012; Roten et al. 2017b], but also partially filter out high-frequency radiation [Duan and Day 2008; Ma and Hirakawa 2013]. Moreover, inelasticity may influence the high-frequency attenuation of the acceleration spectra [Shi and Day 2013]. Rupture velocity, to which high-frequency seismic radiation is sensitive [Madariaga 1977], can also be modified due to off-fault plastic yielding, with consequences for the spectral shape of ground motions.

In this work, we explore the effects of off-fault inelasticity on the near-fault directivity pulse, with particular attention to effects on pulse amplitude and duration. Initially, we revisit the wavefield components contributing to directivity pulses and review their dependence on rupture velocity and rise time, using simplified 2D in-plane kinematic ruptures (Section 2). Next, we simulate fully dynamic unilateral rupture on a vertical strike-slip fault, considering depth-dependent pre-stress and rate-and-state friction (Section 3). Then, we compare the synthetic near-fault ground motions that travel through elastic and inelastic off-fault media, characterizing the results in terms of near-fault directivity, peak ground velocity, and dominant pulse period (Section 4). To test the robustness of the inferred effects, we also examine simulations that incorporate fault surface roughness (with accompanying heterogeneous pre-stress) (Section 5).

4.2 2D kinematic rupture model

Before we consider fully dynamic unilateral ruptures, we first examine a simplified 2D in-plane kinematic rupture. The objective is to elucidate the relationship between near-fault directivity pulses and on-fault slip in a simplified context (e.g., without free surface interactions, and without dynamic spontaneous varying rupture velocities, rise times, and slip velocities) supplementing similar kinematic analyses [e.g., Haskell 1969; Boore et al. 1971; Boore and Zoback 1974; Boatwright and Boore 1975]. For each subfault element, our slip velocity function

is a Brune source time function given by Equation 4.1

$$S(t) = (\frac{\pi}{\tau})^2 t \; exp(-\frac{\pi}{\tau}t)H(t), \tag{4.1}$$

where t is time, $H(t)$ is the Heaviside step function and τ controls the rise time of the slip rate function (representative slip velocity functions are illustrated by green solid lines in Figure 4.2). We generate a kinematic steady-state rupture pulse in which rise time and static slip are constant along the strike except for tapering at the ends of the line fault (to reduce strong stopping phases in near-fault ground motions), as shown in Figure 4.2. The model parameters and discretization of these 2D kinematic ruptures (e.g., domain size, bulk properties, and space/time step) are listed in Table SS4.1. By varying the rupture velocity and rise time, we construct in total 5 scenarios to illustrate how on-fault rupture behaviors modify the near-fault directivity pulse. For Cases 1 to 3, velocities and rise times are fixed along the strike (Figure 4.2a), while Cases 4 and 5 have rupture velocities that are linearly increasing and decreasing functions of distance from the hypocenter, respectively (Table SS4.2 and Figure 4.2b).

As seen in Figure 4.3a, a representative fault-normal wavefield (generated from Case 1) forms a broad pulse accompanying the rightward propagating rupture. This positive-phase pulse (for the right-lateral slip case) is shown in red, denoting motion directed away from the fault. The pulse is bounded by two negative-phase (blue) regions. The fault-normal ground velocities 3km from the fault and 40 km along strike from the hypocenter (dark red triangle in Figure 4.3a) are vertically aligned and plotted in Figure 4.3b. Beginning with the hypocentral P wave arrival (denoted by a blue dashed line in Figure 4.3b), the fault-normal components are negative, and grow in amplitude until the arrival of the hypocentral S wave (denoted by a red dashed line). The long-period negative motions between hypocentral P and S waves come from the near- and intermediate-field terms of the P wave [e.g., Aki and Richards 2002]. Similar near- and intermediate-field terms are seen in the TTRH02 record of the 2000 Tottori earthquake (see

Figure 6 of [2011b]). The directivity pulses begin with the hypocentral S wave and end with smooth decaying phases that are associated with arresting of earlier ruptures [Boore and Zoback 1974].

The directivity pulse is sensitive to the rupture velocity and rise time (Figure 4.3b). By comparing the time histories of Case 1 and Case 2, we see that the faster rupture velocity (Case 2) narrows the fault-normal pulse and both amplifies its peak and shifts it to the left (nearer the S arrival time). The shorter rise time in Case 3 leads to near trapezoid-shaped pulse. In Cases 4 and 5, increasing (decreasing) rupture velocity focuses (defocuses) the later peak, because that final peak is associated with very local rupture behavior (e.g., rupture velocity and rise time) as rupture passes by the station. In general, then, the first increment after the hypocentral S wave arrival time results from cumulative S waves arriving from preceding rupture, and the latter part of the pulse is mainly sensitive to the passage of rupture (highlighted by the dashed circles in Figure 4.3b). In the aforementioned scenarios in which stations are not far from the hypocenter, the total duration of the pulse is related to the overall preceding rupture time. Considering an extreme case (Figure SS4.1) in which a rupture unilaterally propagates along a 200-km long fault (other parameters remain the same as in Case 1), for a station at large (120 km) along-strike distance (but still adjacent to the rupture), the directivity pulse splits into two pulses: a small one arriving with hypocentral S wave and a later large one related to the passage of rupture. To sum up, in the simplified 2D cases, within modest along-strike hypocentral distances, rupture acts to form a fault-normal pulse whose amplitude, duration and shape are cumulatively controlled by the preceding rupture velocity and rise time (and preceding slip distribution, which we neglect for the sake of simplicity in this section).

Figure 4.3c shows 13 stations at varying hypocentral distance but fixed distance of 3 km from the fault (hypocentral distance is color coded, with purple curves for the station closest to the hypocenter, ranging to red at the largest distance). We compute fault-normal velocities and fault-normal pseudospectral velocities (PSV) (5% damping). As seen in Figure 4.3c, durations

of directivity pulse and fault-normal PSV of all 5 models are broadened and intensified over the long-period band (period >8 s) with increasing distance from the hypocenter. This resembles the prediction of directivity effects in ground-motion models [e.g., Bayless and Somerville 2013; Chiou and Spudich 2013; Shahi and Baker 2013; Spudich and Chiou 2013] as seen in background color of Figure 4.1, in which amplification is increased with the epicentral distance at small angles between the receiver direction and the rupture propagation direction.

However, in the intermediate- and high-frequency band, the distance effect departs, to varying degrees, from the simplified, monotonically increasing directivity model. In Case 1 with a constant rupture velocity of 0.8 times the S wave speed, the apparent durations (represented by the period at peak PSV) of fault-normal pulses increase from 2 to 6 s and their peak PSVs vary from about 1 to 2 m/s. However, in that 2-6 second period range, the PSV is not necessarily monotonically intensified with distance (purple being the nearest and red the furthest station), as typically assumed in directivity adjustments to ground-motion models; the Case 1 simulation is only consistent with the latter simplified picture at periods exceeding 6 s, and the amplifications at shorter period are rather complicated. Somerville [2003] introduced the concept of "narrowband directivity", in which the spectral period of peak directivity amplification scales with earthquake magnitude. As we show in Figure 3, spectral period of peak PSV (at points very near the rupture surface) additionally scales with epicentral distance because the overall duration of a fault-normal pulse is roughly confined by the hypocentral S wave and the rupture passing by the observer. This scaling, even in the very simplified 2D steady-state slip-pulse scenario, introduces additional complexity in peak PSVs, such that the maximal peak PSV may occur within the span of the rupture rather than at maximal along-fault distance. While it is inconsistent with current directivity amplification adjustment models, as stated in Spudich et al. [2014], large ground motion records such as the Lucerne record of the Landers earthquake, are observed within the ends of the causative fault. Spudich and Chiou [2008] explain this phenomenon using isochrone synthetics, which inherently includes the scaling of peak period with epicentral distance, leading

to a complex pattern of peak PSV.

A faster rupture velocity (0.9 S wave speed, close to the terminal velocity of an inplane rupture), as seen in Case 2, further contracts ground pulses and leads to a narrower range of pulse durations, from 4 to 2 s. In this case, the range of monotonically amplified directivity effects with epicentral distance is extended downward to 2 s, which is consistent with the common observation that directivity is apparent at periods longer than 1s. While a shorter rise time, as seen in Case 3, does not much vary the range of pulse durations compared to Case 1, the trend of peak PSV from 2 to 6 s becomes complex, with the maximum peak PSV somewhere in the middle-distance range (due to the shorter rise time, the peak PSVs in Case 3 in the range of 2-4 s are intensified compared to those in Case 1). In even more complicated Cases 4 and 5, the long-period directivity effects are observed as expected but the lowest period at which amplification with distance is monotonic goes up to 8 s. In short, in the period band of primary engineering interest (up to, say, $\sim$5 s), the directivity predictions of the simple rupture models are very complex relative to the monotonic distance-amplification at longer period.

In a 3D strike-slip framework, especially in the presence of a free surface that accommodates surface waves (e.g., Rayleigh waves) and surface-reflected secondary ruptures, the composition of the directivity pulse becomes more complex. Moreover, due to the sensitivity to rupture velocity and rise time illustrated in the foregoing simulations, the directivity pulse is likely to be affected by the spontaneity of the earthquake rupture. In subsequent sections, we will explore how the directivity pulse is shaped by a 3D spontaneous rupture, emphasizing how the pulse may be further modified by off-fault plastic yielding.

4.3 Model setup of 3D spontaneous rupture

Building on understanding gained from the simplified 2D kinematic rupture models (and previous studies), we model 3D spontaneous dynamic rupture scenarios on a vertical right-lateral

strike-slip fault embedded into elastic and elastoplastic half-space media (Figure 4.4a). We retain the previous model setups the dimensions, elastic parameters and discretization. Table 4.1 and Figures 4.4b-e describe the elastic/plastic bulk properties, initial stress tensor, and frictional parameters. The parameters of the plasticity model are such that the rupture behaviors, seismic moment and static stress drop in elastic and elastoplastic scenarios are very similar, simplifying the interpretation of the results.

The off-fault inelasticity follows the Drucker-Prager elastoplastic model [Drucker and Prager 1952] that contains a pressure-dependent yield surface, the parameters of which are listed in Table 4.1. Elastoplastic simulations are subject to contamination by both spurious high-frequency oscillations and inaccuracies due to strain localization. To control these artifacts, as suggested in Duan and Day [2008], we implement two schemes of numerical regularization in our computations: one is to introduce artificial Kelvin-Voigt viscosity η in the media [Day and Ely 2002]; the other is to add Maxwellian viscoplasticity that introduces a relaxation time T_v to the adjustment of stress to the yield surface [Andrews 2005] A value of $0.1\Delta t$ times the shear modulus for the former viscosity [Day et al. 2005; Dalguer and Day 2007] and $\Delta x/\beta$ for the characteristic time scale of the latter viscosity [Andrews 2005; Duan and Day 2008] have been found effective in reducing high-frequency noise, and those values are adopted here (Table 4.1). Other regularization schemes [e.g., Dunham et al. 2011a; Hirakawa and Ma 2016] have been similarly introduced to effectively stabilize solutions in elastoplastic models.

As seen in Figure 4.4b, the initial effective normal stress is given by $\overline{\sigma} = min(3 + (\rho - \rho_w)gZ, 80)$ MPa, where Z is a depth in kilometers. That is, effective normal stress increases with depth at a rate given by the excess of lithostatic pressure over hydrostatic pore pressure, to a depth of 4.7 km, below which it is constant, reflecting an assumption that fluid overpressure compensates continued lithostatic pressure increase with depth [Rice 1992]. The ratio between shear stress and effective normal stress is illustrated in Figure 4.4c.

The fault constitutive relation is regularized rate-and-state friction with a strong rate-

weakening feature [e.g., Lapusta et al. 2000; Dunham et al. 2011a; Shi and Day 2013; Wang and Day 2017]. As shown in Figure 4.4d and 4.4e, we add a shallow velocity-strengthening ($a-b>0$) layer with a slightly larger weakened velocity V_w. This feature is important in that its effect is to prevent (or minimize) supershear rupture propagation near the free surface [e.g., Aagaard et al. 2001; Day et al. 2008; Kaneko et al. 2008; Kaneko and Lapusta 2010], and physically justified, in that the presence of a shallow velocity-strengthening layer has support from laboratory experiments [e.g., Marone 1998] and observational findings of interseismic shallow creep [e.g., Lindsey et al. 2014], afterslip of large earthquakes [e.g., Marone et al. 1991; Perfettini and Avouac 2007], and the seismicity deficit[e.g., Shearer et al. 2005].

We numerically solve the 3D elastoplastic spontaneous rupture propagation problem with the Support Operator Rupture Dynamics (SORD) code [Ely et al. 2008; Ely et al. 2009]. This generalized finite-difference method has been used in numerous studies of spontaneous dynamic rupture simulation and strong ground motions [Ely et al. 2010; Ben-Zion et al. 2012; Shi and Day 2013; Song et al. 2013; Baumann and Dalguer 2014; Song 2015; Vyas et al. 2016; Mai et al. 2017; Passone and Mai 2017; Song and Dalguer 2017; Wang and Day 2017; Vyas et al. 2018; Wang et al. 2019]. The code used here has been verified through tens of elastic and elastoplastic benchmarks in the Southern California Earthquake Center/United States Geological Survey dynamics earthquake rupture code validation exercise [Harris et al. 2009; Harris et al. 2018]. Guided by results in Day et al. [2005], we estimate that the discretization interval employed here (50 m) provides accurate waveform solutions for frequencies up to roughly 7 Hz. The computations were performed on MIRA at the Argonne Leadership Computing Facility (Argonne National Laboratory).

4.4 Results of a 3D spontaneous dynamic rupture on a planar fault

In this section, we examine some effects of off-fault nonlinearity on the rupture process and near-fault ground motion pulses. The elastic and inelastic cases compared here have very similar seismic moments ($7.3 \times 10^{19} Nm$ (M_w 7.21) and $6.7 \times 10^{19} Nm$ (M_w 7.19), respectively) and stress drops (5.23 MPa and 5.15 MPa, respectively). Rupture histories are similar in the two cases, except that the plastic case has a somewhat lower overall rupture speed. Figure 4.5 illustrates a typical example of the contrasting depth profiles (averaged along strike) of coseismic slip with and without off-fault nonlinearity (Figure 4.5a). There is a systematic decrease in slip for the plastic case in the upper $\sim$3 km, perhaps related to the geodetically observed phenomenon of shallow slip deficit [e.g., Simons et al. 2002; Fialko et al. 2005]. Shallow slip in both models is affected by the velocity-strengthening layer that accommodates afterslip or fault creep over an interseismic period [Marone et al. 1991; Rice 1993], but an extra deficit is accounted for by shallow off-fault inelastic deformation, as also suggested by earlier dynamic rupture propagation models [e.g., Ma 2008; Kaneko and Fialko 2011; Roten et al. 2017a].

In Figure 4.5b, we illustrate rupture behaviors in the form of space-time plots of slip velocity at the free surface. As in Kaneko and Lapusta [2010], there is a weaker slip pulse preceding the main rupture front that becomes recognizable on a logarithmic scale. It is smaller in amplitude ($\sim$ 0.1 m/s) than the dominant main rupture front ($\sim$1 m/s), and it is supershear (i.e., travels faster than the S wave, as indicated by the occurrence of this pulse prior to the white dashed line in Figure 4.5b). In contrast, velocities of the main rupture fronts in both elastic and plastic cases are slower than the Rayleigh wave speed (white dotted lines), with the plastic case slightly slower than the elastic case [e.g., Andrews 2005]. Moreover, plastic yielding suppresses a very narrow, low-amplitude slip pulse that, in the elastic case, emerges between the initial supershear slip pulse and the main rupture front (thin red streak just above the white dotted line in

Figure 4.5b1). The green dashed lines encircle another brief supershear rupture episode occurring in both elastic and plastic cases. That transient supershear phase is related to rupture reflection at free surface, and under certain conditions it may develop into a persistent supershear rupture front, as in Kaneko and Lapusta [2010].

Figure 4.5b also shows that the initial supershear pulse heals precisely when the hypocentral S wave arrives. This healing is a result of the "forbidden regime" of rupture velocity, enhanced by stress conditions near the free surface. Rupture velocity in the range between Rayleigh and shear wave speed is not possible for Mode II cracks [Broberg 1996; Broberg 1999] because in this regime the energy flux into the rupture front is negative (i.e., such a rupture would not absorb elastic strain energy but create it [Das 2015]). There is thus a stress shadow (Figure SS4.2) initiated by the S wave, strengthened and complicated near the free surface (Figure SS4.2d) as similarly seen in Fig 5b of Kaneko and Lapusta [2010]. Also as pointed out in Kaneko and Lapusta [2010], a transition from SV wave to P wave boosts the shear stress (Figure SS4.2) leading to a supershear slip pulse (more details are in Text S4.1 and Figure SS4.2).

Figure 4.6 compares fault-parallel and fault-normal ground velocities for elastic and plastic cases. A relatively strong fault-normal directivity pulse is present (Figure 4.6a3, 4.6a4, 4.6b3 and 4.6b4) in both elastic and plastic cases. The directivity pulse is bounded by a preceding near-field P wave and a trailing rupture-arrest phase as suggested by the 2D kinematic simulations in Section 3. The shapes of the directivity pulses are very similar in both cases. In Fourier amplitude spectra (FAS) and 5%-damping pseudospectral velocity (PSV), low frequencies show an enhanced directivity pattern in the form of progressive amplitude increase along the rupture direction (Figure 4.6c3, 4.6c4, 4.6d3 and 4.6d4). This pattern applies to both elastic and plastic cases, and is, again, in qualitative agreement with the 2D kinematic ruptures. The elastic pulse durations increase with the distance away from the epicenter, in the range of 2 to 5 s (quantified, as before, by the period of maximal PSV). For comparison, an empirical relationship [Baker 2007; Shahi and Baker 2014] based on regression analysis predicts a pulse duration of about 5 s for an

earthquake with a magnitude of 7.2, consistent with our calculations. Peak PSV at the most distant station in the forward-directivity direction shows a nearly 20% reduction when plastic yielding is introduced (and, in contrast, the peak PSV at the leftmost station is essentially unchanged). That is, the amplification of fault-normal velocity pulses induced by directivity is weakened due to plasticity. This can be understood by reference to the spatial distribution of accumulated plastic strain magnitude (Figure SS4.3), an effect that might also be approximated by introducing a gradually increasing critical slip distance D_c with distance to the epicenter [Andrews 2005]. In addition, the plastic-case pulse widths become wider (Figure 4.6b4 and 4.6d4), mainly because plasticity lowers the overall rupture velocity, to which pulse duration is sensitive (as suggested in 2D kinematic simulations Case 1 and 2 in Section 2).

On the other hand, near-fault fault-parallel velocities do not contain low-frequency pulses comparable to those of fault-normal components, and show little if any along-strike enhancement. In Figure 4.6a1 and 4.6b1 of the elastic case, a strong, high-frequency fault-parallel velocity (a Rayleigh wave) is very clearly seen trailing the rupture front, and we associate this feature with the transient supershear rupture induced by free surface interactions near the epicenter (indicated by dashed green oval in Figure 4.5b). Such high-frequency Rayleigh waves related to the transient supershear near the point where the rupture hits the free surface are similarly reported in other models of predominantly subshear rupture (e.g., Figure 4 of Bizzarri et al. [2010]). However, in the plastic case, this high-frequency phase is strongly attenuated (Figure 4.6a2 and 4.6b2), such that the high-frequency fault-parallel velocity field decays very sharply with a distance from the epicenter, as shown in the FAS plots of Figure 4.6c2. Plastic response also strongly attenuates fault-parallel short-period PSV (see Figure 4.6d2, showing $\sim 80\%$ reduction at a period of 0.5 s, relative to elastic case in Figure 4.6d1). Thus, due to the existence of off-fault plasticity, high-frequency Mach S and Rayleigh waves induced by a localized supershear rupture are subject to very strong absorption by near-fault non-linearity. This effect is likely to inhibit the occurrence of observable Mach waves from shallow, transient supershear ruptures of this sort.

Figure 4.7 compares ground motions (acceleration and velocity) for the elastic and plastic cases 40 km from the epicenter (rightmost triangle in figure 4.6a1), which is the station located in the region of maximum plastic strain. In Figure 4.7a and 4.7b, the fault-normal accelerations and velocities (solid curves) in the two cases are very similar in timing of the near-field P wave, hypocentral S wave and S wave radiated during rupture toward the site, reflecting the similarity in rupture histories noted earlier. The large troughs in fault-normal accelerations and peaks of fault-normal velocities ($\sim$ 14s) show characteristic effects of plasticity, with, in the plastic case, a reduction of peak velocity due to non-linear deformation of the surrounding medium and an increased pulse width due to an overall slower rupture velocity (Figure 4.5b). The pulse broadening for the plastic case agrees with the behavior suggested by the rupture-velocity dependence in the 2D kinematic rupture simulations presented earlier. As already noted, off-fault non-linearity greatly attenuates the high-frequency Rayleigh wave peaks in the fault-parallel acceleration (compare blue and orange dashed curves in Figure 4.7a), resulting in a fault-normal pseudospectral acceleration (PSA, orange solid line in Figure 4.7b) that is systematically larger than the fault-parallel PSA (orange dashed line). This predominance of the fault-normal component in the plastic case is consistent with recordings containing directivity pulses [e.g., Somerville et al. 1997; Day et al. 2008]. In contrast, the elastic case has larger fault-parallel (blue dashed line) than fault-normal (blue solid line) PSA at a short period, which is disfavored by observations. The PSA and PSV (Figure 4.7b and 4.7d) are reduced by the off-fault plasticity over a broad period range.

Figure 4.8 shows the spatial pattern of plasticity effects on the fault-normal directivity pulse. Figure 4.8a illustrates the distribution of peak horizontal velocity (PGV) of the elastic and plastic cases, along with the fractional reduction of PGV due to plasticity. Both cases have spatial distribution of PGV that is roughly wedge-shaped, reflecting forward directivity effects, but in the plastic case PGV is systematically lowered (Figure 4.8a3). The largest reduction ratios, sometimes exceeding 50%, are concentrated near the fault trace [Roten et al. 2014; Withers et al. 2018b].

We quantify pulse durations, by the method of Shahi and Baker [2014], and these durations are plotted in Figure 4.8b. The pulse-period predictions resemble those from the simplified equation (the prediction of pulse period scales with along-strike and normal-to-fault distance) proposed by Fayjaloun et al. [2017] (see their Figure 8), which in turn was shown by Fayjaloun et al [2017] to agree with kinematic rupture simulations. The exceptionally short pulses concentrated from 5 to 20 km away from the epicenter are related to the aforementioned transient supershear associated with free-surface reflection of the main rupture front. The off-fault plasticity extends pulse widths by an average of about 30% near the fault trace, and by up to 100% in a very localized region affected by the transient supershear rupture. As was the case for amplitudes, the pulse-duration effects of the supershear transient are also much diminished by plastic yielding.

Seismic hazard analyses are typically performed for the RotD50 orientation-independent measure of horizontal pseudospectral acceleration introduced by Boore et al. [2006]. RotD50 is a median value of a set of geometric means computed from the as-recorded orthogonal horizontal motions rotated though all period-dependent non-redundant rotation angles, which is adopted in the ground-motion models of Enhancement of Next Generation Attenuation Relationships for Western US (NGA-West2) [Bozorgnia et al. 2014]. We therefore examine the effects of off-fault plasticity on this ground-motion measure (for periods 0.5 s, 1.8 s and 4.8 s). A principal goal is to provide improved (relative to elastodynamic analyses) guidance for the construction of functional forms for representing the spatial distribution of pulse amplitude and duration. As shown in Figure 4.9a, in the elastic case, at short and intermediate period, amplification of RotD50 in the forward-directivity region is mainly concentrated along the fault trace, while long-period amplification follows the classic wedge-shaped directivity models (see Figure 4.1 and Donahue et al. [2019]) whereby near-fault amplification increases with epicentral distance (for sites adjacent to the coseismic faulting segment). The simulated amplification in the forward-directivity region supports the feature of the Somerville et al. [1997]'s empirical model that the directivity slope (rate of amplitude increase with propagation distance toward site) is greater at long period than

at short period. In Figure 4.9b, off-fault plasticity essentially attenuates short- and intermediate-period amplifications of RotD50 concentrated near the fault trace, and saturates the long-period amplification, in the sense that it truncates the expansion of the wedge-shaped amplification contours for epicentral distances exceeding 20 km. That saturation effect is consistent with a similar truncation in the empirical directivity model proposed by [Abrahamson 2000].

The foregoing results demonstrate that off-fault plasticity can reduce the amplitude and broaden the widths of the directivity pulse weakening the tendency for amplification to increase with propagation distance in the forward-directivity region (i.e., promoting the along-strike saturation of directivity suggested by, e.g., the model of Abrahamson, 2000). However, interpretation of the effects shown in Figure 4.8 and 4.9 is complicated by the fact that yielding affects ground motion directly by limiting shear stress levels at the rupture front, and indirectly, by (usually) reducing the average rupture velocity. To obtain further insight into the effect of plasticity, we isolate former effect by artificially fixing the rupture velocity through a simplified friction model, but without change to any other model or numerical-implementation parameters, (e.g., fault dimension, initial stress and discretization). The friction adopted here is employed by Dunham and Bhat [2008]. The shear strength, τ_s, weakens linearly with distance within a cohesive zone:

$$\tau_s(x,t) = max\{\tau_r, \tau_r + A(\mid x \mid - v_r t)\} \tag{4.2}$$

where τ_r is dynamic friction (equals to $-\mu_r \sigma_n$, dynamic frictional coefficient times normal stress), is the forced rupture velocity (we set 0.9 shear wave speed), A is weakening rate (chosen to ensure at least 5 mesh points within resulting cohesive zone), x is a spatial distance and t is time. The fault is locked until stress reaches the fault strength (computed by Equation 4.2) and stress remains constant after fully weakening. By modifying , we can prescribe the static stress drops (here we neglect overshooting caused by stopping phases). We select 3 values of stress drop:

1.6 MPa, 3.2 MPa and 6.4MPa, and implement them in both elastic and plastic media (Figure 4.10a). Thus, in total, 6 cases are simulated and their PGVs along 3 lines normal to the fault trace (located at 15 km, 30 km and 45 km along-strike distance from the epicenter, respectively) are illustrated in Figures 4.10b1 to 4.10b3, on a logarithm scale. As seen in Figure 4.10b, plasticity induces a saturation of the growth of PGV with respect to fault distance, along-strike distance, and stress drop. Within 1 km of the fault trace, plasticity essentially eliminates the growth of PGV with along-strike distance beyond Line 1 (at 15 km), and greatly reduces its stress-drop dependence (which was linear in the elastic case). The maximum near-fault PGV is thereby capped at 2 m/s (reduction by up to a factor of $\sim$3 at some sites, relative to the corresponding elastic model) despite the stress drop and magnitude having been changed from 1.6 MPa and M_w 6.9 to 6.3 MPa and M_w 7.3, respectively.

Empirical data suggest that near-fault peak ground velocity (PGV) saturates as a function of magnitude for large magnitude earthquakes [Boore and Atkinson 2008] and the largest observed PGVs from strike-slip earthquakes are below 2 m/s. Previous suggested explanations are centered on finite fault effects [Schmedes and Archuleta 2008; Baltay and Hanks 2014]. This is consistent with our models for off-fault distance greater than 1-2 km. However, in our models, plastic yielding appears to impose a stronger limit on PGV at closer distance. Ground motion intensities (e.g., PGV), which are often extrapolated from a farther ground motion prediction equation due to near-fault sparseness of data, can be overestimated if the near-fault plasticity limit is neglected. Thus, in addition to a finite-fault effect dominating in an intermediate-distance range (1-10 km), physics-based plasticity is alternatively responsible for the observed magnitude saturation in the near-fault range ($\sim$1-2 km). While it is suggestive that the limiting value of 2 m/s seen in Figure 4.10 roughly coincides with the largest strike-slip PGVs recorded to date, the result is sensitive to our chosen cohesion model and influenced by the absence of complexities in geometry and material properties. For example, Roten et al. [2017b] performed elastoplastic simulations with a range of cohesion and elastic-properties models and found similar near-fault saturation due to

plasticity, but with occasional exceedances of 2 m/s PGV in some models (albeit only at a small fraction of sites and for magnitude exceeding $\sim$7.5).

4.5 Results of a 3D spontaneous dynamic rupture on a rough fault

The foregoing models are smooth, both in the geometry of the fault surface and the propagation of rupture. Since near-field pulses reflect interference of arrivals associated with rupture finiteness, it is appropriate to investigate the extent to which the effects of plasticity noted in the previous section persist when these simplifications are relaxed. In this section, we do so by introducing a rough fault surface. Natural faults manifest varying degrees of geometrical complexities spanning from large-scale branching and segmentation [e.g., Ben-Zion and Sammis 2003] to small-scale variations on the fault surface [e.g., Power and Tullis 1991; Renard et al. 2006; Candela et al. 2009; Sagy and Brodsky 2009]. Recent studies show that geometrical variations of the fault surface lead to ensembles of complex rupture with varying directionalities and magnitudes [e.g., Fang and Dunham 2013], modifying the radiated seismic spectrum and radiation pattern. In particular, those complexities boost high-frequency ground motions [Dunham et al. 2011b], bringing them into general accord with the aggregated statistics of recorded motions, as reflected in ground-motion prediction equations[e.g., Shi and Day 2013; Kieling et al. 2014; Withers et al. 2018a]. The previous rough-fault modeling studies have not focused on the dynamics of low-frequency pulses, nor on the degree to which those pulses are sensitive to off-fault plasticity.

We specify fault roughness using an approach closely following Shi and Day [2013]. The fault roughness model (Figure 4.11a) follows a self-similar (Hurst exponent 1) fractal distribution up to a wavelength cutoff of 200 m. The distribution of deflection distances from a plane is

generated in the wavenumber domain (as in Andrews and Barall, [2011]) and, after transformation to the spatial domain, the amplitudes of the perturbations are scaled by a specified amplitude-to-wavelength ratio α defined as $\alpha = h_{rms}/L$, where L is the total length of the fault in the along-strike direction and h_{rms} is the root-mean-square roughness of the 2-D perturbation profile (more details to see Appendix A of Shi and Day, 2013). Power and Tullis [1991] estimate in a range from 10^{-3} to 10^{-2} for natural faults. We select an intermediate roughness, $\alpha = 10^{-2.3} \approx 0.005$ in subsequent analysis. Apart from fault geometry, we keep the rest of the model inputs (including elastic and plastic parameters) identical to those of the planar fault scenario of the last section. Comparison of the elastic and plastic cases is facilitated by the similarity of the resultant seismic moments and stress drops in the two cases: moments of $5.0 \times 10^{19} Nm$ (M_w 7.10) and $4.5 \times 10^{19} Nm$ (M_w 7.1), respectively, and static stress drops of 5.33 MPa and 5.32 MPa, respectively (see also Figure SS4.4, comparing average static slip and ground-surface slip velocity). Comparison of Figure SS4.4 with Figure 4.5 for the planar fault scenario shows some of the complexities introduced by fault roughness, including transient supershear ruptures between the first supershear pulse and the main, sub-Rayleigh rupture front (especially between about 20 to 40 km along-strike distance). The off-fault plasticity leads to 1) smaller average slip at shallow depth (Figure SS4.4a), and 2) a weakened SV-to-P conversion (Figure SS4.4b2), both of which are consistent with the plasticity effects in the planar-fault scenario.

Figure 4.11 shows simulated ground velocities, Fourier amplitude spectra and pseudospectral velocities for the same station set used in Figure 4.6. Fault-parallel and fault-normal ground velocities (Figure 4.11b and 4.11c) are more complex than in the planar-fault case (Figure 4.6) but the fault-normal velocities still show the long-period pulse-like character, in both elastic and plastic cases. Pulse duration scales with epicentral distance as in the planar fault case (Figure 4.11(cde)3, 4.11(cde)4, compared with the corresponding panels in Figure 4.6). The effects of plasticity noted earlier for the planar fault case persist in the rough-fault case. These including the strong nonlinear damping of high-frequency Rayleigh waves associated with supershear rupture

episodes, especially on the fault-parallel component (Figure 4.11b1 and 4.11b2); broadening of fault-normal pulse widths; and weakening of directivity-enhanced amplifications (Figure 4.11e3 and 4.11e4). In contrast, for the rough fault case, near-fault high-frequency motion does not diminish with epicentral distance as it does in the planar fault case. This feature is especially clear in the plastic case (compare Figure 4.11d2 and 4.11d4 and Figure 4.6c2 and 4.6c4). Roughness systematically strengthens high-frequency seismic energy (both fault-parallel and fault-normal components in Figure 4.11d and 4.11e), compensating losses caused by plasticity. Nonlinear losses decrease the peak fault-normal PSV at the largest along-strike distance (dark red line) by nearly 40% (from 1.1 m/s to 0.7 m/s) while increasing the period corresponding to the peak PSV from 5 to 6 s (Figure 4.11e3 and 4.11e4). The near-fault normal-component pulses are particularly susceptible to this type of nonlinear loss, but we would expect similar nonlinear damping for ground motion whenever comparably high shear-strain levels are reached. For example, comparable amplitude reductions of long-period ground motions due to plasticity were found by Roten et al. [2014], who found up to 70% reductions in Los Angeles Basin for computer simulation of large ($M > 7.8$) southern San Andreas Fault earthquakes.

Figure 4.12 shows ground motions (acceleration and velocity) for the elastic and plastic cases at the rightmost (farthest along-strike distance) station, for comparison with corresponding planar-fault results in Figure 4.7. Ground accelerations are far more complex than in the planar-fault case, but the main effects of plasticity are similar: strong nonlinear damping of peak ground acceleration (associated with the supershear phase) and a reduction of the peak fault-normal velocity combined with an increased pulse width. Figures 4.12b and 4.12d again show the predominance of the fault-normal component over fault-parallel, for both PSA and PSV and in both elastic and plastic cases. Plasticity has a larger effect on the fault-normal component than the fault-parallel component, reflecting the larger strains accompanying the former (apart from the high-strain supershear phase of the latter). In Figure 4.12d, plasticity lowers the peak of fault-normal pulse by 30% and stretches the pulse width from 5 to 6 s, while selectively

attenuating some frequency bands of ground motion (periods shorter than 1 s and longer than 3 s). The strong, short-period impulse in the fault-parallel component is largely absorbed by off-fault plasticity (just as it was in the flat-fault case), as seen in Figures 4.12a and 4.12b. It displays a second characteristic time scale related to the localized rupture time history (e.g., the secondary pulses starting at around 13 second and 15 second). This time scale associated with rupture passage stands out more distinctly in the rough fault simulation than in the planar case (Figure 4.7d). This difference occurs because, in the rough-fault case, the reduced coherence of the accumulated SH arrivals from the full length of the irregular fault weakens their contribution compared with that of the localized slip pulse near the station.

Figure 4.12e and 4.12f compares The TTRH02 (borehole) fault-normal velocity in the 2000 Tottori earthquake and our simulated fault-normal velocity pulses in elastic and plastic case at a similar epicentral ($\sim$ 7km) and off-fault distance ($\sim$ 2km). At this distance, plasticity effects are small, and both simulations follow the recorded velocity closely with respect to the timing of arrivals, and even their shapes (apart from the high simulated amplitude at the S wave onset, perhaps related to the artificial rupture initiation). These arrivals include the prominent near-field P wave, the hypocentral S wave, and the pulse termination associated with healing following rupture passage, and result is close agreement with the recorded pulse duration at this distance. The simulated pulse at 40 km distance has longer duration, reflecting the correlation of duration with distance noted before, and at this distance there is also about a 1-second duration difference, again illustrating a plasticity effect on pulse duration that is cumulative with propagation distance and that becomes pronounced at a large epicentral distance (for, we emphasize again, our restricted focus on sites adjacent to the rupture).

Figure 4.13 shows plasticity effects on the spatial pattern of PGV and duration for the fault-normal directivity-induced pulses. The durations are quantified by the method of Shahi and Baker [2014]. The general wedge shape of near-fault PGV contours, reflecting directivity effects, occurs in both elastic and plastic cases, has superimposed upon it multiple localized

concentrations of PGV that are correlated to the fault geometry (Figure 4.13a). PGV in the plastic case is systematically lowered, with reduction factor up to 70% at some locations. There is a very localized exception (greenish patch) where PGV is actually increased in the plastic case (Figure 4.13a3), apparently related to a patch of fast rupture (around distances of 30 - 35 km and after 10 s in Figure SS4.4b2) in the plastic case. The pulse durations are distributed roughly as in the planar fault case, and are similar to the pulse-period prediction in Fayjaloun et al. [2017], which scales with along-strike and normal-to-fault distance. The anomalously small durations caused by the transient supershear rupture that we noted earlier for the planar fault case are largely removed by fault roughness in both elastic and plastic cases (Figure 4.13b1 and 4.13b2). Plasticity broadens the pulse durations by about 30%, on average, in the directivity-induced wedge of high amplitude.

Figure 4.14 shows the spatial distribution of RotD50 (for periods 0.5s, 1.8 s and 4.8 s). In both elastic and plastic cases, high values of RotD50 are concentrated near the fault in the short- and intermediate-period bands (Figure 4.14a1, 4.14a2, 4.14b1 and 4.14b2). Roughness adds fluctuations to the relatively simple distribution of RotD50 in the planar fault case (Figure 4.9). Off-fault plasticity effects are period-dependent. Plasticity attenuates short-period amplification of RotD50 and constrains the directivity-induced short-period amplification area to a zone very close to the fault trace, while only minimally impacting the spatial pattern of intermediate-period RotD50. Long-period RotD50 largely reflects the amplitude and period of the fault-normal pulse, and is strongly affected by plasticity. In the elastic case, directivity induces a wedge-shaped forward-directivity region (Figure 4.14a3) within which the near-fault RotD50 increases with epicentral distance for rupture-adjacent sites (i.e., those between the rupture endpoints). This behavior is very similar to that of the planar fault case (Figure 4.9). For the plastic case (figure 4.14b3), in contrast, the along-strike increase of the long-period RotD50 ceases at distance of about 25 km from the epicenter. If we measure a fault-normal width by the fault-normal distance to a given (say 1.2 m/s2) RotD50 contour, for example, that reaches a maximum of roughly 8 km at 25 km from the epicenter, after which it remains essentially constant, as seen in Figure 4.14b3.

In summary, losses from plasticity both diminish the overall intensity of the directivity-induced amplification wedge and cause the effect to saturate, i.e., truncate its growth along strike and in the fault-normal direction. In this respect, our simulations with plasticity favor empirical models for near-fault directivity (GMPE directivity factors) that include a distance saturation effect [Abrahamson 2000], and the simulations may also provide guidance for improving distance tapers used in those models, which are otherwise relatively poorly constrained.

4.6 Discussion

4.6.1 Directivity pulse in self-healing rupture

In addition to the pulse induced by directivity in fault-normal ground motions, another commonly noted but conceptually distinct pulse is a pulse-like rupture that, in contrast to a crack-like rupture, is characterized by a slip-velocity rise time much shorter than the total duration of the rupture process. The pulse-like rupture has been broadly recognized in many seismological, analytical, computational, and experimental studies [e.g., Heaton 1990; Zheng and Rice 1998; Nielsen and Madariaga 2003; Lu et al. 2010; Melgar and Hayes 2017]. Numerous mechanisms have been hypothesized to account for pulse-like rupture, including dynamic (velocity) weakening friction such as that expected from flash heating [e.g., Goldsby and Tullis 2011] and thermal pressurization [e.g., Noda et al. 2009] mechanisms, heterogeneity of fault strength/stress [e.g., Beroza and Mikumo 1996], fault zone compliance [e.g., Huang and Ampuero 2011], and minimum rupture dimension [e.g., Day 1982]. These can roughly be classed as local effects, which we term self-healing (slip duration at a point controlled by local frictional resistance), and non-local wave-mediated interactions (slip duration controlled by wave-induced perturbations to the stress field) which we term geometrical. These would by no means be expected to operate independently, but one class may dominate if it has a characteristic time much shorter than the other. For example,

Wang et al. [2019] show that the rupture pulse duration in the 2015 Nepal Gorkha earthquake is strongly associated with a geologically plausible model of MHT (Main Himalayan Thrust) fault geometry, on the basis of modeling that matches the near-field high-rate GPS recording directly (15 km) above the fault. Similarly, the spontaneous rupture models in Sections 4 and 5, although they can support a self-healing behavior, all were set up with parameter choices such that slip duration principally controlled by down-dip fault width (and to some extent by fault roughness effects, in the case of Section 5), i.e., they are geometrically controlled. In contrast, Aagaard and Heaton [2008] show that self-healing dominated rupture can potentially compact the directivity-induced fault-normal ground-velocity pulse. We therefore supplement the results of Sections 4 and 5 by considering self-healing rupture in order to further assess how plasticity affects directivity-induced ground motion pulses.

As noted by Wang and Day [2017], a transition to self-healing dominated rupture can be achieved by tuning the weakening slip rate V_w so as to vary the critical stress level τ_{pulse} defined in Zheng and Rice [1998]. We retain all the model setups of the planar fault scenarios but use a higher weakening slip rate (0.1m/s) than that adopted in preceding sections (0.05 m/s in Table 4.1), so that the average rise time (measured by the period when slip velocity exceeds 0.01 m/s) now is systematically decreased, from about 3 s in the previous cases to 1 s (Figure SS4.5), giving self-healing ruptures in both elastic and plastic cases. Resultant seismic moments of elastic and plastic cases are $4.6 \times 10^{19} Nm$ (M_w 7.08) and $4.0 \times 10^{19} Nm$ (M_w 7.03), respectively. The static stress drops of elastic and plastic cases are 3.98 MPa and 3.84 MPa, respectively.

We perform an analysis of ground motions along the same fault-parallel station line as in Section 4. Results in Figure 4.15 (using the same color convention as in Figure 4.6 to associate stations with spectral plots) are qualitatively very similar to those seen for the longer rise-time cases in Sections 4 and 5. The prominence of the fault-normal directivity-induced pulse, the dominance of fault-normal pseudospectral velocity relative to the fault-parallel component, and the increase of fault-normal pulse duration with along-strike distance resemble the earlier results,

in both elastic and plastic cases. There are some quantitative differences due to the smaller rise time in the self-healing model. In the elastic case, results are in good agreement with expectations from the work of Aagaard and Heaton [2008]. However, the modifications due to plastic yielding remain much the same as we found in Sections 4 and 5. Figure 4.15c1, compared with Figure 4.7c, shows more localized smaller peaks preceding the largest one (and also a lower peak amplitude, as expected in light of the lower moment for the self-healing model). Figure 4.15b shows that multiple prominent short-period peaks (especially around 2 s) in the PSV start to develop with increasing along-strike distance (over 25 km of epicentral distance) and at the most distant station (40 km away) these shorter-period peaks approach the level of the primary peak corresponding to the dominant pulse duration (5 s). This behavior is consistent with what we found in the rough fault scenario (Section 5), and is likewise in agreement with the results of Aagaard and Heaton [2008] that self-healing rupture compacts and splits the directivity-induced fault-normal pulse, enriching the short-period content (see their Figure 4.8) while preserving the long-period pulse. Moreover, the fault-parallel pseudospectral velocity starts to display a systematic peak (also at $\sim$ 2 s, see Figure 4.15a), which is associated with a relatively impulsive fault-parallel velocity (Figure 4.15c1). The prominent short-period peaks corresponding to the localized short rise time from self-healing procedures are similarly found in the rough fault scenario.

Off-fault plasticity influences the directivity pulse in self-healing rupture in essentially the same manner as was the case for the planar and rough fault models discussed earlier. As seen in Figure 4.15c1 and 4.15c2, the directivity pulse in the plastic case becomes weaker and broader, and short- and long-period PSV peaks (1.5 s, 2 s and 5 s) are accordingly shifted in period and reduced in amplitude at the more distance stations, where relatively large strains occur. That is, the stations with greater epicenter distance experience more attenuation of the long-period motion that controls the PSV peak (Figure 4.15b2), which again results in an along-strike saturation of near-fault directivity-induced amplification in the long-period band (Figure SS4.6).

4.6.2 Implications for directivity models used in ground-motion estimation

A number of modifications to empirical GMPE have been proposed to account for rupture directivity and the strong fault-normal pulse [e.g., Spudich and Chiou 2008; Rowshandel 2010; Somerville et al. 1997; Spudich et al. 2014]. As an example for this process, Somerville et al. (1997) introduced (e.g., in the strike-slip case) directivity parameter ($Xcos\theta$), with X representing the proportion of the fault rupture distance that is towards a site of interest and θ representing the effect of the radiation direction relative to the fault strike. Abrahamson [2000] later modified the model such that the predicted effect saturates for directivity parameters larger than 0.4 and the directivity effect is further reduced through the use of tapers for off-fault distance > 30 km (distance taper) and magnitude < 6.5 (magnitude taper). With far larger datasets available (e.g., NGA-West2), more recent models have introduced a number of improvements. The parameterization using normalized rupture length X is now recognized as non-physical [e.g., Bayless and Somerville 2013]. In the NGA-West2 directivity models [Bayless and Somerville 2013; Chiou and Spudich 2013; Rowshandel 2013; Shahi and Baker 2013; Spudich and Chiou 2013], the absolute rupture dimension (toward the site) in km is adopted instead. Moreover, all models except the model of Bayless and Somerville [2013] are now explicitly "narrow-band" models in which the directivity-induced amplification (of response spectra) peaks at a specific period and decreases away from the peak on both sides of the peak. The peak period roughly scales with magnitude, which is consistent with the dependence of pulse period on earthquake magnitude in the NGA-West2 dataset [Somerville 2003; Shahi and Baker 2011].

Our simulation results in the foregoing sections essentially support the two aforementioned features of recent empirical directivity models. That is, the simulated directivity-induced amplification wedge (i.e., the amplified zone in the acute angle about the rupture propagation direction) mirrors the empirical-model dependence on the fault rupture length, and the period-

dependence of that amplification is narrow band. However, our models of directivity-induced amplification, in both 3D elastic and plastic scenarios, demonstrate greater along-strike and off-fault distance- and period-dependent variability of directivity effects and these dependences are inherently intertwined.

First, we discuss the spatial features of directivity-induced amplification. Contours of the directivity amplification adjustment in ground-motion models are wedge-shaped in the near-fault area, as shown in background color of Figure 4.1, in which the directivity-induced amplification increases with along-strike distance. A result is that all directivity models tend to predict that big ground motions occur in a broad zone off the end of fault. However, as found in the 1992 Landers earthquake, the big ground motion records that excited interest in the directivity pulse in ground motions, like the Lucerne recording, are likely to occur at short rupture distances relative to the total rupture length. Our elastic and plastic simulations possibly shed some lights on this issue. In all of our elastic scenarios (including those where the slip pulse is geometrically induced on planar (Section 4) or rough (Section 5) fault surfaces, and those where the rupture is self-healing (Section 6.1)), the spatial pattern of directivity-induced amplification is period-dependent. The long-period contours are wedge-shaped, consistent with directivity models recently developed. In contrast, the maximal motions in the short- and intermediate-period band are very localized near the fault trace and controlled by short-period behaviors of the passing rupture.

The off-fault plasticity as we discussed before can prevent growing of the long-period PSA with the along-strike distance, predicted by directivity amplification adjustment in ground-motion models. As in Figure 4.14b3, the maximal long-period pseudospectral acceleration is located nearly 25 km from the epicenter. The fault-normal width measured by the fault-normal distance to a given PSA contour reaches a maximum (roughly 8 km in Figure 4.14b3) and then remains essentially constant, which in our simulations demonstrates that the plasticity yielding truncate the along-strike and fault-normal growth of directivity amplification. Thus, our simulations may provide guidance for parameterizing distance tapers used in ground-motion models.

In directivity models, the fault-normal width of high-directivity zones is controlled by rather poorly constrained distance tapers. As suggested by the foregoing simulations, this taper should be a function of period, but very few models currently consider this issue (of those cited above, only Rowshandel, [2013] addresses this issue). On the other hand, due to insufficient near-fault (within 10 km) data coverage, the empirical directivity models thus derived may overestimate ground motion in near-fault area. Our plastic simulations in Section 4 imply that PGV saturates (as a function of fault-normal distance) at a level below 2 m/s, an effect not captured by elastic simulations (which can continue to increase above that level at distances less than 2 km or so). Simulations with plasticity also show PGV saturating as stress drop increases, and this stress-drop saturation may be a component of magnitude saturation seen in the near-fault PGV [Schmedes and Archuleta 2008; Baltay and Hanks 2014]. We caution that the quantitative results just cited (i.e., for both the saturation level and fault-normal distance range in which it applies) will require refinement through better constrained cohesion models and more extensive parameter studies. But other recent work supports the concept of stress-drop insensitivity of PGV within a near-fault range of the order of several km, and with a velocity saturation level within about 50% of our 2 m/s estimate [e.g., Roten et al. 2017b]. Further development of dynamic rupture simulations that include inelastic yielding can supplement near-fault constraints on directivity-induced amplification and have the potential to advance development of GMPE directivity models.

Next, we explore the dependence of pulse period on typical GMPE parameters. Several empirical models have related the pulse period to earthquake magnitude, typically inferring almost a linear relationship [Somerville 2003; Shahi and Baker 2011], as seen in Figure 4.16b (where we replot the data from Fayjaloun et al., 2017). However, as suggested by Fayjaloun et al. [2017], the increase of pulse period with magnitude is implicitly expressed though the parameter D, defined as the length of the fault that ruptures toward the site (Figure 4.16a). The idea is that, for the strike-slip earthquakes that are the subject of this study, earthquake magnitude

scales with rupture length, and therefore near-rupture recordings at large values of D can only occur for sufficiently long ruptures. Small values of D can also occur for long ruptures, but, for a random sample of near-rupture records, the mean D of the sample will be proportional to rupture length, and therefore to the event magnitude (Figure 4.7 in Fayjaloun et al. 2017). The D effect on pulse width is consistently present in our 2D kinematic (Section 2), 3D planar (Section 4) and rough fault (Section 5) scenarios. In each case, the pulse period scales with rupture distance toward the site (D), in agreement with the proposed relationship of Fayjaloun et al. [2017]. The suggestion that the apparent magnitude dependence of pulse period actually reflects a dependence on rupture distance toward site (i.e., D) is highlighted in the comparison of Figure 4.16b with Figure 4.16c. In Figure 4.16b, the pulse-period data points for the 10 strike-slip earthquakes in Table 1 of Fayjaloun et al. [2017] are plotted versus magnitude, whereas in Figure 4.16c the same data have been plotted versus D. In Figure 4.16c, the pulse periods for each individual earthquake can be interpreted to follow a common scaling with D, most noticeably in the case of the 1999 Kocaeli and 1979 Imperial Valley earthquakes, for which the scatter of pulse periods with respect to a regression line D is smaller than with respect to one on magnitude. This comparison supports the view that the apparent magnitude scaling in Figure 4.16b results physically from scaling of period with D, combined with the natural correlation of magnitude with D.The scaling of pulse period with D is common to each type of rupture model that we have considered, despite some variations in pulse width among those models. For example, our 3D plastic simulations indicate that the off-fault plasticity can broaden the pulse to varying degrees, depending on the cumulated plastic strain. Moreover, in our simulated self-healing rupture, additional short-period pulses emerge, while nonetheless preserving the primary pulse dominated by D.

The scaling of pulse period with D is common to each type of rupture model that we have considered, despite some variations in pulse width among those models. For example, our 3D plastic simulations indicate that the off-fault plasticity can broaden the pulse to varying degrees, depending on the cumulated plastic strain. Moreover, in our simulated self-healing

rupture, additional short-period pulses emerge, while nonetheless preserving the primary pulse dominated by D.

The inelastic effects seen in the simulations have their greatest effect at distances to the rupture of roughly 2 km or less. Therefore, inelastic effects will be especially important when rupture simulations are used to extrapolate directivity-pulse behavior to sites very near the rupture surface. Roten et al. [2014] suggests that a typical simulation assuming a linear response of rock will overpredict ground motions during potential large earthquakes on the southern San Andreas Fault (e.g., Cybershake). The effects of plasticity depend on the cohesion values used, are also sensitive to a presence of a low-velocity fault damage zone [Roten et al., 2017b]. The results we have presented can provide guidance on the general spatial and period dependencies to be expected for pulses in the near-rupture regime, while much scope remains to use rupture simulations to better quantify those dependencies and their variability.

Conclusion

Rupture directivity strongly modifies ground-motion amplitude and duration, thus leading to the commonly observed dominant pulse-like fault-normal horizontal ground motions, near fault trace where off-fault inelasticity is likely to impact their amplitudes and waveforms. In this paper, we primarily assess the extent to which plastic yielding, which is absent in conventional kinematic models, may systematically affect the amplitude, frequency content and distance scaling of directivity pulse. Simple 2D kinematic modeling is performed to learn that shape of directivity-induced pulse is sensitive to rupture velocity, slip rise time and epicentral distance. From 3D strike-slip ruptures with and without plastic yielding, on a flat and rough fault plane, we find that each of the four 3D models (flat and rough faults, with and without off-fault yielding), scaled to approximately magnitude 7, predicts a fault-normal pulse with characteristic behavior of observed pulses (periods in the range 2-5 second, amplitudes increasing with distance

in the forward-directivity direction but approaching a limiting amplitude). Plastic yielding systematically reduces amplitude and increase dominant period of directivity pulse, compared to models excluding off-fault inelasticity. Plasticity induces a saturation of the growth of PGV with respect to off-fault distance, along-strike distance, and stress drop. Plasticity yielding also prevents along-strike increase of long-period PSA and fault-normal width of wedge-shaped directivity amplification. In addition, off-fault plasticity substantially suppresses the otherwise very strong high-frequency acceleration pulses that otherwise appear in the fault-parallel acceleration when local supershear rupture transients occur. The consideration of nonlinear materials in analysis of seismic pulse dynamics can better understand and more accurately predict near-fault ground motions.

Acknowledge

Chapter 4, in full, is a reformatted version of a paper currently being prepared for submission for publication Journal of Geophysical Research-Solid Earth: Wang, Y. and Day, S. M., “Effects of off-fault inelasticity on near-fault directivity pulses ”, *Journal of Geophysical Research-Solid Earth*, 2019. I was the primary investigator and author of this paper.

References

Aagaard, B. T. and Heaton, T. H. (2004). "Near-source ground motions from simulations of sustained intersonic and supersonic fault ruptures". In: *Bulletin of the Seismological Society of America* 94.6, pp. 2064–2078.

— (2008). "Constraining fault constitutive behavior with slip and stress heterogeneity". In: *Journal of Geophysical Research-Solid Earth* 113.B04301.

Aagaard, B. T., Heaton, T. H., and Hall, J. F. (2001). "Dynamic earthquake ruptures in the presence of lithostatic normal stresses: Implications for friction models and heat production". In: *Bulletin of the Seismological Society of America* 91.6, pp. 1765–1796.

Abrahamson, N. A. (2000). *Effects of rupture directivity on probabilistic seismic hazard analysis*. Conference Paper.

Aki, K. and Richards, P. G. (2002). *Quantitative Seismology*. Sausalito, Calif: University Science Books.

Andrews, D. J. (2005). "Rupture dynamics with energy loss outside the slip zone". In: *Journal of Geophysical Research-Solid Earth* 110.B1.

Andrews, D. J. and Barall, M. (2011). "Specifying Initial Stress for Dynamic Heterogeneous Earthquake Source Models". In: *Bulletin of the Seismological Society of America* 101.5, pp. 2408–2417.

Baker, J. W. (2007). "Quantitative classification of near-fault ground motions using wavelet analysis". In: *Bulletin of the Seismological Society of America* 97.5, pp. 1486–1501.

Baltay, A. and Hanks, T. (2014). "Understanding the magnitude dependence of PGA and PGV in NGA-West 2 data". In: *Bulletin of the Seismological Society of America* 104.6, pp. 2851–2865.

Baumann, C. and Dalguer, L. A. (2014). "Evaluating the compatibility of dynamic rupture-based synthetic ground motion with empirical ground-motion prediction equation". In: *Bulletin of the Seismological Society of America* 104.2, pp. 634–652.

Bayless, J. R. and Somerville, P. G. (2013). *Final Report of the NGA-West2 Directivity Working Group, Chapter 2*. Report. Pacific Earthquake Engineering Research Center, University of California, Berkeley.

Ben-Zion, Y. and Sammis, C. G. (2003). "Characterization of fault zones". In: *Pure and Applied Geophysics* 160.3-4, pp. 677–715.

Ben-Zion, Y., Rockwell, T. K., Shi, Z. Q., and Xu, S. Q. (2012). "Reversed-polarity secondary deformation structures near fault stepovers". In: *Journal of Applied Mechanics* 79.3, p. 031025.

Bernard, P. and Madariaga, R. (1984). "High-frequency seismic radiation from a buried circular fault". In: *Geophysical Journal of the Royal Astronomical Society* 78.1, pp. 1–17.

Beroza, G. C. and Mikumo, T. (1996). "Short slip duration in dynamic rupture in the presence of heterogeneous fault properties". In: *Journal of Geophysical Research-Solid Earth* 101.B10, pp. 22449–22460.

Bizzarri, A., Dunham, E. M., and Spudich, P. (2010). "Coherence of Mach fronts during heterogeneous supershear earthquake rupture propagation: Simulations and comparison with observations". In: *Journal of Geophysical Research-Solid Earth* 115.

Boatwright, J. and Boore, D. M. (1975). "Simplification in calculation of motions near a propagating dislocation". In: *Bulletin of the Seismological Society of America* 65.1, pp. 133–138.

Boore, D. M. and Zoback, M. D. (1974). "Near-field motions from kinematic models of propagating faults". In: *Bulletin of the Seismological Society of America* 64.2, pp. 321–342.

Boore, D. M., Aki, K., and Todd, T. (1971). "A two-dimensional moving dislocation model for a strike-slip fault". In: *Bulletin of the Seismological Society of America* 61.1, pp. 177–194.

Boore, D. M. and Atkinson, G. M. (2008). "Ground-motion prediction equations for the average horizontal component of PGA, PGV, and 5%-damped PSA at spectral periods between 0.01 s and 10.0 s". In: *Earthquake Spectra* 24.1, pp. 99–138.

Boore, D. M., Watson-Lamprey, J., and Abrahamson, N. A. (2006). "Orientation-independent measures of ground motion". In: *Bulletin of the Seismological Society of America* 96.4, pp. 1502–1511.

Bozorgnia, Y and Campbell, A. (2004). "Engineering characterization of ground motion". In: *Earthquake Engineering: From Engineering Seismology to Performance-Based Engineering*. Ed. by Y Bozorgnia and V Bertero. Boca Raton, FL: CRC Press.

Bozorgnia, Y., Abrahamson, N. A., Al Atik, L., Ancheta, T. D., Atkinson, G. M., Baker, J. W., Baltay, A., Boore, D. M., Campbell, K. W., Chiou, B. S. J., Darragh, R., Day, S., Donahue, J., Graves, R. W., Gregor, N., Hanks, T., Idriss, I. M., Kamai, R., Kishida, T., Kottke, A., Mahin, S. A., Rezaeian, S., Rowshandel, B., Seyhan, E., Shahi, S., Shantz, T., Silva, W., Spudich, P., Stewart, J. P., Watson-Lamprey, J., Wooddell, K., and Youngs, R. (2014). "NGA-West2 Research Project". In: *Earthquake Spectra* 30.3, pp. 973–987.

Broberg, K. B. (1996). "How fast can a crack go?" In: *Materials Science* 32.1, pp. 80–86.

— (1999). "Intersonic mode II crack acceleration". In: *Fatigue & Fracture of Engineering Materials & Structures* 22.1, pp. 17–24.

Candela, T., Renard, F., Bouchon, M., Brouste, A., Marsan, D., Schmittbuhl, J., and Voisin, C. (2009). "Characterization of Fault Roughness at Various Scales: Implications of Three-Dimensional High Resolution Topography Measurements". In: *Pure and Applied Geophysics* 166.10-11, pp. 1817–1851.

Chiou, B. S. J. and Spudich, P. (2013). *Final Report of the NGA-West2 Directivity Working Group, Chapter 6*. Report. Pacific Earthquake Engineering Research Center, University of California, Berkeley.

Dalguer, L. A. and Day, S. M. (2007). "Staggered-grid split-node method for spontaneous rupture simulation". In: *Journal of Geophysical Research-Solid Earth* 112.B2.

Das, S. (2015). "Supershear Earthquake Ruptures - Theory, Methods, Laboratory Experiments and Fault Superhighways: An Update". In: *Perspectives on European Earthquake Engineering and Seismology, Vol 2*. Ed. by A. Ansal. Geotechnical, geological and earthquake engineering, pp. 1–20.

Day, S. M. (1982). "Three-dimensional finite difference simulation of fault dynamics: rectangular faults with fixed rupture velocity". In: *Bulletin of the Seismological Society of America* 72.3, pp. 705–727.

Day, S. M. and Ely, G. P. (2002). "Effect of a shallow weak zone on fault rupture: Numerical simulation of scale-model experiments". In: *Bulletin of the Seismological Society of America* 92.8, pp. 3022–3041.

Day, S. M., Dalguer, L. A., Lapusta, N., and Liu, Y. (2005). "Comparison of finite difference and boundary integral solutions to three-dimensional spontaneous rupture". In: *Journal of Geophysical Research-Solid Earth* 110.

Day, S. M., Gonzalez, S. H., Anooshehpoor, R., and Brune, J. N. (2008). "Scale-model and numerical simulations of near-fault seismic directivity". In: *Bulletin of the Seismological Society of America* 98.3, pp. 1186–1206.

Donahue, J., Stewart, J., Gregor, N., and Bozorgnia, Y. (2019). *Ground-Motion Directivity Modeling for Seismic Hazard Applications*. Report. Pacific Earthquake Engineering Research Center Headquarters at the University of California, Berkeley.

Douglas, A., Hudson, J. A., and Pearce, R. G. (1988). "Directivity and the Doppler-Effect". In: *Bulletin of the Seismological Society of America* 78.3, pp. 1367–1372.

Drucker, D. C. and Prager, W. (1952). "Soil mechanics and plastic analysis or limit design". In: *Quarterly of Applied Mathematics* 10.2, pp. 157–165.

Duan, B. and Day, S. M. (2008). "Inelastic strain distribution and seismic radiation from rupture of a fault kink". In: *Journal of Geophysical Research-Solid Earth* 113.B12.

Dunham, E. M. and Bhat, H. S. (2008). “Attenuation of radiated ground motion and stresses from three-dimensional supershear ruptures”. In: *Journal of Geophysical Research-Solid Earth* 113.B8.

Dunham, E. M., Belanger, D., Cong, L., and Kozdon, J. E. (2011a). “Earthquake ruptures with strongly rate-weakening friction and off-fault plasticity, part 1: Planar faults”. In: *Bulletin of the Seismological Society of America* 101.5, pp. 2296–2307.

— (2011b). “Earthquake Ruptures with Strongly Rate-Weakening Friction and Off-Fault Plasticity, Part 2: Nonplanar Faults”. In: *Bulletin of the Seismological Society of America* 101.5, pp. 2308–2322.

Ely, G. P., Day, S. M., and Minster, J.-B. (2008). “A support-operator method for viscoelastic wave modelling in 3-D heterogeneous media”. In: *Geophysical Journal International* 172.1, pp. 331–344.

— (2009). “A support-operator method for 3-D rupture dynamics”. In: *Geophysical Journal International* 177.3, pp. 1140–1150.

— (2010). “Dynamic Rupture Models for the Southern San Andreas Fault”. In: *Bulletin of the Seismological Society of America* 100.1, pp. 131–150.

Esmaeilzadeh, A., Motazedian, D., and Hunter, J. (2019). “3D Nonlinear Ground-Motion Simulation Using a Physics-Based Method for the Kinburn Basin”. In: *Bulletin of the Seismological Society of America* 109.4, pp. 1282–1311.

Fang, Z. J. and Dunham, E. M. (2013). “Additional shear resistance from fault roughness and stress levels on geometrically complex faults”. In: *Journal of Geophysical Research-Solid Earth* 118.7, pp. 3642–3654.

Fayjaloun, R., Causse, M., Voisin, C., Cornou, C., and Cotton, F. (2017). “Spatial Variability of the Directivity Pulse Periods Observed during an Earthquake”. In: *Bulletin of the Seismological Society of America* 107.1, pp. 308–318.

Fialko, Y., Sandwell, D., Simons, M., and Rosen, P. (2005). “Three-dimensional deformation caused by the Bam, Iran, earthquake and the origin of shallow slip deficit”. In: *Nature* 435.7040, pp. 295–299.

Gallovic, F. (2016). “Modeling Velocity Recordings of the M-w 6.0 South Napa, California, Earthquake: Unilateral Event with Weak High-Frequency Directivity”. In: *Seismological Research Letters* 87.1, pp. 2–14.

Goldsby, D. L. and Tullis, T. E. (2011). “Flash Heating Leads to Low Frictional Strength of Crustal Rocks at Earthquake Slip Rates”. In: *Science* 334.6053, pp. 216–218.

Gritz, A. (2009). “Effect of heterogeneous prestress on near-field rupture directivity”. PhD thesis.

Hall, J. F., Heaton, T. H., Halling, M. W., and Wald, D. J. (1995). "Near-Source Ground Motion and its Effects on Flexible Buildings". In: *Earthquake Spectra* 11.4, pp. 569–605.

Harris, R. A., Barall, M., Archuleta, R., Dunham, E., Aagaard, B., Ampuero, J. P., Bhat, H., Cruz-Atienza, V., Dalguer, L., Dawson, P., Day, S., Duan, B., Ely, G., Kaneko, Y., Kase, Y., Lapusta, N., Liu, Y., Ma, S., Oglesby, D., Olsen, K., Pitarka, A., Song, S., and Templeton, E. (2009). "The SCEC/USGS dynamic earthquake rupture code verification exercise". In: *Seismological Research Letters* 80.1, pp. 119–126.

Harris, R. A., Barall, M., Aagaard, B., Ma, S., Roten, D., Olsen, K., Duan, B. C., Liu, D. Y., Luo, B., Bai, K. C., Ampuero, J. P., Kaneko, Y., Gabriel, A. A., Duru, K., Ulrich, T., Wollherr, S., Shi, Z. Q., Dunham, E., Bydlon, S., Zhang, Z. G., Chen, X. F., Somala, S. N., Pelties, C., Tago, J., Cruz-Atienza, V. M., Kozdon, J., Daub, E., Aslam, K., Kase, Y., Withers, K., and Dalguer, L. (2018). "A Suite of Exercises for Verifying Dynamic Earthquake Rupture Codes". In: *Seismological Research Letters* 89.3, pp. 1146–1162.

Haskell, N. A. (1969). "Elastic displacements in near-field of a propagating fault". In: *Bulletin of the Seismological Society of America* 59.2, pp. 865–908.

Heaton, T. H. (1990). "Evidence for and Implications of Self-Healing Pulses of Slip in Earthquake Rupture". In: *Physics of the Earth and Planetary Interiors* 64.1, pp. 1–20.

Hirakawa, E. and Ma, S. (2016). "Dynamic fault weakening and strengthening by gouge compaction and dilatancy in a fluid-saturated fault zone". In: *Journal of Geophysical Research-Solid Earth* 121.8, pp. 5988–6008.

Huang, Y. H. and Ampuero, J. P. (2011). "Pulse-like ruptures induced by low-velocity fault zones". In: *Journal of Geophysical Research-Solid Earth* 116.

Kaneko, Y. and Fialko, Y. (2011). "Shallow slip deficit due to large strike-slip earthquakes in dynamic rupture simulations with elasto-plastic off-fault response". In: *Geophysical Journal International* 186.3, pp. 1389–1403.

Kaneko, Y. and Lapusta, N. (2010). "Supershear transition due to a free surface in 3-D simulations of spontaneous dynamic rupture on vertical strike-slip faults". In: *Tectonophysics* 493.3-4, pp. 272–284.

Kaneko, Y., Lapusta, N., and Ampuero, J. P. (2008). "Spectral element modeling of spontaneous earthquake rupture on rate and state faults: Effect of velocity-strengthening friction at shallow depths". In: *Journal of Geophysical Research-Solid Earth* 113.B9.

Kieling, K., Wang, R. J., and Hainzl, S. (2014). "Broadband Ground-Motion Simulation Using Energy-Constrained Rise-Time Scaling". In: *Bulletin of the Seismological Society of America* 104.6, pp. 2683–2697.

Lapusta, N., Rice, J. R., Ben-Zion, Y., and Zheng, G. T. (2000). "Elastodynamic analysis for slow tectonic loading with spontaneous rupture episodes on faults with rate- and state-dependent friction". In: *Journal of Geophysical Research-Solid Earth* 105.B10, pp. 23765–23789.

Lindsey, E. O., Fialko, Y., Bock, Y., Sandwell, D. T., and Bilham, R. (2014). "Localized and distributed creep along the southern San Andreas Fault". In: *Journal of Geophysical Research-Solid Earth* 119.10, pp. 7909–7922.

Lu, X., Lapusta, N., and Rosakis, A. J. (2010). "Pulse-like and crack-like dynamic shear ruptures on frictional interfaces: experimental evidence, numerical modeling, and implications". In: *International Journal of Fracture* 163.1-2, pp. 27–39.

Ma, S. (2008). "A physical model for widespread near-surface and fault zone damage induced by earthquakes". In: *Geochemistry Geophysics Geosystems* 9.

Ma, S. and Hirakawa, E. T. (2013). "Dynamic wedge failure reveals anomalous energy radiation of shallow subduction earthquakes". In: *Earth and Planetary Science Letters* 375, pp. 113–122.

Madariaga, R. (1977). "Implications of stress-drop models of earthquakes for the inversion of stress drop from seismic observations". In: *Pure and Applied Geophysics PAGEOPH* 115.1-2, pp. 301–316.

Mai, P., Galis, M., Thingbaijam, K., Vyas, J., and Dunham, E. (2017). "Accounting for Fault Roughness in Pseudo-Dynamic Ground-Motion Simulations". In: *Pure and Applied Geophysics* 174.9, pp. 3419–3450.

Makris, N. and Black, C. J. (2004). "Dimensional analysis of rigid-plastic and elastoplastic structures under pulse-type excitations". In: *Journal of Engineering Mechanics-Asce* 130.9, pp. 1006–1018.

Marone, C. (1998). "Laboratory-derived friction laws and their application to seismic faulting". In: *Annual Review of Earth and Planetary Sciences* 26, pp. 643–696.

Marone, C. J., Scholtz, C. H., and Bilham, R. (1991). "On the Mechanics of Earthquake Afterslip". In: *Journal of Geophysical Research-Solid Earth and Planets* 96.B5, pp. 8441–8452.

Mavroeidis, G. P., Dong, G., and Papageorgiou, A. S. (2004). "Near-fault ground motions, and the response of elastic and inelastic single-degree-of-freedom (SDOF) systems". In: *Earthquake Engineering & Structural Dynamics* 33.9, pp. 1023–1049.

Melgar, D. and Hayes, G. P. (2017). "Systematic observations of the slip pulse properties of large earthquake ruptures". In: *Geophysical Research Letters* 44.19, pp. 9691–9698.

Nielsen, S. and Madariaga, R. (2003). “On the self-healing fracture mode”. In: *Bulletin of the Seismological Society of America* 93.6, pp. 2375–2388.

Noda, H., Dunham, E. M., and Rice, J. R. (2009). “Earthquake ruptures with thermal weakening and the operation of major faults at low overall stress levels”. In: *Journal of Geophysical Research-Solid Earth* 114.

Passone, L. and Mai, P. M. (2017). “Kinematic Earthquake Ground-Motion Simulations on Listric Normal Faults”. In: *Bulletin of the Seismological Society of America* 107.6, pp. 2980–2993.

Perfettini, H. and Avouac, J. P. (2007). “Modeling afterslip and aftershocks following the 1992 Landers earthquake”. In: *Journal of Geophysical Research-Solid Earth* 112.B7.

Power, W. L. and Tullis, T. E. (1991). “Euclidean and fractal models for the description of rock surface-roughness”. In: *Journal of Geophysical Research-Solid Earth and Planets* 96.B1, pp. 415–424.

Renard, F., Voisin, C., Marsan, D., and Schmittbuhl, J. (2006). “High resolution 3D laser scanner measurements of a strike-slip fault quantify its morphological anisotropy at all scales”. In: *Geophysical Research Letters* 33.4.

Rice, J. R. (1993). “Spatiotemporal complexity of slip on a fault”. In: *Journal of Geophysical Research-Solid Earth* 98.B6, pp. 9885–9907.

Rice, J. R. (1992). “Fault stress states, pore pressure distributions, and the weakness of the san andreas fault”. In: *Fault Mechanics and Transport Properties of Rocks - A Festschrift in Honor of W. F. Brace*. Ed. by B. Evans and T.-f. Wong. Vol. 51. International Geophysics. San Diego: Academic Press, pp. 475–503. ISBN: 9780122437809.

Roten, D., Olsen, K. B., and Pechmann, J. C. (2012). “3D Simulations of M 7 Earthquakes on the Wasatch Fault, Utah, Part II: Broadband (0-10 Hz) Ground Motions and Nonlinear Soil Behavior”. In: *Bulletin of the Seismological Society of America* 102.5, pp. 2008–2030.

Roten, D., Olsen, K. B., Day, S. M., Cui, Y., and Fah, D. (2014). “Expected seismic shaking in Los Angeles reduced by San Andreas fault zone plasticity”. In: *Geophysical Research Letters* 41.8, pp. 2769–2777.

Roten, D., Olsen, K. B., and Day, S. M. (2017a). “Off-fault deformations and shallow slip deficit from dynamic rupture simulations with fault zone plasticity”. In: *Geophysical Research Letters* 44.15, pp. 7733–7742.

Roten, D., Olsen, K. B., Day, S. M., and Cui, Y. (2017b). “Quantification of Fault-Zone Plasticity Effects with Spontaneous Rupture Simulations”. In: *Pure and Applied Geophysics* 174.9, pp. 3369–3391.

Rowshandel, B. (2010). “Directivity Correction for the Next Generation Attenuation (NGA) Relations”. In: *Earthquake Spectra* 26.2, pp. 525–559.

— (2013). *Final Report of the NGA-West2 Directivity Working Group, Chapter 3*. Report. Pacific Earthquake Engineering Research Center, University of California, Berkeley.

Sagy, A. and Brodsky, E. E. (2009). “Geometric and rheological asperities in an exposed fault zone”. In: *Journal of Geophysical Research-Solid Earth* 114.

Scala, A., Festa, G., and Del Gaudio, S. (2018). “Relation Between Near-Fault Ground Motion Impulsive Signals and Source Parameters”. In: *Journal of Geophysical Research: Solid Earth* 123.9, pp. 7707–7721.

Schmedes, J. and Archuleta, R. J. (2008). “Near-source ground motion along strike-slip faults: Insights into magnitude saturation of PGV and PGA”. In: *Bulletin of the Seismological Society of America* 98.5, pp. 2278–2290.

Shahi, S. K. and Baker, J. W. (2011). *Regression models for predicting the probability of near-fault earthquake ground motion pulses, and their period*. Conference Paper.

— (2013). *Final Report of the NGA-West2 Directivity Working Group, Chapter 4*. Report. Pacific Earthquake Engineering Research Center, University of California, Berkeley.

— (2014). “An Efficient Algorithm to Identify Strong-Velocity Pulses in Multicomponent Ground Motions”. In: *Bulletin of the Seismological Society of America* 104.5, pp. 2456–2466.

Shearer, P., Hauksson, E., and Lin, G. Q. (2005). “Southern california hypocenter relocation with waveform cross-correlation, part 2: Results using source-specific station terms and cluster analysis”. In: *Bulletin of the Seismological Society of America* 95.3, pp. 904–915.

Shi, Z. Q. and Day, S. M. (2013). “Rupture dynamics and ground motion from 3-D rough-fault simulations”. In: *Journal of Geophysical Research-Solid Earth* 118.3, pp. 1122–1141.

Simons, M., Fialko, Y., and Rivera, L. (2002). “Coseismic deformation from the 1999 M-w 7.1 Hector Mine, California, earthquake as inferred from InSAR and GPS observations”. In: *Bulletin of the Seismological Society of America* 92.4, pp. 1390–1402.

Somerville, P. G. (2003). “Magnitude scaling of the near fault rupture directivity pulse”. In: *Physics of the Earth and Planetary Interiors* 137.1-4, pp. 201–212.

Somerville, P. G., Smith, N. F., Graves, R. W., and Abrahamson, N. A. (1997). “Modification of Empirical Strong Ground Motion Attenuation Relations to Include the Amplitude and Duration Effects of Rupture Directivity”. In: *Seismological Research Letters* 68.1, pp. 199–222.

Song, S. G. (2015). "The effect of fracture energy on earthquake source correlation statistics". In: *Bulletin of the Seismological Society of America* 105.2a, pp. 1042–1048.

Song, S. G. and Dalguer, L. A. (2017). "Synthetic Source Inversion Tests with the Full Complexity of Earthquake Source Processes, Including Both Supershear Rupture and Slip Reactivation". In: *Pure and Applied Geophysics* 174.9, pp. 3393–3418.

Song, S. G., Dalguer, L. A., and Mai, P. M. (2013). "Pseudo-dynamic source modelling with 1-point and 2-point statistics of earthquake source parameters". In: *Geophysical Journal International* 196.3, pp. 1770–1786.

Spudich, P. and Chiou, B. S. J. (2008). "Directivity in NGA earthquake ground motions: Analysis using isochrone theory". In: *Earthquake Spectra* 24.1, pp. 279–298.

— (2013). *Final Report of the NGA-West2 Directivity Working Group, Chapter 5*. Report. Pacific Earthquake Engineering Research Center, University of California, Berkeley.

Spudich, P., Rowshandel, B., Shahi, S. K., Baker, J. W., and Chiou, B. S. J. (2014). "Comparison of NGA-West2 Directivity Models". In: *Earthquake Spectra* 30.3, pp. 1199–1221.

Strasser, F. O. and Bommer, J. J. (2009). "Review: Strong Ground Motions-Have We Seen the Worst?" In: *Bulletin of the Seismological Society of America* 99.5, pp. 2613–2637.

Vyas, J. C., Mai, P. M., and Galis, M. (2016). "Distance and azimuthal dependence of ground-motion variability for unilateral strike-slip ruptures". In: *Bulletin of the Seismological Society of America* 106.4, pp. 1584–1599.

Vyas, J. C., Mai, P. M., Galis, M., Dunham, E. M., and Imperatori, W. (2018). "Mach wave properties in the presence of source and medium heterogeneity". In: *Geophysical Journal International* 214.3, pp. 2035–2052.

Wang, Y. and Day, S. M. (2017). "Seismic source spectral properties of crack-like and pulse-like modes of dynamic rupture". In: *Journal of Geophysical Research-Solid Earth* 122.8, pp. 6657–6684.

Wang, Y., Day, S. M., and Denolle, M. A. (2019). "Geometric Controls on Pulse-Like Rupture in a Dynamic Model of the 2015 Gorkha Earthquake". In: *Journal of Geophysical Research: Solid Earth* 124.2, pp. 1544–1568.

Withers, K. B., Olsen, K. B., Day, S. M., and Shi, Z. (2018a). "Ground Motion and Intraevent Variability from 3D Deterministic Broadband (0-7.5-Hz) Simulations along a Nonplanar Strike-Slip Fault". In: *Bulletin of the Seismological Society of America* 109.1, pp. 229–250.

Withers, K. B., Olsen, K. B., Shi, Z., and Day, S. M. (2018b). "Validation of Deterministic Broadband Ground Motion and Variability from Dynamic Rupture Simulations of Buried

Thrust Earthquakes". In: *Bulletin of the Seismological Society of America* 109.1, pp. 212–228.

Wollherr, S., Gabriel, A. A., and Uphoff, C. (2018). "Off-fault plasticity in three-dimensional dynamic rupture simulations using a modal Discontinuous Galerkin method on unstructured meshes: implementation, verification and application". In: *Geophysical Journal International* 214.3, pp. 1556–1584.

Wollherr, S., Gabriel, A., and Mai, P. M. (2019). "Landers 1992 "reloaded": Integrative dynamic earthquake rupture modeling". In: *Journal of Geophysical Research: Solid Earth* 0.ja.

Zheng, G. and Rice, J. R. (1998). "Conditions under which velocity-weakening friction allows a self-healing versus a cracklike mode of rupture". In: *Bulletin of the Seismological Society of America* 88.6, pp. 1466–1483.

Tables and Figures

Table 4.1: Model bulk properties, initial stress tensor, frictional properties and nucleation parameters. The values of parameters labeled as "Depth dependent" can be found in Figure 4.4. τ^b is a local shear stress at the hypocenter, which is derived from the initial stress tensor.

Parameter	Symbol	Value
Bulk Properties		
P wave speed	α	6,000 m/s
S wave speed	β	3,464 m/s
Density	ρ	2,670 kg/m^3
Kelvin-Voigt Viscosity	η	4×10^{-4}s
Maxwellian time scale	T_v	0.014 s
Cohesion	c	3 MPa
Internal friction coefficient	tan(ϕ)	0.75
Initial stress state		
Initial stress tensor components	σ_{xx}	Depth dependent
	σ_{yy}	Depth dependent
	σ_{zz}	Depth dependent
	σ_{xz}	Depth dependent
Frictional properties		
Direct-effect parameter	a	Depth dependent
Evolution-effect parameter	b	0.014
Reference slip rate	V_0	1μ m/s
Steady state coefficient at slip rate V_0	f_0	0.6
Evolution distance of state variable	L	0.2
Weakening slip rate	V_w	Depth dependent
Fully weakened friction coefficient	f_w	0.3
Initial fault slip rate	V^{ini}	$1 \times 10^{-9} m/s$
Nucleation parameters		
Nucleation radius	R	3,000 m
Nucleation depth	D	9 km
Overstress	$\Delta\tau^b$	$1 \times \tau^b$

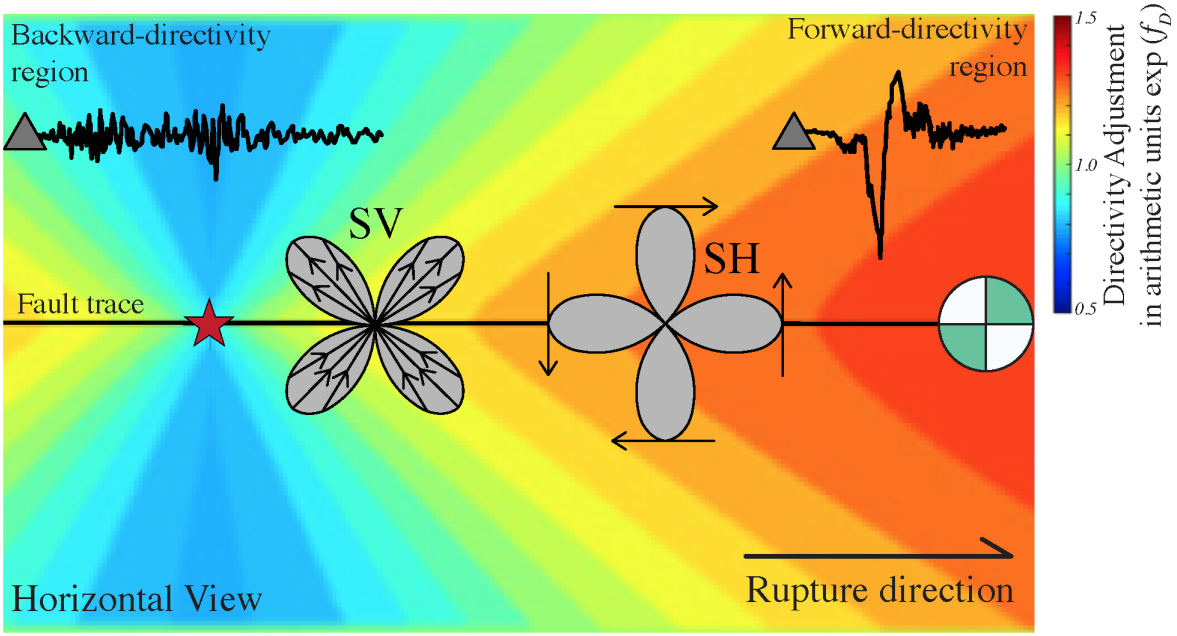

Figure 4.1: Schematic plan view showing near-fault directivity effects of a vertical right-lateral strike-slip event, modified from Somerville et al. (1997). Representative ground velocities of forward- and backward-directivity sites are extracted from Lucerne and Joshua Tree stations in the 1992 Landers earthquake (Source: Somerville, P. G. et al. (1997). "Modification of Empirical Strong Ground Motion Attenuation Relations to Include the Amplitude and Duration Effects of Rupture Directivity". In: *Seismological Research Letters* 68.1, pp. 199–222. Radiation patterns of SV and SH waves are plotted along the fault trace, respectively. The background colored map is a directivity adjustment in ground-motion models (GMMs). This particular directivity correction is based Bayless and Somerville [2013], which generally illustrates near-fault wedge-shaped amplifications in forward-directivity regions.

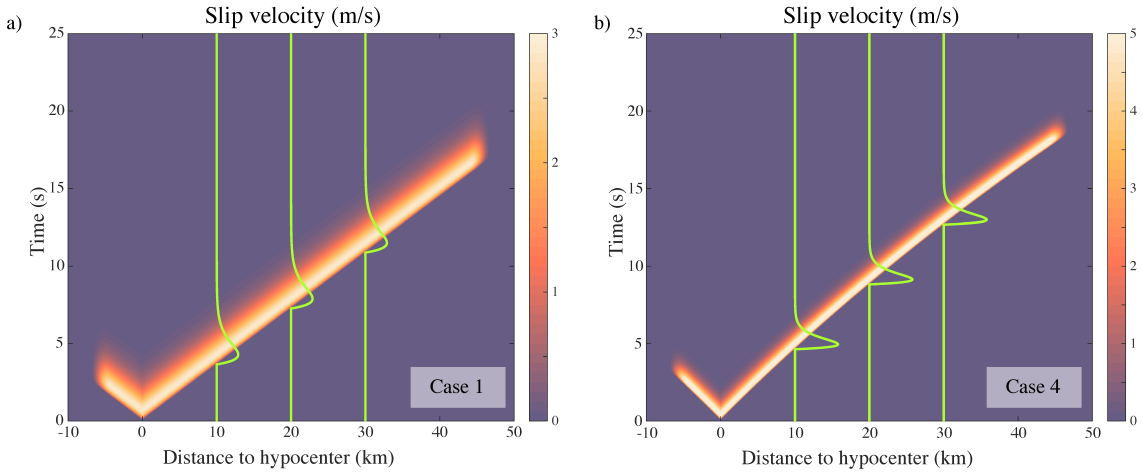

Figure 4.2: Representative generated spatial-temporal slip velocities (Case 1 and 4). Green curves show slip velocity time histories at different stations on fault.

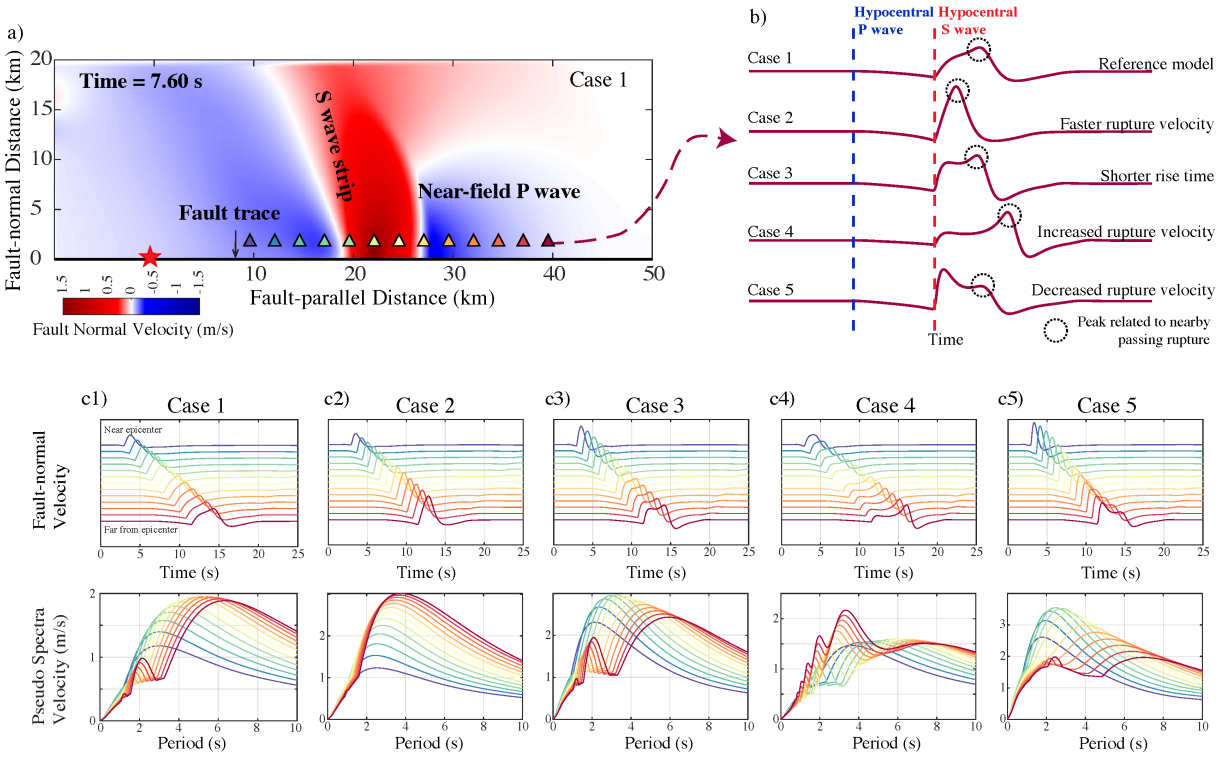

Figure 4.3: a) Spatial distribution of 13 stations aligned with the fault trace (black line), superimposed on a wavefield snapshot of fault-normal velocity for Case 1. b) Fault-normal velocity time histories and c) pseudospectral velocities (PSV) of stations in the 5 cases described in the text and in Table SS4.1.

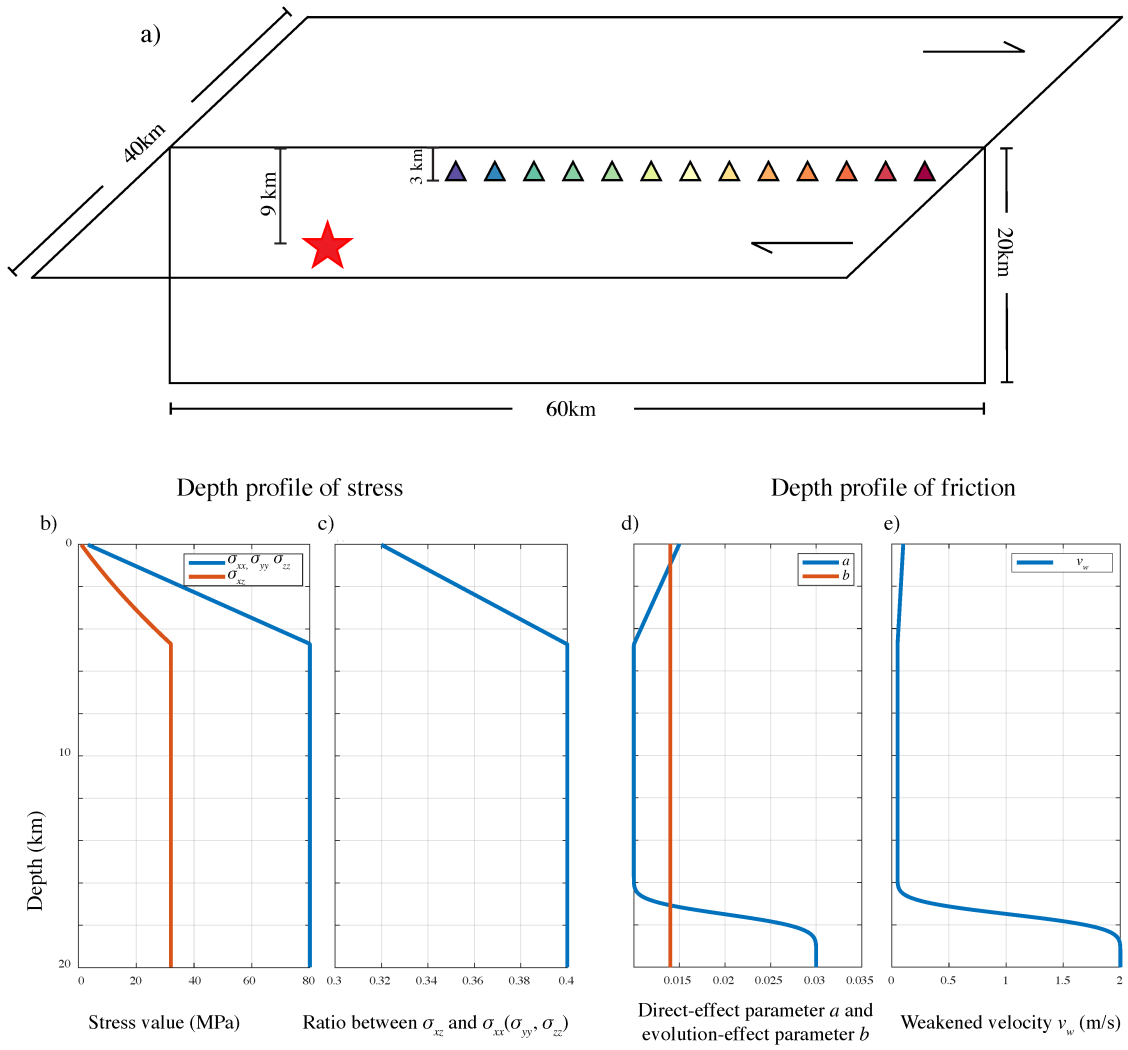

Figure 4.4: Computational domain size and depth profile of initial stress and friction. These profiles illustrate the parameters labeled as "Depth dependent" in Table 4.1. Colored triangles are locations of ground motion samplers used for subsequent analysis

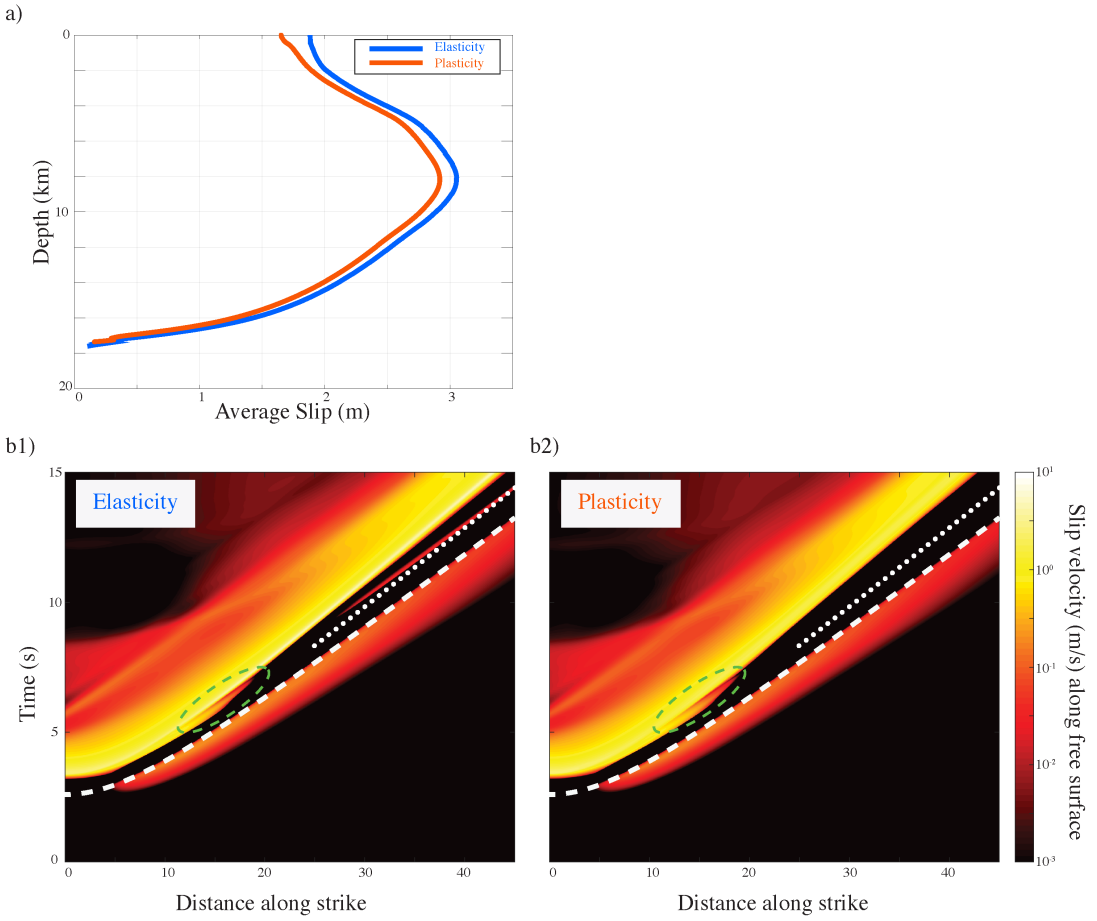

Figure 4.5: a) Along-strike averaged slip profiles versus depth and b) space-time plot of surface slip velocities, in elastic and plastic cases. White dashed lines indicate travel-time curves of the hypocentral S wave. White dotted lines indicate Rayleigh wave speed. Green dashed circles enclose transient supershear phases occurring when ruptures reflect at free surface in both elastic and plastic cases.

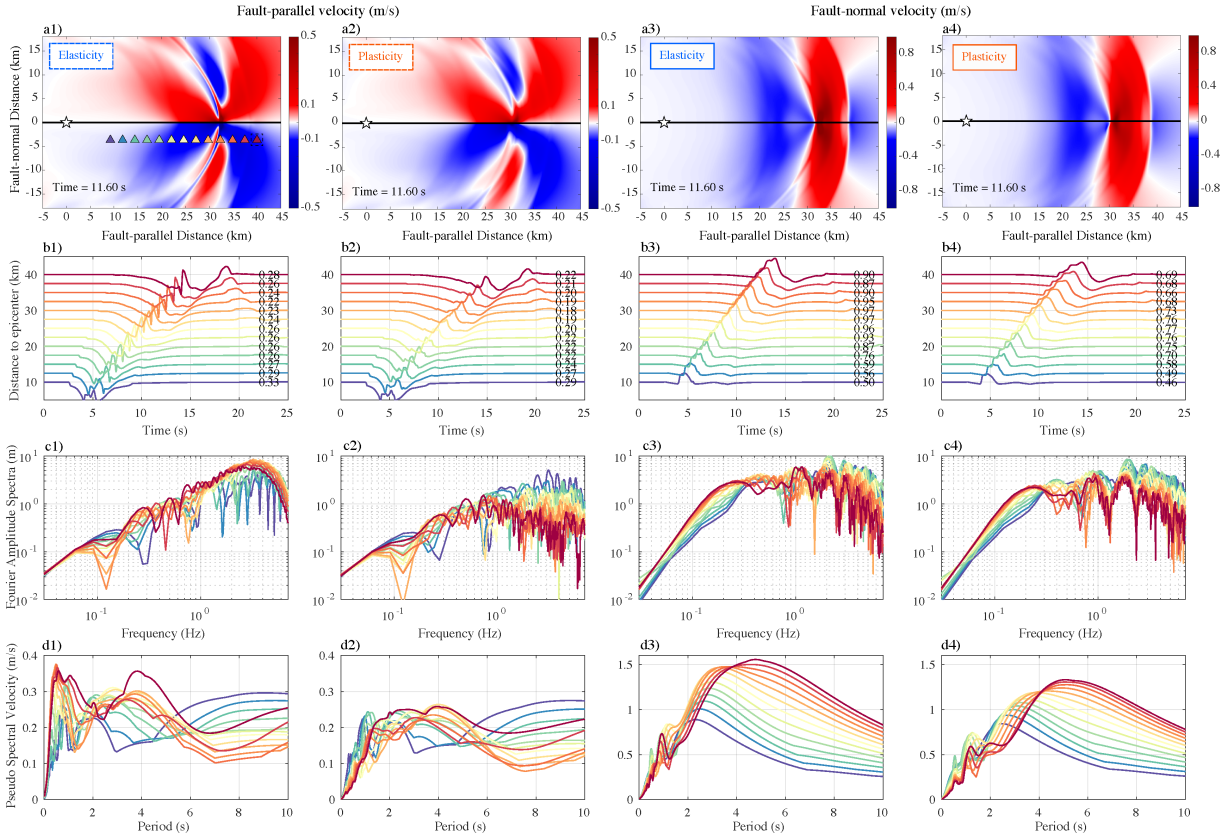

Figure 4.6: a) Snapshots of fault-parallel and fault-normal velocities in elastic and plastic cases. A white star locates the epicenter and a black solid line shows the fault trace. The stations are 3 km away from the fault trace. b) Time series of fault-parallel and fault-normal velocities of stations denoted by colored triangles in Figure 4.6a1. Numbers on the right side indicate PGV of each trace. c) Fourier amplitude spectra (FAS) of times series in Figure 4.6b. d) 5%-damping pseudospectral velocities (PSV) corresponding to those time series.

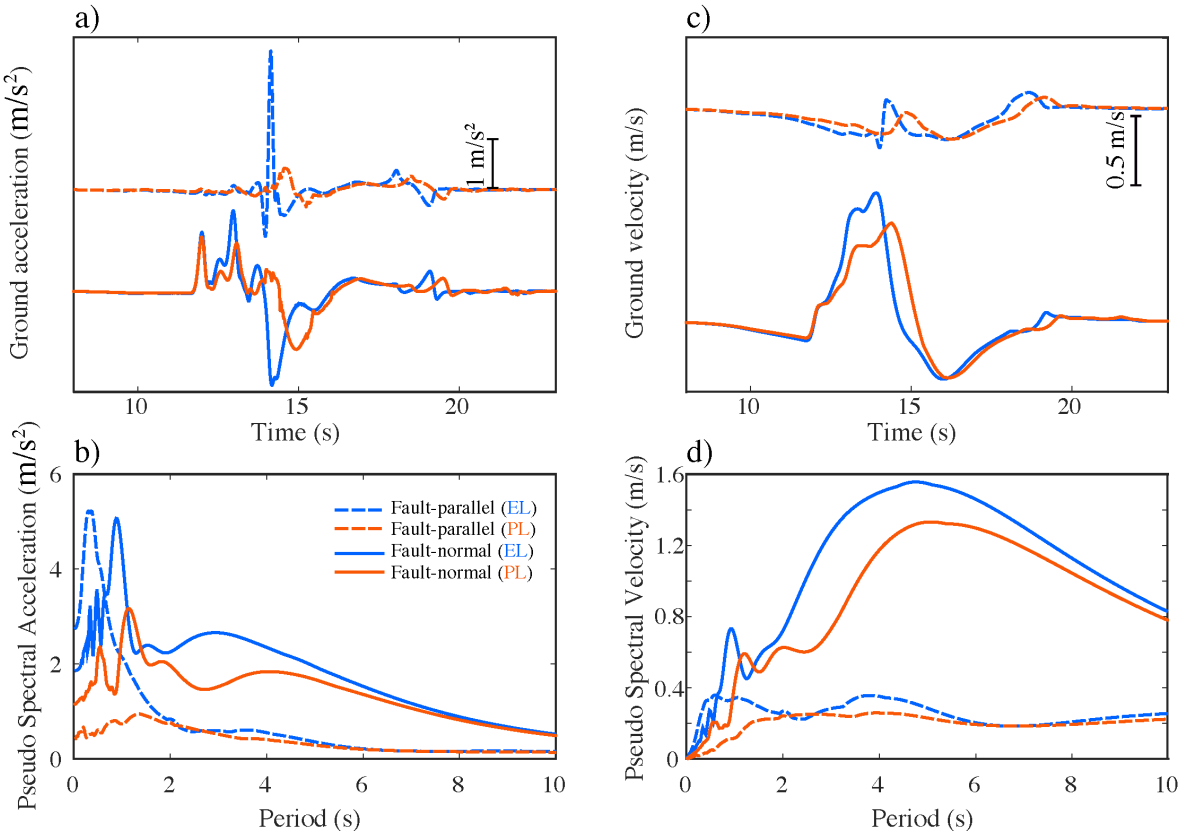

Figure 4.7: a) Fault-parallel and fault-normal accelerations at the distant (dark red rightmost triangle in Figure 4.6a1) station in elastic and plastic cases. b) 5%-damping pseudospectral acceleration of fault-parallel and fault-normal components in elastic and plastic cases. c) Fault-parallel and fault-normal velocities and d) 5%-damping pseudospectral velocities in elastic and plastic cases. Solid and dashed lines denote fault-normal and fault-parallel components, respectively. Blue and orange colors denote elastic and plastic cases, respectively.

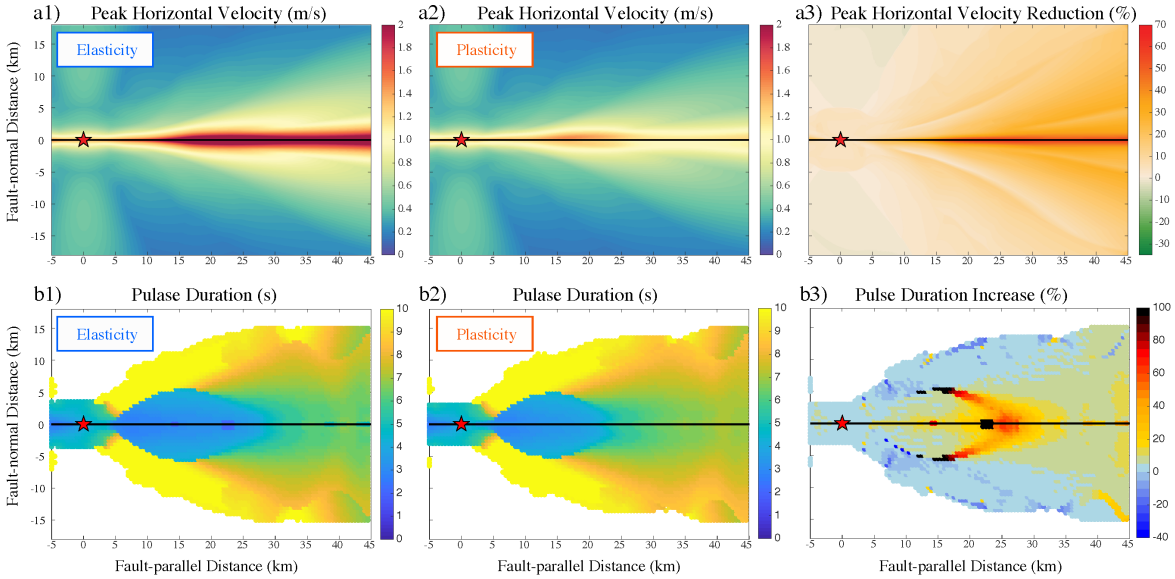

Figure 4.8: a) Peak horizontal velocity (PGV) of the a1) elastic and a2) plastic cases, and their a3) difference as a percentage. b) Pulse duration of the b1) elastic and b2) plastic cases, and their b3) difference as a percentage.

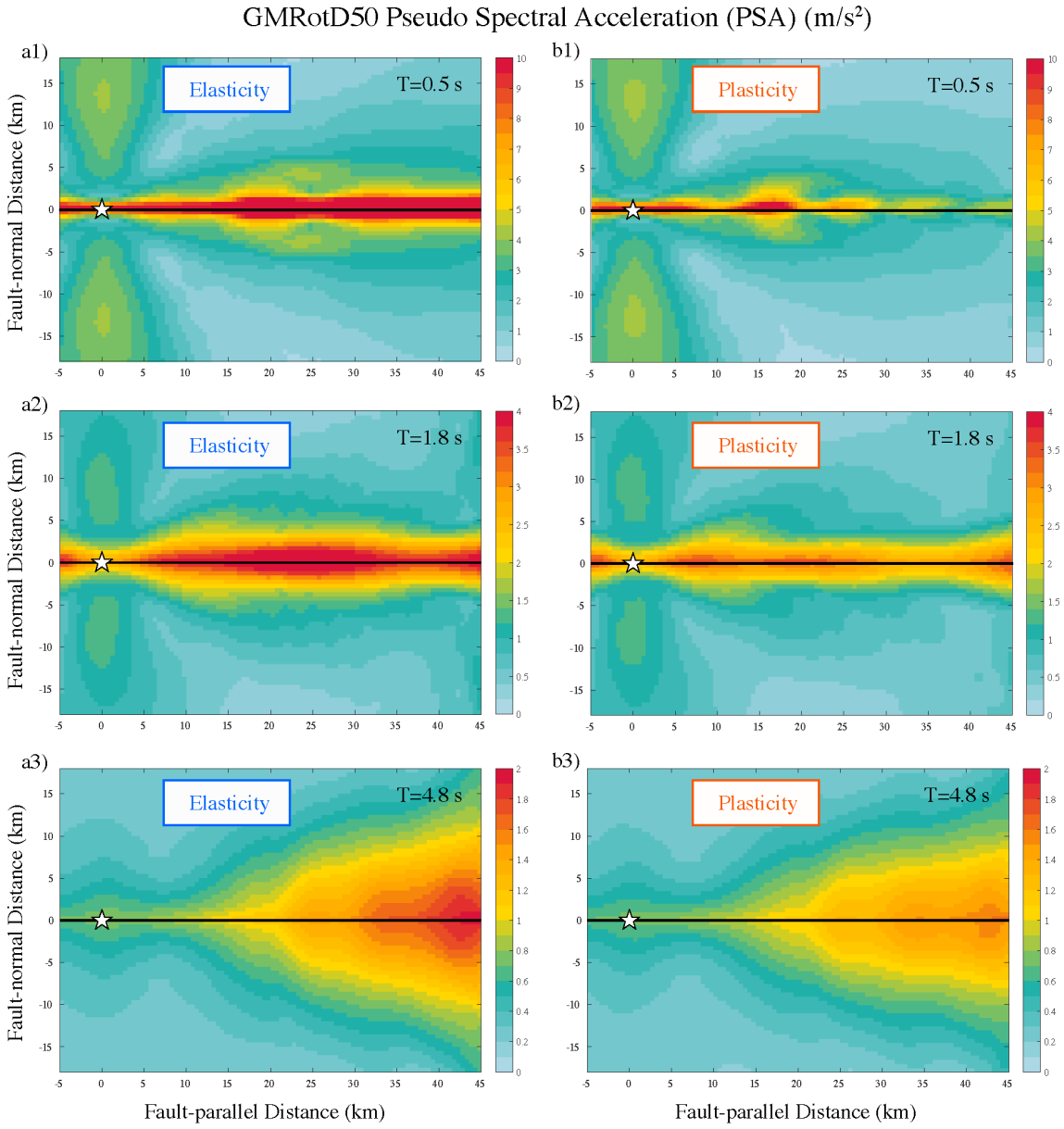

Figure 4.9: a) RotD50 maps of 5%-damping Pseudospectral acceleration (PSA) at a1) 0.5 s, a2) 1.8 s and a3) 4.8 s in the elastic case. b) RotD50 5%-damping Pseudospectral acceleration (PSA) at b1) 0.5 s, b2) 1.8 s and b3) 4.8 s in the plastic case

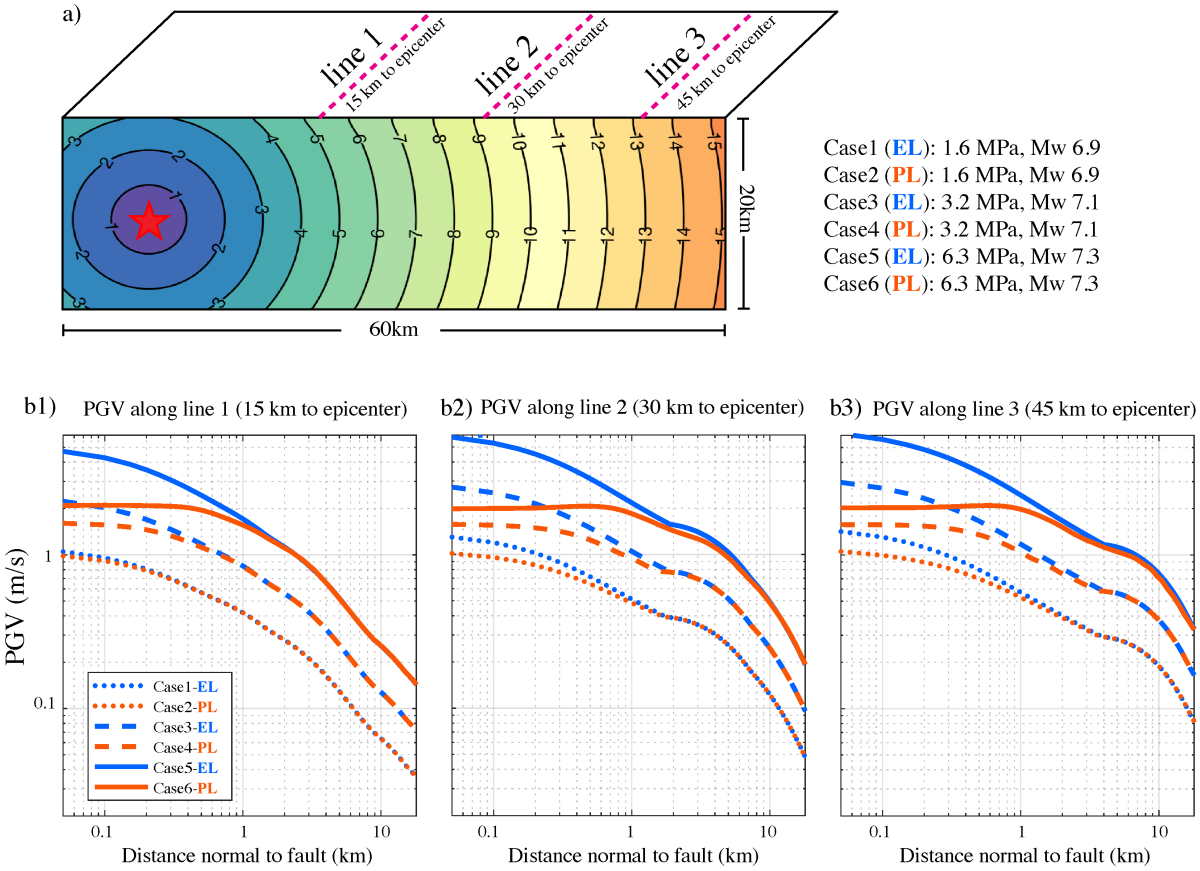

Figure 4.10: a) Quasi-dynamic rupture model setup. Rupture-front time contours are plotted on the fault plane, showing the prescribed constant rupture velocity (90% shear wave speed). 6 elastic and plastic cases with 3 variable prescribed stress drops are simulated. Resultant magnitudes are labeled. b) Peak horizontal velocity (PGV) along the normal-to-fault lines at along-strike distances of b1) 15 km, b2) 30 km and b3) 45 km from the epicenter.

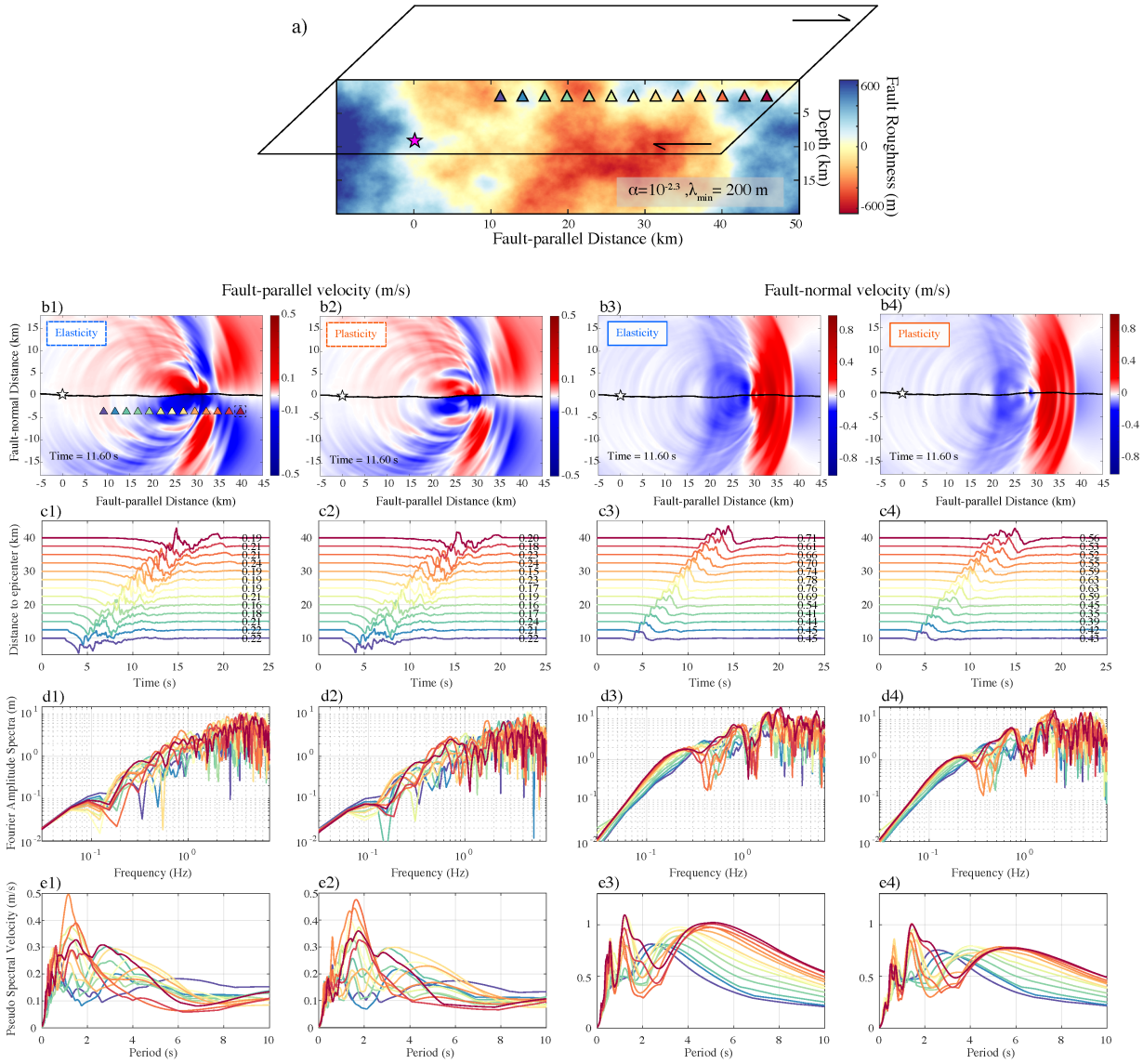

Figure 4.11: a) Fault roughness realization ($\alpha = 10^{-2.3}$ and minimum wavelength, λ_{min}=200 m). b) Fault-parallel and fault-normal velocity snapshot at t = 11.6 s in elastic and plastic cases. c) Fault-parallel and fault-normal velocity time series at stations denoted by triangles in b1. The colors of subsequent synthetic recordings and stations are consistent hereafter. d) Fourier amplitude spectra (FAS) of fault-parallel and fault-normal velocity time series in elastic and plastic cases. e) Fault-parallel and fault-normal pseudospectral velocity (PSV) with a 5% damping. Locations of station line in Figure 4.11b1 are identical to Figure 4.6a (3km to the mean fault trace).

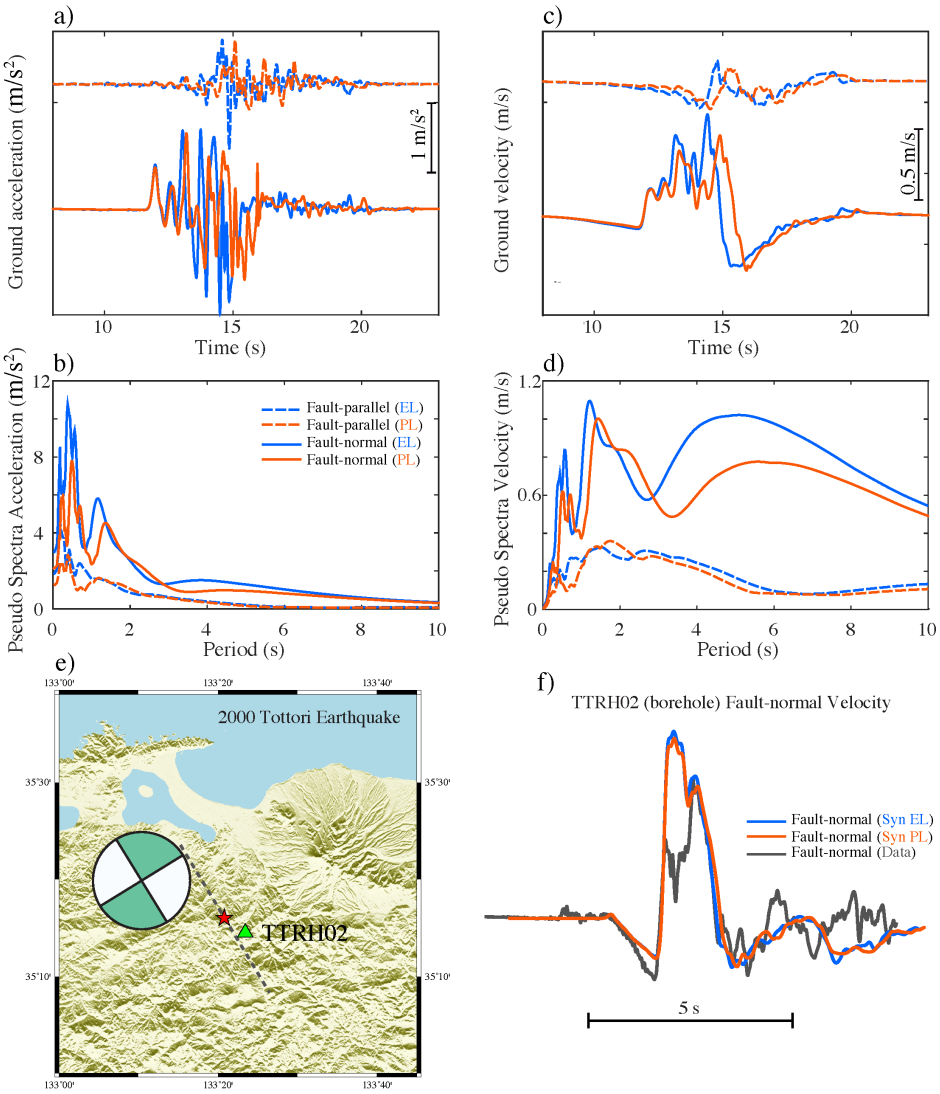

Figure 4.12: a) Fault-parallel and fault-normal accelerations at the distant (dark red rightmost triangle in Figure 4.11b1) station in elastic and plastic cases. b) 5%-damping pseudospectral acceleration of Fault-parallel and fault-normal components in elastic and plastic cases. c) Fault-parallel and fault-normal velocities and d) 5%-damping pseudospectral velocities in elastic and plastic cases. Solid and dashed lines denote fault-normal and fault-parallel components, respectively. Blue and orange colors denote elastic and plastic cases, respectively. e) Location map for 2000 Tottori earthquake. f) Gray solid line indicates an observed fault-normal velocity trace at a site of TTRH02 (borehole) in the 2000 Tottori earthquake.

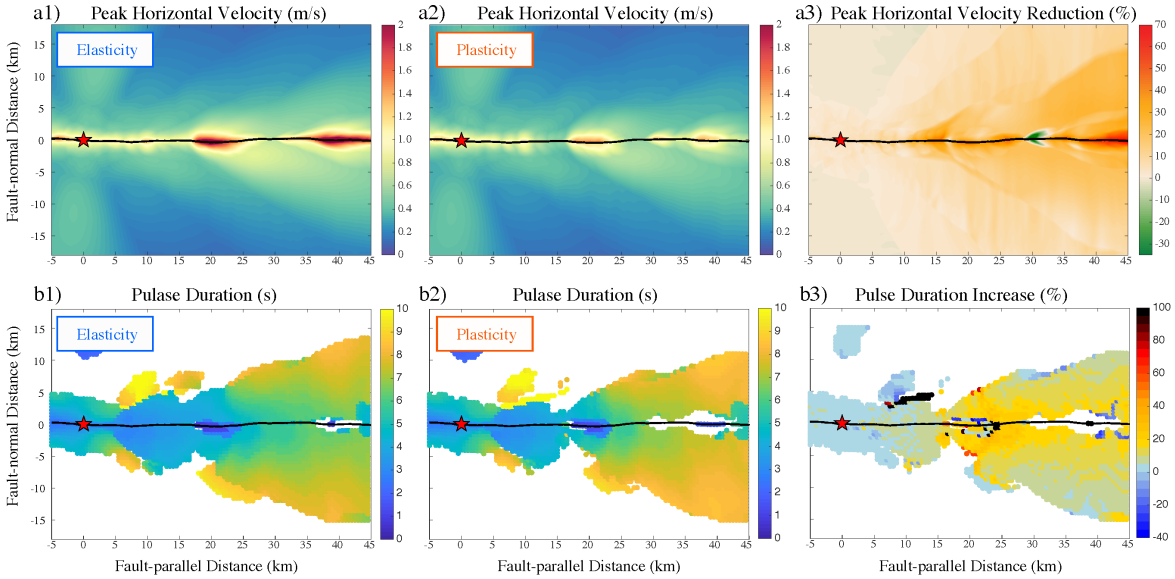

Figure 4.13: a) Peak horizontal velocity (PGV) of the a1) elastic and a2) plastic cases, and their a3) difference as a percentage in the rough fault scenario. b) Pulse duration of the b1) elastic and b2) plastic cases, and their b3) difference as a percentage in the rough fault scenario.

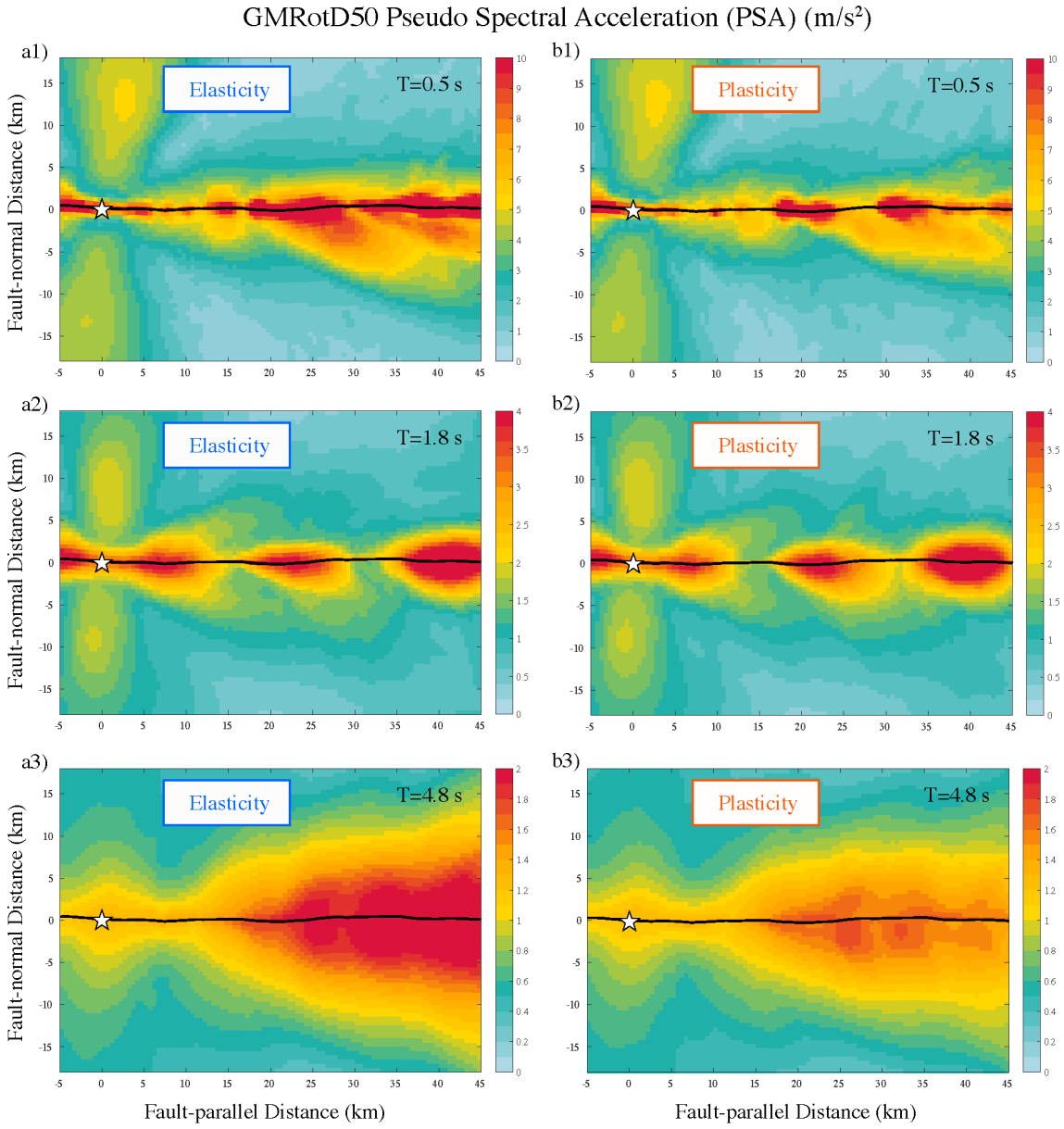

Figure 4.14: a) RotD50 maps of 5%-damping pseudospectral acceleration at a1) 0.5 s, a2) 1.8 s and a3) 4.8 s near a rough fault in the elastic case. b) RotD50 5%-damping pseudospectral acceleration at b1) 0.5 s, b2) 1.8 s and b3) 4.8 s near a rough fault in the plastic case.

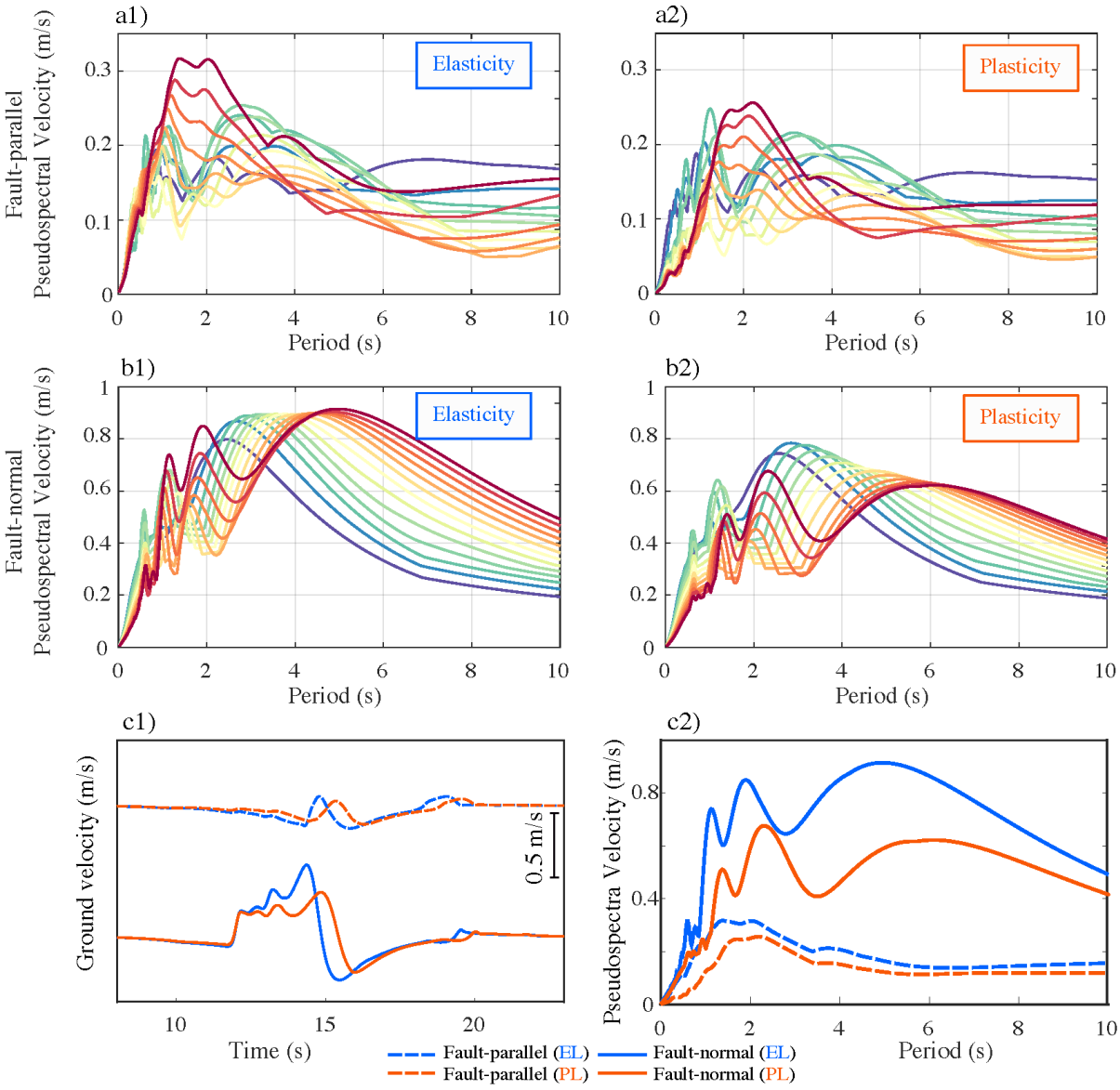

Figure 4.15: a) Fault-parallel and b) fault-normal pseudospectral velocities in both elastic and plastic cases in the self-healing rupture scenarios. c) Fault-parallel and fault-normal velocities at the most distant station (dark red triangle in Figure 4.6a), and their pseudospectral velocities.

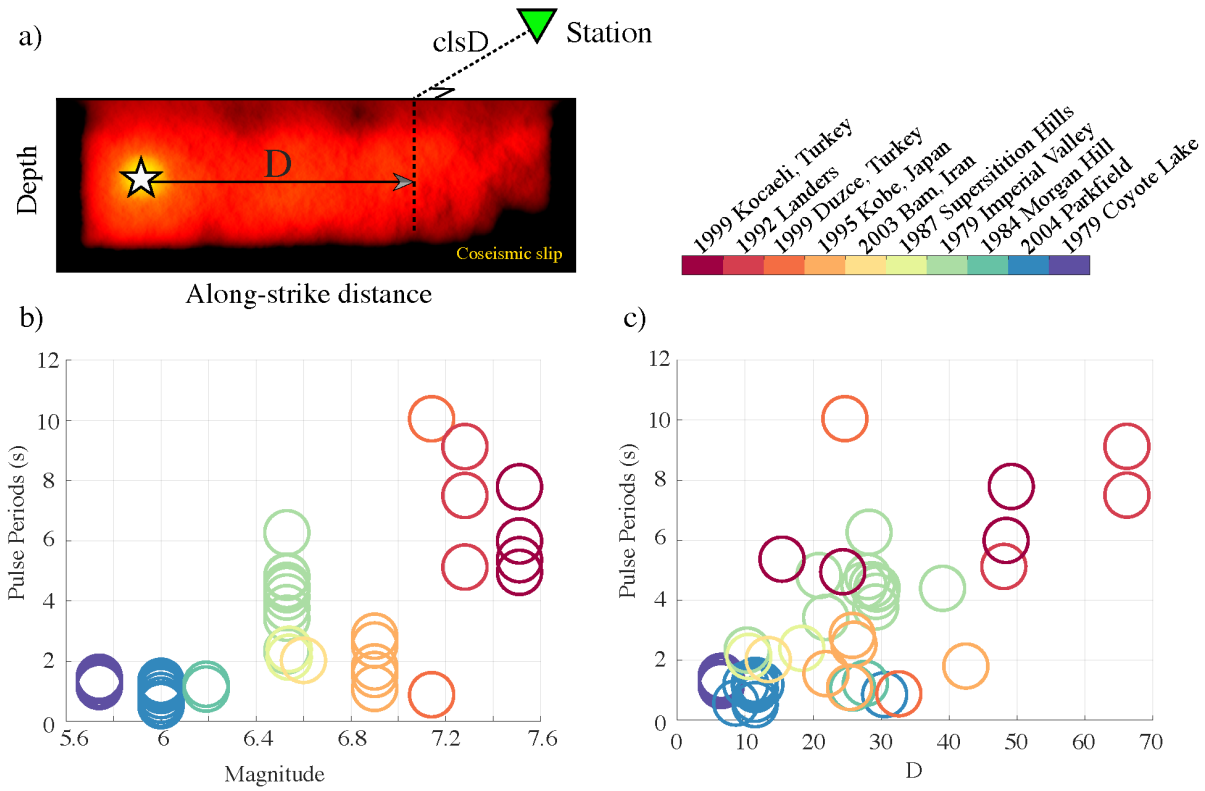

Figure 4.16: a) Conceptual definition of rupture length parameter D, the length of the fault that ruptures toward the site. b) The relationship between pulse periods and magnitudes of 10 strike-slip earthquakes. c) The relationship between pulse periods and D for 10 strike-slip earthquakes.

Supplementary Material

4.6.3 Text S4.1

As seen in Figure S4.1a (also Figure 4.5b), the earlier supershear slip pulse is concurrently arrested by hypocentral S wave (white dashed lines in Figure S4.1). Seen in Figure S4.1b, a stress shadow between preceding supershear slip pulse and main rupture front emerges, which even lower than initial shear stress (also see Figure S4.1d). This stress shadow behind S wave is due to a "forbidden regime" of rupture velocity that the rupture velocity between Rayleigh and shear wave speed is not energetically permitted for Mode II crack. This shadow is more preeminent near free than in depth (Figure S4.1d). Additionally, the free surface incurs a conversion from S wave to P wave (Figure S4.1c and S4.1e), which increase shear stress leading to the aforementioned very shallow supershear slip pulse. Thus, the rupture forbidden regime and free surface together form the rupture behaviors preceding the main rupture front.

Table S4.1: Model setup and discretization of 5 kinematic rupture models

Parameter name	Value
Fault-parallel length	60 km
Fault-normal length	20 km
P wave speed	6,000 m/s
S wave speed	3,464 m/s
Density	2,670 kg/m^3
Static slip	5 m
Viscosity	4×10^{-4}s
Discretization	Value
Δx	50 m
Δt	0.004s
Duration	25 s

Table S4.2: Parameter values for the 5 models. For Cases 1 to 3, the rupture velocity and rise time are set constant. In Case 4, the rupture velocity increases from 0.6 S wave speed at the hypocenter to 0.9 S wave speed at the rightmost end of the fault. In contrast, the rupture velocity in Case 5 decreases from 0.9 to 0.6 S wave speed. In both cases, the rise times are invariant.

Model name	Rupture velocity ($\times$ S wave speed)	Rise time (s)
Case 1	0.8	2
Case 2	0.9	2
Case 3	0.8	1
Case 4	Linearly increase from 0.6 to 0.9	1
Case 5	Linearly decrease from 0.9 to 0.6	1

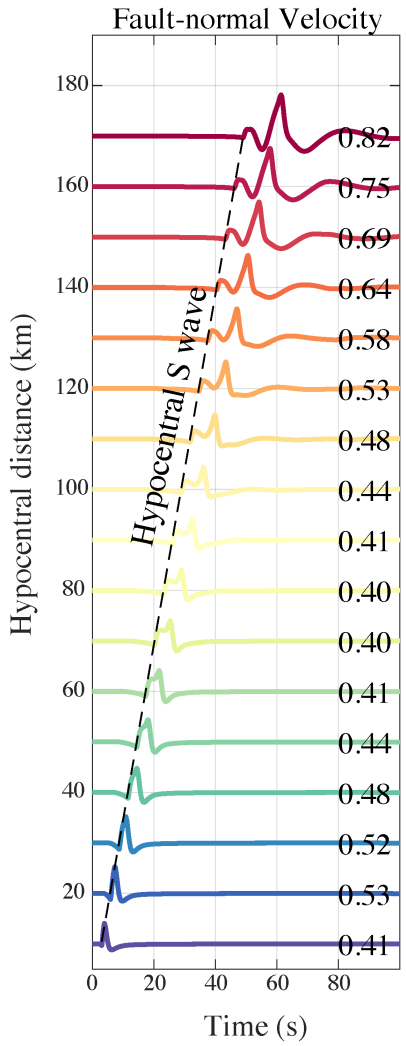

Figure S4.1: a) Fault-parallel and b) fault-normal velocity time series (at 3 km distance normal to fault line) radiated from a long strike-slip fault. Rupture velocity and rise time are identical to Case 1 in Figure 4.3. Numbers labeled at the ends of traces are peak amplitudes of the time series in m/s

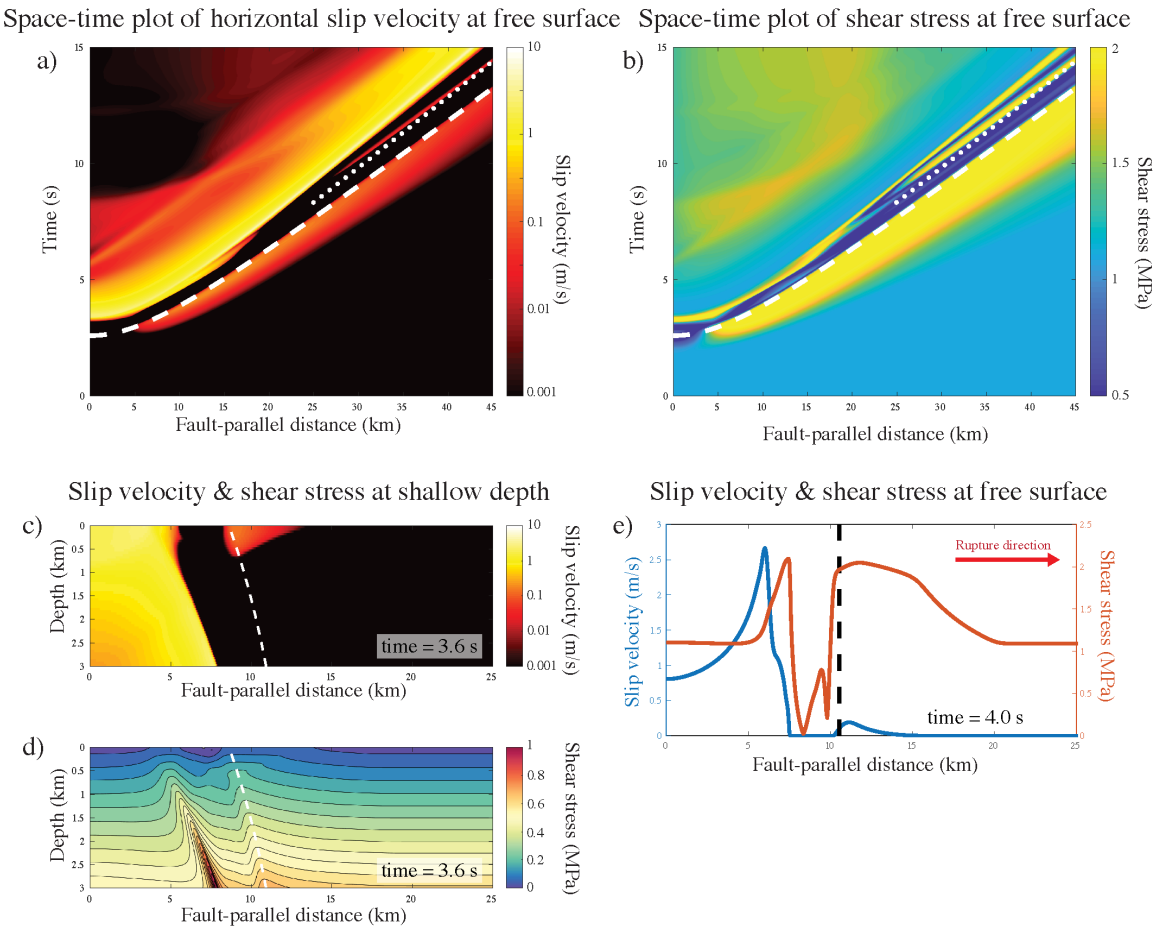

Figure S4.2: a) Space-time plot of slip velocity at free surface in the elastic case (identical to Figure 5b1). b) Space-time plot of shear stress at free surface in the elastic case. c) Slip velocity snapshot at a shallow depth (0-3 km deep). d) Shear stress snapshot at a shallow depth (0-3 km). In foregoing figures, white dashed lines denote hypocentral S wave and white dotted lines denote Rayleigh wave speed. e) Slip velocity and shear stress along strike at time = 4 s. A black dashed line denotes the location of the hypocentral S wave front at free surface and when time is 4 s.

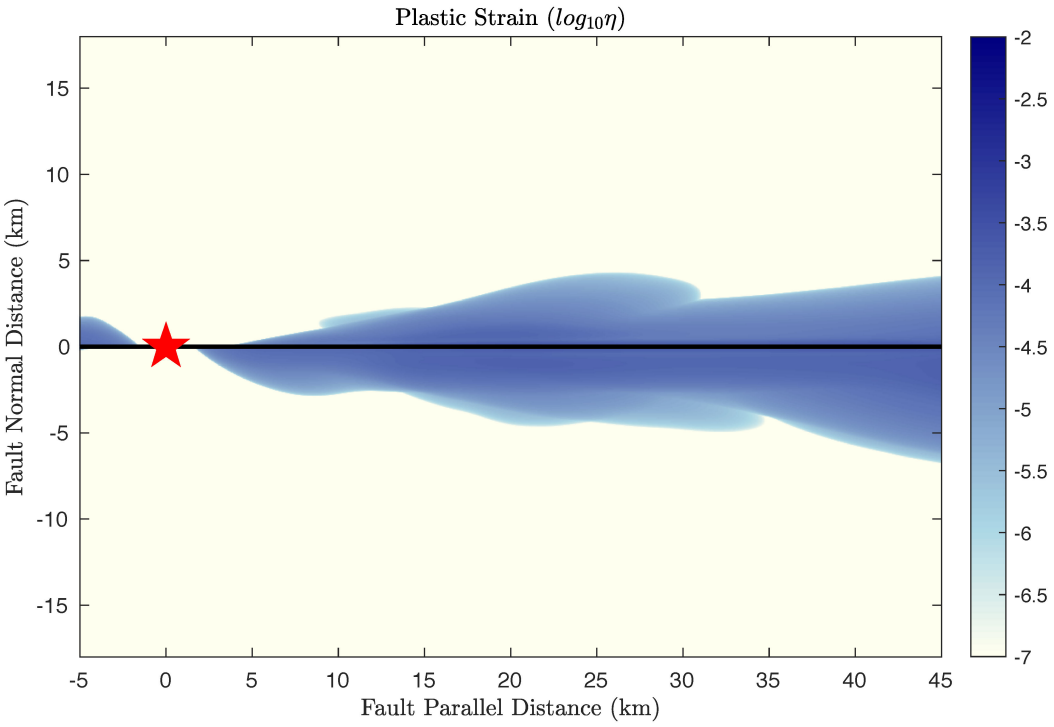

Figure S4.3: Accumulated plastic strain on the free surface. The calculation of plastic strain can be found in Appendix of Wang et al. [2019]

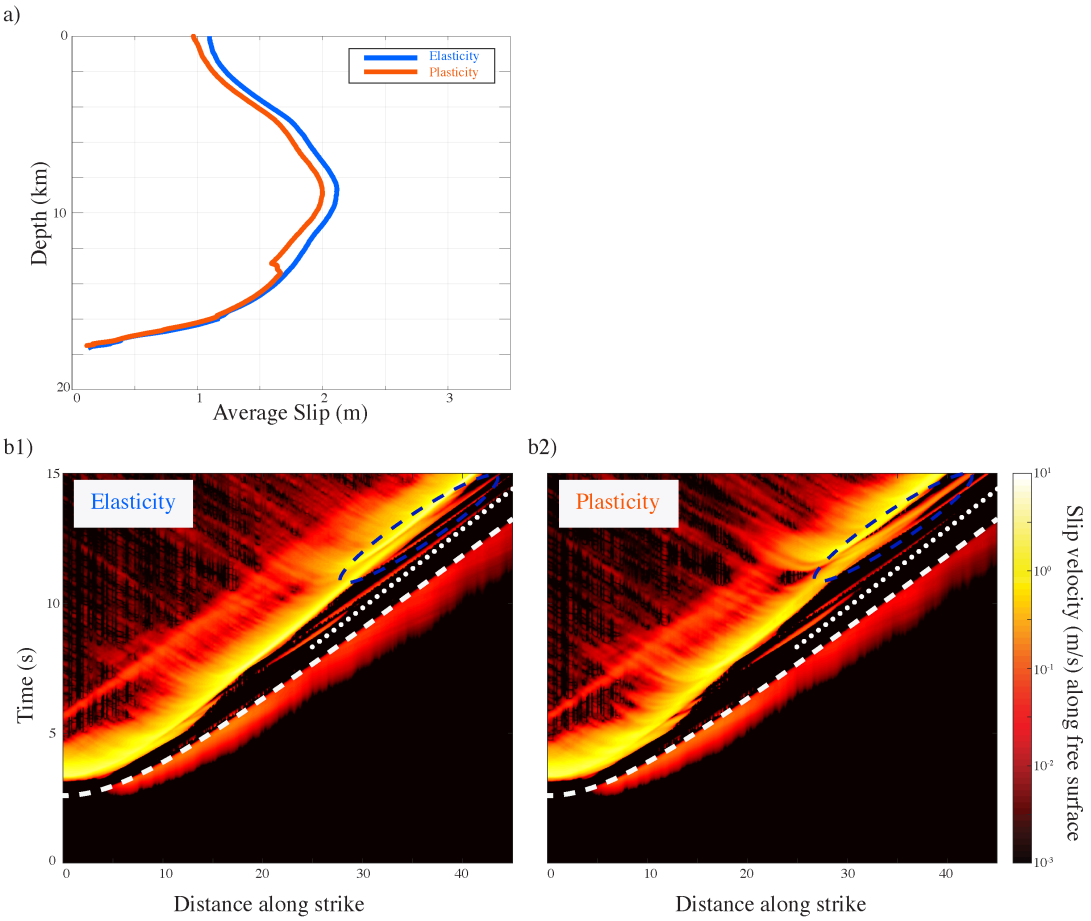

Figure S4.4: a) Along-strike averaged slip profiles versus depth and b) space-time plot of surface slip velocities on a rough fault plane, in elastic and plastic cases. White dashed lines indicate travel-time curves of the hypocentral S wave. White dotted lines indicate the Rayleigh wave speed. Blue dashed circles enclose an enhanced rupture feature associated with off-fault plasticity.

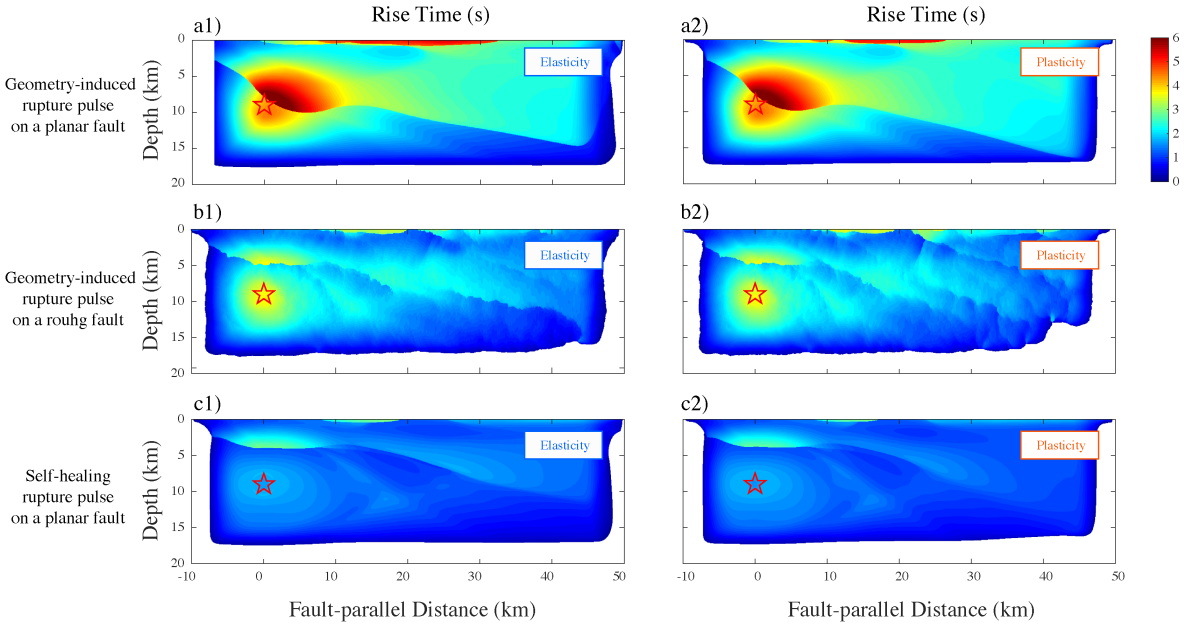

Figure S4.5: Rise time distribution on the fault plane in a) geometry-induced rupture pulse on a planar fault, b) geometry-induced rupture pulse on a rough fault, and c) self-healing rupture pulse on a planar fault.

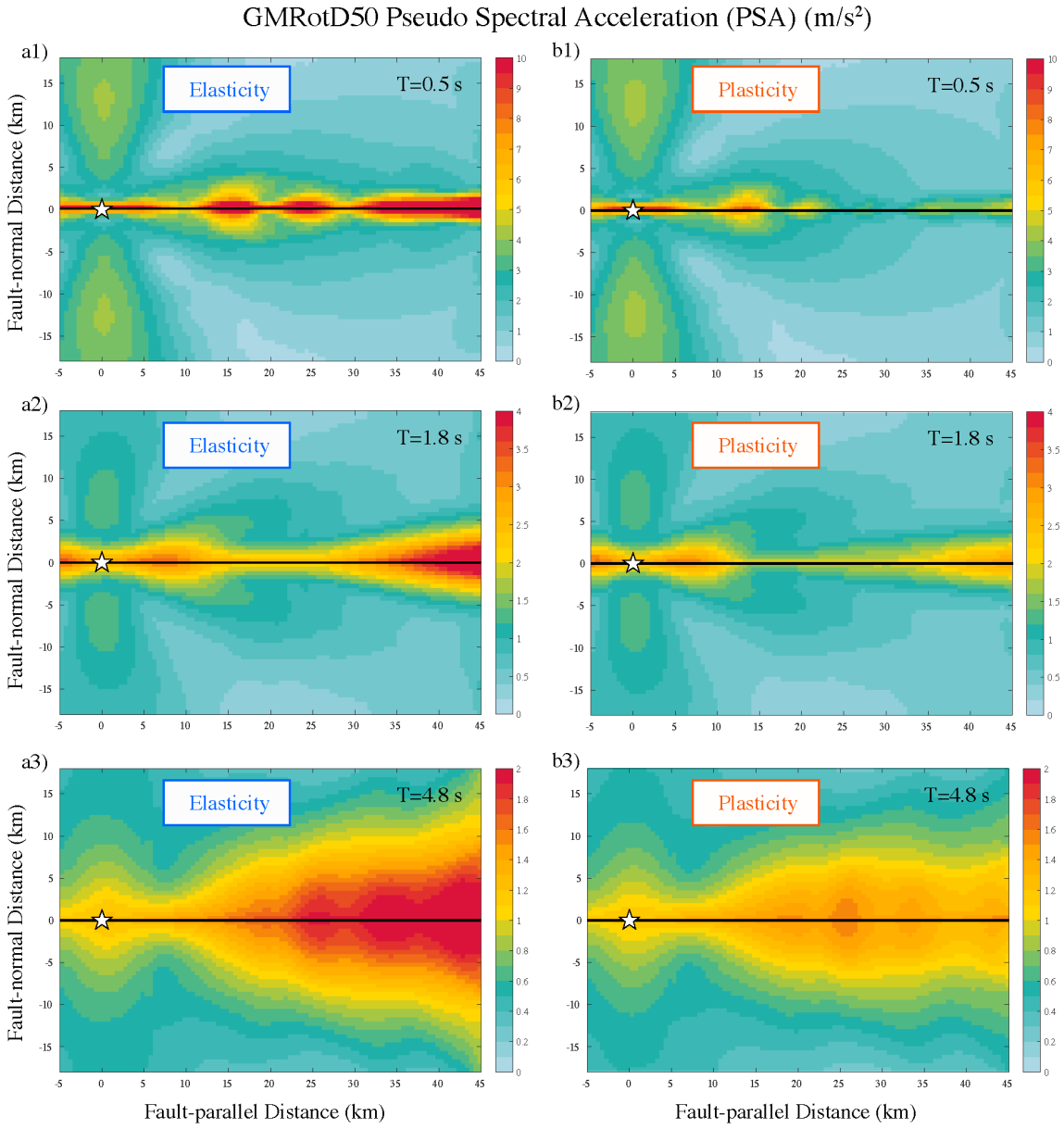

Figure S4.6: a) RotD50 maps of 5%-damping PSA at a1) 0.5 s, a2) 1.8 s and a3) 4.8 s near a self-healing rupture in the elastic case. b) RotD50 5%-damping PSA at b1) 0.5 s, b2) 1.8 s and b3) 4.8 s near a self-healing rupture in the plastic case.